Title
Understanding Grafted Cations in Controlled Environments for Heterogeneous Catalysis

Author
Grosso Giordano, Nicolas Andres

Publication Date
2019

Understanding Grafted Cations in Controlled Environments for Heterogeneous Catalysis

By

Nicolas Andres Grosso Giordano

A dissertation submitted in partial satisfaction of the

requirements for the degree of

Doctor of Philosophy

in

Chemical Engineering

in the

Graduate Division

of the

University of California, Berkeley

Committee in charge:

Professor Alexander Katz, Chair
Professor Enrique Iglesia
Professor T. Don Tilley

Fall 2019

Abstract

Understanding Grafted Cations in Controlled Environments for Heterogeneous Catalysis

by

Nicolas Andres Grosso Giordano

Doctor of Philosophy in Chemical Engineering

University of California, Berkeley

Professor Alexander Katz, Chair

Catalytic processes occurring on the surfaces of heterogeneous catalysts are controlled by the molecular structures of active sites where these reactions occur. These active sites can be broadly thought to consist of an active center, where bond making and breaking events occur, surrounding by the surface of the support. These are the inner-sphere (i.e. active center) and outer-sphere (i.e. surface) environments of the active site. Catalyst design typically focuses on the choice of the optimal inner-sphere environment, while surfaces are often regarded as inert oxide supports onto which active sites are dispersed to facilitate catalyst recovery. In this thesis, I demonstrate that the outer-sphere surface environment is, in fact, an essential element for controlling the structure and reactivity of active sites supported on silicates.

The theoretical concepts, silicate supports, and synthetic approaches that are used in this thesis are introduced in Chapter 1. Given the importance of silanol groups as grafting sites in synthetic approaches used in this thesis, I begin by providing a detailed study of silanol speciation across zeotypes and amorphous supports, in Chapter 2. Subsequently, I provide an example of how silanol environments control grafting processes and how crystalline silicates provide stable support environments for Fe^{III} cations, in Chapter 3. I then introduce an approach to synthesizing well-defined active sites by controlling the structure of a grafted cation using an organic ligand, applied to calix[4]arene-Ti^{IV} complexes grafted on amorphous SiO_2 as epoxidation catalysts, in Chapter 4.

Having established the structure of silicates and approaches to synthesize well-defined active sites on their surface, I present three studies where this enables the study of structure and catalytic properties. In Chapter 5, I demonstrate how this approach enables the unambiguous deconvolution of the effect of support outer-sphere on epoxidation catalysis. In Chapter 6, I investigate how the support outer-sphere can also control the conformation and structure of grafted complexes, while providing insight into adsorption processes occurring on surfaces. Finally, in Chapter 7, I provide a detailed mechanistic study of how partially confining outer-sphere environments impact catalytic reactivity for olefin epoxidation.

Taken together, this work provides fresh insights into the structure of silicate supports and their ability to control catalysis, providing an additional and important avenue to the design of heterogeneous catalysts.

To my parents,
For selflessly inspiring us to learn

A mis padres,
por inspirarnos a aprender
incondicionalmente

Table of Contents

Acknowledgements

This thesis represents is the culmination of more than 20 years of education. I do not have the space to acknowledge all the teachers who formed me over the years, but I want to mention the ones without which I would not have ever found a path to Berkeley. I have to especially thank Anne Brearley, my high school chemistry teacher who encouraged me to come to the US for my undergraduate. I also have to thank Prof. Justin Notestein at Northwestern, who early on let me into his lab to learn about catalysis. And in particular, I have to thank Dr. Christian Canlas, who was my first lab mentor and set me in the path to become an independent researcher.

For my thesis, first and foremost I have to thank my advisor Prof. Alexander Katz, who supported, encouraged and mentored me patiently for these five years. A very deep appreciation goes to my co-advisor Dr. Stacey Zones, who has been a fresh source mentorship and inspiration of how to be a well-rounded scientist. Our collaborators, in particular Prof. Hubert Koller and Dr. Simon Bare and their research groups, have been an invaluable source of insight. I also have to thank Dr. Dave W. Small for his patience and education on electronic structure calculations. I am very thankful to the Katz group for their support and continuous discussions, in particular Alex Okrut, who has been there throughout. The CBE staff, in particular Carlet Altamirano and Polly Ng, have been instrumental in navigating five years at Berkeley.

Beyond the academic, my friends have been a constant source of support, intellectual stimulation, and needed distractions in difficult times, in particular Matt Witman, Dogan Gidon, Nathan Haouzi, Gabriel Sanoja, Paloma Navarro, and Jon Lee. My family, especially my parents, who have patiently watched me from afar as I have navigated these years, and have given me unconditional support. Finally, Hannah, who has seen me through it all.

Chapter 1

Introduction: Controlling Catalysis by Designing Molecular Environments Around Active Sites

Reprinted in part with permission from Grosso-Giordano, N. A.; Zones, S. I.; Katz, A. Opportunities for Controlling Catalysis by Designing Molecular Environments around Active Sites: Cations Supported on Amorphous versus Crystalline Zeolitic Silicate Supports. In *Catalysis: Volume 31*, **2019**, 72–126 with permission from the Royal Society of Chemistry.

The molecular architecture of catalytic active sites supported on amorphous silica versus zeolitic silicates is critically examined, with an emphasis of the role that support crystallinity could play on their synthesis, structure, and catalytic properties. First, the structural features and catalytic influences of the inner- and outer- sphere of active sites is discussed, using aluminosilicate zeolite solid-acid catalysts as an example. Then, the contrast of disorder in amorphous silica supports to the order of crystalline zeotypes is presented, and examples are given on how synthesis can be used to control the structure and properties of active sites in these two types of silicates. Particular emphasis is given to delaminated zeotypes as supports, which are used in the remainder or the work in this thesis. Finally, an outline this thesis is presented, which addresses outstanding questions of how to synthetically control the structures and properties of grafted active sites on silicates in order to facilitate understanding of heterogenous catalysts, and facilitate their rational design.

1.1. Introduction

Amorphous silicate supports are extensively used in heterogeneous catalysis, including in industrial processes involving Brønsted- and Lewis-acid catalysis, selective oxidation of hydrocarbons, olefin metathesis, and ethylene polymerization.[1–7] In many of these catalysts, active sites comprise highly dispersed, isolated metal cations grafted on a siliceous (SiO_2) network, with the identity of the cation (i.e. Ti^{IV}, Fe^{III}, Ta^{V}, Al^{III}, etc) being critical for catalysis.[8,9] In this context, siliceous supports are typically regarded as inert oxides onto which active sites are dispersed, mainly to facilitate catalyst recovery and reuse.[10] Yet there are reports that challenge this belief – that the support is inert in catalysis –[11] and support the hypothesis that the molecular environment provided by the silicate support can be a critical and necessary component of the active site and the catalytic mechanism, affecting both rate and selectivity of reactions.

This hypothesis – that the silicate support is critical for catalysis – has been demonstrated for the case of Ti^{IV}-catalyzed olefin epoxidation (discussed in Chapters 4, 5, and 7), which we describe here as a prelude to more detailed discussion in the rest of this thesis. Coordinatively saturated (i.e. octahedral) Ti^{IV} centers as found in bulk TiO_2 are known to be inactive for epoxidation, as are low-coordinate (i.e tetrahedral) Ti^{IV} centers in solution (i.e. homogeneous catalysts). Yet, such low-coordination tetrahedral Ti^{IV} centers become highly active for epoxidation with organic hydroperoxides (and are currently used industrially as such) when grafted onto amorphous silica supports in Ti/SiO_2 catalysts.[1,12,13] However, when these tetrahedral Ti^{IV} centers are dispersed inside a crystalline zeotype framework, as in TS-1 zeotypes (Ti-MFI), activity is poorer, despite the identical elemental composition of TS-1 to Ti/SiO_2.[14] These effects on the catalytic properties of Ti^{IV} illustrate how (i) the presence of a support surface can change the reactivity of an isolated metal center relative to its properties as a homogeneous catalyst, and (ii) the structure of the silicate support, while remaining compositionally-identical, can also have profound catalytic consequences.

The goal of this chapter is to conceptually introduce how silicate supports affect the architecture (i.e. structure) of active sites. Understanding this active site architecture is critical to understanding how the silicate support can be an integral part of these active site, and how it can be synthetically tuned, which is the aim of the remainder of my thesis. I first summarize the key features defining the environment and surface architecture of an active site on a silicate support, using Brønsted acid aluminosilicate zeolite catalysts as an example of a system where the role of inner- vs. outer-sphere on catalysis is well understood. I then introduce the contrast between disordered amorphous vs. crystalline zeolitic silicates, which act as supports of identical elemental composition but different molecular structure and order. This contrast between amorphous and crystalline silicate supports is a central approach in the work in this thesis. In particular, I propose that catalyst design could be aided by moving away from traditional amorphous supports, and making use of 2-dimensional zeolites as supports instead. These materials, which combine accessibility of active sites on their external surface with a well-defined crystalline surface environment,[15–17] are therefore also introduced. Finally, I present an outline of this thesis and its constituent chapters, which helps understand how molecular environments influence catalytic active sites supported on silicates, and how these structures may be controlled through synthesis.

1.2. The Molecular Environment of a Grafted Cation Active Site on a Silicate Surface: Inner- vs. Outer-Spheres

The support effects described in the introduction for Ti^{IV}-catalyzed epoxidation (section 1.1) originate from the role of the support in defining the structural details and coordination environment within and surrounding a catalytically active site. We refer to this as the molecular-scale *architecture* of the active site. This architecture is defined by both (i) the specific geometrical arrangement of ligands bound to the active center (e.g a Ti^{IV} metal cation in the example above), together with (ii) the surrounding support structures and surface moieties that are not covalently bound to the metal center. We broadly define these two components of active site architecture, which are schematically represented for an isolated cation grafted on a silicate surface in Scheme 1.1., as:

(i) the *inner-sphere environment* of the active site, which consists of the 1st coordination shell of ligands directly bound to the cation, including those that anchor the cation to the solid support (SiO^-), as well as ligands remaining from the cation precursor used for synthesis, any coordinated solvent molecules, or any reactive intermediates (during catalytic activity); and

(ii) the *outer-sphere environment* of the active site, consisting of structures and functional groups that are not directly coordinated to the cation and lie beyond the first coordination sphere. These include the bulk chemical composition of the support itself (SiO_2 together with any other modifiers), silanol (SiOH) groups present on the support surface, and structural features such as pores, pockets, or siloxane rings. Differences in outer-sphere environments between amorphous and crystalline zeotype supports will be discussed in detail in sections 1.3.

Scheme 1.1. The molecular environment of a cation grafted on a siliceous surface: inner- and outer-spheres

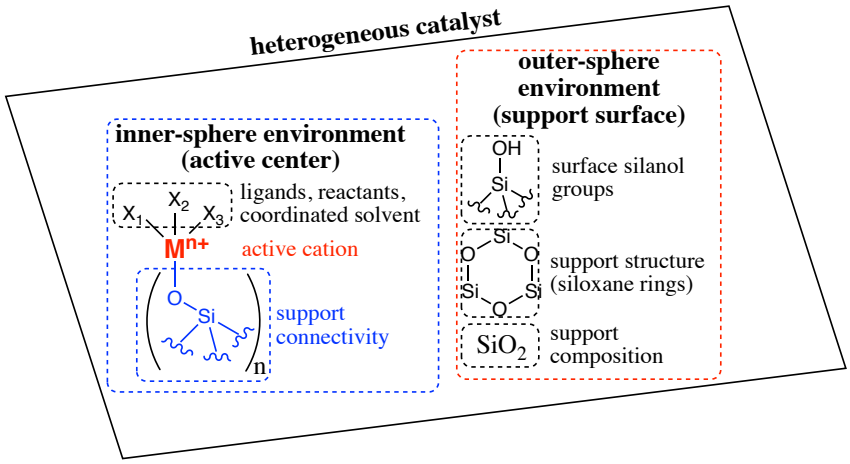

Both the inner- and outer-sphere affect active site architecture and can, in principle, mediate catalytic activity. Inner-sphere environments tend to be more easily characterized because they involve changing the identity of the support or the cation coordination environment, which are properties that typically affect the physicochemical and spectroscopic characteristics of the cation in a sensitive manner.[18–21] The effects of outer-sphere environments on structure and reactivity

are typically more difficult to characterize because conventional spectroscopic techniques (EXAFS, UV-visible spectroscopy, etc.) typically probe only the inner-sphere ligands of a grafted cation, rather than effects of the surrounding support environment that is not directly bonded to the cation.[22,23] In amorphous materials, these environments are significantly difficult if not impossible to study because of the inherent disorder and structural heterogeneity of their surface structures, which may even be changing at temperatures relevant to some catalytic applications.

Inner- and outer-sphere effects on catalysis are well-established in Brønsted acidic zeolites, where environments within pores gives rise to shape-selectivity and confinement effects. We therefore discuss these effects in section 1.2.1 as an introduction to inner- vs. outer-sphere control on catalysis.[7,24–27] These types of effects may also extend to many other catalytic systems, but their current understanding is limited because of challenges in synthetically controlling the structure of silicate supports in a manner that is conducive to studying the effect of active-site architecture on reactivity.

1.2.1. Inner-Sphere vs. Outer-Sphere Effects on Catalysis: Brønsted Acid Catalysis by Aluminosilicates

In aluminosilicates, the substitution of a tetrahedrally coordinated Al^{III} cation into an otherwise siliceous network ($Si^{IV}O_2$) introduces a negative charge that is balanced by a H^+, as represented in scheme 1.2. This leads to Brønsted acidity,[7,28] responsible for the catalytic activity of aluminosilicates, which are used ubiquitously in industry for acid catalysis. Among aluminosilicates, zeolites represent a class of materials that are crystalline and microporous, adopting well-established crystalline framework topologies.[29] They have successfully replaced hazardous mineral acid catalysts, as illustrated by the replacement of HF with zeolites in several petrochemical conversions,[30] thereby helping improve safety and economics, even in established industrial processes such as aromatic alkylation.[31] In principle, both amorphous and zeolite aluminosilicates can perform Brønsted acid catalysis; nevertheless, the versatility and synthetic control over zeolite structures that enables tuning of reaction pathways through shape selectivity and confinement effects of zeolite micropores (see Section 1.2.1.2), has led to the replacements of amorphous catalysts by zeolites for most applications.[32]

Scheme 1.2. Schematic representation of a Brønsted acid site in an aluminosilicate.

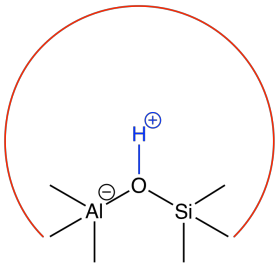

The acidic proton in blue. The surrounding pore structure, responsible for outer-sphere effects, is represented in red.

1.2.1.1. Effects of Inner-Sphere Environments

The inner-sphere environment of Al^{III} in Brønsted acidic aluminosilicates consists of tetrahedral coordination of Al^{III} by four $\equiv SiO^-$ ligands of the silicate framework ($Si^{IV}O_2$), which results in a negative charge that gives rise to a charge-balancing acidic proton, shown in Scheme 1.2. Trigonal (instead of tetrahedral) inner-sphere coordination of Al^{III}, which is also favored given its trivalent state, does not result in this charge imbalance or the associated proton, and instead gives rise to Lewis acid centers that are not active for Brønsted acid catalysis.[33] Thus, uniform tetrahedral coordination in Al^{III} inner-sphere environments is essential to achieving a high density of strongly acidic active sites in aluminosilicates. This occurs more readily in crystalline zeolites rather than in amorphous aluminosilicates, because in the former Al^{III} is located at uniform tetrahedral crystalline T-site framework positions within a stable zeolite framework, whereas tetrahedral coordination of Al^{III} occurs much less frequently in amorphous materials. Because of their structural order as part of a uniform crystalline framework, acid-site in zeolites are uniform, in contrast to the nonuniformity observed in amorphous disordered aluminosilicates. This is experimentally demonstrated by examining differential heats of NH_3 adsorption as a proxy for acid site environment.[34] For a given zeolite framework, a plateau in differential heats of NH_3 adsorption with surface coverage is observed, indicating uniform acid site envrioment (i.e. the heat of adsorption does not change as more acid sites are titrated); in contrast, no such plateau is seen in amorphous aluminosilicates, indicating a nonuniform distribution of acid site enviorments.[34]

The acid strength of a Brønsted acidic proton in zeolites depends on its deprotonation energy, which reflects the energy required to separate a H^+ from its conjugate anion (where the negative charge is located in the zeolite framework) to non-interacting distances..[35,36] Following earlier work by the group of Sauer,[35,37] Jones and Iglesia used periodic density functional theory calculations to elegantly show that these energies, when properly averaged around all four framework oxygens adjacent to a tetrahedral Al^{III} atom and across all T-atom positions within a zeolite framework, are independent of the framework topology, and simply reflect the presence of Al^{III} within a tetrahedral silicate inner-sphere, independent of its surrounding (outer-sphere) molecular environment.[36] Thus, for inner-sphere environments consisting of tetrahedrally coordinated Al^{III} centers, the associated Brønsted-acid site strength is essentially the same in all zeolites. These acid sites of similar strengths are expected to give similar rates of reactions, independent of the specific zeolite framework topology. In reality, however, the unique pore topologies in zeolites lead to outer-sphere effects that are separate from inner-sphere (acid-strength) effects and can radically alter catalytic activity and selectivity.

1.2.1.2. Effects of Outer-Sphere Environments

Zeolite frameworks exhibit a variety of micropore topologies, including straight and sinusoidal pores, windows, cages, etc., with typical pore openings of the order ~ 4 Å (small pore) to 8 Å (large pore; extra-large pore zeolites also exist with larger micropores).[38] These dimensions approach those of molecules which react at Brønsted acid sites within pores, and can thus dramatically affect catalytic properties, despite Brønsted acid sites having essentially the same intrinsic inner-sphere (acid strength),[7,24] as measured by the deprotonation energy.[36] These *outer-sphere effects* in Brønsted-acid catalysis originate from steric constraints imposed on reactants

and products by pore openings, and from noncovalent interactions occurring between reactants and transition states with the pore walls; these lead to shape selectivity and confinement effects, respectively. These effects have been examined in detail elsewhere,[7,24–27] and are only briefly mentioned here as an illustration of outer-sphere effects on catalysis.

Briefly, shape selectivity effects are schematically illustrated in Scheme 1.3, as summarized in Csicsery's classic paper.[25] Shape selectivity occurs when zeolite pores approach the molecular dimensions of reactants and products, thereby affecting their diffusion, configuration, and reactivity. This can occur in the form of (i) reactant, (ii) product, or (iii) transition state selectivity. (i) *Reactant shape selectivity* occurs when only reactant molecules that are smaller than pore openings can diffuse into pores to reach active sites, resulting in the exclusion of reactants larger than the pore opening; (ii) *product shape selectivity* occurs when only products that are smaller than the molecular dimensions of the pores can diffuse out, resulting in selectivity for products smaller than pore openings; and (iii) *restricted transition state selectivity* occurs when reactions are precluded from occurring because the transition state involved requires more space than that available within the pores,[25] leading to the suppression of reactions that proceed through those transitions states. This latter may explain why 10-MR zeotype titanosilicates are not able to catalyze epoxidation with organic hydroperoxides, despite all individual reactants being small enough to access pores.[14] These steric effects therefore discriminate tune reactivity based on the shape of molecules in relation to pore environments.

Scheme 1.3. Shape selectivity effects from zeolite pores on catalysis.

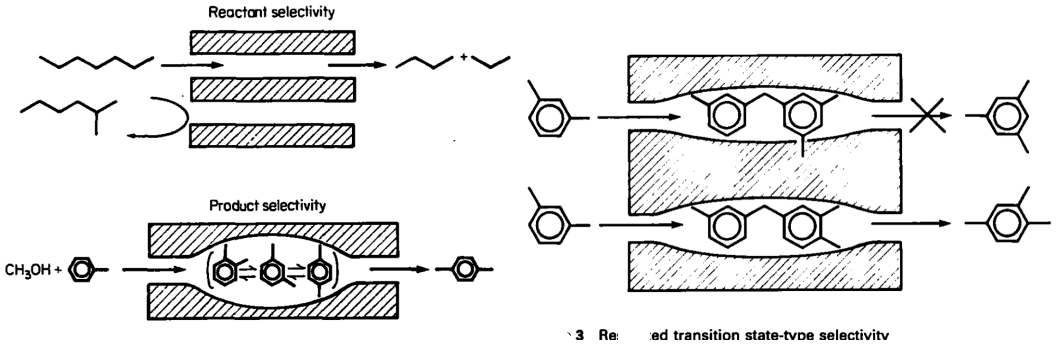

Reprinted from Zeolites, 4, S.M Csicsery, Shape selective catalysis in zeolites, 202-213, 1984, with permission from Elsevier.[25]

Confinement effects constitute a different avenue by which outer-sphere environments influence catalytic properties. They arise from the ability of the pore walls surrounding acid sites in zeolites to undergo dispersive (van der Waals) attractive interactions with molecular species confined within them. This can lead to enthalpic and entropic (de)stabilization of reactants, transitions states and/or products, altering reaction pathways and dramatically affecting rates.[7,26,2739] Confinement effects are illustrated by the data in Figure 1.1, which shows the reaction intermediates involved in methanol dehydration to form dimethyl ether (A) and how rate constants are influenced by void size (B).[40] Decreasing the void size of the zeolite catalyst (supercage > 14-MR > 12-MR > 10-MR, where MR indicates "member rings", the number of T atoms involved in defining the pore size) increases the van der Waals interaction energy of the dimethyl ether product (Q_{LJ}(DME)) with pore walls, as show in Figure 1.1(A). This is because smaller, more confining voids result in tighter fits and increase attractive dispersive interactions

between the product and pore walls, represented schematically in Figure 1.1(A) by the confining pore in orange. These attractive interactions stabilize the transition state of first-order processes for methanol dehydration, relative to the reactants; thus, more confining (smaller) voids stabilize this transition state more and result in an exponential increase in rates with decreasing pore size (Figure 1.1(B)).

These confinement and shape selectivity effects arise because of pore environments unique to zeolites and are sensitive to the location of acid sites even within the same zeolite framework.[41,42] Such effects are not possible in amorphous aluminosilicates: even if local surface undulations in amorphous materials could provide a local environment that leads to rate enhancements or shape selectivity, such environments will be scarce and part of a distribution of less reactive surface environments. Thus, it is the uniform outer-sphere environments (and inner-sphere environments) in crystalline zeolites, which can be rationally designed by choice of zeolite framework and synthesis conditions, that makes them such productive and versatile industrial acid catalysts.

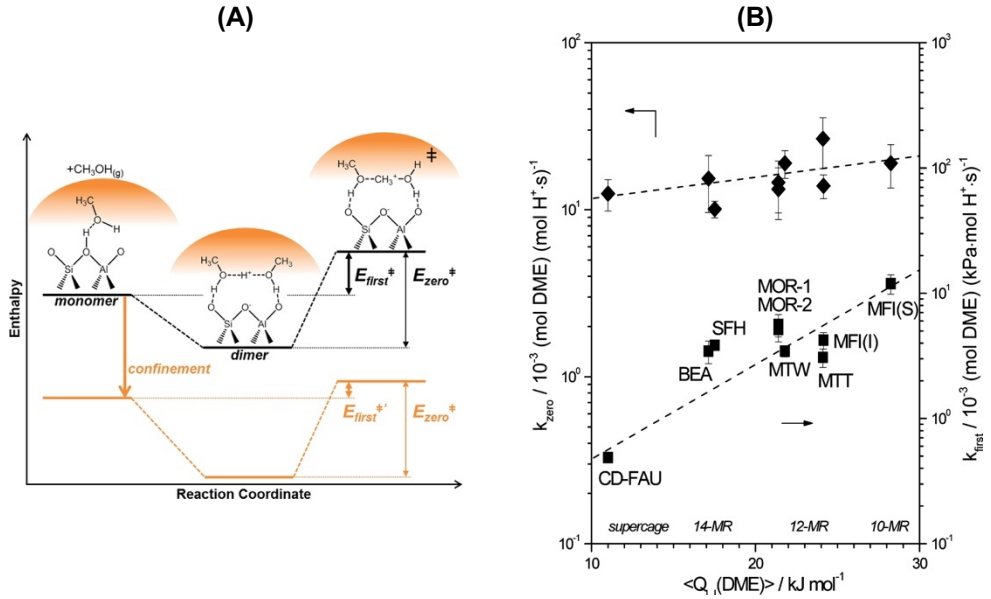

Figure 1.1. (A) Schematic reaction coordinate diagram depicting transition state and reactive intermediates involved in CH_3OH dehydration and their relation to measured first-order ($E_{first}^{\ddagger}$) and zero-order ($E_{zero}^{\ddagger}$) CH_3OH dehydration rate constants; H-bonded CH_3OH monomers (left) are influenced less by tighter confinement (orange) than protonated CH_3OH dimers (middle) and cationic dimethyl ether formation transition states (right), because of the smaller size and number of van der Waals contacts of monomers. **(B)** CH_3OH dehydration rate constants at 433 K as a function of reaction averaged DME van der Waals interaction energies (433 K) calculated with Lennard-Jones potentials at all accessible H^+ in FAU, BEA, SFH, MTW, MTT, MOR, and MFI (MFI(S)) and for dimethyl ether located in H^+ in the channel intersection void of MFI (MFI(I)); dotted lines are provided to guide the eye. Reprinted with permission from A. J. Jones, S. I. Zones and E. Iglesia, Implications of Transition State Confinement within Small Voids for Acid Catalysis, *J. Phys. Chem. C*, 2014, **118**, 17787–17800. Copyright 2014 American Chemical Society.[40]

1.3. Amorphous vs. Crystalline Zeolitic Silicates: Supports of Identical Composition but Different Structural Environments

1.3.1. Amorphous Silica (SiO_2): a non-Ordered Support

Amorphous silica (SiO_2) is widely employed as a support for dispersing active sites in heterogeneous catalysts, both in industrial applications and in model studies.[1,4,6,43–45] It is an inorganic oxide consisting of a network of four-connected $SiO_{4/2}$ tetrahedra lacking any long-range order (i.e. amorphous). Its surface is terminated by silanol (SiOH) groups that complete the tetrahedral coordination of Si^{IV} when this network is interrupted at a surface. SiO_2 can be economically prepared by various methods,[46] and its textural properties can be tuned to exhibit regular mesoporosity and surface areas as high as 1000 m^2/g,[47] making it an attractive material for catalyst supports. Its amorphous nature, however, makes it an inherently non-uniform and mechanically flexible support surface.

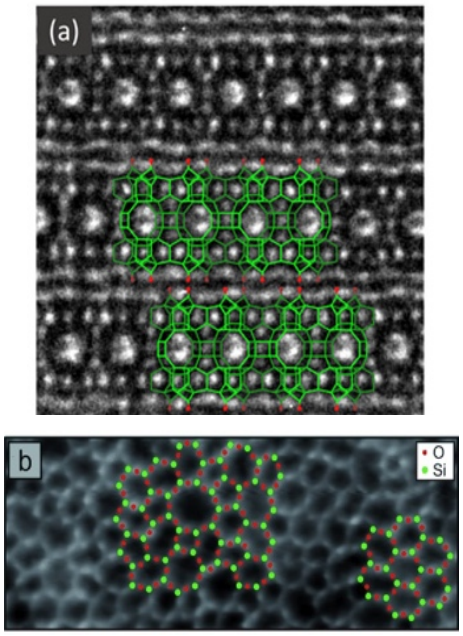

Figure 1.2. The contrasting molecular structure of amorphous silica vs. crystalline zeotypes as supports: **(a)** HRTEM images along the b-axis of as-synthesized Al-SSZ-70 with an outline of the MWW-layers overlaid; each line representing the connection, through a bridging O, between two tetrahedral centers. Adapted with permission from S. Smeets, Z. J. Berkson, D. Xie, S. I. Zones, W. Wan, X. Zou, M. F. Hsieh, B. F. Chmelka, L. B. McCusker and C. Baerlocher, Well-Defined Silanols in the Structure of the Calcined High-Silica Zeolite SSZ-70: New Understanding of a Successful Catalytic Material, *J. Am. Chem. Soc.*, 2017, **139**, 16803–16812. Copyright 2017 American Chemical Society.[48] (b) Atomic resolution constant current STM image of a vitreous silica film on Ru(0001) (scan range 8.0 x 2.0 nm^2, V_s = 100 mV, I_T = 100 pA), which serves as a model to the amorphous silica surface; a model of siloxane ring structural units is superimposed, with green dots representing Si and red dots representing O positions. Reprinted with permission from L. Lichtenstein, C. Büchner, B. Yang, S. Shaikhutdinov, M. Heyde, M. Sierka, R. Włodarczyk, J. Sauer and H. J. Freund, *Angew. Chem. Int. Ed.* , 2012, **51**, 404–407. Copyright © 2012 John Wiley and Sons.[49]

This nonuniformity is apparent in Figure 1.2(b), which shows an STM image of a supported silica thin-film reported recently by the group of Freund,[49] with oxygen and silicon positions of SiO_2 network highlighted in red and green, respectively. The surface structures formed by the SiO_2 network exhibit a high degree of heterogeneity, comprising 4 to 9-member rings, with different shapes apparent even for the same ring size. Such heterogeneity in the structure of the silica surface inevitably leads to heterogeneity in the active centers supported on this nonuniform surface, making it challenging to obtain active sites with uniform molecular environments. Furthermore, the flexibility of the amorphous silicate network can also lead to changes in the structure of active sites after thermal and catalytic treatments, as discussed in detail for the case Fe^{III} active sites in Chapter 3. This lack of uniformity in local structures makes studying catalytic structure function-relationships challenging on amorphous materials.

1.3.2. Zeotypes: Ordered Supports

On a local length scale, silicate zeotypes are constructed of the same $SiO_{4/2}$ tetrahedra that make up amorphous SiO_2, but comprise ordered microporous crystalline frameworks instead of amorphous disordered phases. Zeotype frameworks are isostructural to zeolites (a name reserved exclusively for aluminosilicates), exhibiting channels and cavities of uniform molecular dimensions.[7] Isomorphous substitution of Si^{IV} framework positions by other cations such as Al^{III} (zeolite aluminosilicates), B^{III} (borosilicate zeotypes), Fe^{III} (ferrosilicate zeotypes), Ti^{IV} (titanosilicate zeotypes), and others is also possible, giving rise a wide range of compositions. Just like in amorphous SiO_2, zeotypes also exhibit silanol groups (SiOH) wherever the silicate network is terminated by a surface, defect, or vacancy.

Figure 1.2(a) shows a HRTEM image of an Al-SSZ-70 zeolite. The uniformity and atomic order in this crystalline material is readily apparent, as evident by the superimposed image in green of the crystallographic structure of the SSZ-70 framework. This contrasts with the nonuniformity of the disordered amorphous SiO_2 phase shown in Figure 1.2(b). The uniform microporous channel structure of the SSZ-70 zeolite is also evident by the uniform 10 membered-ring channel openings visible in Figure 1.2(a). Such pores structures cannot occur in amorphous silicates because formation of pores would require long-range order (amorphous silicates can, nonetheless, be synthesized with uniform mesopores; the walls of these, however remain amorphous and lack long-range order).[50] Structural uniformity and crystallinity are significant advantages of zeotypes over their amorphous counterparts, because they provide well-defined crystallographic positions to synthesize uniform active sites with known framework coordination and surrounding structural environment.

1.4. Delaminated Zeotypes as Silicate Supports

The location of acid sites within microporous environments enables the diversity of outer-sphere effects that makes zeolites exceptional catalytic materials (section 1.2.1.2); however, shape selectivity limits the size of reactants that can be activated to that of zeolite pore openings (< 1 nm).[15] Thus, substrates with dimensions larger than pore diameters will not be able to access micropores and will only be activated at the small fraction of active sites located on the external crystal surface (rather than in micropores), thus limiting the productivity of zeolite catalysts.[51,52]

To extend the application of zeotypes to a wider scope of reactions involving larger substrates, as occurring in the manufacture of pharmaceuticals or fine chemicals for example, new approaches have been developed.[53] These include introducing mesoporosity (pores >2 nm) into zeolite crystals through post-synthetic treatments, to enable accessibility of larger reactants to intercrystallite active sites, or decreasing zeolite crystalline size to ease diffusional constraints.[53–55] A recent, elegant approach pioneered by the group of Ryoo involves the rational design of structure directing agent (SDA) heads attached to long chain hydrocarbon tails. When used in hydrothermal synthesis, these SDA result in zeolites that crystallize as nanosheets at the SDA head, while each nanosheet is separated by the long hydrocarbon tails.[56] Thus, after calcination to remove organics SDAs, each nanosheet is separated by accessible mesopores that were templated by these hydrocarbon tails, resulting in most of the active surface being external and accessible (with the exception of small fraction of intra-nanosheet channels). This approach, originally pioneered for the MFI framework,[56] has since been extended also to BEA and MWW zeolite frameworks by other groups.[57–59]

A different approach that has been investigated by us and others is delamination, which also increases the accessible external surface of zeotypes while preserving the structural integrity of their framework.[22,51,52,60–65] This approach was developed following the discovery, by scientists at Mobil research, of a class of zeotypes related to MCM-22 (MWW),[66] which can crystallize as layered precursor structures.[67–69] This class of materials enabled the development of delamination, initially for the synthesis of ITQ-2 by the group of Corma,[70] and which has since been studied by many others. Several excellent reviews have been published on this subject,[15–17] but we briefly focus on summarizing the delamination of borosilicate B-SSZ-70 here,[61] because it relates to other material covered in the rest of this thesis. Delamination treatments can only be applied to zeotype frameworks that crystallize as layered zeolite precursors during hydrothermal synthesis. As summarized in Scheme 1.4, these layered precursors comprise fully-connected frameworks within each layer, but the layers are loosely held together by weak H-bonding interactions. Calcination of these precursors would result in condensation of these H-bonded lamellae to form a 3-D structure of the zeolite B-SSZ-70. If, instead, appropriate treatments are applied, H-bonding interactions can be disrupted between the lamellae, and the layers exfoliated into a disordered arrangement, exposing some areas between layers to the external surface, thereby increasing the portion of the zeolite crystal that is accessible to the external surface relative to the nondelaminated B-SSZ-70. This delamination process typically proceeds by swelling of zeotype layers, which increases the spacing between layers by intercalation with surfactants and is fully reversible,[71] followed by irreversible disordering of layers, often accomplished by sonication.[60,61,70] A final calcination step is used to remove any organics present from synthesis.

The consequences of delamination treatments are shown in Table 1.1.[22] An increase in external surface area of ~2-fold compared to the nondelaminated 3-D zeotype is observed. This is accompanied by a decrease in micropore volume, which can be explained by internal voids in 3-dimensional B-SZZ-70 being exposed as external surface in delaminated B-UCB-4. The increase in total pore volume is a consequence of additional mesoporosity in the region between disordered layers. Additionally, delamination treatment can also fragment zeotype sheets into smaller fragments, also decreasing diffusion pathways for reactants during catalysis.[52] It should be noted, however, that the delamination should not be regarded as exposing every single precursor layer

to the external surface, i.e. the process is only partially effective in exposing the space that separates the zeotype precursor layers to the external surface. Otherwise, if the entirety of every single precursor layer were exposed to the external surface, external surface areas ~ 500 m^2/g would be expected,[58] but much lower surface areas ~ 130 m^2/g are observed in practice (Table 1.1). Thus, delaminated zeotypes are materials with hierarchical porosity: mesopores expose external surface areas that will be accessible to bulky reactants too large to enter micropores; however, reactants that are small enough are still able to access micropores, just as they would in conventional zeotypes.

Scheme 1.4. Schematic representation of zeotype delamination.

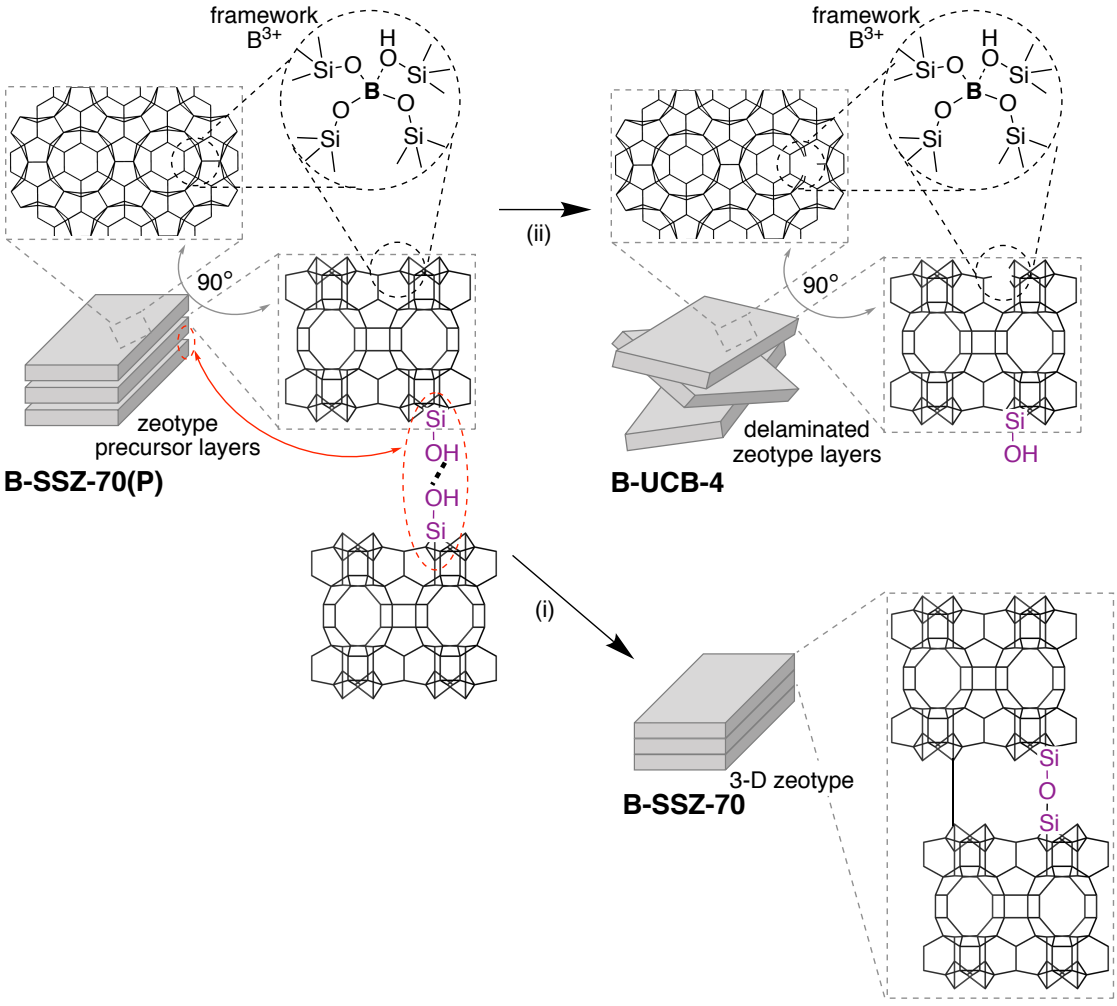

(i) Calcination of layered zeotype precursor B-SSZ-70(P) results in condensation of zeolite layers that were previously H-bonded, resulting in a 3-D zeolite. (ii) Delamination occurs by exfoliation of these non-covalently bound zeotype layers (rectangles) into a disordered arrangement through heating in the presence of surfactant and ammonium halide salts, followed by sonication, washing, calcination. Details of the crystalline zeotype framework of SSZ-70 and UCB-4 are shown along the a-c plane and rotated 90° along the a-b plane (top left), with vertices representing $SiO_{4/2}$ tetrahedra centers and lines Si-O-Si bonds.

In grafting approaches for active-site synthesis, discussed in section 1.5.2, cation precursors too large to enter micropores will graft only on the external surface, so catalytic activity will be limited to this region only; therefore, increasing external surface-areas provides a method to increase active-site loading. This phenomenon has been studied in detail by Zones *et al.* during the incorporation of Al^{III} sites into zeotypes by post-synthetic replacement of B^{III} in borosilicates, where hydrated Al^{III} are too large to access pores smaller than 10-MR and are therefore incorporated only on the external surface of zeotypes with pore openings with 10-MR or smaller.[72] As discussed in chapters 5, 6 and 7, this also occurs during grafting of Ti^{IV} active sites for epoxidation using bulky Ti precursors, limiting Ti loadings on delaminated UCB-4 zeolites to < 1 wt% because grafting occurs only on the external surface area. If, instead, the entirety of each precursor layer surface could be accessible for grafting, much higher active site loadings could be achieved. Such an approach was indeed demonstrated in a recent report on the preparation a crystalline layered titanosilicate with exceptionally low Si/Ti ratio of 6 (i.e. very high Ti content).[73]

In summary, the increase in accessible external surface area enabled by delamination results in open materials that are analogous to SiO_2 in reactant accessibility, but which possess an intact crystalline silicate framework with features.[74] This provides an avenue to using the advantages of crystalline zeotype supports in catalytic applications involving bulky substrates, for which zeotypes are typically not suitable because of the lack of accessibly of active sites within pores.

Table 1.1. Effect of delamination on textural properties.

Support	S_{ext} $(m^2/g)^a$	V_{micro} $(m^2/g)^a$	V_{tot} $(m^2/g)^b$
B-SSZ-70	68.9	0.197	0.32
B-UCB-4	136	0.166	0.47

[a]External surface (S_{ext}) area and micropore volumes (V_{micro}) determined from the t-pot method. [b]Determined from total analysis gas uptakes. Data adapted from reference 22.

1.5. Challenges in Controlling the Incorporation of Cations into Silicates

Controlling the molecular environment of catalytic active sites comprising isolated cations on silicate supports requires understanding of the methods by which these sites are synthesized. Different methods for incorporation of isolated cations onto silicate supports are summarized in Scheme 1.5, which is now discussed. We emphasize how the structural differences between zeolitic vs. amorphous supports, discussed in sections 1.3, affects cation incorporation and its inner- and outer-sphere molecular environments.

1.5.1. Direct Isomorphous Substitutions of Cations During Hydrothermal Synthesis

Isolated cations can be incorporated into a silicate matrix directly during hydrothermal synthesis to result in amorphous or crystalline zeotype materials, as depicted in Scheme 1.5A. Such approaches have been extensively reviewed for both amorphous materials[75–77] and zeotypes,[78,79] so we only briefly mention them here. In this approach, molecular precursors of the

desired cations, such as salts or alkoxides, are hydrolyzed in the presence of molecular precursors to the silicate matrix, such as organosilicon compounds or colloidal silica. The presence of base ensures the solubility of silicate species, which undergo equilibrated hydrolysis and condensation with themselves and with cation precursors, resulting in a tetrahedral silicate network that is occasionally substituted by the cation. This network can be amorphous, as is typical with materials prepared by sol-gel or coprecipitation methods or it can be a crystalline in a zeotype, where the network adopts a regular framework structure and the cation occupies a crystallographic T-atom position. Crystallization into a zeotype typically requires an organic or inorganic structure direction agent (SDA).

Scheme 1.5. Incorporation of a cation site in a silicate support.

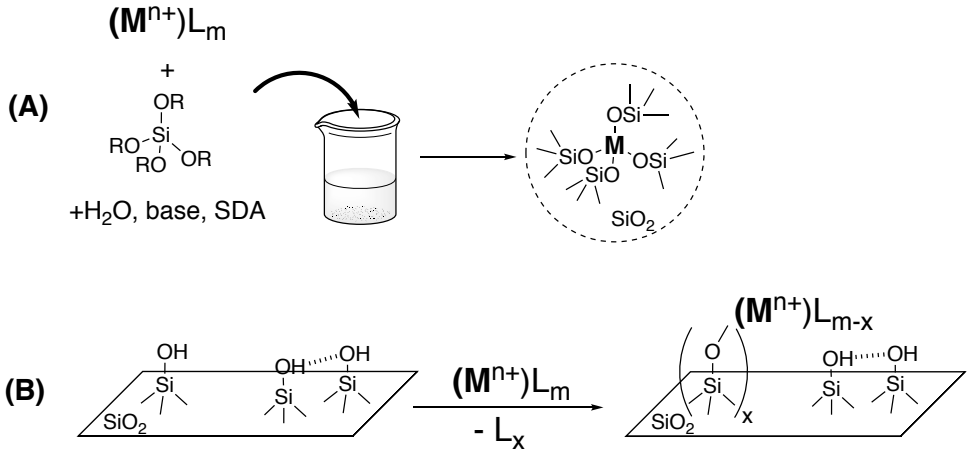

(A) Direct isomorphous substitution into an amorphous or crystalline metallosilicate. **(B)** Grafting, where a cation precursor reacts with silanols on the support surface.

Because of the largely uncontrolled nature of the hydrothermal reaction occurring freely in solution, self-condensation of cation precursors can occur and result in rather poor dispersion (i.e. lack of isolation) of the cations within the silicate matrix, especially at higher cation loadings. This is typical for the case of Ti^{IV}, where amorphous titanosilicates prepared by sol-gel techniques consistently showed presence of bulk TiO_2 anatase phases even when isolated sites were also present.[80] When crystalline titanosilicates are synthesized instead, certain crystallographic positions, which are isolated from each other, may be favored for Ti^{IV} incorporation,[81,82] resulting in better cation isolation. Similarly, there is growing evidence that B^{III} adopts certain preferential crystallographic locations when it is incorporated into a borosilicate zeotype framework.[83–89] However, achieving site isolation even in crystalline zeotypes can be challenging, as exemplified by the difficulty of obtaining TS-1 (MFI silica zeolite with tetrahedral Ti^{IV} centers) free of extra-framework TiO_2.[90] Thus, while direct isomorphous substitution is straightforward to perform and leads to higher active site loadings, achieving control over the speciation and uniformity of cation species can be synthetically challenging, and a mixture of isolated and aggregated oxide species of the cation are often observed.

1.5.2. Grafting of Cation Precursors onto Silanols

A different approach consists of grafting of cations, represented in Scheme 1.5B, in which a cation precursor reacts with silanol groups (SiOH) on the support surface. A cation precursor is generically depicted as $M^{n+}L_m$ in Scheme 1.5B, but the identities of the ligands can range in complexity form simple metal halides or alkoxides to complex molecular precursors[91,92] that include chelating ligands.[65] When grafting occurs, ligands in this precursor react with silanols through condensation, i.e. $M^{n+}L_m + SiOH \rightarrow (SiO)_xM^{n+}L_{m-x} + xHL$. This results in covalent attachment of the cation to the support surface through siloxy (SiO^-) ligands. We consider silanol as grafting environments in detail in Chapter 2, and explore grafting approaches to cation incorporation in Chapters 3 for Fe^{III} centers, and Chapter 4 to 7 for Ti^{IV} centers.

If cation precursors and grafting conditions are chosen such that mutual reaction between cation precursors is avoided, then cation species should in principle be isolated from each other once grafted on the surface. However, the reality is that a distribution of environments may be actually observed both because (i) self-condensation of cation precursors often occurs, leading to oligomeric and bulk oxide phases of the cation,[80,93,94] and (ii) it is not possible to control the surrounding molecular environment of the cation when the support is amorphous and therefore lacks long-range structural order. We now consider these challenges in detail, and postulate how using zeotypes as supports instead may help in their mitigation.

(i) *A distribution of isolated cation species as well as oligomers and oxide phases can exist after grafting, resulting in a distribution of catalytic environments.* We consider as an example Ti^{IV} grafted on amorphous silica, an industrial epoxidation catalyst. Conventional catalyst synthesis procedures rely on grafting simple titanium alkoxides, halides, or other reactive titanium complexes which react with silanols on the silica surface. For example, the following condensation reaction is observed when grafting titanium precursor vapors onto silica: $Ti(NEt_2)_4 + 2 \equiv SiOH \rightarrow (SiO)_2Ti(NEt_2)_2 + 2\ HNEt_2$, leading to dipodal grafted Ti^{IV} species.[20] In principle, no cross-condensation of the $Ti(NEt_2)_4$ is possible to form Ti-O-Ti linkages, as the condensation reaction self-terminates upon consuming silanols. However, trace amounts of water present under typical synthesis conditions can actually result in self-condensation of titanium precursors: $2\ Ti(NEt_2)_4 + H_2O \rightarrow (NEt_2)_3TiOTi(NEt_2)_3 + 2\ HNEt_2$, which would result in grafting of an oligomeric species. Such self-condensation can also occur with titanium species already grafted on the support, and a progressively increasing degree of self-condensation results in sites ranging from isolated Ti^{IV} centers to clustered, polymeric, and fully crystalline layers and bulk phases of TiO_2, as depicted in Figure 1.3.[80]

(ii) *The molecular environment of a grafted cation depends on the environment provided by the surrounding silicate surface, which is nonuniform on amorphous supports.*[94–96] The nonuniformity of amorphous supports ultimately leads to a distribution in surface environments of grafted cations,[97] and may lead to a distribution in catalytic reactivities for active sites.[13,22,65,98–100] This is exemplified by the distribution of polymer molecular weights produced by Cr/SiO_2, which McDaniel attributes to the distribution of types of Cr catalytic environments that polymerize ethylene.[3] Because crystalline supports such as zeotypes comprise uniform molecular structures, they offer an opportunity to graft active sites within well-defined molecular environments instead.[101,102] Such uniformity in molecular structure helps ensure uniformity in the reactivity of active sites, more straightforward characterization and connection to molecular

modeling studies, and better understanding of structure-function relationships that facilitate catalyst design.

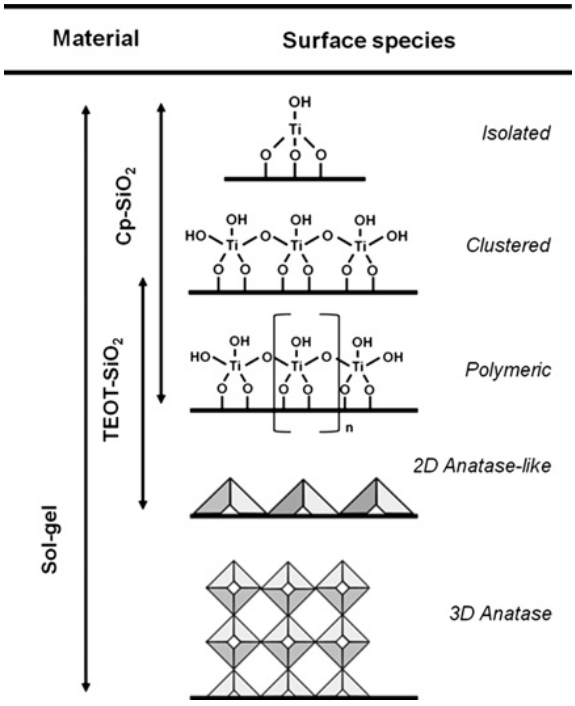

Figure 1.3. Heterogeneity in surface environment in titanosilicates, showing different states of aggregation of grafted $Ti^{IV}O_x$ centers. Reprinted from Journal of Catalysis, 309, T. R. Eaton, M. P. Campos, K. A. Gray and J. M. Notestein, Quantifying accessible sites and reactivity on titania–silica (photo)catalysts: Refining TOF calculations, 156-165, 2016, with permission from Elsevier.[80]

The most abundant grafting environment in purely siliceous zeoties (as opposed to AlO(H)Si containing aluminosilicates) consists of hydroxyl-rich framework vacancies ("silanol nests", described chapter 2 and subsequent chapters). These silanols can easily react with cation precursors to graft a cation, as shown by recent work where zeotypes were functionalized with Sn, Ti, Zr, Hf, Nb, and Ta.[8] A long-used strategy to synthesize the vacancies is the removal of framework heteroatoms, such as Al^{III} from zeolites (dealumination).[103] Our research group has focused on removing B^{III} from borosilicates zeotypes instead (deboronation).[104] Deboronation provides several advantages over dealumination: (i) milder conditions for removal of B^{III} relative to Al^{III} lead to better structural preservation of the zeotype framework, and (ii) the crystallographic location of B^{III} zeotype framework is tunable by synthesis, and these locations are different and less randomly distributed than those which Al^{III} occupies.[83–89] This latter observation is very important, because it provides a synthetic strategy to direct the location of grafted active sites into the particular zeotype framework location. This strategy consists in controlling the framework location of B^{III} by synthesis,[83,86] followed by isomorphous substitution of a cation into the B^{III} T-site (i.e. deboronation followed by cation grafting).[8,72] This, in principle, allows for an exquisite control over the environment of an active site by controlling the environment around a B^{III} T-site which is then substituted with a cation.

Grafting environments within zeotype framework vacancies also help mitigate the challenges associated with self-condensation of cation precursors during synthesis, by virtue of their chelating and self-isolated nature. This is discussed in relation to grafting of Fe^{III} centers in Chapter 3.

1.6. Thesis Outline

This thesis explores synthetic approaches to control the molecular environments of active sites on silicate surfaces in order to understand catalytic processes. In particular, I explore how well-defined molecular complexes can be grafted onto well-defined surface environments on zeotype supports, leading to precise control over the structure of the active sites. Throughout, I compare these zeotype supported structures to those supported on amorphous support, and highlight the benefit of using zeotypes as supports, in particular 2-D zeotype supports that provide enhanced external surface-area accessibility.

Given the reliance of grafting approaches on silanols as 'tethers' of a cation to a support (see 1.5.2), I begin by providing a detailed study of silanol speciation across zeotypes and amorphous supports in Chapter 2. Then, I proceed with an example of how silanol environments control grafting processes and how crystalline silicates provide stable support environments for Fe^{III} cations in Chapter 3. I then introduce an approach to control the structure of a grafted cation by using an organic ligand that 'protects' the cation center during grafting, applied to calix[4]arene-Ti^{IV} complexes grafted on amorphous SiO_2 in Chapter 4.

Having established how silanols on a support and how organic ligands in a cation complex can control the grafting of cations during catalyst synthesis, I present three studies where this approach of controlling environments form the 'top' using an organic ligand and from the 'bottom' using a support enables the synthesis of well-defined molecular structures. In Chapter 5, I present how this approach enables the unambiguous deconvolution of the effect of support outer-sphere on epoxidation catalysis. In Chapter 6, I demonstrate an example of how this support outer sphere can also control the conformation and structure of grafted complexes, while providing insight into adsorption processes occurring on surfaces. Finally, in Chapter 7, I provide a detailed mechanistic study of how partially confining outer-sphere environments can influence the formation of transition states to improve catalytic reactivity.

Taken together, this thesis provides fresh insights into the structure of silicate surfaces and their ability to control catalysis. In particular, I demonstrate the ability to control the environment of cations not only through organic ligands, but also by using the support as a 'macromolecular ligand' with well-defined structures that are able to directly influence catalytic reactivity. These approaches allow a new understanding of the consequences of outer-sphere environments on catalysis (Chapter 7), yielding new insights for aiding future catalyst design.

1.7. References

(1) Oyama, S. T. *Mechanisms in Homogeneous and Heterogeneous Epoxidation Catalysis*; Elsevier: Amsterdam, 2011.

(2) Mol, J. C. Industrial Applications of Olefin Metathesis. *J. Mol. Catal. A Chem.* **2004**, *213*, 39–45.

(3) McDaniel, M. P. A Review of the Phillips Supported Chromium Catalyst and Its Commercial Use for Ethylene Polymerization. *Adv. Catal.* **2010**, *53*, 123–606.

(4) Soled, S. Silica-Supported Catalysts Get a New Breath of Life. *Science* **2015**, *350*, 1171–1172.

(5) Lefebvre, F. Chapter 1 Synthesis of Well-Defined Solid Catalysts by Surface Organometallic Chemistry. In *Atomically-Precise Methods for Synthesis of Solid Catalysts*; The Royal Society of Chemistry, 2015; pp 1–26.

(6) Copéret, C.; Allouche, F.; Chan, K. W.; Conley, M. P.; Delley, M. F.; Fedorov, A.; Moroz, I. B.; Mougel, V.; Pucino, M.; Searles, K.; Yamamoto, K.; Zhizhko, P. A. Bridging the Gap between Industrial and Well-Defined Supported Catalysts. *Angew. Chem. Int. Ed.* **2018**, *57*, 6398–6440.

(7) Corma, A. State of the Art and Future Challenges of Zeolites as Catalysts. *J. Catal.* **2003**, *216*, 298–312.

(8) Ouyang, X.; Hwang, S.-J.; Xie, D.; Rea, T.; Zones, S. I.; Katz, A. Heteroatom-Substituted Delaminated Zeolites as Solid Lewis Acid Catalysts. *ACS Catal.* **2015**, *5*, 3108–3119.

(9) Luo, H. Y.; Lewis, J. D.; Román-Leshkov, Y. Lewis Acid Zeolites for Biomass Conversion: Perspectives and Challenges on Reactivity, Synthesis, and Stability. *Annu. Rev. Chem. Biomol. Eng.* **2016**, *7*, 663–692.

(10) Notestein, J. M.; Katz, A. Enhancing Heterogeneous Catalysis through Cooperative Hybrid Organic-Inorganic Interfaces. *Chem. - A Eur. J.* **2006**, *12*, 3954–3965.

(11) Palermo, A.; Zhang, S.; Hwang, S.; Dixon, D. A.; Gates, B. C.; Katz, A. Weakly Interacting Solvation Spheres Surrounding a Calixarene-Protected Tetrairidium Carbonyl Cluster: Contrasting Effects on Reactivity of Alkane Solvent and Silica Support. *Dalt. Trans.* **2018**, *47*, 13550.

(12) Sheldon, R. A. Synthetic and Mechanistic Aspects of Metal-Catalysed Epoxidations with Hydroperoxides. *J. Mol. Catal.* **1980**, *7*, 107–126.

(13) Notestein, J. M.; Solovyov, A.; Andrini, L. R.; Requejo, F. G.; Katz, A.; Iglesia, E. The Role of Outer-Sphere Surface Acidity in Alkene Epoxidation Catalyzed by Calixarene-Ti(IV) Complexes. *J. Am. Chem. Soc.* **2007**, *129*, 15585–15595.

(14) Khouw, C.; Dartt, C. B.; Labinger, J. A.; Davis, M. E. Studies on the Catalytic-Oxidation of Alkanes and Alkenes by Titanium Silicates. *J. Catal.* **1994**, *149*, 195–205.

(15) Roth, W. J.; Čejka, J. Two-Dimensional Zeolites: Dream or Reality? *Catal. Sci. Technol.* **2011**, *1*, 43.

(16) Roth, W. J.; Nachtigall, P.; Morris, R. E.; Čejka, J. Two-Dimensional Zeolites: Current Status and Perspectives. *Chem. Rev.* **2014**, *114*, 4807–4837.

(17) Opanasenko, M. V; Roth, W. J.; Cejka, J. Two-Dimensional Zeolites in Catalysis: Current Status and Perspectives. *Catal. Sci. Technol.* **2016**, 2467–2484.

(18) Lu, J.; Aydin, C.; Liang, A. J.; Chen, C. Y.; Browning, N. D.; Gates, B. C. Site-Isolated Molecular Iridium Complex Catalyst Supported in the 1-Dimensional Channels of Zeolite Hssz-53: Characterization by Spectroscopy and Aberration-Corrected Scanning Transmission Electron

Microscopy. *ACS Catal.* **2012**, *2*, 1002–1012.
(19) Radhakrishnan, R.; Oyama, S. T.; Chen, J. G.; Asakura, K. Electron Transfer Effects in Ozone Decomposition on Supported Manganese Oxide. *J. Phys. Chem. B* **2001**, *105*, 4245–4253.
(20) Bouh, A. O.; Rice, G. L.; Scott, S. L. Mono- and Dinuclear Silica-Supported Titanium(IV) Complexes and the Effect of TiOTi Connectivity on Reactivity. *J. Am. Chem. Soc.* **1999**, *121*, 7201–7210.
(21) Nandi, P.; Tang, W.; Okrut, A.; Kong, X.; Hwang, S.-J.; Neurock, M.; Katz, A. Catalytic Consequences of Open and Closed Grafted Al(III)-Calix[4]Arene Complexes for Hydride and Oxo Transfer Reactions. *Proc. Natl. Acad. Sci. U. S. A.* **2013**, *110*, 2484–2489.
(22) Grosso-Giordano, N. A.; Schroeder, C.; Okrut, A.; Solovyov, A.; Schöttle, C.; Chassé, W.; Marinković, N.; Koller, H.; Zones, S. I.; Katz, A. Outer-Sphere Control of Catalysis on Surfaces: A Comparative Study of Ti(IV) Single-Sites Grafted on Amorphous versus Crystalline Silicates for Alkene Epoxidation. *J. Am. Chem. Soc.* **2018**, *140*, 4956–4960.
(23) Bass, J. D.; Anderson, S. L.; Katz, A. The Effect of Outer-Sphere Acidity on Chemical Reactivity in a Synthetic Heterogeneous Base Catalyst. *Angew. Chem. Int. Ed.* **2003**, *42*, 5219–5222.
(24) Gounder, R.; Iglesia, E. The Catalytic Diversity of Zeolites: Confinement and Solvation Effects within Voids of Molecular Dimensions. *Chem. Commun.* **2013**, *49*, 3491.
(25) Csicsery, S. M. Shape-Selective Catalysis in Zeolites. *Zeolites* **1984**, *4*, 202–213.
(26) Bhan, A.; Iglesia, E. A Link between Reactivity and Local Structure in Acid Catalysis on Zeolites. *Acc. Chem. Res.* **2008**, *41*, 559–567.
(27) Gounder, R.; Iglesia, E. The Roles of Entropy and Enthalpy in Stabilizing Ion-Pairs at Transition States in Zeolite Acid Catalysis. *Acc. Chem. Res.* **2012**, *42*, 229–238.
(28) Čejka, J.; Corma, A.; Zones, S. *Zeolites and Catalysis: Synthesis, Reactions and Applications*; 2010; Vol. 1–2.
(29) Baerlocher, C.; McCusker, L.; Olson, D. *Atlas of Zeolite Framework Types*, 6th ed.; Elsevier: Amsterdam, 2007.
(30) Perego, C.; Ingallina, P. Recent Advances in the Industrial Alkylation of Aromatics: New Catalysts and New Processes. *Catal. Today* **2002**, *73*, 3–22.
(31) Kocal, J. A.; Vora, B. V.; Imai, T. Production of Linear Alkylbenzenes. *Appl. Catal. A Gen.* **2001**, *221*, 295–301.
(32) Weitkamp, J.; Puppe, L. *Catalysis and Zeolites: Fundamentals and Applications*; 1999.
(33) Woolery, G. L.; Kuehl, G. H.; Timken, H. C.; Chester, a. W.; Vartuli, J. C. On the Nature of Framework Brønsted and Lewis Acid Sites in ZSM-5. *Zeolites* **1997**, *19*, 288–296.
(34) Dragoi, B.; Gervasini, A.; Dumitriu, E.; Auroux, A. Calorimetric Determination of the Acidic Character of Amorphous and Crystalline Aluminosilicates. *Thermochim. Acta* **2004**, *420*, 127–13.
(35) Eichler, U.; Brändle, M.; Sauer, J. Predicting Absolute and Site Specific Acidities for Zeolite Catalysts by a Combined Quantum Mechanics/Interatomic Potential Function Approach. *J. Phys. Chem. B* **1997**, *101*, 10035–10050.
(36) Jones, A. J.; Iglesia, E. The Strength of Brønsted Acid Sites in Microporous Aluminosilicates. *ACS Catal.* **2015**, *5*, 5741–5755.
(37) Brändle, M.; Sauer, J. Acidity Differences between Inorganic Solids Induced by Their Framework Structure. A Combined Quantum Mechanics/Molecular Mechanics Ab Initio Study on Zeolites. *J. Am. Chem. Soc.* **1998**, *120*, 1556–1570.

(38) Ramos, F. S. O.; Pietre, M. K. de; Pastore, H. O. Lamellar Zeolites: An Oxymoron? *RSC Adv.* **2013**, *3*, 2084–2111.
(39) Gounder, R.; Iglesia, E. Catalytic Consequences of Spatial Constraints and Acid Site Location for Monomolecular Alkane Activation on Zeolites. *J. Am. Chem. Soc.* **2009**, *131*, 1958–1971.
(40) Jones, A. J.; Zones, S. I.; Iglesia, E. Implications of Transition State Confinement within Small Voids for Acid Catalysis. *J. Phys. Chem. C* **2014**, *118*, 17787–17800.
(41) Gounder, R.; Iglesia, E. Consequences of Spatial Constraints within Zeolites for Monomolecular Activation of Alkanes on Acid Sites. *J. Am. Chem. Soc.* **2009**, *131*, 1958–1971.
(42) Bhan, A.; Allian, A. D.; Sunley, G. J.; Law, D. J.; Iglesia, E. Specificity of Sites within Eight-Membered Ring Zeolite Channels for Carbonylation of Methyls to Acetyls. *J. Am. Chem. Soc.* **2007**, *129*, 4919–4924.
(43) Copéret, C.; Comas-Vives, A.; Conley, M. P.; Estes, D. P.; Fedorov, A.; Mougel, V.; Nagae, H.; Núnez-Zarur, F.; Zhizhko, P. A. Surface Organometallic and Coordination Chemistry toward Single-Site Heterogeneous Catalysts: Strategies, Methods, Structures, and Activities. *Chem. Rev.* **2016**, *116*, 323–421.
(44) Notestein, J. M.; Iglesia, E.; Katz, A. Grafted Metallocalixarenes as Single-Site Surface Organometallic Catalysts. *J. Am. Chem. Soc.* **2004**, *126*, 16478–16486.
(45) Jiang, C.; Hara, K.; Fukuoka, A. Low-Temperature Oxidation of Ethylene over Platinum Nanoparticles Supported on Mesoporous Silica. *Angew. Chem. Int. Ed. Engl.* **2013**, *52*, 6265–6268.
(46) Vansant, E. F.; Voort, P. Van Der; Vrancken, K. C. *Characterization and Chemical Modification of the Silica Surface*, 1st ed.; Elsevier, 1995; Vol. 93.
(47) Alothman, Z. A. A Review: Fundamental Aspects of Silicate Mesoporous Materials. *Materials (Basel)*. **2012**, *5*, 2874–2902.
(48) Smeets, S.; Berkson, Z. J.; Xie, D.; Zones, S. I.; Wan, W.; Zou, X.; Hsieh, M. F.; Chmelka, B. F.; McCusker, L. B.; Baerlocher, C. Well-Defined Silanols in the Structure of the Calcined High-Silica Zeolite SSZ-70: New Understanding of a Successful Catalytic Material. *J. Am. Chem. Soc.* **2017**, *139*, 16803–16812.
(49) Lichtenstein, L.; Büchner, C.; Yang, B.; Shaikhutdinov, S.; Heyde, M.; Sierka, M.; Włoodarczyk, R.; Sauer, J.; Freund, H. J. The Atomic Structure of a Metal-Supported Vitreous Thin Silica Film. *Angew. Chem. Int. Ed.* **2012**, *51*, 404–407.
(50) Chen, C.-Y.; Li, H.-X.; Davis, M. E. Studies on Mesoporous Materials I. Synthesis and Characterization of MCM-41. *Microporous Mater.* **1993**, *2*, 17–26.
(51) Ouyang, X.; Hwang, S.-J.; Runnebaum, R. C.; Xie, D.; Wanglee, Y. J.; Rea, T.; Zones, S. I.; Katz, A. Single-Step Delamination of a MWW Borosilicate Layered Zeolite Precursor under Mild Conditions without Surfactant and Sonication. *J. Am. Chem. Soc.* **2014**, *136*, 1449–1461.
(52) Runnebaum, R. C.; Ouyang, X.; Edsinga, J. A.; Rea, T.; Arslan, I.; Hwang, S.-J. J.; Zones, S. I.; Katz, A. Role of Delamination in Zeolite-Catalyzed Aromatic Alkylation: UCB-3 versus 3-D Al-SSZ-70. *ACS Catal.* **2014**, *4*, 2364–2368.
(53) Pérez-Ramírez, J.; Christensen, C. H.; Egeblad, K.; Christensen, C. H.; Groen, J. C. Hierarchical Zeolites: Enhanced Utilisation of Microporous Crystals in Catalysis by Advances in Materials Design. *Chem. Soc. Rev.* **2008**, *37*, 2530–2542.
(54) Garcia-Martinez, J.; Johnson, M.; Valla, J.; Li, K.; Ying, J. Y. Mesostructured Zeolite Y - High Hydrothermal Stability and Superior FCC Catalytic Performance. *Catal. Sci. Technol.*

2012, *2*, 987–994.
(55) Prasomsri, T.; Jiao, W.; Weng, S. Z.; Garcia Martinez, J. Mesostructured Zeolites: Bridging the Gap between Zeolites and MCM-41. *Chem. Commun.* **2015**, *51*, 8900–8911.
(56) Choi, M.; Na, K.; Kim, J.; Sakamoto, Y.; Terasaki, O.; Ryoo, R. Stable Single-Unit-Cell Nanosheets of Zeolite MFI as Active and Long-Lived Catalysts. *Nature* **2009**, *461*, 246–249.
(57) Kim, J.; Park, W.; Ryoo, R. Surfactant-Directed Zeolite Nanosheets: A High-Performance Catalyst for Gas-Phase Beckmann Rearrangement. *ACS Catal.* **2011**, *1*, 337–341.
(58) Luo, H. Y.; Michaelis, V. K.; Hodges, S.; Griffin, R. G.; Román-Leshkov, Y.; Roman-Leshkov, Y. One-Pot Synthesis of MWW Zeolite Nanosheets Using a Rationally Designed Organic Structure-Directing Agent. *Chem. Sci.* **2015**, *6*, 6320–6324.
(59) Margarit, V. J.; Martínez-Armero, M. E.; Navarro, M. T.; Martínez, C.; Corma, A. Direct Dual-Template Synthesis of MWW Zeolite Monolayers. *Angew. Chemie* **2015**, *127*, 13928–13932.
(60) Ogino, I.; Nigra, M. M.; Hwang, S.-J.; Ha, J. M.; Rea, T.; Zones, S. I.; Katz, A. Delamination of Layered Zeolite Precursors under Mild Conditions: Synthesis of UCB-1 via Fluoride/Chloride Anion-Promoted Exfoliation. *J. Am. Chem. Soc.* **2011**, *133*, 3288–3291.
(61) Ogino, I.; Eilertsen, E. A.; Hwang, S.-J.; Rea, T.; Xie, D.; Ouyang, X.; Zones, S. I.; Katz, A. Heteroatom-Tolerant Delamination of Layered Zeolite Precursor Materials. *Chem. Mater.* **2013**, *25*, 1502–1509.
(62) Eilertsen, E. A.; Ogino, I.; Hwang, S.-J.; Rea, T.; Yeh, S.; Zones, S. I.; Katz, A. Nonaqueous Fluoride/Chloride Anion-Promoted Delamination of Layered Zeolite Precursors: Synthesis and Characterization of UCB-2. *Chem. Mater.* **2011**, *23*, 5404–5408.
(63) Aigner, M.; Grosso-Giordano, N. A.; Okrut, A.; Zones, S. I.; Katz, A. Epoxidation of 1-Octene under Harsh Tail-End Conditions in a Flow Reactor I: A Comparative Study of Crystalline vs. Amorphous Catalysts. *React. Chem. Eng.* **2017**, *2*, 842–851.
(64) Aigner, M.; Grosso-Giordano, N. A.; Schottle, C.; Okrut, A.; Zones, S.; Katz, A. Epoxidation of 1-Octene under Harsh Tail-End Conditions in a Flow Reactor II: Impact of Delaminated-Zeolite Catalyst Surface Area and Structural Integrity on Catalytic Performance. *React. Chem. Eng.* **2017**, *2*, 852–861.
(65) Grosso-Giordano, N. A.; Yeh, A. J.; Okrut, A.; Xiao, D. J.; Grandjean, F.; Long, G. J.; Zones, S. I.; Katz, A. Effect of Defect Site Preorganization on Fe(III) Grafting and Stability: A Comparative Study of Delaminated Zeolite vs Amorphous Silica Supports. *Chem. Mater.* **2017**, *29*, 6480–6492.
(66) Leonowicz, M. E.; Lawton, J. A.; Lawton, S. L.; Rubin, M. K. MCM-22: A Molecular Sieve with Two Independent Multidimensional Channel Systems. *Science* **1994**, *264*, 1910–1913.
(67) Lawton, S. L.; Fung, A. S.; Kennedy, G. J.; Alemany, L. B.; Chang, C. D.; Hatzikos, G. H.; Lissy, D. N.; Rubin, M. K.; Timken, H.-K. C.; Steuernagel, S.; Woessner, D. E. Zeolite MCM-49: A Three-Dimensional MCM-22 Analogue Synthesized by in Situ Crystallization. *J. Phys. Chem.* **1996**, *100*, 3788–3798.
(68) Roth, W. J.; Kresge, C. T.; Vartuli, J. C.; Leonowicz, M. E.; Fung, A. S.; McCullen, S. B. MCM-36: The First Pillared Molecular Sieve with Zeoliteproperties. *Stud. Surf. Sci. Catal.* **1995**, *94*, 301–308.
(69) Fung, A. S.; Lawton, S. L.; Roth, W. J. Synthetic Layered MCM-56, Its Synthesis and Use. 5,362,697, 1994.
(70) Corma, A.; Fornes, V.; Pergher, S. B.; Maesen, T. L. M.; Buglass, J. G. Delaminated

Zeolite Precursors as Selective Acidic Catalysts. *Nature* **1998**, *396*, 353–356.
(71) Maheshwari, S.; Jordan, E.; Kumar, S.; Bates, F. S.; Penn, R. L.; Shantz, D. F.; Tsapatsis, M. Layer Structure Preservation during Swelling, Pillaring, and Exfoliation of a Zeolite Precursor. *J. Am. Chem. Soc.* **2008**, *130*, 1507–1516.
(72) Zones, S. I.; Benin, A.; Hwang, S.-J.; Xie, D.; Elomari, S.; Hsieh, M.-F. Studies of Aluminum Reinsertion into Borosilicate Zeolites with Intersecting Channels of 10- and 12-Ring Channel Systems. *J. Am. Chem. Soc.* **2014**, *136*, 1462–1471.
(73) Tsunoji, N.; Opanasenko, M. V.; Kubů, M.; Čejka, J.; Nishida, H.; Hayakawa, S.; Ide, Y.; Sadakane, M.; Sano, T. Highly Active Layered Titanosilicate Catalyst with High Surface Density of Isolated Titanium on the Accessible Interlayer Surface. *ChemCatChem* **2018**, *10*, 2536–2540.
(74) Ouyang, X.; Wanglee, Y.-J.; Hwang, S.-J.; Xie, D.; Rea, T.; Zones, S. I.; Katz, A. Novel Surfactant-Free Route to Delaminated All-Silica and Titanosilicate Zeolites Derived from a Layered Borosilicate MWW Precursor. *Dalton Trans.* **2014**, *43*, 10417–10429.
(75) Regalbuto, J. *Catalyst Preparation : Science and Engineering*; CRC Press, 2006.
(76) Heinrichs, B.; Lambert, S.; Job, N.; Pirard, J.-P. Sol-Gel Synthesis of Supported Metals. In *Catalyst Preparation: Science and Engineering*; Regalbuto, J., Ed.; CRC Press: Boca Raton, 2016; pp 163–208.
(77) Knowles, W. V.; Nutt, M. O.; Wong, M. . Supported Metal Oxides and the Surface Density Metric. In *Catalyst Preparation: Science and Engineering*; Regalbuto, J., Ed.; CRC Press: Boca Raton, 2016; pp 251–281.
(78) Cundy, C. S.; Cox, P. A. The Hydrothermal Synthesis of Zeolites: History and Development from the Earliest Days to the Present Time. *Chem. Rev.* **2003**, *103*, 663–701.
(79) Cundy, C. S.; Cox, P. A. The Hydrothermal Synthesis of Zeolites: Precursors, Intermediates and Reaction Mechanism. *Microporous Mesoporous Mater.* **2005**, *82*, 1–78.
(80) Eaton, T. R.; Campos, M. P.; Gray, K. A.; Notestein, J. M. Quantifying Accessible Sites and Reactivity on Titania-Silica (Photo)Catalysts: Refining TOF Calculations. *J. Catal.* **2014**, *309*, 156–165.
(81) Lamberti, C.; Bordiga, S.; Zecchina, A.; Artioli, G.; Marra, G.; Spanò, G. Ti Location in the MFI Framework of Ti-Silicalite-1: A Neutron Powder Diffraction Study. *J. Am. Chem. Soc.* **2001**, *123*, 2204–2212.
(82) Henry, P. F.; Weller, M. T.; Wilson, C. C. Structural Investigation of TS-1: Determination of the True Nonrandom Titanium Framework Substitution and Silicon Vacancy Distribution from Powder Neutron Diffraction Studies Using Isotopes. *J. Phys. Chem. B* **2001**, *105*, 7452–7458.
(83) Hsieh, M.-F. Ph.D. Dissertation, University of California, Santa Barbara, CA, 2014.
(84) Chen, J.; Liang, T.; Li, J.; Wang, S.; Qin, Z.; Wang, P.; Huang, L.; Fan, W.; Wang, J. Regulation of Framework Aluminum Siting and Acid Distribution in H-MCM-22 by Boron Incorporation and Its Effect on the Catalytic Performance in Methanol to Hydrocarbons. *ACS Catal.* **2016**, *6*, 2299–2313.
(85) Korányi, T. I.; Nagy, J. B. Garaga. *J. Phys. Chem. B* **2006**, *110*, 14728–14735.
(86) Garaga, M. N.; Hsieh, M.-F.; Nour, Z.; Deschamps, M.; Massiot, D.; Chmelka, B. F.; Cadars, S. Local Environments of Boron Heteroatoms in Non-Crystalline Layered Borosilicates. *Phys. Chem. Chem. Phys.* **2015**, *17*, 21664–21682.
(87) Yokoi, T.; Mochizuki, H.; Namba, S.; Kondo, J. N.; Tatsumi, T. Control of the Al Distribution in the Framework of ZSM-5 Zeolite and Its Evaluation by Solid-State NMR Technique and Catalytic Properties. *J. Phys. Chem. C* **2015**, *119*, 15303–15315.

(88) Zhu, Q.; Kondo, J. N.; Yokoi, T.; Setoyama, T.; Yamaguchi, M.; Takewaki, T.; Domen, K.; Tatsumi, T. The Influence of Acidities of Boron- and Aluminium-Containing MFI Zeolites on Co-Reaction of Methanol and Ethene. *Phys. Chem. Chem. Phys.* **2011**, *13*, 14598–14605.
(89) Qiao, Q.; Wang, R.; Gou, M.; Yang, X. Catalytic Performance of Boron and Aluminium Incorporated ZSM-5 Zeolites for Isomerization of Styrene Oxide to Phenylacetaldehyde. *Microporous Mesoporous Mater.* **2014**, *195*, 250–257.
(90) Fan, W.; Duan, R.-G.; Yokoi, T.; Wu, P.; Kubota, Y.; Tatsumi, T. Synthesis, Crystallization Mechanism, and Catalytic Properties of Titanium-Rich TS-1 Free of Extraframework Titanium Species. *J. Am. Chem. Soc.* **2008**, *130*, 10150–10164.
(91) Jarupatrakorn, J.; Tilley, T. D. Silica-Supported, Single-Site Titanium Catalysts for Olefin Epoxidation. A Molecular Precursor Strategy for Control of Catalyst Structure. *J. Am. Chem. Soc.* **2002**, *124*, 8380–8388.
(92) Fujdala, K. L.; Tilley, T. D. Design and Synthesis of Heterogeneous Catalysts: The Thermolytic Molecular Precursor Approach. *J. Catal.* **2003**, *216*, 265–275.
(93) Barton, D. G.; Shtein, M.; Wilson, R. D.; Soled, S. L.; Iglesia, E. Structure and Electronic Properties of Solid Acids Based on Tungsten Oxide Nanostructures. *J. Phys. Chem. B* **1999**, *103*, 630–640.
(94) Prieto-Centurion, D.; Boston, A. M.; Notestein, J. M. Structural and Electronic Promotion with Alkali Cations of Silica-Supported Fe(III) Sites for Alkane Oxidation. *J. Catal.* **2012**, *296*, 77–85.
(95) Wegener, S. L.; Marks, T. J.; Stair, P. C. Design Strategies for the Molecular Level Synthesis of Supported Catalysts. *Acc Chem Res* **2012**, *45*, 206–214.
(96) Eaton, T. R.; Boston, A. M.; Thompson, A. B.; Gray, K. A.; Notestein, J. M. Counting Active Sites on Titanium Oxide-Silica Catalysts for Hydrogen Peroxide Activation through In Situ Poisoning with Phenylphosphonic Acid. *ChemCatChem* **2014**, *6*, 3215–3222.
(97) Hoffman, A. S.; Fang, C. Y.; Gates, B. C. Homogeneity of Surface Sites in Supported Single-Site Metal Catalysts: Assessment with Band Widths of Metal Carbonyl Infrared Spectra. *J. Phys. Chem. Lett.* **2016**, *7*, 3854–3860.
(98) Peters, B.; Scott, S. L. Single Atom Catalysts on Amorphous Supports: A Quenched Disorder Perspective. *J. Chem. Phys.* **2015**, *142*, 104708.
(99) Goldsmith, B. R.; Sanderson, E. D.; Bean, D.; Peters, B. Isolated Catalyst Sites on Amorphous Supports: A Systematic Algorithm for Understanding Heterogeneities in Structure and Reactivity. *J. Chem. Phys.* **2013**, *138*, 204105.
(100) Goldsmith, B. R.; Peters, B.; Johnson, J. K.; Gates, B. C.; Scott, S. L. Beyond Ordered Materials: Understanding Catalytic Sites on Amorphous Solids. *ACS Catal.* **2017**, *7*, 7543–7557.
(101) Ogino, I. Chapter 2 Zeolite-Supported Molecular Metal Complex Catalysts. In *Atomically-Precise Methods for Synthesis of Solid Catalysts*; The Royal Society of Chemistry, 2015; pp 27–54.
(102) Bell, A. T. The Impact of Nanoscience on Heterogeneous Catalysis. *Science* **2003**, *299*, 1688–1691.
(103) Bregante, D. T.; Flaherty, D. W. Periodic Trends in Olefin Epoxidation over Group IV and v Framework-Substituted Zeolite Catalysts: A Kinetic and Spectroscopic Study. *J. Am. Chem. Soc.* **2017**, *139*, 6888–6898.
(104) Koller, H.; Chen, C. Y.; Zones, S. I. Selectivities in Post-Synthetic Modification of Borosilicate Zeolites. *Top. Catal.* **2015**, *58*, 451–479

Chapter 2

Speciation and H-Bonding Interactions of Silanols in Zeolitic and Amorphous Silicates: an Infrared and 2-Dimensional NMR Spectroscopic Study

The speciation of silanols (SiOH) on crystalline zeolitic (-SVY* framework) and amorphous (Aerosil) silicates is studied by a combination of infrared (IR) spectroscopy and multi-dimensional MAS NMR spectroscopy. Infrared spectroscopy identifies four distinct silanol species with SiO-H vibrations (υ_{OH}) at **I** 3747 cm^{-1}, **II** 3725 cm^{-1}, **III** 3690 cm^{-1}, **IV** 3530 cm^{-1}. These species exhibit sharper bands in zeotypes than in amorphous silica, reflecting the zeotype's structural uniformity. Species **I** corresponds to free silanols present at the crystal terminating surface of zeotypes and dehydroxylated amorphous silica. Acid treatment induces hydroxylation, leading to an increase in the population of species **II**, **III** and **IV**, which correspond to silanols engaged in H-bonding. ^{1}H MAS NMR also indicates four distinct silanol species, with chemical shifts at δ_{H} **I** 1.8, **II** 2.2, **III** 3.1-3.3, **IV** 3.9-4.0 ppm, which are assigned to the same species observed by IR spectroscopy based on previously developed correlations. Single quantum – double quantum dipolar correlation ^{1}H MAS NMR spectroscopy provides information of through-space interactions of silanols. It indicates that species **III** and **IV** are spatially adjacent; we therefore assign these species to mutually H-bound silanols. Instead, silanol species **II** is not adjacent to other silanols and is only observed in zeotypes; we therefore assign it to silanol defects inside pores that interact with bridging siloxane oxygens, but not with other silanols. *In situ* variable temperature IR indicates that dehydroxylation proceeds at lower temperature on amorphous silica, as compared to zeotypes. We therefore conclude that framework crystallinity stabilizes silanols against dehydroxylation, by stabilizing the framework against structural rearrangements that accompany dehydroxylation. This uniformity and stability correlate with higher catalytic activity of zeotypes for the Beckmann rearrangement reaction, as compared to amorphous silica. These observations improve our understanding of silanols on the surface of silicates, and point towards the benefits of using crystalline rather than amorphous silicates for functional applications.

2.1. Introduction

Silicate materials, comprised of networks of oxygen-sharing $SiO_{4/2}$ tetrahedra, are ubiquitously used as catalyst supports, adsorbents, binders, sensors, and other applications, all of which rely on molecular processes occurring on the surface of the silicate.[1,2] Despite their importance, a full molecular picture of surface structures on silicates is still incomplete. Contributing to this challenge is the amorphous nature of many commonly used silicates, which are economical and facile to synthesize with many morphologies,[2] but are inherently non-uniform and therefore difficult to study at the molecular level. In contrast, silicate zeotypes comprise crystalline materials that form well-defined framework topologies,[3] while remaining compositionally identical to amorphous SiO_2. In this contribution, we study the surface and structural properties of amorphous and zeolitic silicates by examining the speciation of silanol groups on their surface.

Silanols (SiOH) occur where the four-fold $Si(OSi)_{4/2}$ connectivity of the bulk silicate network is interrupted at a surface, i.e. $(OSi)_3SiOH$. Given their ubiquitous presence on surfaces, silanols control many of the functional properties of silicates. For example, they serve as reactive centers for condensation of surface modifying groups, enabling adsorption properties to be tuned and catalytic functionality to be incorporated.[2,4–10] Silanols are also capable of acting as catalytic sites on their own, where they catalyze the Beckman rearrangement of an oxime to a lactam.[11–16] They can act as weak Brønsted acid in cooperative catalysis,[17–20] and have also been implicated in catalyst deactivation processes.[21] They have therefore been the subject of numerous studies and continue to gather research attention,[2,22–24] both in amorphous [2,22,23,25] and crystalline zeolitic silicates.[24,26–31]

Across the literature, silanols are thought to adopt a variety of species,[2,25,32] depending on their local molecular environment. A free silanol, such as that occurring on the surface of dehydroxylated amorphous silica, is free from H-bonding interactions with any other species (see **1** in Scheme 1).[2,26] Because of their protic nature, silanols also can engage in H-bonding interactions with other H-bond acceptors or donors. When the SiOH density on the silicate surface is sufficiently high, H-bonding interactions will occur amon neighboring silanol groups (see **1-a** in Scheme 1), causing a weakening of the SiO-H bond.[33] The formation of H-bonds typically requires an O···O distance < 3.3 Å,[32] to result in OH···O distances < 2.2 Å.[33] When a silanol engages in H-bonding interactions with another silanol in a SiOH···O(H)Si arrangement, the former acts as a proton donor and is said to be O-perturbed, while the latter acts as a proton acceptor and is said to be H-perturbed;[2] these species are respectively represented by species **IV** and **III** in Scheme 2. Beyond this simple silanol pairing, assemblies of multiple clusters of H-bonds are also thought to occur.[25–28]

Despite this vigorous research attention to the speciation of silanols, there exists significant contradictions in the spectroscopic assignment of silanol species, and few studies have attempted to provide an overall picture of silanol speciation across both amorphous and crystalline silicates. To address these issues, in this manuscript, we study silanols on amorphous and zeolitic silicates by combining infrared (IR) spectroscopy with single quantum – double quantum (SQ-DQ) ^{1}H MAS NMR dipolar correlation spectroscopy. Vibrational IR spectroscopy has been extensively used to characterize silanols, because it can very effectively probe the ν(O-H) SiO-H stretching vibrations of silanols. These ν(O-H) occur at 3747 cm^{-1} for free silanols,[2,26] and are redshifted and broadened to values below 3740 cm^{-1} when silanols are hydrogen bonded.[2,22,26,33] Despite its sensitivity, spectroscopic assignments based on IR alone have remained conflicting,[2,22,23,26,28] in

part because the suffer from lack of quantitation (the extinction coefficient of silanol species is not known) and band broadening due to H-bonding.[33] ^{1}H MAS NMR does not suffer from these two shortcomings, and provides a quantitative technique to examine silanol speciation and complement IR. In addition, here we use single quantum – double quantum (SQ-DQ) dipolar correlation ^{1}H MAS NMR spectroscopy to also obtain information on how different silanol species are spatially arranged. In this spectroscopy, species which exhibit DQ coherence are adacent in space. Therefore, signals that exhibit cross-correlations, with different SQ chemical shifts but the same DQ coherence, correspond to distinct ^{1}H chemical environments that are proximal in space. In addition, there are auto-correlations, when the SQ chemical shifts of two proximal species are the same; these correspond to spatially adjacent species within the same ^{1}H chemical environment. Combining insights from these two spectroscopic probes, we arrive at an overall picture of silanol speciation across crystalline and amorphous silicates.

The range of silicates examined is summarized in Scheme 1, with physicochemical properties summarized in the Supplementary Information 1. We study fumed Aerosil 200 as a model of amorphous silica, both as dehydroxylated amorphous silica **1** (silanol surface density of ~ 1 nm^{-2}) or hydroxylated amorphous silica **1-a** (silanol surface density of ~ 4 nm^{-2}).[34] **1-a** is synthesized by hydroxylation of **1** through acid-treatment (we denote this treatment **1→1-a**). In these non-porous amorphous silicates, the surface essentially 'flat' and lacks long range order, consisting of a variety of siloxane rings sizes;[35] therefore, no information about the location of silanols is possible.

We compare these amorphous supports to delaminated zeolitic silicate (**2**) and borosilicate (**3**) with SSZ-70 (SVY*-) topology, and their acid-treated variants **2-a** and **3-a**; their synthesis is described in Supplementary Information 1. In contrast to amorphous silicates, these zeotypes exhibit crystalline framework structures with well-defined porous environments where silanols can be located. The SSZ-70 framework layers of the zeotypes studied here are isostructural to MWW, and contain four possible pore environments, denoted (**i**), (**ii**), (**iii**), and (**iv**) in Scheme 1. (**i**) consists of terminal T-atom positions, spaced 8.3 Å apart, on a crystal surface where the framework is interrupted. This crystal surface can occur on the external surface of the zeotype; in addition, the disordered stacking of MWW layers in SSZ-70 results in some terminal T-sites (**i**) being located within interlayer space (**iv**), as shown in Scheme 1.[36] Terminal T-atoms (**i**) share only three oxygens with other framework T-sites, while the fourth oxygen forms a silanol (SiOH). In contrast, environments (**ii**) – (**iv**) consist of a fully connected $SiO_{4/2}$ network within different porous structures:

(**ii**) Pockets defined by a 12 membered-ring (12-MR) of T-atoms on the crystal terminating external surface of the zeotype; these pockets comprise hemispherical cavities 7.1 Å in diameter and 7.0 Å deep.[37]

(**iii**) Sinusoidal 10-MR channels inside the a zeotype layer, which are < 4.0 × 5.9 Å wide.[37]

(**iv**) Micropores formed between *-SVY layers. In native SSZ-70 these form the 14-MR windows 4.0 × 5.9 Å shown in Scheme 2.1;[36] however, delamination may lead to additional variability in the pore sizes between layers.[38] Silanols are known to be located within these micropores at vacancy defects in the native SSZ-70 framework structure.[36]

The synthesis of silanols in environments (**ii**) – (**iv**) can be achieved through acid treatment of **2** or **3**, which consist of pure silicate (**2**) or borosilicate (**3**) forms of the same zeolite

framework.[36,39,40] The acid treated materials are denoted **2-a** and **3-a**, and the acid treatment processes is denoted **2→2-a** and **3→3-a**.

Acid treatment of **3→3-a** causes 'deboronation', in which B^{III} atoms from **3** are hydrolyzed and removed from the framework,[41–43], as shown in the grey box in Scheme 2.1. This results in a purely siliceous **3-a** containing vacancy defects at framework locations previously occupied by B^{III}, populated by silanol pairs.[44] These vacancies are often referred to as a "silanol nest".[43,45] Acid treatment of silicate **2→2-a**, can also lead to the formation of silanols through structural rearrangements, which we discuss in section 2.4.1.

We begin by examining the properties of the speciation of silanols by infrared spectroscopy (2.3.1), 1-dimensional ^{1}H MAS NMR (2.3.2), and 2-dimensioanl SQ-DQ dipolar correlation ^{1}H MAS NMR spectroscopy (2.3.3), ^{31}P MAS NMR of TMPO adsorbed on silanols (2.3.4), and molecular mechanics calculations (2.3.5). We also examine the catalytic implications of silanol speciation for the Beckmann rearrangement (2.3.6), consisting of the rearrangement of cyclohexanone oxime into ε-caprolactam (Scheme 2.3), which is known to be catalyzed by weakly acidic assemblies of H-bound silanols.[11–16,46] In view of this data, we discuss how acid treatments affect borosilicates and silicate frameworks (2.4.1). We then examine the speciation and assignment of silanol species in detail across crystalline zeotype and amorphous silicates (2.4.2). Finally, using this understanding, we contrast the structural information of amorphous vs. crystalline silicates, and their relative structural stability and catalytic proficiency (2.4.3). These results shed light into outstanding issues of the speciation of silanols on silicates, and point toward advantages of using crystalline supports over non-uniform amorphous ones for catalytic applications.[47,48]

Scheme 2.1. Schematic representation of silicate framework structures

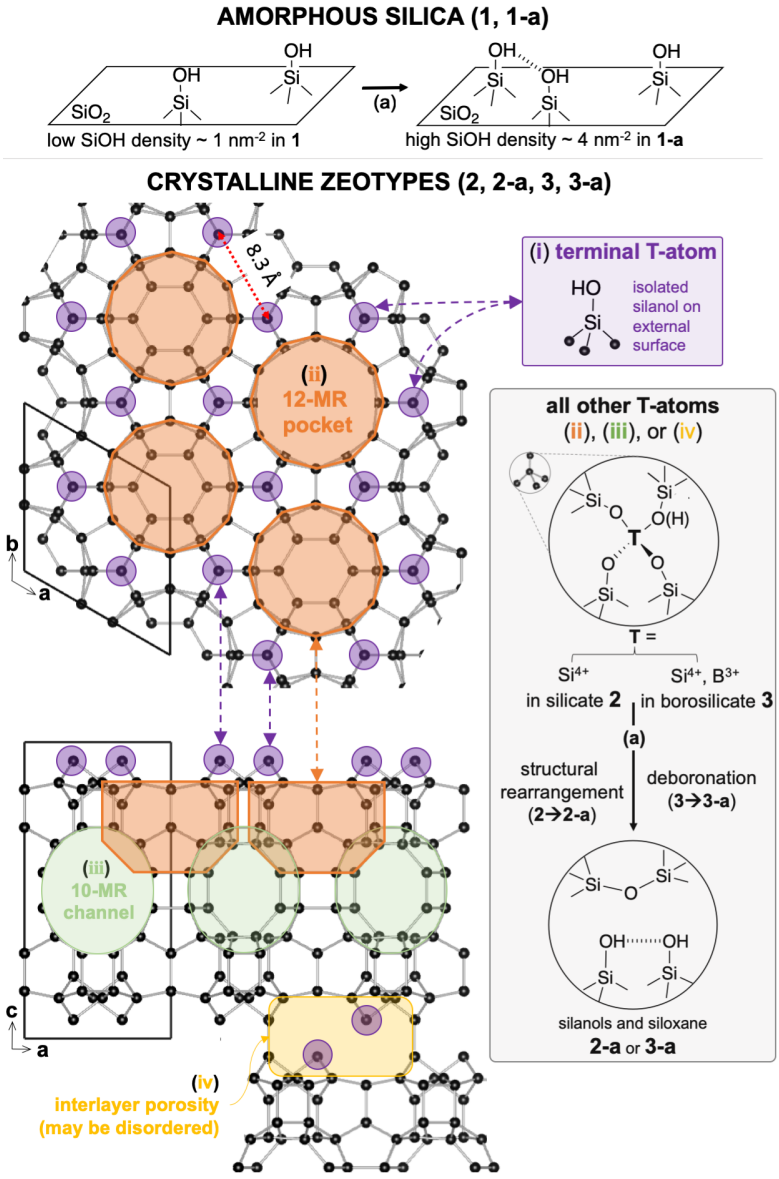

Amorphous silica surfaces **1** and **1-a** contain silanols but lack long-range order; their surface density is ~ 1 SiOH nm^{-2} for dehydroxylated silica **1** and ~ 4 SiOH nm^{-2} for fully hydroxylated silica **1-a**, which is prepared by (a) acid-washing induced hydroxylation of **1**.[34] In contrast, delaminated SSZ-70 zeotypes comprise well-defined crystalline framework layers (*-SVY topology),[36] shown along their crystallographic a-b and a-c planes, with their unit cell highlighted in black lines. Vertices correspond to tetrahedrally coordinated T-atoms that comprise the zeotype framework; they are connected through oxygen bridges shown as grey lines. This framework exhibits four environments where silanols may be located, denoted (**i**), (**ii**), (**iii**), and (**iv**) – see main text for explanation. To the right, the consequences of acid washing (a) are depicted, which causes structural rearrangements in silicate **2** to synthesize **2-a**, or vacancy formation upon deboronation of borosilicate **3** to synthesize **3-a**.

2.2. Experimental Methods

2.2.1. General Material Synthesis

The general materials synthesis strategy is depicted in Scheme 2.1, with physicochemical properties summarized in Table A2.1. Aerosil® 200 (Evonik) was used as a representative amorphous silica support. Dehydroxylated amorphous SiO_2 **1** (~1 /nm^2)[34] and hydroxylated amorphous SiO_2 **1-a** (~4 /nm^2)[34] were synthesized by previously described protocols.[18] Delaminated silicate UCB-4 zeotypes[38] were synthesized from SSZ-70(P) precursors.[36,39,40] Si-UCB-4 (**2**) and B-UCB-4 (**3**) correspond purely siliceous delaminated variants for Si-SSZ-70(P) **2-p** and borosilicate B-SSZ-70(P) **3-p**, which were synthesized as described elsewhere.[18]

Acid washing of amorphous **1** synthesizes **1-a**, acid washing of silicate **2** synthesizes **2-a**, while acid washing of borosilicate **3** synthesizes **3-a**, as depicted in Scheme 2.1(a), and was accomplished by treating 500 mg of silicate with 50 mL of 2N HNO_3 at 373 K for 18 h, followed by filtration and washing with copious amounts of H_2O. The properties of the synthesized silicates is described in 2.6.1.

2.2.2. Infrared Spectroscopy

Infrared (IR) vibrational spectra were acquired in either diffuse reflectance (DRIFTS) or in transmission (FTIR) mode. Spectra were recorded using a Thermo Scientific Nicolet 6700 Fourier Transform Infrared Spectrometer with a spectral resolution of 2 cm^{-1}, fitted with either a Diffuse Reflectance cell in DRIFTS, or an *in-situ* flow cell (In-situ Research Instruments, Inc., South Bend, IN) in transmission mode. Samples were treated under He flow at 473 K (unless otherwise noted) to remove moisture during spectral acquisition. For transmission experiments, self-supported wafers of the samples were prepared, while neat powder samples were used for DRIFTS experiments. Background spectra were collected under identical conditions in the absence of wafer. For isotope exchange experiments, the pellet was treated *in-situ* with 10 torr of D_2O or 2-ethylphenol, and subsequently evacuated at 573 K, until no further spectral changes were detected. Kubelka-Munk formalisms where used to calculate absorbance of measurements in diffuse reflectance mode. Integrated intensities of skeleton Si-O-Si overtones in the range 1740 – 2080 cm^{-1} were used to normalize spectra;[2] spectra were baseline corrected assuming intensity of ν(SiO-H) occurs in the 3750 – 3200 cm^{-1} range.

2.2.3. NMR Spectroscopy

Samples were treated under dynamic vacuum at 393 K for 1 h to remove atmospheric water prior to measurements. Samples **3** and **3-a** in ^{1}H MAS NMR are 3-dimensional borosilicate SSZ-70 variants previously investigated,[44] and not delaminated versions studied by FTIR in Figures 1 and 2. Notwithstanding, FTIR spectra of these 3-D SSZ-70 variants are shown in Figure A2.2, and exhibit the same frequencies and general features as FTIR spectra in Figures 1 and 2. We therefore use our prior results on these 3-D materials to study silanol speciation in **3** and **3-a**. ^{1}H MAS NMR measurement conditions are included in section 5.5.1.3.

3-a was treated with trimethylphosphine oxide (TMPO), by adding 1 – 5 mg of TMPO dissolved in dichloromethane to 100 mg of **3-a** (dehydrated at 473 K for 4 h), followed by evaporation to dryness.

MAS NMR experiments in Figure 2.6 were performed on a 11.7 T Bruker AVANCE III spectrometer equipped with a triple-resonance 4 mm probehead, operating at 500.13 and 202.46 MHz for ^{1}H and ^{31}P respectively. The sample was carefully packed under argon atmosphere into 4 mm zirconium rotors. All MAS NMR spectra were recorded at a spinning rate of 14 kHz. Single pulse sequences were used for the acquisitions of 1D spectra, with $\pi/2$ pulses set to 4 and 8 μs for ^{1}H and ^{31}P respectively. Two-dimensional homonuclear ^{31}P-^{31}P radio-frequency driven recoupling (RFDR)[49] experiments were also performed, using 64 scans and 4K complex points in the t_2 dimension. The t_1-dwell was rotor-synchronized, and 64 time increments were set for 0.71 ms mixing time. ^{31}P and ^{1}H chemical shifts and RF pulses were calibrated on phosphoric acid (85%) and TMS respectively.

2.2.4. Force Field Calculations

All geometry optimizations were performed with Schrödinger Release 2019-2: Maestro, Schrödinger, LLC, New York, NY, 2019, using the OPLS3e force field.[50] Models were constructed based on the SSZ-70 framework structure,[36] shown schematically in Scheme 2.1. A full 12-MR pocket structure and next-nearest Si neighbors were used as the basis of the cluster model terminated by hydrides. The position of these hydrides was frozen to simulate the rigidity of the zeolite framework. Geometry optimization of this cluster model (where all Si and O atoms are allowed to relax) does not alter the framework geometry significantly (Figure A2.5), indicating that this force field satisfactorily represent the structure of the silicate backbone.

To study the possible structures adopted by silanol within a silicate, vacancy defects were generated by removing T-atoms from 2 possible framework locations (D-3 and D-8), indicated in Figure A2.5. Upon removal of such a T-atom, a vacancy nominally terminated by four silanols is generated in a so called "silanol nest";[43,51] however, we have recently shown that only two silanols are involved in such vacancy structures,[44] because hydroxyl groups in such proximity would likely spontaneously condense.[52] Based on these experimental observations, hydroxyls with shortest O-— O distances in the T-atom vacancies where connected via a single -O- link (i.e. "condensed"). All six possible O — O pairs were condensed, and the geometry optimized, to result in six possible structures for each of the T-sites shown in Figure A2.6. H-bonds were considered to be present when the OH···O distances < 2.1 Å.[33]

2.2.5. Beckmann Rearrangement Reaction

A stainless-steel flow reactor was packed with 100 mg of catalyst, shaped to uniform particle sizes between 180 and 300 μm. The catalyst was pretreated at 673 K for 1 h under a constant stream of Ar (12.24 mL/min). The reactor was then cooled to 573 K, and a reactant solution consisting of 1 g of cyclohexanone oxime, 20.6 g of toluene, and 0.437 g methyl undecanoate as an internal standard was injected and vaporized into the Ar stream at a liquid rate of 2.4 mL/h, under atmospheric pressure. The resulting WHSV was 1.0 $g_{oxime} \times (g_{catalyst} \times h)^{-1}$. After 1 h, the condensable fraction of the product stream was collected in a Schlenk flask for 1 h by cooling the Schlenk walls with an ice/water mixture. The condensed product solution was analyzed via gas chromatography using a flame ionization detector (Agilent Technologies 789A GC).

2.3. Results

2.3.1. FT Infrared Spectroscopy

The vibrational stretching frequencies ν(O-H) of silanols (SiO-H), which are sensitive to the speciation and H-bonding environment of silanols,[28] were studied by Diffuse Reflectance Fourier-transform Infrared Spectroscopy (DRIFTS), with results shown in Figure 2.1A. Bands at ν(O-H) frequencies in the region 3750 – 3200 cm^{-1} are observed for all silicates. Zeotypes (**2**, **2-a**, **3**, **3-a**) exhibit four distinct local maxima centered at 3747, 3725, 3690, and 3530 cm^{-1}, which we denote as species **I**, **II**, **III**, and **IV** in order of decreasing frequency; these bands are indicated by dashed vertical lines in Figure 2.1. Silanol species **I** (ν(O-H) at 3747 cm^{-1}) corresponds to free silanols, which are not H-bound.[2,26] Frequencies less than 3740 cm^{-1}, for bands **II**, **III**, and **IV**, correspond to silanols perturbed by hydrogen bonding[2,22,26,33] which causes a redshift in ν(O-H) relative to the sharp ν(O-H) at 3747 cm^{-1}.

Free silanols **I** dominate the spectrum of silicate **2**, borosilicate **3**, and dehydroxylated amorphous SiO_2 **1**, and appear as a shoulder in **2-a** and **3-a**. Comparison of spectra before and after acid washing treatments (**1** to **1-a**, **2** to **2-a**, **3** to **3-a**) indicate that acid washing causes increased contributions form H-bound species **II**, **III**, and **IV**. These differences are apparent in quantitative difference spectra in Figure 2.1B. In contrast to these large increases for **II**, **III**, and **IV**, small – if any – changes occur to the intensity for silanol species **I** upon acid washing zeotypes **2→2-a** or **3→3-a** (Figure 2.1B). In stark contrast, band **I** significantly decreases in intensity upon acid washing amorphous silica **1→1-a** (Figure 2.1B), and its position shifts slightly to ~ 3741 cm^{-1}. In addition, a broad absorption envelope (i.e. no distinct maxima) between 3740 and 3200 cm^{-1} is observed for H-bound silanols in **1-a**, with shoulders visible for bands **III** and **IV**, but not **II** (these shoulders are also clearly visible in Figure 2.2B).

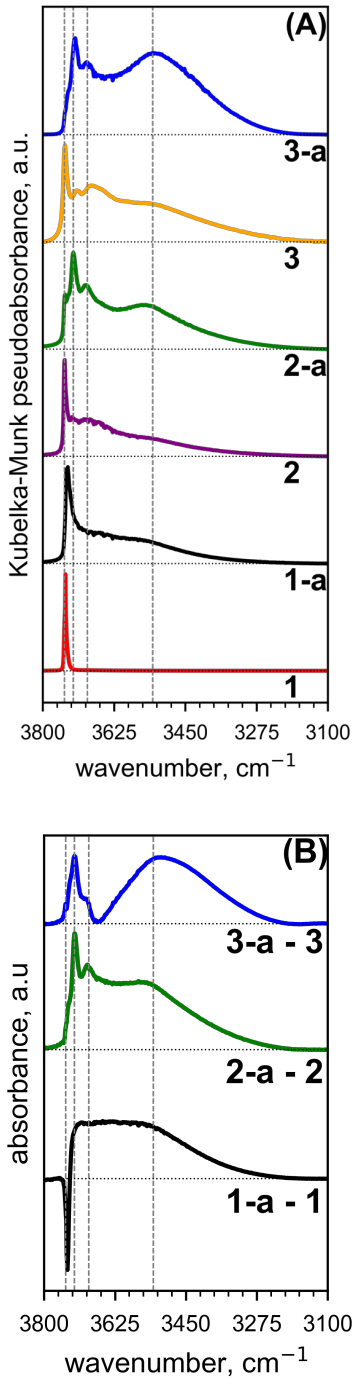

Figure 2.1. (A) Diffuse reflectance Fourier-transform infrared spectra (DRIFTS) of the *ν*(SiO-H) region of silicate materials, normalized to their maximum value. **(B)** Quantitative subtraction difference spectra of samples indicated, based on transmission measurements; full spectra Figure A2.4. Dotted horizontal lines indicate baseline, while dashed vertical lines indicate stretching bands at 3747, 3725, 3690, 3530 cm^{-1} corresponding to silanol species **I**, **II**, **III**, and **IV**. All spectra acquired while the sample was treated under He flow at 473 K.

Figure 2.2 shows FTIR spectral changes induced by *in-situ* thermal treatment of silicate wafers, which causes dehydroxylation by mutual condensation of silanols (2Si—OH → Si—O—Si + H_2O; see Scheme 2.4)[23]. For **3-a** (Figure 2.2A), thermal treatment causes a progressive decrease (i.e. condensation) of silanol species **IV** with treatment above 473 K; species **I** and **II** are stable to thermal treatment up to 723 K, while species **III** is stable up to 673 K. These stability temperatures are summarized in Table 2.2. A wafer of **3-a** was calcined at 823 K, with results shown in Figure 2.2C. Calcination retains the intensity of species **I**, and greatly diminishes the intensity of **II**, **III**, and **IV**. Thus, the thermal stability of silanol species decreases in the order **I** (completely stable) > **II** > **III** > **IV**. Dehydroxylation results for amorphous **1-a** indicate that all H-bound species < 3740 cm^{-1} decrease in intensity due to thermal dehydroxylation above > 573 K (Figure 2.2B), and almost completely disappears upon calcination (Figure 2.2C), after which only free silanol species **I** remain.

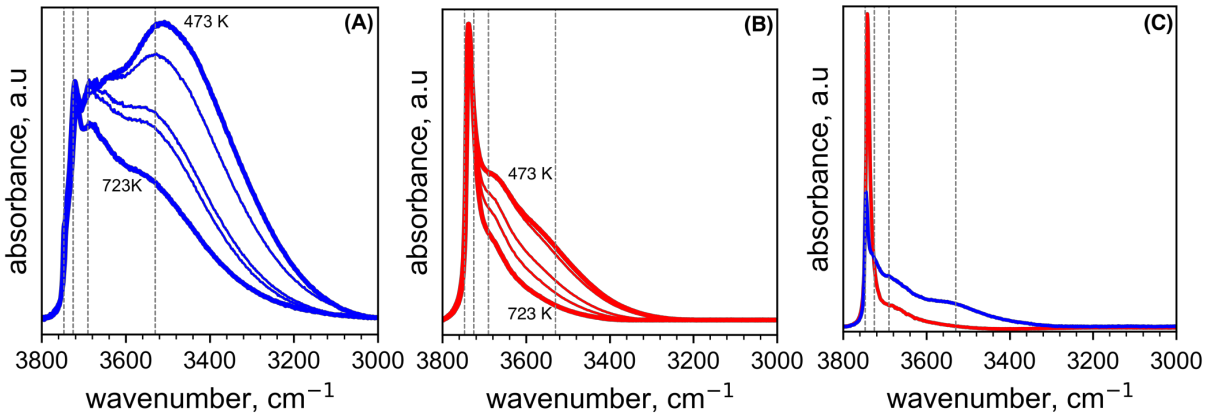

Figure 2.2. Normalized transmission Fourier-transform infrared spectra of the ν(SiO-H) region at increasing temperatures of 473 K (He flow), 573 K (He flow), 623 K (vacuum), 673 K (vacuum), and 723 K (vacuum) for **(A) 3-a** and **(B) 1-a**. **(C)** Spectra comparing **3-a** (blue) and **1-a** (red), after calcination of the wafer in air at 823 K, acquired under He flow at 473 K. Dashed vertical lines indicate stretching bands at 3747, 3725, 3690, 3530 cm^{-1} corresponding to silanol species **I**, **II**, **III**, and **IV**.

To understand the steric accessibility of silanols and their location within porous environments (**i**) – (**iv**), we performed H→D→H isotope exchange experiments on **3-a**, described in section 2.2.2. Such exchange experiments were previously used to elegantly probe accessibility of silanols on amorphous silica.[23] The results are shown in Figure 2.3. A wafer of **3-a** (reference) was dehydrated and treated with D_2O vapor, resulting in exchange of silanols (SiOH) into their deuterated counterparts (SiOD). The resulting deuterated wafer (red) exhibits the same spectral bands for species **I** – **IV**, but shifted $\nu_{OH}/\nu_{OD} = 1.36$, as expected according to a harmonic model.[53]

The H→D exchange spectrum retains a very small SiOH contribution at 3650 cm^{-1}, which is distinct to the silanol species **I** – **IV**. The lack of H→D exchange for this minor species indicates that it is located within sterically constrained environments that are not accessible to D_2O molecules (diameter 1.7 Å, determined from room temperature densities), consistent with the assignment of this frequency to "intraglobular" / inaccessible silanols on amorphous silica.[2]

The deuterated wafer was subsequently D→H back-exchanged with a bulky alcohol, 2-ethylphenol with a molecular diameter of 3.3 Å. The results in Figure 2.3 show a spectrum that appears almost identical to the original (reference) spectrum, indicating that all silanols **I** – **IV** are accessible for D→H back-exchange within steric environments at least 3.3 Å in diameter. This is consistent with the location of silanols within microporous structures (**ii**), (**iii**), and (**iv**), all of which are > 3.3 Å or larger. Future studies will examine bulkier alcohols to discriminate between silanol located within each of these environments.

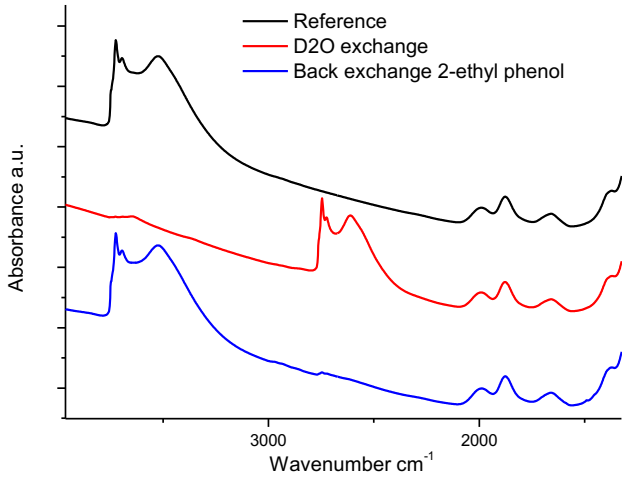

Figure 2.3. Transmission Fourier-transform infrared spectra of **3-a** after activation at 473 K (reference), exchange with D_2O vapor, and subsequent back-exchange with 2-ethyl phenol.

2.3.2. ^{1}H MAS NMR Spectroscopy

We examined all silicates by ^{1}H MAS NMR spectroscopy, with results in Figure 2.4. Table 2.1 summarizes the chemical shifts of silanol species observed, and the qualitative changes to these species upon acid treatment. A variety of ^{1}H chemical environments with differing chemical shifts, in the range 1.8 – 9 ppm, are observed for all silicates. Signals less than 1.8 ppm appear in acid-treated materials, which we do not attribute to silanol species. For the purposes of spectral assignments, four colored bands in Figure 2.4 indicate the four principal resonances for silanols observed across silicates that exhibit similar chemical shift (within 0.3 ppm).

The signal at 1.8 ppm, observed in all silicates, is known to correspond to free silanols that do not engage in H-bonding.[54] This signal dominates the spectra of calcined materials **1**, **2**, and **3**, which have not been subject acid treatment. Chemical environments with chemical downfield of 1.8 ppm arise from protons that are deshielded (relative to free silanols) by H-bonding interactions.[54] As summarized in Table 2.1, the spectral contribution of these H-bound chemical environments increases markedly upon acid treatment of **1**→**1-a**, **2**→**2-a**, and **3**→**3-a**. More specifically, resonances at ~2.3 ppm, ~ 3.2 ppm, and ~3.9 ppm are observed to correspond to H-bound silanols in all silicates. In addition, shoulders at 5.6, 6.4 and 7.5 ppm are observed in **2-a**, but do not appear distinct shoulders **3-a**.

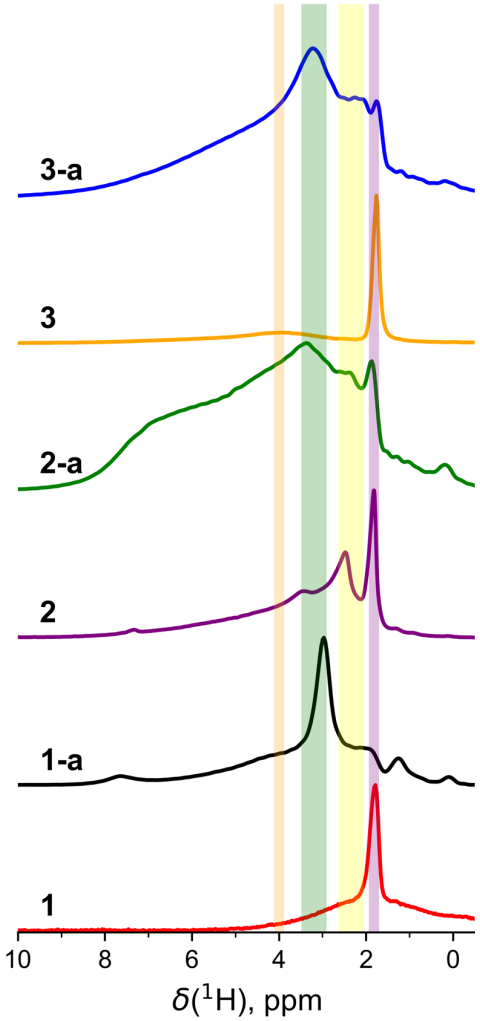

Figure 2.4. ^{1}H MAS NMR spectra of **1, 1-a, 2, 2-a, 3, 3-a**, normalized to maximum intensity. Highlighted by a band in purple, yellow, green, and orange are resonances at 1.8, 2.2-2.5, 3.1-3.3, and 4.0 ppm assigned to silanol species that are discussed in the text. All materials were treated under vacuum at 473 K prior to measurements. Spectra of **3** and **3-a** correspond to 3-dimenstonal SSZ-70 zeotype spectra that have been previously reported (see Figure A2.2) and are included here for completeness.[44]

Table 2.1. Summary of qualitative effect of acid washing on the ^{1}H NMR signal intensity

Sample	Species (ppm) change (+ indicates increase, - indicate no change, n/a indicates species is not present)						
	0.8-1.3	**1.8**	**2.2 - 2.5**	**3.1 - 3.3**	**3.9 - 4.0**	**5.6**	**6.4**
SQ-DQ correlation	self	self	self	cross with 3.9 - 4.0	cross with 3.1 - 3.3	cross with 6.4	cross with 5.6
1→1-a	+	-	+	+	+	n/a	n/a
2→2-a	-	-	+	+	+	+	+
3→3-a*	+	-	+	+	+	n/a	n/a

*Corresponds to 3-D version of zeolite that was previously published;[44] see Figure A2.2

2.3.3. SQ-DQ ^{1}H MAS NMR Spectroscopy

We investigated the through-space correlation of different silanol species by single quantum – double quantum (SQ-DQ) ^{1}H MAS NMR dipolar correlation spectroscopy. Results are shown in Figure 2.5. In SQ-DQ spectra, only species that are correlated through-space exhibit signal intensity; therefore, cross-correlated species that exhibit different SQ signals but the same DQ coherence correspond to ^{1}H species in different chemical environment but adjacent in space, while self-correlated species that lie along the diagonal (i.e. the same SQ and DQ coherences) represent closely spaced silanols of the same species.

Resonances in SQ-DQ spectra Figure 2.5 correspond to the same silanol species as in Figure 2.4, with signals at 1.8, 2.2, 3.0 – 3.3, and 3.9 – 4.0 ppm being observed in all acid treated silicates; the former two exhibit self-correlation, while the latter two are cross-correlated, as summarized in Table 2.2. We now examine the effects of acid treatment **1→1-a**, **2→2-a**, and **3→3-a** on the speciation of silanols detected in SQ-DQ spectra.

The double quantum spectra show clear differences in homonuclear coupling upon treatment of **3→3-a**, shown in Figure 2.5E and 2.5F, respectively. Calcined **3** exhibits predominantly an autocorrelation signal at ~ 1.8 ppm, due to silanols that are not engaged in H-bonding, but sufficiently adjacent in space for homonuclear coupling to occur. The spectrum of the deboronated **3-a** is instead dominated by two well-resolved cross-correlation peaks for H-bound silanols, at 3.3 and 4.0 ppm. In addition, the autocorrelation signal at 1.8 ppm remains in **3-a**, and a new broad auto-correlation signal center ~ 2.2 ppm appears. All attempts by ^{1}H NMR to show the presence of more than two silanols employing 3Q or 4Q excitation in **3-a** were unsuccessful.[44]

Treatment **2→2-a** also causes significant changes to homonuclear coupling in spectra in Figure 2.5C and 2.5D. Calcined silicate **2** exhibits a weak signal, with an autocorrelation at ~ 1.8 ppm as the only distinct resonance. The spectrum of **2-a** is instead dominated by several well-resolved cross-correlation peaks for H-bound silanols. These appear at 3.3 and 3.9 ppm, which are the same chemical shifts observed in **3-a**, as well as at 5.6 and 6.4 ppm, which do not appear in any other spectrum in Figure 2.5. In addition, the autocorrelation signal at 1.8 ppm remains in **2-a**, and a new broad auto-correlation signal center ~ 2.2 ppm appears.

For the amorphous SiO_2 support, hydroxylation **1→1-a** also results in dramatic changes to the homonuclear coupling in spectra shown in Figure 2.5A and 5B. Only a weak autocorrelation signal at 1.8 ppm is observed for **1**. Instead, in **1-a**, broad and intense cross-correlation peaks appear at 3.1 and 3.9 ppm, together with a predominant autocorrelation signal at ~ 2.2 ppm in **2-a**.

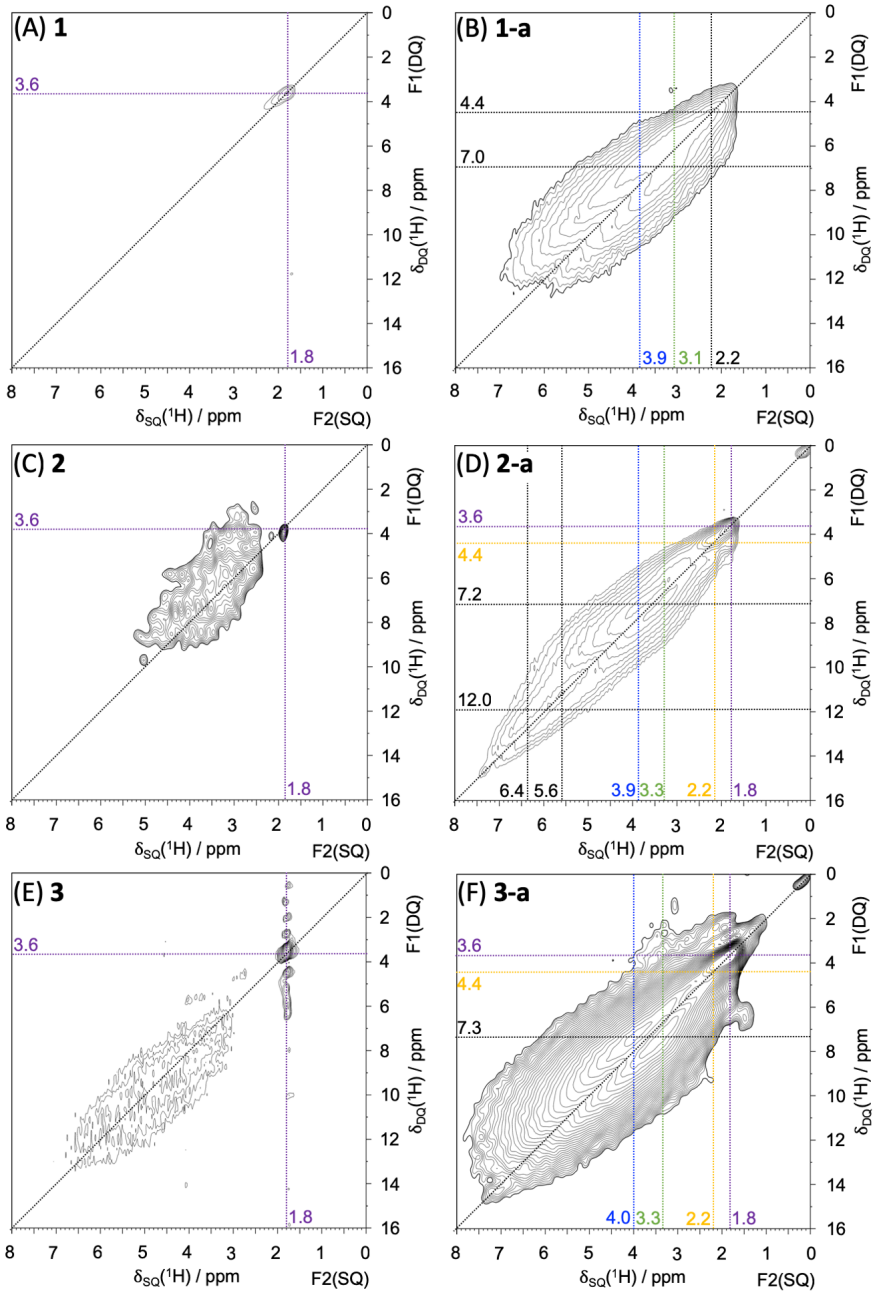

Figure 2.5. ^{1}H single-quantum double-quantum (SQ-DQ) ^{1}H MAS NMR dipolar correlation spectra acquired of **(A) 1** (previously published),[44] **(B) 1-a**, **(C) 2**, **(D) 2-a**, together with previously published[44] **(E)** B-SSZ-70 as an analogue to **3**, and **(F)** B-SSZ-70 as an analogue to **3-a**. All materials were treated under vacuum at 473 K prior to measurement. Dashed line indicates cross-correlated species, which exhibit double-quantum coherence; species that exhibit different SQ chemical shift but the same DQ coherence are cross-correlated, while species that exhibit the same SQ and DQ coherence (i.e along the diagonal) are self-correlated.

2.3.4. ^{31}P NMR Spectroscopy of 3-a Treated with TMPO

Sample **3-a** was treated with an excess of TMPO, because the $\delta(^{31}P)$ of this molecule in interaction with the surface of zeotypes reports on the speciation acidic sites.[55] The 1D ^{31}P MS NMR spectrum of the TMPO-treated **3-a** sample is shown in Figure 2.6, and exhibits two broad resonances. To gain greater resolution into the different chemical environments present within these broad resonances, ^{31}P-^{31}P 2D RFDR MAS NMR spectra were measured, with results also shown in Figure 2.6. The latter spectrum exhibits a variety of well-distinguished resonances, indicating the presence of several different ^{31}P environments of the adsorbed TMPO. Signals at $\delta(^{31}P)$ 32 ppm correspond to TMPO physisorbed on the silicate surface. The resonances at $\delta(^{31}P)$ 42 and 44 ppm correspond to TMPO in its crystalline state, present here due to the excess of TMPO used to treat **3-a**. ^{31}P resonances downfield of 45 ppm, highlighted in grey, correspond to TMPO interacting with silanol groups, at 46, 50, and 53 ppm. This indicates that TMPO experiences at least three distinct chemical environments due to interactions with three different silanol species. It is possible that additional species exist, but are not manifested as distinct maxima.

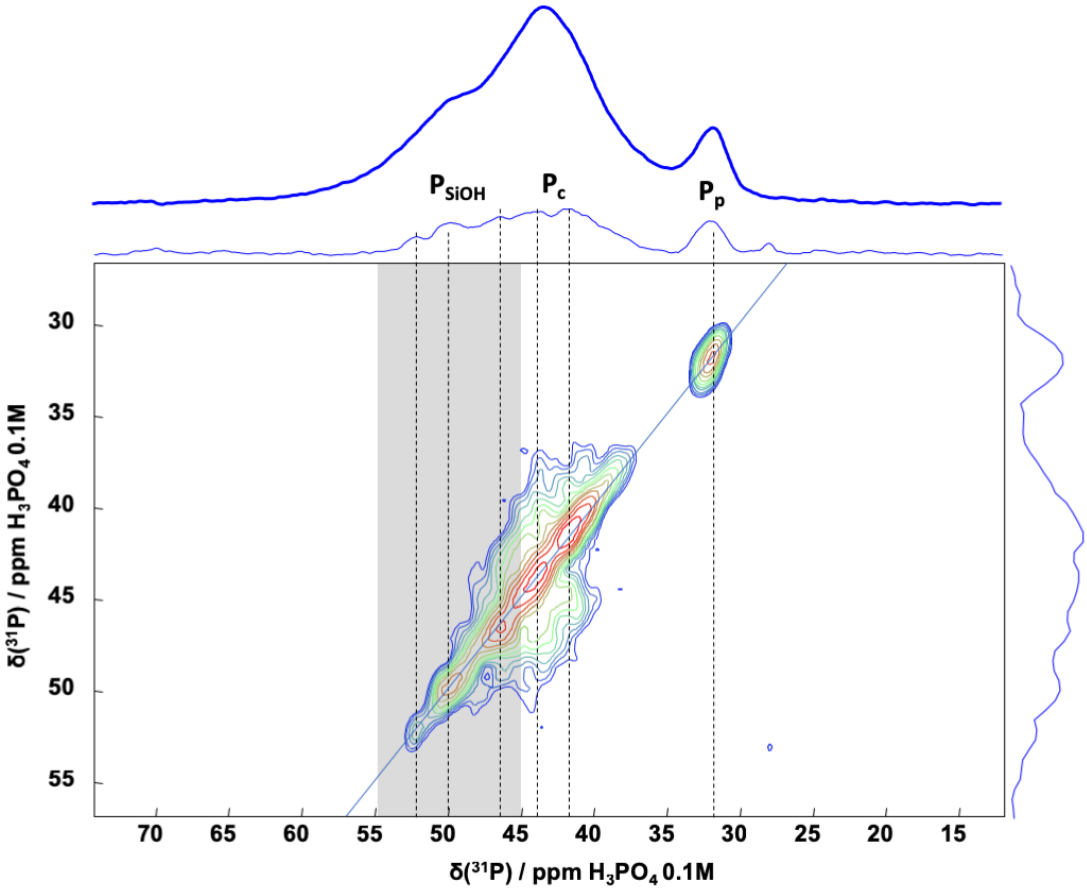

Figure 2.6. ^{31}P-^{31}P 2D RFDR MAS NMR spectrum of **3-a** treated with an excess of TMPO, as detailed in section 2.2.3. ^{1}D ^{31}P MAS NMR spectrum is shown as a thick blue line on the top.

2.3.5. Calculated Geometries of Silanol Structures

To determine possible structures adopted by mutually interacting silanols, force field calculations where performed to simulate defect sites formed by removal of a T-atom from two different crystallographic positions (details in section 2.2.4). Such a defect site would nominally be occupied by four silanols (see **D3_full** and **D8_full** in Figure A2.6); however, because only two silanols adjacent in space are observed by SQ-DQ NMR, we decided to mutually condense two silanols to form a siloxy Si-O-Si. Selected optimized geometries of the resulting two silanols are shown in Figure 2.7, while all calculated structures are shown in Figure A2.6.

Structures in Figure 2.7 exhibit two silanols and a Si-O-Si structure (from condensation) that are closely adjacent in space (within the vacancy formed by the removal of a T-atom). Structures **D3_II** and **D3_VI** originate from different choices for silanol condensation starting from the same vacancy defect structure (see **D3_full** in Figure A2.6). Therefore, even within the same T-site vacancy, several possible silanol structures can result depending on subtle geometric details. Three such possible structures are shown in Figure 2.7, to illustrate the possible arrangement of mutually H-bound silanols:

- **D3_II**: silanols can mutually interact by forming a proton donor/acceptor pair, also termed O-perturbed and H-perturbed silanols.[2]
- **D3_IV**: One of the silanols in this pair is can also interacting with a siloxane (Si-O-Si) backbone of the silicate
- **D8_IV**: It is also possible for two silanols to engage in H-bonding interactions with the same Si-O-Si of the siloxane, but not with each other.

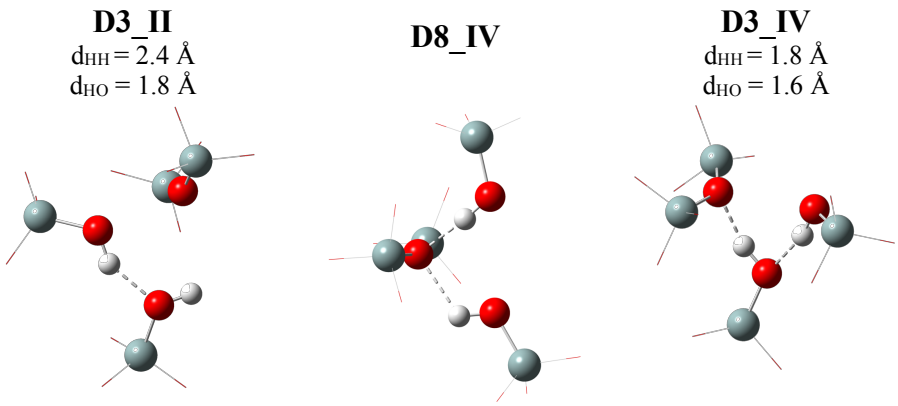

Figure 2.7. Selected optimized geometries adopted by silanols upon vacancy defect formation and condensation of a silanol pair. Only Si (grey), oxygen (red), and H (white) atoms that are part of the framework defect are shown, while H-bonding is indicated as a dashed line. All structures are included in Figure A2.6, while the full cluster model files are included in the supplementary information. H-H and H-O distances of the silanol H-bond pair are also given.

2.3.6. Catalytic Beckman rearrangement

The ramifications of silanol location on catalytic performance were investigated by using selected materials as catalysts for the Beckmann rearrangement (Scheme 2.3), with results shown in Figure 2.8. **3-p-a** and **3-a**, corresponding to non-delaminated and delaminated versions of SSZ-

70 that have been deboronated, respectively. Both materials are active catalysts for this reaction. Delamination, which increases the external surface area (Table A2.1) also increases conversion (with a modest decrease in selectivity) as evident when comparing **3-p-a** to **3-a**, consistent with this reaction occurring on the external surface of zeotypes (i.e. a higher external surface results in a higher conversion).[11] In comparison to both of these zeotypes, amorphous **1-a** exhibits significantly lower selectivity at similar levels of conversions, resulting in significantly diminished product yields. This is consistent with prior results indicating that crystalline supports are more effective catalysts for this reaction.[15]

Scheme 2.3. Beckmann rearrangement of cyclohexanone oxime into ε-caprolactam.

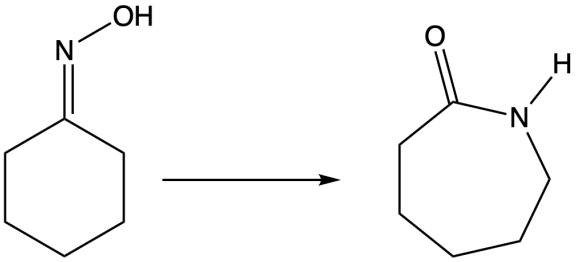

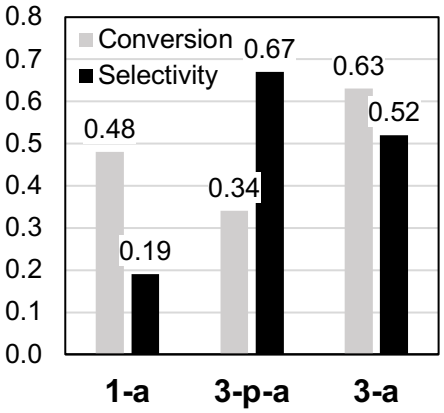

Figure 2.8. Catalytic activity (conversion and selectivity) in the Beckmann rearrangement reaction for **1-a** and **3-p-a**, and **3-a** as catalysts. **3-p-a** is an acid treated (i.e. deboronated) borosilicate SSZ-70 with lower external surface area than **3-a** (Table A2.1). Conversion indicates the amount of cyclohexanone oxime consumed, while selectivity indicates the fraction of this consumption that produced the ε-caprolactam product.

2.4. Discussion

2.4.1. Effect of Acid Treatment on Zeotype Frameworks and Silanols

Comparison of IR (Figure 2.1) and ^{1}H MAS NMR (Figure 2.4) spectra for samples before and after acid treatment (i.e. **1** to **1-a**, **2** to **2-a**, and **3** to **3-a**) indicate that acid treatment induces the formation of H-bound silanol species, manifested by υ_{OH} redshifted frmo 3740 cm^{-1} in FTIR spectra and δ_{H} downfield from 1.8 ppm in ^{1}H MAS NMR spectra.

The comparison of both FTIR and ^{1}H MAS NMR spectra for **3** to **3-a** indicate increased spectral contributions from H-bound silanols in **3-a**. This is consistent with vacancy formation upon deboronation **3→3-a**, in which $(SiO)_x$-B bonds are converted to x adjacent SiO-H species. Arrangements of silanols in vacancies synthesized by deboronation have been referred to as "silanol nests" and nominally consist of four silanol groups (i.e. $x = 4$),[43] as observed in calculated structures **D3_full** and **D8_full** (Figure A2.6). However, the existence of such closely spaced silanols at room temperature conditions has been debated, because of the tendency of silanols to condense.[51,52] Cross-correlated signals at 3.3 and 4.0 ppm observed in the SQ DQ ^{1}H MAS NMR spectrum of **3-a** in Figure 2.5F, indicating that at least two mutually H-bound paired silanols are closely adjacent in space. No triple or quadruple quantum resonances for silanols were observed (results not shown), however, suggesting no more than two silanols are spatially proximal within these vacancies. We therefore conclude that two of the silanols that would nominally comprise as "silanol nest" of four silanols spontaneously condense below 393 K (the dehydration temperature for these samples), as depicted in Scheme 2.1.

This observation is the basis for considering partially-condensed silanols within vacancies in force field calculations, with results in Figure 2.7 and Figure A2.6. These calculations demonstrate that even in these partially condensed two-silanol "nests", the close spatial proximity of silanols can lead to mutual H-bonding in a variety of spatial arrangements.

Acid treatment of purely siliceous **2** to synthesize **2-a** changes the predominant silanol species from free silanols (i.e. non-H-bound) in **2** to H-bound silanols in **2-a**, as observed by IR (Figure 2.1) and ^{1}H MAS NMR (Figure 2.4 and Figure 2.5) spectra. Indeed, these spectra for **2-a** and **3-a** appear broadly similar, because both of these acid-treated silicates contain an abundance of silanol groups. However, upon close inspection, SQ-DQ ^{1}H MAS NMR for **2-a** in Figure 2.5D exhibit resonances at 5.6 and 6.4 ppm, and 7.5 ppm, which are not observed in **3-a** (Figure 2.5F). We therefore conclude that, despite being isostructural, the speciation and location of H-bound silanols in in **2-a** is different from that of framework vacancies in **3-a**.

Such difference can be rationalized by a difference in the mechanism of silanol formation in **3→3-a** vs. **2→2-a**. This difference occurs because hydrolysis and leaching of framework T-atoms (B^{III}) catalyzed by acid in **3→3-a** – which result in the formation of a vacancy defect – is unlikely in purely siliceous **2→2-a**, given the almost negligible solubility of silica in acid.[56] Instead, we conclude that the formation of H-bound silanols in **2→2-a** occurs through structural rearrangements that lead to the formation of connectivity defects. These could include Si-O-Si → 2SiOH ring opening, as known to occur upon steaming zeolites, or desilication.[57] Indeed, connectivity defects are known to give rise to H-bonds[58,59] and can be formed through mechanisms that do not require removal of framework T-atoms, such as Si migration observed upon steam treatment of high-silica zeolites.[60]

2.4.2. Spectroscopic Assignment of Silanol Species

Four distinct maxima are observed in FTIR spectra of zeotypes in Figure 2.1A, which were denoted species **I**, **II**, **III**, and **IV**. Results of H→D→H exchange, shown in Figure 2.3 and discussed in 2.3.1, demonstrate that all of these species **I** - **IV** are located within sterically accessible environments. This suggest that at least four distinct silanol environments are possible. Consistent with this, at least three distinct chemical environments are detected for TMPO interacting with silanols (Figure 2.6).

Calculated structures in section 2.3.5 (Figure 2.7 and Figure A2.6) indicate that silanols can adopt a variety of H-bonded structures, depending on the local geometry of defects. This suggest that the different species **I** – **IV** detected spectroscopically may correspond to different H-bonding arrangements of silanols.

We now combine all spectroscopic observations to arrive at conclusions about the nature speciation and framework location of these silanol species in silicate zeotypes. We focus our discussion on the four distinct bands observed by FTIR spectroscopy in all zeotypes, **I**, **II**, **III**, and **IV**, before discussing the additional chemical environment observed by ^{1}H MAS NMR spectroscopy in **2-a**, and interpreting results for amorphous SiO_2. The assignments are summarized in Table 2.2 and Scheme 2.2.

2.4.2.1. Correlation Between Infrared and ^{1}H MAS NMR Spectroscopies

The population of H-bound silanol species **II**, **III**, and **IV** increase upon acid washing **2→2-a** and **3→3-a** (Figure 1B). A clear analogy to this behavior is observed in results of NMR spectroscopy, summarized in Table 2.1, where bands at 2.2 – 2.5 ppm, 3.1 – 3.3 ppm, and 4.0 ppm become more prominent upon acid washing **2→2-a** and **3→3-a**. Indeed, H-bonding is known to cause deshielding of δ_{H} analogously to the redshift of υ_{OH} for silanols. This relationship has been quantified by Brunner et al. for zeolites:[33,61]

$$\frac{\delta_{\mathrm{H}}}{\mathrm{ppm}} = 57 - 0.015\frac{\upsilon_{OH}}{\mathrm{cm}^{-1}} \qquad (1)$$

where δ_{H} is the ^{1}H NMR chemical shift and υ_{OH} the infrared stretching frequency.

We use equation (1) to establish a correlation between the υ_{OH} observed by infrared spectroscopy to the δ_{H} of chemical environments observed by ^{1}H MAS NMR. In results shown in Figure 2.9, the solid line corresponds to predicted values of equation (1), while squares correspond to the observed values δ_{H} (Table 2.1, Figure 2.4) and υ_{OH} (Figure 2.1). It can be seen that experimental observations of δ_{H} to υ_{OH} are in reasonable agreement to predictions from equation (1); we therefore postulate that these δ_{H} to υ_{OH} values are essentially spectroscopic reporters for the same silanol species. Based on this correspondence, we assign values of δ_{H} to υ_{OH} to species **I**, **II**, **III**, and **IV**, as summarized in Table 2.2 and color-coded throughout this paper for ease of visualization.

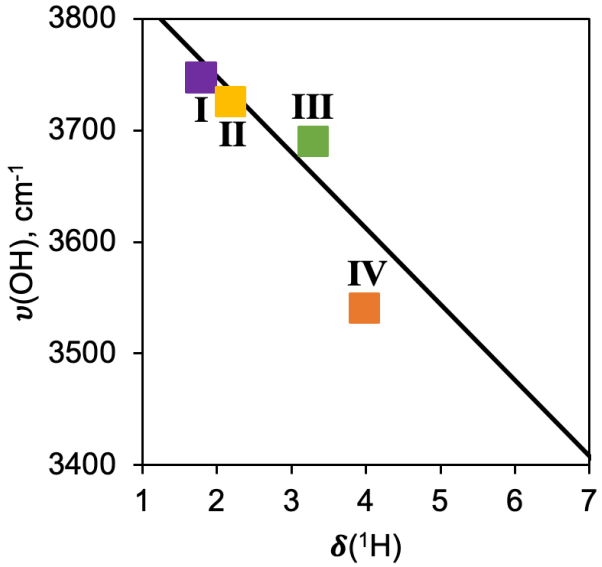

Figure 2.9. Correlation of observed infrared frequencies υ_{OH} with chemical shifts δ_{H} in Table 2.2 (squares), along with prediction from equation (1) (solid line). For species **I**, **II**, **III**, and **IV**, the value of υ_{OH} were chosen based on the four distinct maxima in Figure 2.1A, while the value of δ_{H} were chosen based on the four principal chemical environments observed across all zeotypes in Figures 4 and 5. Given the breadth of band **IV**, other species may exist beneath the absorbance envelope 3200 – 3600 cm^{-1} (Table 2.2), but they do not appear as distinct maxima in FTIR spectra.

Scheme 2.2. Depiction of silanol species assigned in Table 2.2.

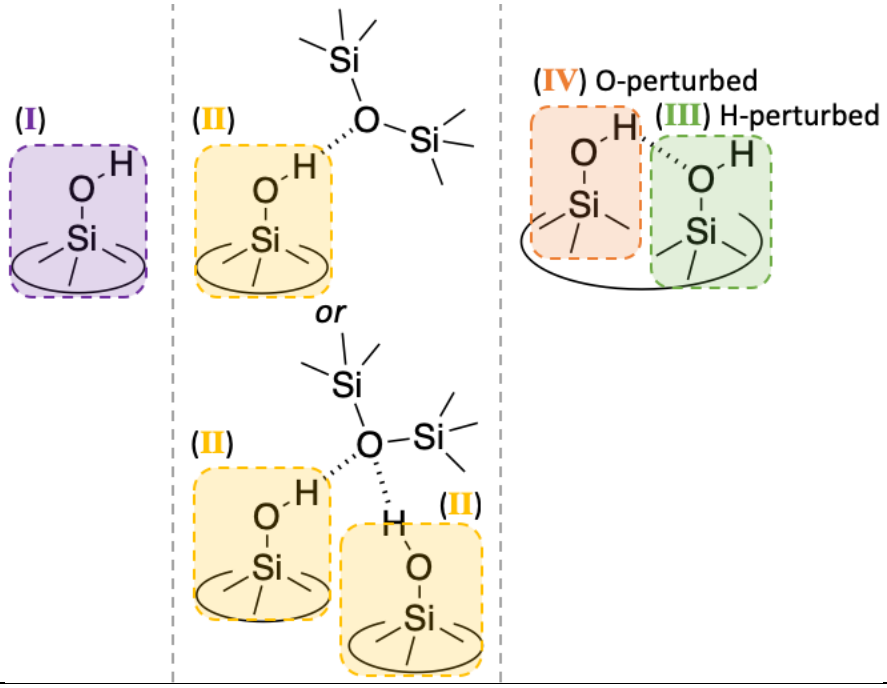

Table 2.2. Summary of results from FTIR and NMR spectroscopies for assignment of silanol species

Species	FTIR			^{1}H MAS NMR		Assignment
	frequency, cm^{-1}	effect of acid-treatment	effect of thermal dehydroxylation	**δ(^{1}H)**	SQ-DQ coherence	
I	**3747**	no change	no change	**1.8**	self	free silanol
II	**3725**	increase	no change to 723 K	**2.2**	self	silanols interacting with Si-O-Si framework siloxane in zeotypes
III	**3690**	increase	no change to 673 K	**3.1 - 3.3**	cross to **3.9 - 4.0**	H-bound silanols in pairs, perturbed by H
IV	**3530**	increase	decrease	**3.9 - 4.0**	cross to **3.0 - 3.3**	H-bound silanols in pairs, perturbed by O

2.4.2.2. Silanol Species I

Silanol species **I**, with υ_{OH} at 3747 cm^{-1} and δ_{H} at 1.8 ppm, is known to correspond to free silanols that are not H-bound,[2,26,54] as represented in Scheme 2.2.

This assignment is consistent with the prominence of this band in the IR (Figure 2.1A) and ^{1}H MAS NMR (Figure 2.4) spectra of silicate **2** and **3**, which can be rationalized as follows. Terminal T-sites (**i**), where the SSZ-70 crystalline framework is interrupted (purple in Scheme 2.1) share only three O-atoms with other framework T-sites (as opposed to the typical four). The fourth Si-O bond is terminated by a H^+ to form a silanol (SiOH). Based on the crystallographic location of these T-sites, which are uniformly separated by 8.3 Å, silanols are too far apart for H-bonding interactions.[2,22,32] Therefore, non-H-bound silanols species **I** at 3747 cm^{-1} (Figure 2.1A) and 1.8 ppm (Figure 2.4) predominate in the spectra of **2** and **3**, which lack any post-synthetic vacancy defects, but which contain terminal T-atom positions (**i**) populated by free silanols. Terminal T-sites (**i**) with silanols species **I** are also present in **2-a** and **3-a**, but are observed as a shoulder because H-bound silanols in other environments dominate the spectra after acid treatment.

Difference IR spectra quantifying the effect of acid treatments **2→2-a** and **3→3-b** (Figure 2.1B) show little change in the signal for species **I** upon acid washing of zeotypes **2** and **3**. Given these negligible changes, we surmise that silanols in framework defects, formed upon acid treatment, do not interact with silanol species **I**. This is further evidence of the assignment of the location of silanol species **I** to terminal T-atom positions (**i**), because these T-atom positions are located away from vacancy defects in other framework locations ((**ii**), (**iii**), and (**iv**)), as depicted in Scheme 2.1. This in contrast from the behavior observed on a 'flat' amorphous silica surface where the formation of nearby silanols forces previously free and isolated silanols to engage in H-bonding (decrease in band **I** for **1→1-a** in Figure 2.1B; see further discussion in section 2.4.2.6). This highlights the independence of silanols in T-atom positions (**i**) from those elsewhere in the zeolite framework.

2.4.2.3. Silanol Species III and IV

Silanol species **III** exhibits a υ_{OH} at ~ 3690 cm^{-1} and δ_{H} at 3.1 – 3.3 ppm, while species **IV** exhibits a υ_{OH} at ~ 3530 cm^{-1} and δ_{H} at 3.9 – 4.0 ppm, values that are indicative of H-bound silanols. We consider the assignment of **III** and **IV** together, because of their cross-correlation in SQ-DQ ^{1}H MAS NMR spectra of **2-a** and **3-a** in Figure 2.5D and 5F. This cross-correlation indicates that silanol species **III** and **IV**, with different chemical shift, are sufficiently adjacent to each other in space for effective dipolar coupling. Given this close spatial proximity, we conclude that **III** and **IV** are mutually hydrogen bonded.

Consistent with this spatial proximity, quantitative measurements of ^{1}H DQ build-up curves previously demonstrated that, in **3-a**, species **III** and **IV** are located 2.5 Å apart,[44] a distance that is sufficiently close for H-bonding (see chapter 5.3).[32] Indeed, this measured distance is in reasonable agreement with H-H distances of 2.4 Å for calculated structures **D3_II** in Figure 2.7, which serve as a model for plausible spatial arrangement of interacting H-bound silanols.

In any mutually H-bound silanol pair, one silanol must necessarily act as a proton acceptor, and another as a proton donor. Given the weaker redshift of **III** relative to **IV**, we assign species **III** to H-perturbed silanols (i.e. proton acceptor) and **IV** to an O-perturbed silanol (i.e. proton

donor), as depicted in Scheme 2.2. This is based on prior observations that H-perturbed silanols are more weakly redshifted than O-perturbed silanols.[2,22,28,30]

Significant discrepancies in the assignments of H-perturbed and O-perturbed silanols exist in the literature. For example, Blasco et al. assigned bands at 3736 and 3690 cm^{-1} to H-perturbed and O-perturbed silanols, respectively, in a titanosilicate zeotype.[30] In prior studies of amorphous silica, O-perturbed silanols have been assigned to υ_{OH} ~ 3530 cm^{-1}, consistent with our assignment; however, H-perturbed species have been instead assigned to a υ_{OH} at ~ 3725 cm^{-1},[2,22,28] rather than the υ_{OH} at ~ 3690 cm^{-1} for species **III** that we observe here. These prior assignments were based on careful experimentation, but crucially lacked experimental methods to correlate through-space interactions between mutually H-bonding silanol species. Our approach of using zeotypes as well-defined silicates and multi-dimensional NMR spectroscopy to probe through-space interactions addresses these challenges, and has enabled us to assign this species with unprecedented certainty here.

2.4.2.4. Silanol Species II

Silanol species **II** exhibits a υ_{OH} of 3725 cm^{-1} and a δ_{H} of 2.2 ppm, corresponding to a slight redshift and deshielding from free silanol groups **I**. This shift indicates that the Si-OH bond is weakened by perturbing H-bonding interactions, which are however weaker than those in mutually H-bound silanols **III** and **IV**.

SQ-DQ ^{1}H MAS NMR dipolar correlation spectra of **2-a** and **3-a** exhibit only self-correlated signals of **II** at 2.2 ppm, in contrast to the cross-correlation observed between species **III** and **IV**. Thus, species **II** do not engage with H-bonding interactions with any other silanol species; otherwise a DQ coherence with a species with different δ_{H} would be expected. The thermal stability of species **II** up to 723 K (Figure 2.2B, Table 2.2) is also consistent with lack of H-bonding of **II** to other silanols, as such H-bonding results in thermal dehydroxylation for mutually H-bound **III** and **IV** below this temperature (Figure 2.2B and Table 2.2).

To reconcile the apparently contradictory nature of a silanol perturbed by H-bonding, but not H-bound to any other silanols, we postulate that **II** corresponds to silanols engaging in H-bonding interactions with the Si-O-Si backbone of the zeotype framework, as depicted in Scheme 2.2. Such an assignment accounts for H-bonding of **II** without invoking H-bonding to another silanol. Geometrically, such silanol species can readily occur within highly-curved internal micropore geometries (i.e. environments **ii**, **iii**, or **iv** in Scheme 2.1). Also consistent with this interpretation, no band for **II** is observed by IR amorphous SiO_2, where a "flat" non-uniform surface precludes geometric arrangements where a silanol could interact with the Si-O-Si backbone.

Calculated structure **D8_IV** shows a possible structure adopted by silanols H-bonding to the Si-O-Si backbone of the framework. Interestingly, in this structure, both silanols engage in H-bonding interactions with the Si-O-Si backbone, but not with each other. Such an arrangement accounts for why significant intensity for species **II** at 2.2 ppm is observed in the SQ-DQ ^{1}H MAS NMR spectra of **2-a** and **3-a** (Figure 2.5D and 5F), which indicates spatial proximity between silanols species **II**. This possibility is also considered in Scheme 2.2.

There has been considerable debate in the literature about the assignment of this species with υ_{OH} at ~ 3725 cm^{-1}, and we now place our interpretation within this context. Vansant *et al*, in

their classic text on amorphous silica, assign this species to H-perturbed silanols.[2] Zecchina *et al* also postulate that this frequency corresponds to "internal terminal silanols" in zeotypes,[28] whereby a silanol is H-perturbed at the end of a chain of H-bonded silanols. However, all of these interpretations would require that a neighboring O-perturbed silanol be detected by SQ-DQ ^{1}H MAS NMR (much in the way that species **III** and **IV** are cross-correlated; section 4.2.3). Instead, we only observe a self-correlation for **II**, which precludes these prior assignments. This further demonstrates the importance of the SQ-DQ ^{1}H MAS NMR methods that we introduce here for understanding the speciation of silanols in silicates.

Other authors have alluded to assignments that are in better agreement with our interpretation. In Vansant's text,[2] the authors make reference to the work of Fink,[62] who attributes this frequency to inter-particle interactions of a silanol to a siloxane. Such interpretation is consistent with our assignment here, where inter-particle interactions can be thought of interactions within a curved zeotype pore. Separately, Barbera *et al.*[21] and Bordiga *et al.*[31] postulate "internal silanols" (in zeolite channels) at this frequency, occurring within pores, but not engaged in H-boding. Our interpretation here accounts for such "free internal silanols", but differs in that such internal silanols are likely engaged in H-bonding interactions with the siloxane backbone to account for the redshift in their frequency with respect to "truly free" silanols with υ_{OH} at 3747 cm^{-1}.

2.4.2.5. Other H-bound Species

Our assignment of species **I**, **II**, **III**, and **IV**, summarized in Scheme 2.2 and Table 2.2, corresponds to the principal spectral components observed across all silicate zeotypes. In addition to signals for bands **I**, **II**, **III**, and **IV**, less prominent silanol species are detected at even more deshielded environments by ^{1}H MAS NMR spectroscopy in **2-a**. These are resonances at 5.6 and 6.4 ppm, which are cross-correlated in the SQ-DQ spectrum (Figure 2.4 and Figure 2.5, Table 2.1 and Table 2.2). According to equation (1), these species would be expected to result in υ_{OH} at 3500 and 3450 cm^{-1}. However, no distinct bands in the FTIR spectrum in Figure 2.1A are observed in this region, which we attribute to the very broad signal expected for these υ_{OH} (stronger H-bonding causes broader spectral bands),[33] and to their occlusion by the band for species **IV** at 3530 cm^{-1}. Nonetheless, it is likely that these "other" silanol species may contribute to infrared absorbance in this broad absorbance region (3200 – 3600 cm^{-1}) in **2-a** (and possibly other silicates).

The cross-correlation between species at δ_{H} 5.6 and 6.4 ppm in **2-a** suggests that they are mutually H-bound, but are more strongly perturbed by H-bonding that species **III** and **IV**. We posit that such strongly perturbed species may arise from either:

- H-bonding with additional silanol species, consistent with prior work suggesting that longer H-bonding chains results in higher degree of SiO-H bond weakening,[26,28] or
- Silanol pairs located within framework environments that give rise to geometric orientations resulting in very strongly perturbed environments. Consistent with this latter explanation, several authors have suggested that υ_{OH} of silanols engaged in H-bonding interactions can be affected by the geometric orientation between H-bonds.[22,32,33] One such possible highly-perturbed silanol orientation is illustrated by calculated structure **D3_IV** in Figure 2.7, where silanols form part of a highly strained structure with an H-bonding distance of only 1.6 Å. In

addition, this particular geometry results in additional H-bonding for the H-perturbed silanol to the Si-O-Si framework, likely resulting in additional perturbation.

Notably, a difference in chemical shift of 0.8 ppm is observed for these "other" mutually H-bound silanols at δ_H 5.6 and 6.4 ppm, the same ppm difference between species **III** and **IV**. This observation suggests that mutually H-bound silanols become more deshielded *together*, when affected by a perturbing chemical environment. This can be rationalized as follows. If a silanol group forms a (first) hydrogen bond to another oxygen atom (either in an adjacent silanol or adjacent Si-O-Si backbone), then it will become a better H-bond acceptor for a second donating silanol group. For reasons of bond order conservation, the strength of this "perturbation" with the first hydrogen bond will affect the strength of the second hydrogen bond.[63] This effect may also explain, why the broadening of cross-correlation signals along the diagonal in the SQ-DQ ^{1}H MAS NMR spectra of **2-a** (Figure 2.5D) leaves the difference between the two coupling protons relatively unaffected at ~0.8 ppm.

The presence of these other highly H-bound silanols, beyond **I** – **IV**, may also account for the dehydroxylation behavior of **3-a** in Figure 2.2A. If species **IV** were paired with **III** exclusively, as represented in Scheme 2.2, dehydroxylation would necessarily consume both **III** and **IV**; however, dehydroxylation occurs for **IV** at a temperature in which **III** is stable, contradicting this interpretation. This observation can be reconciled by the presence of "other" species in the region ~ 3530 cm^{-1}, which are more strongly H-bound than and therefore condense at a lower temperature than **IV**.

2.4.2.6. Silanol Speciation in Amorphous SiO_2

Amorphous dehydroxylated **1** exhibits sharp band at υ_{OH} 3747 cm^{-1} in its IR spectrum (Figure 2.1A). This frequency coincides with free (non H-bound) silanols **I** on zeotypes (see section 2.4.2.2), leading us to conclude that free silanols of type **I** are *chemically* equivalent whether they are part of dense amorphous network – as in **1** – or a crystalline framework – as in **2** –.

The surface silanol densities in **1** is ~ 1 nm^{-2},[34] which leads to an average O···O distance ~ 10 Å, too far to H-bond. Such distances indicate predominantly isolated silanols, consistent with measurements of DQ build-up curves which indicated silanols predominantly (82%) isolated from each other in **1** (see chapter 5.3).[64] However, some dipolar coupling between free silanols is observed in the SQ DQ ^{1}H MAS NMR spectrum of **1** (Figure 2.5A), indicating spatial proximity between these silanols. We attribute this to the non-ordered nature of **1**, which allows some hydroxyl groups to be closer than 10 Å *average* O···O distance (and, as a corollary, some may be farther).

Hydroxylation of amorphous **1→1-a** induces a shift of the highest frequency band from υ_{OH} 3747 cm^{-1} in **1** to 3741 cm^{-1} in **1-a** (Figure 2.1A). Based on the frequency shift from υ_{OH} 3747 cm^{-1} in **1** to 3741 cm^{-1}, no truly free silanols persist in **1-a**. Indeed, difference spectra in Figure 2.1B showing the intensity of band **I** in **1** decrease dramatically upon **1→1-a** treatment, accompanied by an increase in the shoulder corresponding to H-bonded silanols. Consistent with this, comparison of ^{1}H MAS NMR spectra of **1** to **1-a** show a disappearance of free silanol species **I** at 1.8 ppm in **1** to form predominantly H-bound species < 1.8 ppm in **1-a** (Figure 2.3). Taken together, data implies that previously free silanols now engage in H-bonding interactions with

silanols that are newly formed upon hydroxylation.

This behavior contrast with the site independence of species **I** in zeotypes, which are unaffected by acid treatment (Figure 2.1B; see discussion in 2.4.2.2). We posited that this independence is due to silanol species **I** in zeotypes being structurally isolated at terminal T-sites (**i**). On a "flat" amorphous surface with non-uniform structural features, instead, no such site isolation is possible. Therefore, despite this *chemical equivalence* of **I** across crystalline and amorphous silicates, their *structural environments are not equivalent*, and subject to changes occurring on the surrounding surface. This highlights how crystalline zeotype supports can enforce independent molecular environments for functional applications, not possible with traditional amorphous supports, as demonstrated recently for silicates analogous to the ones studied here.[18]

In hydroxylated amorphous **1-a**, a broad absorption envelope is observed at frequencies below **I** (< 3747 cm^{-1}) by IR in Figure 2.1A, rather than three distinct maxima for **II**, **III**, and **IV** observed in zeotypes. IR spectral linewidths are known to be reporters on the uniformity of molecular environments for vibrating species;[48] broadness of linewidths therefore reflects a non-uniform distribution of molecular environments. Therefore, we interpret this absorption envelope as a continuous distribution of local H-bonded silanol environments (and associated υ_{OH}) in **1-a**, instead of the three distinct environments observed in zeotypes. This non-uniform distribution of H-bonded silanol environments on amorphous **1-a** reflects the well-known non-uniform surface structures on amorphous silicates,[35] and highlights how crystalline zeotype supports are capable of exhibiting well-defined silanol environments, even for H-bound silanols.

This non-uniform distribution of silanol environments in amorphous silica is analogous to the non-uniform vs. uniform distribution of Al^{3+} environments in amorphous silica-alumina vs. zeolites, inferred on the basis on ^{27}Al MAS NMR spectroscopic measurements.[65] This uniformity of Al^{3+} environments in zeolites was ascribed to the constraints that crystallinity imposes on the Al-O-Al angles, which are absent in an amorphous network.[65] Such uniformity is, according to Rabo and Gadja,[66] also important in dictating the stability of zeolites. They posit that the long-range order of the zeolite framework prevents local distortions caused by the presence of acidic protons, and leads to symmetric bridging hydroxyls (Si-O(H)-Al) acid sites. These are intrinsically stronger than sites in amorphous aluminosilicates, where the aluminosilicate network instead accommodates asymmetric (and weaker) acidic protons, corresponding to Si-O(H)→Al.[66]

Resonances at 3.1 and 3.9 ppm are mutually cross-correlated in the SQ-DQ ^{1}H MAS NMR spectrum of **1-a** (Figure 2.5B). Based on their similarity of δ_H in zeotypes (Table 2.2), we also assign these silanols to mutually H-bound silanols, which are H-perturbed (**III**) and O-perturbed (**IV**) respectively, as shown in Scheme 2.2. The local distribution of surface structures on the amorphous silica surface, however, causes their maxima in the infrared spectrum to be faint and part of a broad distribution of local environments (i.e. a broad shoulder in Figure 2.2B). This distribution of environments is also seen in SQ-DQ 1H MAS NMR spectra for **1-a** (Figure 2.5B), which show broadening along the diagonal for species **III** and **IV**, in contrast to exhibit two well-resolved peaks for zeotypes (Figure 2.5D and 2.5F).

The speciation of silanols in silica has been subject to extensive investigation,[2,22,23,32,34,54,67] with conflicting conclusions. Our assignments of bands at 3747 cm^{-1} to free silanols, and the band at 3530 cm^{-1} to O-perturbed silanols are mostly consistent with the literature. However, as

discussed in section 2.4.2.3, our demonstration that H-perturbed silanols exhibit a υ_{OH} ~ 3690 cm^{-1} is in contrast with prior assignments (often attributed to υ_{OH} = 3725 cm^{-1}).[2,22,28] Yet, our assignment is more certain than previous studies, because of evidence of through-space correlation of silanols provided by two-dimensional NMR measurements, and we consider it to resolve the long-standing debate about the frequency of H-perturbed silanols.

2.4.3. Structural Stability of Silanols and their Catalytic Repercussions

We now discuss the implications of the different thermal dehydroxylation behavior observed for amorphous **1-a** (Figure 2.2B) and compared it to zeotype **3-a** (Figure 2.2A). As depicted in Scheme 4, thermal dehydroxylation causes neighboring H-bound silanols to condense (2Si—OH → Si—O—Si + H_2O), with progressively higher temperatures leading to a higher degree of silanol condensation. This is reflected in the progressive disappearance of H-bound silanol species with increasing temperature in Figure 2.2.

The stability of different silanol species is summarized in Table 2.2, and decreases in the order **I** (stable) > **II** (stable to 723 K) > **III** (stable to 673 K) > **IV** for **3-a**. For amorphous **1-a**, instead, all species < 3741 cm^{-1} undergo dehydroxylation above 473 K. Notably, these observations indicate that species **II** and **III** in zeotype **3-a** are stable at temperatures where silanols within equivalent H-bonding environments (i.e. similar IR frequencies) on amorphous **1-a** condense. This suggest that otherwise similar H-bound silanol pairs (i.e. involving silanol pairs of **III** and **IV** depicted in Scheme 2.2) are more stable to thermal dehydroxylation in crystalline **3-a** than in amorphous **1-a**. This is depicted in Scheme 2.4.

Structural rearrangements are necessary for the formation of strained siloxane structures upon silanol condensation (i.e the closing of a Si-O-Si results in siloxane ring strain).[67] Such structural rearrangements are accompanied by energetic barriers, as has been observed in sodium silicate glasses.[68] Based on our observation of higher thermal stability of silanols in zeotypes, we conclude that structural rearrangements necessary for dehydroxylation are less favored in crystalline zeotype framework than in amorphous silica. We therefore postulate that crystalline zeolitic silicates resist local structural rearrangements than amorphous networks, because such rearrangements would need to overcome a significant energetic barrier associated with disrupting the long-range order of the crystalline framework. This compares to amorphous networks whose non-uniformity facilitates local rearrangements during dehydroxylation.

The speciation and structure of silanols are essential in designing silicates for specific applications. For example, they control adsorption of water on silica,[23] or catalytic effects mediated by water adsorbed or excluded from hydrophilic or hydrophobic pores.[19,69] Therefore, the stabilization of H-bound environments by a crystalline framework which resists structural rearrangements, observed here, can aid in the design of more stable functional materials. Indeed, we have recently observed that silanols crystalline zeotypes stabilize Fe^{III} centers within tetrahedral framework environments, which are otherwise unstable in amorphous silicates.[45] This will be the subject of Chapter 3.

To obtain further evidence of the functional consequences of the structural stability of zeotypes compared to amorphous silica, we consider the catalytic activities of **1-a** and **3-a** for the Beckmann rearrangement reaction (Scheme 2.3). This reaction is known to be catalyzed by silanol assemblies (i.e. "silanol nests") on both crystalline silicate zeotypes or amorphous silicates.[15]

Results in Figure 2.8 show that deboronated zeotypes in their non-delaminated (**3-p-a**) and delaminated forms (**3-a**) are more active and selective towards the desired product than amorphous **1-a**, even though the latter amorphous silica has a higher external surface area. We therefore surmise that the stability of the silanol assemblies in zeotype **3-a** are beneficial for their catalytic activity, demonstrating an advantage of using crystalline zeotype silicates, not only for making better defined active sites, but also for catalysis.

We posit that this stability of crystalline frameworks extends beyond the systems discussed here, and may be helpful in maintaining the required active site structures under harsh conditions that may otherwise elicit structural changes in amorphous supports. This points towards advantages of using crystalline silicates as supports, rather than amorphous ones.[47]

Scheme 2.4. Dehydroxylation in crystalline vs. amorphous silicates

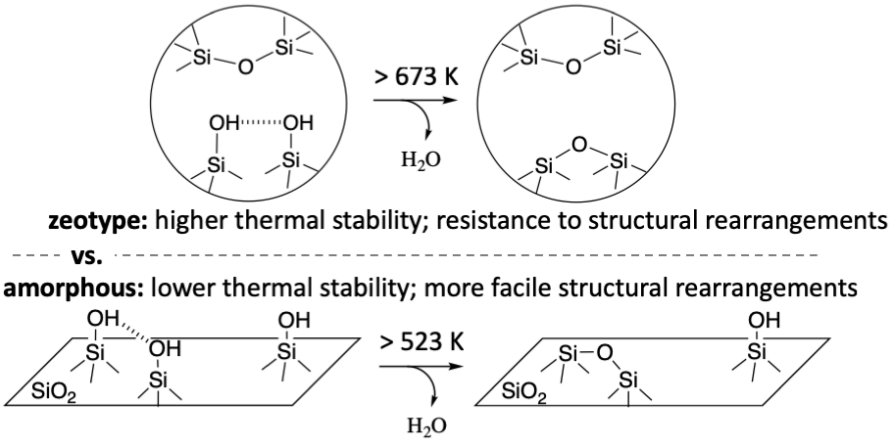

2.5. Conclusions

Combining vibrational IR spectroscopy and multi-dimensional ^{1}H MAS NMR spectroscopy, our results here clarify the speciation of silanols in silicates. This combination has enabled us to assign silanol species based on a rigorous measurement of their spatial arrangement. These assignments, summarized Scheme 2.2 and Table 2.2, are:

(**I**) Silanols with υ_{OH} 3747 cm^{-1} and δ_{H} 1.8 ppm: free (non H-bound) silanols on the crystal terminating surface of zeotypes or on the surface of dehydroxylated silica.

(**II**) Silanols with υ_{OH} 3725 cm^{-1} and δ_{H} 2.2 ppm: silanols H-bound to a siloxane in a zeolitic micropore.

(**III**) Silanols with υ_{OH} 3690 cm^{-1} and δ_{H} 3.1-3.3 ppm: H-perturbed (proton acceptor) silanols in an H-bonding silanol pair.

(**IV**) Silanols with υ_{OH} 3530 cm^{-1} and δ_{H} 3.9-4.0 ppm: O-perturbed (proton donor) silanols in an H-bonding silanol pair.

These assignments resolve outstanding discrepancies in the literature about the speciation of silanols on silicates, as discussed in section 2.4.2. We note, however, that subtle variations in local geometry and pore-wall curvature may result in variations of spectroscopic signatures and silanol speciation, and are likely responsible for the broad contribution in the region υ_{OH} 3200 – 3600 cm^{-1}. Our assignments above therefore represent predominant silanol species, but the presence of other species with varying structure and geometry cannot be discarded.

Based on these assignments, we studied the different behavior of zeolitic silicates vs. amorphous silica upon acid treatment, thermal dehydroxylation, and catalysis for the Beckmann rearrangement reaction, demonstrating that:

- Acid treatment of purely siliceous zeotypes (**2→2-a**) can engender defect site formation through the formation of connectivity defects (section 2.4.1).
- Despite the *chemical equivalence* of silanols in crystalline vs. amorphous silicates, their *structural environments are not equivalent*, and are more uniform and thermally stable in crystalline zeotypes (section 2.4.2.6).
- H-bound silanols are more stable to dehydroxylation in zeolitic compared to amorphous silicates, leading us to postulate that crystallinity stabilizes the silicate framework against structural rearrangements (section 2.4.3).
- Structural uniformity and stability of silanols can be beneficial for the functional applications of silicates, as exemplified by the higher catalytic activity of vacancy-rich deboronated **3-a** for the Beckman rearrangement reaction (section 2.4.3) compared with amorphous silica.

These observations improve our understanding of the behavior of silicates as a broad class of materials with important technological relevance, and in general point towards the benefits of using crystalline rather than amorphous silicates due to the higher stability and uniformity of the former, for functional applications.

2.6. Appendices

2.6.1 Synthesis of Silicates and Delaminated Zeotypes

The textural properties of all silicates are summarized in Table A2.1. **2-p** and **3-p** are the silicate and borosilicate precursors that are delaminated to synthesize **2** and **3**. Delamination increases external surface area, increase in total pore volume, and decrease in micropore volume, without affecting the framework structures of the zeotypes (as confirmed by PXRD patterns that remain unchanged by delamination, reported in reference [18]). Acid treatment does not significantly affect frameworks structures, as evidenced by the lack of significant changes to the textural properties between **2** and **2-a**, and **3** and **3-a**.

Delamination treatment appears to modify silanols present in pure silicate **2** from those present in precursor **2-p**. Infrared data in Figure A2.3 exhibits and intense band centered around 3530 cm^{-1} for (nondelaminated) **2-p**, which decreases upon delamination in spectrum of **2**. This can be rationalized by the fact that framework vacancies are present in the native framework of SSZ-70 / SVY*-,[36] giving rise to H-bound silanols with vibrations at 3530 cm^{-1} (section 3.1). We surmise that the presence of F^- ions (from ammonium salts) during delamination, which act as mineralizing agents during zeolite synthesis,[70] causes some of these framework vacancies to be filled by Si^{IV} (i.e the framework is 'healed'). This results in a less-defective framework in **2** than in **2-p**. Such 'healing' may also be occurring during the synthesis of **3** from **3-p**.

Table A2.1. Summary of textural properties of silicate materials investigated. [a]

Sample	Description	S_{acc} (m^2/g)[b]	V_{tot} (cm^3/g)	V_{micro} (cm^3/g)[c]
1	dehydroxylated amorphous SiO_2	190	1.19	-
1-a	hydroxylated amorphous SiO_2	181	1.26	-
2-p	silicate Si-SSZ-70	30	0.24	0.17
2	delaminated Si-SSZ-70 2-p	83	0.40	0.14
2-a	acid-treated (desilicated) 2	71	0.37	0.11
3-p	borosilicate SSZ-70	66	0.32	0.20
3	delaminated B-SSZ-70 3-p	135	0.46	0.16
3-a	acid-treated (deboronated) 3-a	136	0.47	0.15

[a]Textural properties of **1**, **3-p**, **3**, and **3-a** adapted from reference [18]. [b]Accessible surface area, determined by the BET method for SiO_2, and from the t-plot external surface area for microporous zeotypes. [c]Micropore volume; amorphous silicates lack microporosity. N_2 adsorption-desorption physisorption isotherms are included in Figure A2.1.

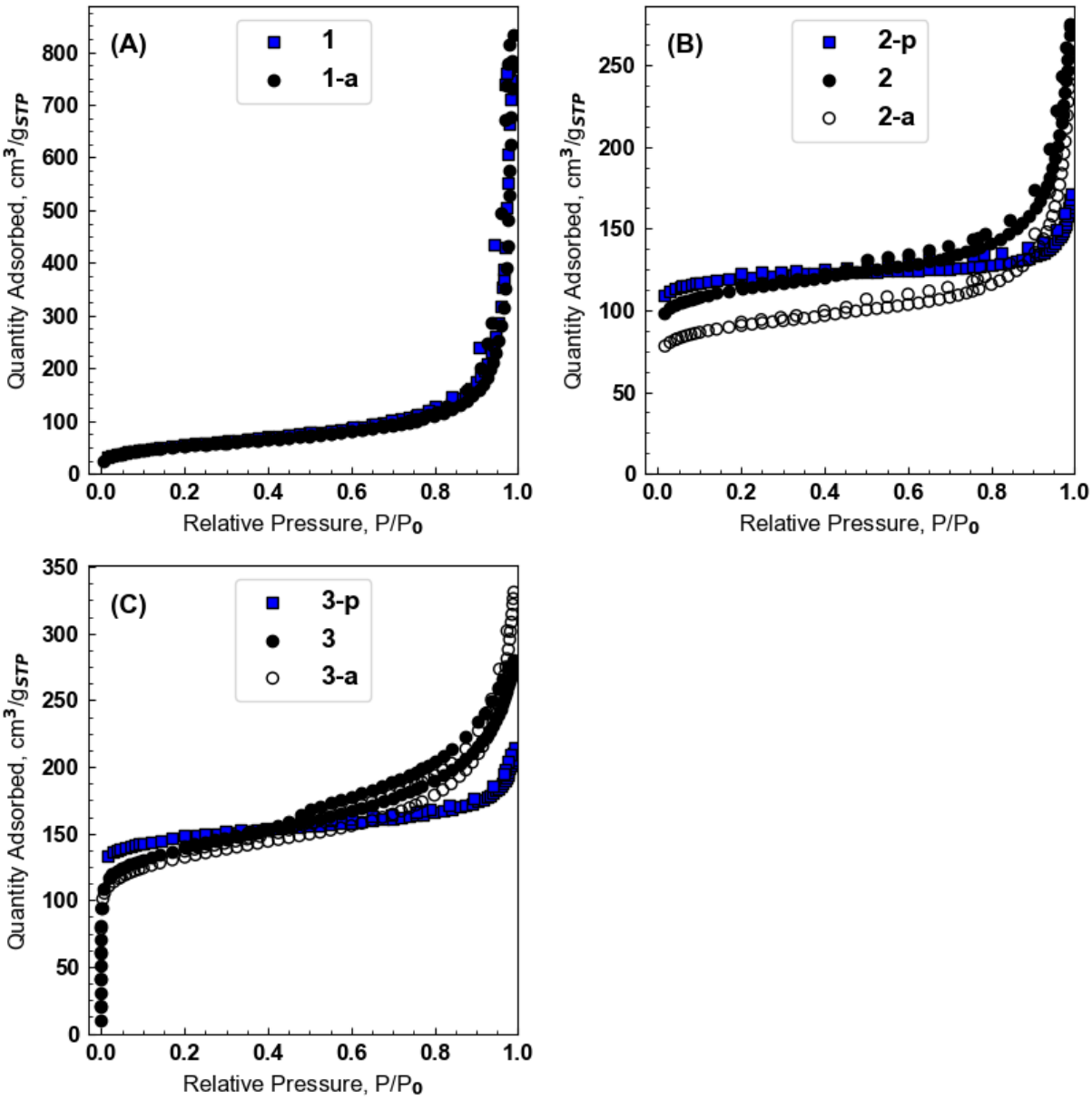

Figure A2.1. N_2 adsorption-desorption physisorption isotherms at 77 K used to calculate textural properties for materials in Table A2.1. All silicates were calcined at 823 K prior to measurements. Results for **1**, **1-a**, **3-p**, **3**, and **3-a** are partially reproduced from reference [18].

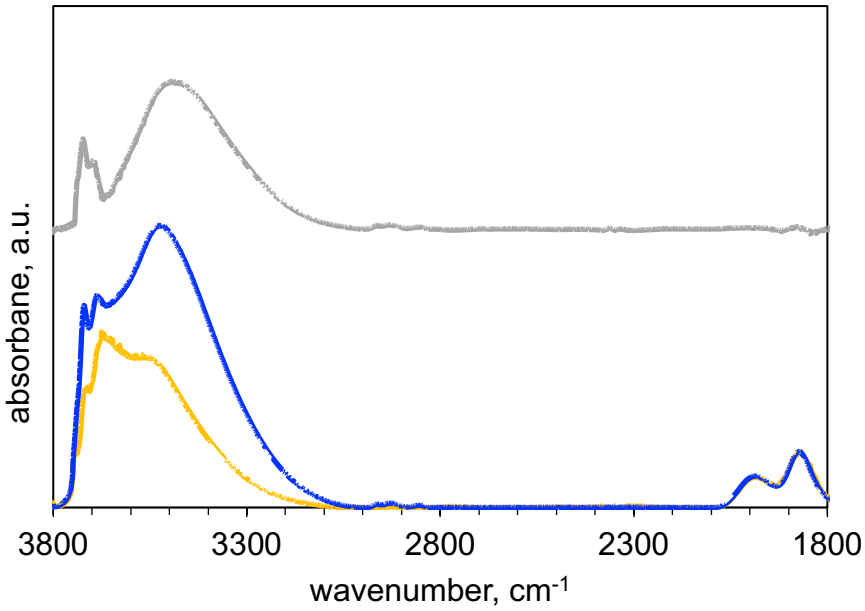

Figure A2.2. Normalized transmission FTIR spectra for materials indicated as **3** and **3-a** studied by ^{1}H MAS NMR in Figure 2.4 and Figure 2.5. These are previously studied[44] non-delaminated 3-D borosilicate SSZ-70 (as opposed to delaminated materials whose infrared spectra are shown in Figures 1 and 2). Color coding corresponds to that in Figure 2.1A: orange B-SSZ-70 **3-p**, while blue is deboronated SSZ-70 **3-p-a**. The same silanol bands and the same change in silanol bands upon acid treatment **3-p→3-p-a** (gray) are observed for this 3-D version in Figure A2.2 as for delaminated (**3→3-a**) variants whose spectra are reported in Figure 2.1. Thus, delamination does not affect the speciation of silanols or their change upon acid treatment in borosilicates. We therefore use previously reported data on this 3-D zeotype in the ^{1}H MAS NMR spectra reported in Figure 2.3 and Figure 2.4,[44] *in lieu* of data for the delaminated variant.

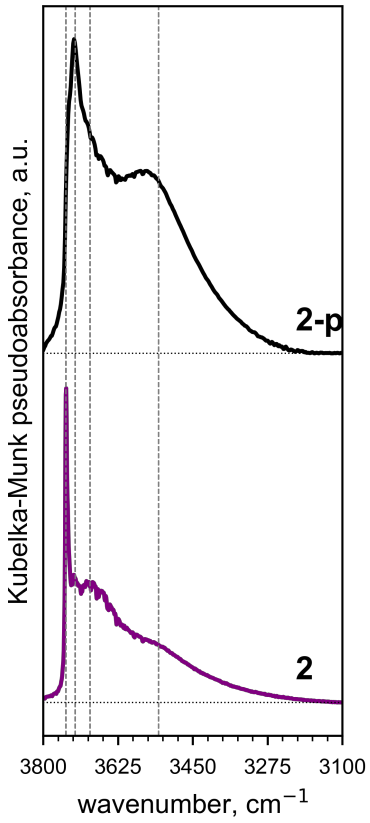

Figure A2.3. Normalized transmission DRIFT spectra of **2-p** (black) and **2** (purple). The spectral contributions of H-bound species in **2-p** are significantly diminished in **2**.

2.6.2. Additional Infrared Characterization

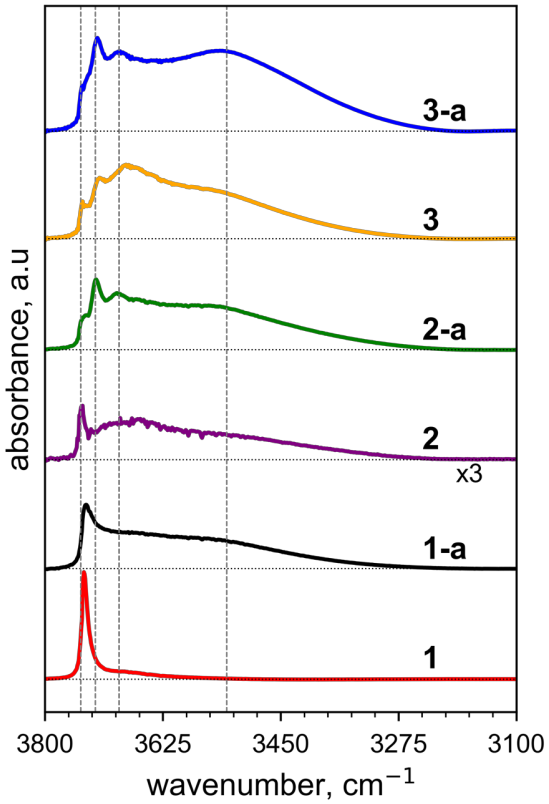

Figure A2.4. Transmission Fourier-transform infrared spectra of the *ν*(SiO-H) region of silicate materials; spectrum of **2** is magnified by 3 times. Spectra correspond to self-supported wafers treated under flowing He at 473 K. All results except for that of **2-a** are adapted from reference [18]. Comparison of spectra in Figure 2.1 (DRIFTS) and Figure A2.4 (transmission) indicate that wafer-pressing for transmission experiments may cause some surface hydroxylation of samples **1** and **2**; therefore, we base our discussions on silanol speciation in the main text on DRIFTS results. However, diffuse-reflectance measurements are not quantitative across samples; therefore, we use transmission results of Figure A2.4 to compute difference spectra in Figure 2.1B. Dotted horizontal lines indicate baseline, while dashed vertical lines indicate stretching bands at 3747, 3725, 3690, 3530 cm^{-1} corresponding to silanol species **I**, **II**, **III**, and **IV**.

2.6.3. Force Field Calculations

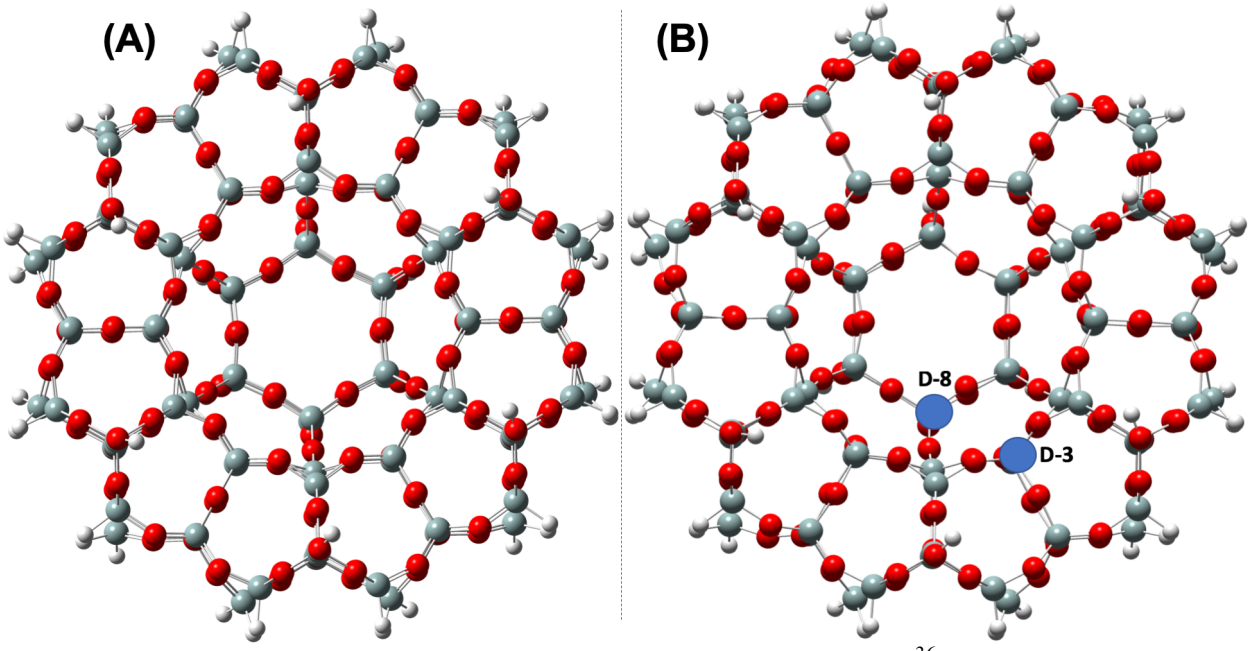

Figure A2.5. (A) SSZ-70 cluster model derived from the crystal structure,[36] which includes a full 12-MR pocket structure and next-nearest Si neighbors, terminated by hydrides that are frozen in space. **(B)** Geometry optimization of the cluster in **(A)**, while maintaining hydrides frozen in space, does not significantly alter the cluster geometry. O: red, Si: grey, H: white.

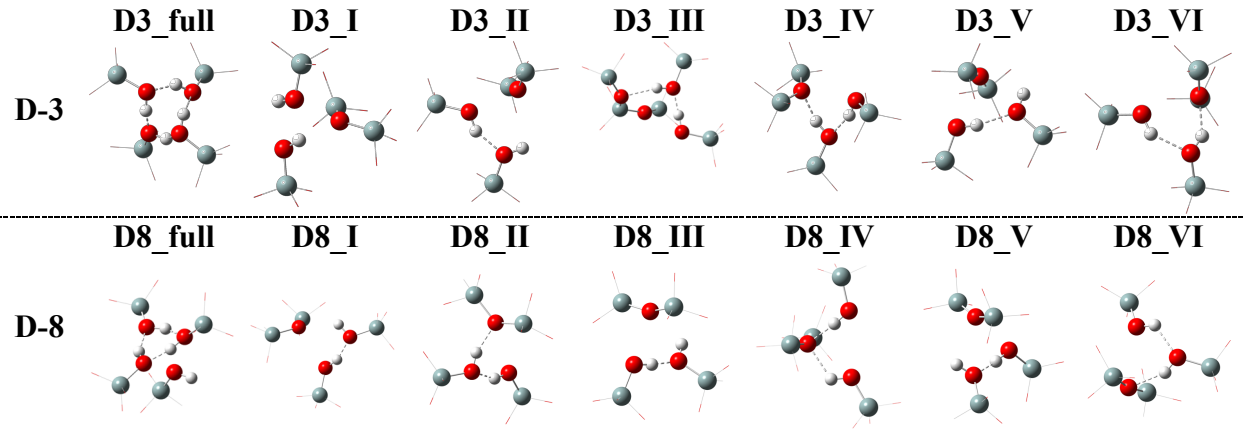

Figure A2.6. Optimized geometry of the full silanol defect upon a T-atom removal from positions D-3 and D-8 (see Figure A2.5) is shown left, followed by the six optimized geometries resulting from the mutual condensation of two silanols in each of these T-atom positions. Only the defect structure is shown and only Si (grey), oxygen (red), and H (white) atoms that were condensed or are involved in H-bonding are shown as ball and stick models. H-bonding is shown as a dashed bond. Structures of the full cluster models are included in the supplementary information.

2.7 Acknowledgements

Funding from the US Department of Energy (DE-FG02-05ER15696) for catalyst characterization, and the Management and Transfer of Hydrogen via Catalysis Program funded by Chevron Corporation for catalyst synthesis is gratefully acknowledged. The Molecular Graphics and Computation Facility is funded by the NIH (S10OD023532). CS and HK gratefully acknowledge funding from the Deutsche Forschungsgemeinschaft (DFG, German Research Foundation – KO 1817/3-1). NG would like to thank Julie E. Rorrer for her assistance in performing DRIFTS measurements. Christian Schroeder and Hubert Koller are acknowledged for ^{1}H MAS NMR measurements. Dr. Louwanda Lakiss is acknowledged for assistance with isotopic exchange measurements (Figure 2.3). Dr. Cassandre Kouvatas, Florent Dubray, and Prof. Svetlana Mintova are acknowledged for ^{31}P MAS NMR measurements. Dr. Dave W. Small is acknowledged for assistance in force field calculations. Dr. Alexnder Okrut is acknowledged for measurements of Beckmann rearrangement reaction rates.

2.8 References

(1) Bergna, H. E. The Colloid Chemistry of Silica. *Advences Chem.* **1994**, *234*, 1–47.

(2) Vansant, E. F.; Voort, P. Van Der; Vrancken, K. C. *Characterization and Chemical Modification of the Silica Surface*, 1st ed.; Elsevier, 1995; Vol. 93.

(3) Baerlocher, C.; McCusker, L.; Olson, D. *Atlas of Zeolite Framework Types*, 6th ed.; Elsevier: Amsterdam, 2007.

(4) Notestein, J. M.; Iglesia, E.; Katz, A. Grafted Metallocalixarenes as Single-Site Surface Organometallic Catalysts. *J. Am. Chem. Soc.* **2004**, *126* (50), 16478–16486.

(5) Yabushita, M.; Grosso-Giordano, N. A.; Fukuoka, A.; Katz, A. Selective Sequestration of Aromatics from Aqueous Mixtures with Sugars by Hydrophobic Molecular Calixarene Cavities Grafted on Silica. *ACS Appl. Mater. Interfaces* **2018**, *10*, 39670–39678.

(6) Grosso-Giordano, N. A.; Eaton, T. R.; Bo, Z.; Yacob, S.; Yang, C. C.; Notestein, J. M. Silica Support Modifications to Enhance Pd-Catalyzed Deoxygenation of Stearic Acid. *Appl. Catal. B Environ.* **2016**, *192*, 93–100.

(7) Bouh, A. O.; Rice, G. L.; Scott, S. L. Mono- and Dinuclear Silica-Supported Titanium(IV) Complexes and the Effect of TiOTi Connectivity on Reactivity. *J. Am. Chem. Soc.* **1999**, *121* (31), 7201–7210.

(8) Tucker, M. H.; Crisci, A. J.; Wigington, B. N.; Phadke, N.; Alamillo, R.; Zhang, J.; Scott, S. L.; Dumesic, J. A. Acid-Functionalized SBA-15-Type Periodic Mesoporous Organosilicas and Their Use in the Continuous Production of 5-Hydroxymethylfurfural. *ACS Catal.* **2012**, *2* (9), 1865–1876.

(9) Demmelmaier, C. A.; White, R. E.; van Bokhoven, J. A.; Scott, S. L. Evidence for a Chromasiloxane Ring Size Effect in Phillips (Cr/SiO2) Polymerization Catalysts. *J. Catal.* **2009**, *262* (1), 44–56.

(10) Copéret, C.; Allouche, F.; Chan, K. W.; Conley, M. P.; Delley, M. F.; Fedorov, A.; Moroz, I. B.; Mougel, V.; Pucino, M.; Searles, K.; et al. Bridging the Gap between Industrial and Well-Defined Supported Catalysts. *Angew. Chem. Int. Ed.* **2018**, *57* (22), 6398–6440.

(11) Sato, H. Acidity Control and Catalysis of Pentasil Zeolites. *Catal. Rev. - Sci. Eng.* **1997**, *39* (4), 395–424.

(12) Ichihashi, H.; Sato, H. The Development of New Heterogeneous Catalytic Processes for the Production of ε-Caprolactam. *Appl. Catal. A Gen.* **2001**, *221* (1–2), 359–366.

(13) Ichihashi, H.; Kitamura, M. Some Aspects of the Vapor Phase Beckmann Rearrangement for the Production of ε-Caprolactam over High Silica MFI Zeolites. *Catal. Today* **2002**, *73* (1–2), 23–28.

(14) Röseler, J.; Heitmann, G.; Hölderich, W. F. Vapour-Phase Beckmann Rearrangement Using B-MFI Zeolites. *Appl. Catal. A Gen.* **1996**, *144* (1–2), 319–333.

(15) Heitmann, G. P.; Dahlhoff, G.; Hölderich, W. F. Catalytically Active Sites for the Beckmann Rearrangement of Cyclohexanone Oxime to ε-Caprolactam. *J. Catal.* **1999**, *186* (1), 12–19.

(16) Kumar, R.; Chowdhury, B. Comprehensive Study for Vapor Phase Beckmann Rearrangement Reaction over Zeolite Systems. *Ind. Eng. Chem. Res.* **2014**, *53* (43), 16587–16599.

(17) Notestein, J. M.; Solovyov, A.; Andrini, L. R.; Requejo, F. G.; Katz, A.; Iglesia, E. The Role of Outer-Sphere Surface Acidity in Alkene Epoxidation Catalyzed by Calixarene-Ti(IV) Complexes. *J. Am. Chem. Soc.* **2007**, *129* (50), 15585–15595.

(18) Grosso-Giordano, N. A.; Hoffman, A. S.; Boubnov, A.; Small, D. W.; Bare, S. R.; Zones, S. I.; Katz, A. Dynamic Reorganization and Confinement of Ti(IV) Active Sites Controls Olefin Epoxidation Catalysis on Two-Dimensional Zeotypes. *J. Am. Chem. Soc.* **2019**, *141* (17), 7090–7106.
(19) Bregante, D. T.; Johnson, A. M.; Patel, A. Y.; Ayla, E. Z.; Cordon, M. J.; Bukowski, B. C.; Greeley, J.; Gounder, R.; Flaherty, D. W. Cooperative Effects between Hydrophilic Pores and Solvents: Catalytic Consequences of Hydrogen Bonding on Alkene Epoxidation in Zeolites. *J. Am. Chem. Soc.* **2019**.
(20) Bass, J. D.; Solovyov, A.; Pascall, A. J.; Katz, A. Acid-Base Bifunctional and Dielectric Outer-Sphere Effects in Heterogeneous Catalysis: A Comparative Investigation of Model Primary Amine Catalysts. *J. Am. Chem. Soc.* **2006**, *128* (11), 3737–3747.
(21) Barbera, K.; Bonino, F.; Bordiga, S.; Janssens, T. V. W.; Beato, P. Structure-Deactivation Relationship for ZSM-5 Catalysts Governed by Framework Defects. *J. Catal.* **2011**, *280* (2), 196–205.
(22) Hoffmann, P.; Knözinger, E. Novel Aspects of Mid and Far IR Fourier Spectroscopy Applied to Surface and Adsorption Studies on SiO2. *Surf. Sci.* **1987**, *188* (1–2), 181–198.
(23) Gallas, J. P.; Goupil, J. M.; Vimont, A.; Lavalley, J. C.; Gil, B.; Gilson, J. P.; Miserque, O. Quantification of Water and Silanol Species on Various Silicas by Coupling IR Spectroscopy and In-Situ Thermogravimetry. *Langmuir* **2009**, *25* (10), 5825–5834.
(24) Ihli, J.; Krumeich, F.; Pinar, A. B.; Ishikawa, T.; Li, T.; Ma, Z.; van Bokhoven, J. A. Heavy Atom Labeling Enables Silanol Defect Visualization in Silicalite-1 Crystals. *Chem. Commun.* **2019**, *55*, 482.
(25) Zhuravlev, L. T. The Surface Chemistry of Amorphous Silica. Zhuravlev Model. *Colloids Surfaces A Physicochem. Eng. Asp.* **2000**, *173* (1), 1–38.
(26) Bordiga, S.; Roggero, I.; Ugliengo, P.; Zecchina, A.; Bolis, V.; Artioli, G.; Buzzoni, R.; Marra, G.; Rivetti, F.; Spanò, G.; et al. Characterisation of Defective Silicalites. *J. Chem. Soc. Dalt. Trans.* **2000**, No. 21, 3921–3929.
(27) Bolis, V.; Busco, C.; Bordiga, S.; Ugliengo, P.; Lamberti, C.; Zecchina, A. Calorimetric and IR Spectroscopic Study of the Interaction of NH3 with Variously Prepared Defective Silicalites: Comparison with Ab Initio Computational Data. *Appl. Surf. Sci.* **2002**, *196* (1–4), 56–70.
(28) Zecchina, A.; Bordiga, S.; Spoto, G.; Marchese, L.; Petrini, G.; Leofanti, G.; Padovan, M. Silicalite Characterization. 2. IR Spectroscopy of the Interaction of Carbon Monoxide with Internal and External Hydroxyl Groups. *J. Phys. Chem.* **1992**, *96* (12), 4991–4997.
(29) Sastre, G.; Fornes, V.; Corma, A. Preferential Siting of Bridging Hydroxyls and Their Different Acid Strengths in the Two-Channel System of MCM-22 Zeolite. *J. Phys. Chem. B* **2002**, *104* (19), 4349–4354.
(30) Blasco, T.; Camblor, M. A.; Corma, A.; Esteve, P.; Guil, J. M.; Martínez, A.; Perdigón-Melón, J. A.; Valencia, S. Direct Synthesis and Characterization of Hydrophobic Aluminum-Free Ti−Beta Zeolite. *J. Phys. Chem. B* **1998**, *102*, 75-88 75.
(31) Bordiga, S.; Ugliengo, P.; Damin, A.; Lamberti, C.; Spoto, G.; Zecchina, A.; Spanò, G.; Buzzoni, R.; Dalloro, L.; Rivetti, F. Hydroxyls Nests in Defective Silicalites and Strained Structures Derived upon Dehydroxylation: Vibrational Properties and Theoretical Modelling. *Top. Catal.* **2001**, *15* (1), 43–52.
(32) Chuang, I.; Maciel, G. A Detailed Model of Local Structure and Silanol Hydrogen

Bonding of Silica Gel Surfaces. *J. Phys. Chem. B* **1997**, *101* (16), 3052–3064.
(33) Brunner, E.; Sternberg, U. Solid-State NMR Investigations on the Nature of Hydrogen Bonds. *Prog. Nucl. Magn. Reson. Spectrosc.* **1998**, *32* (1), 21–57.
(34) Ek, S.; Root, A.; Peussa, M.; Niinistö, L. Determination of the Hydroxyl Group Content in Silica by Thermogravimetry and a Comparison with ^{1}H MAS NMR Results. *Thermochim. Acta* **2001**, *379* (1), 201–212.
(35) Lichtenstein, L.; Büchner, C.; Yang, B.; Shaikhutdinov, S.; Heyde, M.; Sierka, M.; Włoodarczyk, R.; Sauer, J.; Freund, H. J. The Atomic Structure of a Metal-Supported Vitreous Thin Silica Film. *Angew. Chem. Int. Ed.* **2012**, *51* (2), 404–407.
(36) Smeets, S.; Berkson, Z. J.; Xie, D.; Zones, S. I.; Wan, W.; Zou, X.; Hsieh, M. F.; Chmelka, B. F.; McCusker, L. B.; Baerlocher, C. Well-Defined Silanols in the Structure of the Calcined High-Silica Zeolite SSZ-70: New Understanding of a Successful Catalytic Material. *J. Am. Chem. Soc.* **2017**, *139* (46), 16803–16812.
(37) Lawton, S. L.; Leonowicz, M. E.; Partridge, R. D.; Chu, P.; Rubin, M. K. Twelve-Ring Pockets on the External Surface of MCM-22 Crystals. *Microporous Mesoporous Mater.* **1998**, *23* (1–2), 109–117.
(38) Ogino, I.; Eilertsen, E. A.; Hwang, S.-J.; Rea, T.; Xie, D.; Ouyang, X.; Zones, S. I.; Katz, A. Heteroatom-Tolerant Delamination of Layered Zeolite Precursor Materials. *Chem. Mater.* **2013**, *25* (9), 1502–1509.
(39) Archer, R. H.; Zones, S. I.; Davis, M. E. Imidazolium Structure Directing Agents in Zeolite Synthesis: Exploring Guest/Host Relationships in the Synthesis of SSZ-70. *Microporous Mesoporous Mater.* **2010**, *130* (1–3), 255–265.
(40) Archer, R. H.; Carpenter, J. R.; Hwang, S.-J.; Burton, A. W.; Chen, C.-Y.; Zones, S. I.; Davis, M. E. Physicochemical Properties and Catalytic Behavior of the Molecular Sieve SSZ-70. *Chem. Mater.* **2010**, *22* (8), 2563–2572.
(41) Koller, H.; Fild, C.; Lobo, R. F. Variable Anchoring of Boron in Zeolite Beta. *Microporous Mesoporous Mater.* **2005**, *79* (1–3), 215–224.
(42) Hwang, S.-J.; Chen, C. Y.; Zones, S. I. Boron Sites in Borosilicate Zeolites at Various Stages of Hydration Studied by Solid State NMR Spectroscopy. *J. Phys. Chem. B* **2004**, *108* (48), 18535–18546.
(43) Koller, H.; Chen, C. Y.; Zones, S. I. Selectivities in Post-Synthetic Modification of Borosilicate Zeolites. *Top. Catal.* **2015**, *58* (7–9), 451–479.
(44) Grosso-Giordano, N. A.; Schroeder, C.; Okrut, A.; Solovyov, A.; Schöttle, C.; Chassé, W.; Marinković, N.; Koller, H.; Zones, S. I.; Katz, A. Outer-Sphere Control of Catalysis on Surfaces: A Comparative Study of Ti(IV) Single-Sites Grafted on Amorphous versus Crystalline Silicates for Alkene Epoxidation. *J. Am. Chem. Soc.* **2018**, *140* (15), 4956–4960.
(45) Grosso-Giordano, N. A.; Yeh, A. J.; Okrut, A.; Xiao, D. J.; Grandjean, F.; Long, G. J.; Zones, S. I.; Katz, A. Effect of Defect Site Preorganization on Fe(III) Grafting and Stability: A Comparative Study of Delaminated Zeolite vs Amorphous Silica Supports. *Chem. Mater.* **2017**, *29* (15), 6480–6492.
(46) Izumi, Y.; Ichihashi, H.; Shimazu, Y.; Kitamura, M.; Sato, H. Development and Industrialization of the Vapor-Phase Beekmann Rearrangement Process. *Bull. Chem. Soc. Jpn.* **2007**, *80* (7), 1280–1287.
(47) Grosso-Giordano, N. A.; Zones, S. I.; Katz, A. Opportunities for Controlling Catalysis by Designing Molecular Environments around Active Sites: Cations Supported on Amorphous

versus Crystalline Zeolitic Silicate Supports. In *Catalysis: Volume 31*; 2019; pp 72–126.
(48) Hoffman, A. S.; Fang, C. Y.; Gates, B. C. Homogeneity of Surface Sites in Supported Single-Site Metal Catalysts: Assessment with Band Widths of Metal Carbonyl Infrared Spectra. *J. Phys. Chem. Lett.* **2016**, *7* (19), 3854–3860.
(49) Bennett, A. E.; Ok, J. H.; Griffin, R. G.; Vega, S. Chemical Shift Correlation Spectroscopy in Rotating Solids: Radio Frequency-Driven Dipolar Recoupling and Longitudinal Exchange. *J. Chem. Phys.* **1992**, *96* (11), 8624–8627.
(50) Harder, E.; Damm, W.; Maple, J.; Wu, C.; Reboul, M.; Xiang, J. Y.; Wang, L.; Lupyan, D.; Dahlgren, M. K.; Knight, J. L.; et al. OPLS3: A Force Field Providing Broad Coverage of Drug-like Small Molecules and Proteins. *J. Chem. Theory Comput.* **2016**, *12*, 281–296.
(51) Senderov, E.; Halasz, I.; Olson, D. H. On Existence of Hydroxyl Nests in Acid Dealuminated Zeolite Y. *Microporous Mesoporous Mater.* **2014**, *186*, 94–100.
(52) Halasz, I.; Senderov, E.; Olson, D. H.; Liang, J. J. Further Search for Hydroxyl Nests in Acid Dealuminated Zeolite Y. *J. Phys. Chem. C* **2015**, *119* (16), 8619–8625.
(53) Chakarova, K.; Drenchev, N.; Mihaylov, M.; Nikolov, P.; Hadjiivanov, K. OH/OD Isotopic Shift Factors of Isolated and H-Bonded Surface Silanol Groups. *J. Phys. Chem. C* **2013**, *117*, 5242–5248.
(54) Bronnimann, C. E.; Zeigler, R. C.; Maciel, G. E. Proton NMR Study of Dehydration of the Silica Gel Surface. *J. Am. Chem. Soc.* **1988**, *110* (7), 2023–2026.
(55) Dubray, F.; Moldovan, S.; Kouvatas, C.; Grand, J.; Aquino, C.; Barrier, N.; Gilson, J.-P.; Nesterenko, N.; Minoux, D.; Mintova, S. Direct Evidence for Single Molybdenum Atoms Incorporated in the Framework of MFI Zeolite Nanocrystals. *J. Am. Chem. Soc.* **2019**, *141* (22), 8689–8693.
(56) Alexander, G. B.; Heston, W. M.; Iler, R. K. The Solubility of Amorphous Silica in Water. *J. Phys. Chem.* **1954**, *58* (6), 453–455.
(57) Malola, S.; Svelle, S.; Bleken, F. L.; Swang, O. Detailed Reaction Paths for Zeolite Dealumination and Desilication from Density Functional Calculations. *Angew. Chem. Int. Ed.* **2012**, *51*, 652–655.
(58) Koller, H.; Lobo, R. F.; Burkett, S. L.; Davis, M. E. SiO-...HOSi Hydrogen Bonds in As-Synthesized High-Silica Zeolites. *J. Phys. Chem.* **1995**, *99* (33), 12588–12596.
(59) Shantz, D. F.; Schmedt Auf Der Günne, J.; Koller, H.; Lobo, R. F. Multiple-Quantum ^{1}H MAS NMR Studies of Defect Sites in as-Made All- Silica ZSM-12 Zeolite. *J. Am. Chem. Soc.* **2000**, *122* (28), 6659–6663.
(60) Ikeda, T.; Inagaki, S.; Hanaoka, T. A.; Kubota, Y. Investigation of Si Atom Migration in the Framework of MSE-Type Zeolite YNU-2. *J. Phys. Chem. C* **2010**, *114*, 19641–19648.
(61) Brunner, E.; Pfeifer, H.; Karge, H. G. On the Correlation Between the 1H NMR Chemical Shift and the Stretching Vibration Frequency of Hydroxyl Groups in Solids. *Zeitschrift fur Phys. Chemie* **1992**, *176* (2), 173–183.
(62) Fink, P.; Hobert, H.; Rudakoff, G. No. *Wiss. Ztschr. F.S.U.,* **1987**, *R36*, 581.
(63) Steiner, T. The Hydrogen Bond in the Solid State. *Angew. Chem. Int. Ed.* **2002**, *41* (48–76).
(64) Grosso-Giordano, N.; Schroeder, C.; Okrut, A.; Solovyov, A.; Schöttle, C.; Chassé, W.; Marinković, N.; Koller, H.; Zones, S.; Katz, A. Outer-Sphere Control of Catalysis on Surfaces: A Comparative Study of Ti(IV) Single-Sites Grafted on Amorphous versus Crystalline Silicates for Alkene Epoxidation. *J. Am. Chem. Soc. 140* (15), 4956–4960.

(65) Oldfield, E.; Haase, J.; Schmitt, K. D.; Schramm, S. E. Characterization of Zeolites and Amorphous Silica—Aluminas by Means of Aluminum-27 Nuclear Magnetic Resonance Spectroscopy: A Multifield, Multiparameter Investigation. *Zeolites* **1994**, *14* (2), 101–109.
(66) Rabo, J. A.; Gajda, G. J. Acid Function in Zeolites: Recent Progress. *Catal. Rev. - Sci. Eng.* **1989**, *31* (4), 385–430.
(67) Comas-Vives, A. Amorphous SiO_2 Surface Models: Energetics of the Dehydroxylation Process, Strain, Ab Initio Atomistic Thermodynamics and IR Spectroscopic Signatures. *Phys. Chem. Chem. Phys.* **2016**, *18* (10), 7475–7482.
(68) Ruta, B.; Baldi, G.; Chushkin, Y.; Rufflé, B.; Cristofolini, L.; Fontana, A.; Zanatta, M.; Nazzani, F. Revealing the Fast Atomic Motion of Network Glasses. *Nat. Commun.* **2014**, *5* (1), 3939.
(69) Cordon, M. J.; Harris, J. W.; Vega-Vila, J. C.; Bates, J. S.; Kaur, S.; Gupta, M.; Witzke, M. E.; Wegener, E. C.; Miller, J. T.; Flaherty, D. W.; et al. The Dominant Role of Entropy in Stabilizing Sugar Isomerization Transition States within Hydrophobic Zeolite Pores. *J. Am. Chem. Soc.* **2018**, *140* (43), 14244–14266.
(70) Cundy, C. S.; Cox, P. A. The Hydrothermal Synthesis of Zeolites: Precursors, Intermediates and Reaction Mechanism. *Microporous Mesoporous Mater.* **2005**, *82* (1–2), 1–78.

Chapter 3

Effect of Defect Site Pre-Organization on Fe(III) Grafting and Stability: A Comparative Study of Delaminated Zeolite vs. Amorphous Silica Supports

Reprinted in part with permission from Grosso-Giordano, N. A.; Yeh, A. J.; Okrut, A.; Xiao, D. J.; Grandjean, F.; Long, G. J.; Zones, S. I.; Katz, A. Effect of Defect Site Preorganization on Fe(III) Grafting and Stability: A Comparative Study of Delaminated Zeolite vs Amorphous Silica Supports. *Chem. Mater.* **2017**, *29* (15), 6480–6492.

The stabilization of isolated grafted Fe^{3+} sites on siliceous supports is investigated by a comparative study of crystalline versus amorphous materials. The synthetic approach treats crystalline delaminated zeolite DZ-1 and amorphous silica (SiO_2) with an aqueous NaFeEDTA cation precursor complex, to result in grafting of isolated Fe^{3+} sites via covalent attachment to support hydroxyl groups. Thermogravimetric analysis and UV-visible spectroscopy demonstrate the complete detachment of chelating EDTA ligand upon Fe^{3+} grafting on both supports. Before calcination treatment, both Fe/DZ-1 and Fe/SiO_2 have similar UV-visible spectral features, with absorption bands at 208-225 nm and 257 nm, characteristic of framework Fe^{3+} sites in zeolites. Calcination does not affect the UV-visible spectroscopic characteristics Fe/DZ-1, but changes the spectrum of Fe/SiO_2 to a single absorption band at 260 nm, indicating better thermal stability of Fe^{3+} sites in Fe/DZ-1 as compared to Fe/SiO_2. This stability persists for Fe/DZ-1 even during alkane oxidation catalysis in the presence of hydrogen peroxide, which causes aggregation of Fe^{3+} into oxide oligomers for Fe/SiO_2. ^{57}Fe Mössbauer spectroscopy of calcined materials indicates a more uniform distribution of sites in Fe/DZ-1 relative to Fe/SiO_2. We thus attribute the greater robustness and site uniformity of Fe/DZ-1 to the chelation of Fe^{3+} by the rigid crystalline silicate DZ-1 framework, engendered by the spatial pre-organization of grafting hydroxyls groups within its uniform defect sites, which are templated by framework B^{3+} removal during delamination. Such pre-organization enables cooperativity between neighboring hydroxyl groups. This contrasts with more randomly distributed hydroxyl groups on SiO_2, which lack such pre-organization, leading to decreased hydrothermal stability and an Fe^{3+} grafting density that is ~6-fold lower for Fe/SiO_2 relative to Fe/DZ-1. These observations reveal how the silicate surface onto which a cation is grafted can act as a relevant ligand, capable of controlling material synthesis and functionality akin to ligands in homogeneous metal complexes, and demonstrates the advantages of support crystallinity in having this ligand be hydrothermally stable and tunable via templating.

3.1. Introduction

The grafting of cations in precise oxo-ligand environments on metal-oxide supports is central to preparing functional materials for molecular recognition, sensing, and heterogeneous catalysis. In these materials, isolated cations uniformly distributed on the support are typically desired, as their coordinative unsaturation facilitates substrate bonding and activation. However, achieving such isolation is synthetically challenging, as cations tend to agglomerate into bulk-oxide phases during deposition, activation, and application, leading to the degradation of functional properties.[1–7] Many synthetic approaches have used amorphous silica as a convenient support with tunable textural properties,[8] while focusing on controlling cation incorporation through careful choice of the ligand sphere of soluble cationic metal precursors that are grafted onto supports.[8–14] No efforts, however, have fully addressed the implications that the grafting ligand environment, defined by the silicate network anchoring the cation to the support, may have on materials synthesis and application.[15]

In this manuscript, we address these implications from the perspective of incorporating Fe^{3+} sites on two different siliceous supports, consisting of amorphous silica (SiO_2) vs. crystalline delaminated zeolite DZ-1. This general class of supported iron oxide materials has found widespread application in alkane oxidation catalysis, with active sites generally attributed to isolated Fe^{3+} species.[4,5,12,16–18] Our synthetic approach is outlined in Scheme 3.1 and involves treating each support with aqueous NaFeEDTA. Through a comparative study of the resulting Fe/SiO_2 and Fe/DZ-1 materials, our goal is to elucidate how the grafting environment influences the Fe^{3+} incorporation process, the grafted Fe^{3+} species, and their activity and stability under catalytic application. We anticipate this grafting environment to be defined by the contrasting organization of silanol grafting sites and mechanical stability of the silica network when comparing crystalline vs. amorphous silicates, which were discussed in Chapter 2.

Zeolitic materials are microporous and consist of SiO_2 frameworks with well-defined crystallographic topologies. Micropores (<2 nm), however, sterically preclude diffusion of bulky reactants, thus limiting substrate activation to accessible functional sites on the external surface only. Delaminated zeolites, such as DZ-1, partially overcome these diffusional constraints by increasing the accessible external surface area of zeolitic materials.[19,20] We and others[21,22] have developed mild methods for swelling and delamination of layered zeolite precursors that preserve their crystalline framework, resulting in open materials that are analogous to amorphous SiO_2 in reactant accessibility, but which possess an intact crystalline silicate framework with external surface “cups” or “pockets”, intrinsic to the MWW zeolitic framework (see MWW layer in Scheme 3.1).[23] Our approach for the synthesis of DZ-1 uses $Zn(NO)_3$ to induce partial exfoliation of non-covalently bound zeolite layers of ERB-1(P) into a disordered arrangement, a process termed delamination. Such exfoliation and disordering of precursor layers before calcination exposes some areas between layers in the precursor material to the external surface, increasing the accessible external surface area. These layers would otherwise condense to form microporous voids in ERB-1 zeolite if calcined prior to delamination. The delamination process is depicted in the synthesis of DZ-1 from ERB-1(P) in Scheme 3.1.[23] By choosing NaFeEDTA as precursor for Fe^{3+} incorporation, with a steric bulk that prevents diffusion into micropores, the deposition of Fe^{3+} is limited to the external surface of the support only. This ensures that Fe^{3+} sites are equally accessible to reactants on both amorphous SiO_2 and crystalline DZ-1, despite their drastically different textural properties, thereby enabling a rigorous assessment of the role of the support on Fe^{3+} incorporation, active site structure, and catalytic application.

Scheme 3.1. Synthetic protocols for the synthesis of supports and Fe^{3+} containing materials.

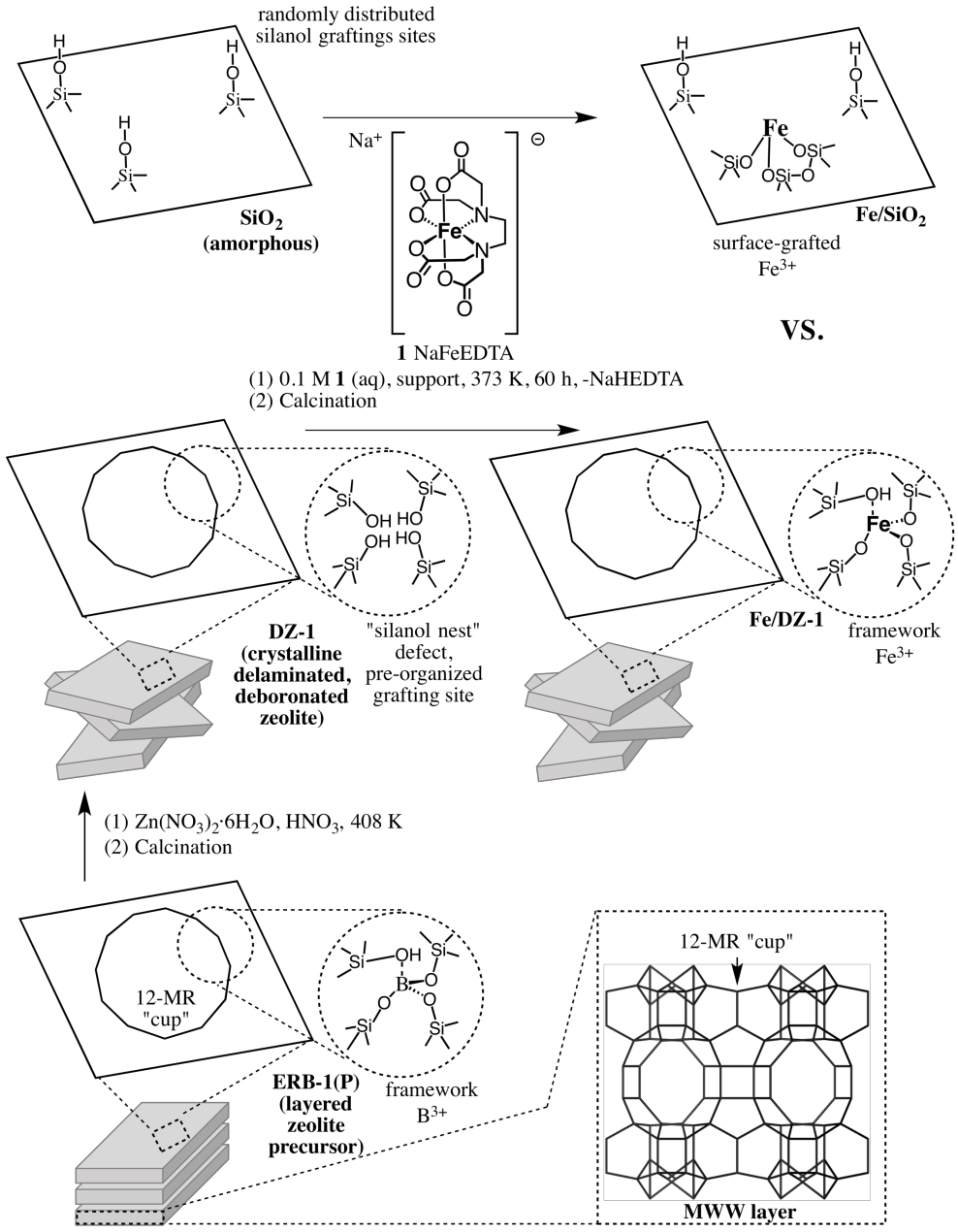

12-MR "cups" represent the upper-rim of 12-member ring openings/pockets on the DZ-1 surface; their location within the full MWW zeolitic topology of DZ-1 is shown at the bottom right (MWW layer). Vertices represent individual Si^{4+} ions at the center of $SiO_{4/2}$ tetrahedra that constitute the zeolite framework, while lines represent Si-O-Si bonds. Possibly coordinated water is not shown. Zeolite layers are schematically shown as rectangles; delamination causes extensive disordering of these layers and increases the accessible external surface of the zeolite support in DZ-1. Reaction of the NaFeEDTA precursor with silanol ligands on the surface of the support releases EDTA and grafts isolated Fe^{3+} sites onto the support, as a surface grafted cation in Fe/SiO_2 and as a framework incorporated cation in Fe/DZ-1.

This role of the support involves defining the molecular coordination environment surrounding a grafted cation, with the support essentially acting as a ligand, akin to those of in cation complexes used as homogeneous catalysts.[24] On siliceous supports, this grafting environment is defined by surface-bound hydroxyl defect sites (i.e. silanol Si-OH functionality), which serve as attachment points to graft cationic metal precursors by condensation.[12,14,25,26] In a fully hydroxylated amorphous SiO_2 surface, silanols can be isolated, geminal, and H-bonded vicinal, but their distribution lacks order due to the amorphous nature of the support.[27,28] In contrast, zeolites may contain crystallographically well-defined silanol framework defects, both within framework vacancies and as isolated silanols on the external crystal-terminating surfaces.[29,30] The former comprise uniform arrangements of proximal hydroxyl groups in close interaction, termed "silanol nests", which serve as pre-organized tripodal grafting sites for Fe^{3+};[31] the latter are crystal-terminating hydroxyl groups and are thus predicted to be unable to act as a chelating surface ligand because of their lack of proximity. In DZ-1, silanol nests are synthesized via a templating process, which involves removal of tetrahedral B^{3+} from crystallographic T-sites in the borosilicate framework of ERB-1(P) during delamination, thereby exposing a vacancy with four neighboring silanol groups in tetrahedral organization.[32,33] This is depicted in Scheme 3.1. Silanol nests in DZ-1 are subsequently repopulated with grafted Fe^{3+} heteroatoms,[31] which become part of the zeolite framework at well-defined crystallographic positions. This isomorphous substitution of framework Fe^{3+} for B^{3+} is in contrast with cations grafted onto the more random silanols of amorphous SiO_2. This distinction is important, as has been demonstrated by the pioneering work of Gates comparing grafted metal complexes in crystalline zeolites to those amorphous inorganic-oxide supports, which result in structural uniformity in the crystalline former vs. non-uniformity in the amorphous latter.[34-36] Uniformity enables more precise control over the structure of active sites, facilitating fundamental structure-function studies and catalyst design.[37]

In general, uniformly-isolated and stable Fe^{3+} sites cannot be incorporated onto amorphous SiO_2 when simple inorganic Fe^{3+} salts are used as precursors, because unconstrained incorporation of Fe^{3+} from solution leads to formation of FeO_x phases.[12] Instead, successful synthesis has relied upon molecular precursors that are either grafted onto the support by condensation with surface hydroxyl groups,[10–13] or by support impregnation with protected/multidentate Fe^{3+} complexes.[4,5] In these approaches, the use of bulky organic ligands, such as chelating ethylenediaminetetraacetate (EDTA), has been found to prevent the formation of undesired oxide agglomerates, by a mechanism involving both sterically limiting the approach and hindering the mutual reaction of Fe^{3+} precursors.[4,5] While these elegant strategies demonstrate uniform site isolation and high activity in the catalytic oxidation of hydrocarbons with H_2O_2, the stability of these sites during catalytic oxidation was not investigated, even though corrosive catalytic conditions are known to cause leaching and agglomeration of grafted Fe^{3+} sites, leading to catalyst deactivation.[7]

An additional challenge in these approaches is that full tripodal connectivity of Fe^{3+} to the support has necessitated oxidative heat treatment for organic-ligand removal via combustion,[4,5,12,13] a treatment that may also contribute to the generation of FeO_x agglomerates.[5] In the absence of this treatment, chelation of Fe^{3+} by EDTA would prevent Fe^{3+} connectivity to siloxy ligands anchoring it to the support (no exchange in Scheme 3.2, bottom).[5] In our synthetic approach, where NaFeEDTA in solution is contacted with the support, Fe^{3+} grafting requires at

least partial exchange of the organic ligand for support silanols. This motivates an important question that we address in this work: when a grafting site consists of silanols in close proximity, does full vs. partial exchange of EDTA ligand for support silanols occur (Scheme 3.2, top vs. center)? Isolated silanols on dehydroxylated amorphous silica are not spatially pre-organized, in contrast to silanol nests; thus, only partial exchange has been observed when grafting Fe molecular precursors with labile monodentate ligands,[10–13] to leave behind a cation with partial coordination to both organic ligands and support (Scheme 3.2, center). Full exchange would obviate the need for oxidative heat treatment in catalyst preparation, and demonstrate the importance of pre-organization of silanols in enabling grafting as an isolated cation.

Scheme 3.2. Possible grafting of Fe^{3+} onto silanols.

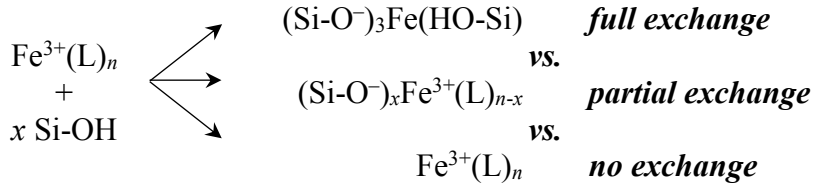

$(L)_n$ represent *n*-fold coordination of an organic ligand, which may be chelating and may possess formal charge, to the Fe^{3+} cation. Upon interaction of $Fe^{3+}(L)_n$ precursor with silanol Si-OH grafting sites, three possibilities exist: (1) *full exchange* of chelating $(L)_n$ for 4-fold coordination to the support, and tripodal attachment to silanols, (2) *partial exchange*, in which Fe^{3+} is coordinated to both the support through silanols and to the precursor ligand(s), and (3) *no exchange* with no covalent support-Fe^{3+} connectivity.

In this manuscript, we begin by first describing a novel strategy for Fe^{3+} incorporation onto amorphous SiO_2 and crystalline delaminated zeolite DZ-1, as shown in Scheme 3.1. We then extensively characterize these materials by thermogravimetric analysis, and UV-visible and ^{57}Fe Mössbauer spectroscopies, as a means to elucidating the role of competing chelation by EDTA and silanol nests in the grafting process, the nature of the grafted species, and their thermal stability. Finally, we compare Fe^{3+} on both supports as catalysts for the oxidation of adamantane with H_2O_2 (Scheme 3.3) and evaluate the stability of active sites.

These comparative studies expand our understanding of amorphous versus crystalline supports as ligands for grafted cations,[34-36] and provide guiding principles for the design of crystalline and robust supported oxides as functional materials by tailoring the environment onto which cations are grafted.

3.2. Materials and Methods

All chemicals, HPLC grade purity or better, were purchased from Sigma-Aldrich and used without further purification unless otherwise stated. The Fe^{3+} sodium salt of ethylenediaminetetraacetic acid, NaFeEDTA, was purchased from Sigma-Aldrich. Water was purified using a Barnstead Nanopure model D11901 water purification system operating at 18 MΩ·cm resistivity.

3.2.1. General Analytical Methods

Support surface areas were determined by the BET method from N_2 physisorption measurements performed with a Micromeritics ASAP 2020 instrument at 77 K after sample evacuation at 623 K for 4 h. External surface areas and micropore volumes were calculated by the t-plot method.[38]

Thermogravimetric analysis (TGA) was performed with a Netzsch 449C Jupiter TGA instrument by treating a sample in a mixed gas flow consisting of 20% O_2 and 80% Ar from room temperature to 1073 K at a ramp rate of 5 K/min. EDTA ligand contents were determined by assuming that any additional mass loss between 473 and 1073 K in NaFeEDTA-containing materials when compared to the bare support was due to combustion of the ligand minus 4 O atoms.[4,5]

Diffuse reflectance UV-visible spectra were measured at ambient conditions by using a Varian Cary 4000 Spectrophotometer fitted with a Praying Mantis attachment from Harrick Scientific Instruments. Compacted poly-(tetrafluroethylene) powder was used as a standard perfect reflector for the baseline corrections, and all spectra are reported using Kubelka-Munk pseudoabsorbance, F(R), and normalized to the maximum value of absorbance.

Iron-57 Mössbauer spectra were obtained at 5 K with a constant acceleration spectrometer and a room-temperature cobalt-57 rhodium source. Prior to measurements the spectrometer was calibrated at 295 K with α-iron foil. Each Mössbauer spectral absorber contained ca. 50 mg per cm^2 of the sample as a fine powder. Except as noted, all spectra were fit with symmetric Lorentzian quadrupole doublets.[39] Because of the very limited amount of iron present in the Mössbauer spectral absorbers, the folded spectra obtained as 512 channels exhibited a rather poor signal to noise ratio. As a consequence, the initial spectral refinements yielded χ^2 goodness of fit parameters that were substantially below 1.00, indicating an over parameterization of the fits. This problem was overcome by adding adjacent channels to yield 256 channel spectra, which improved the signal to noise ratio by $\sqrt{2}$. The fits of the resulting spectra yielded χ^2 parameters that were only slightly below 1.00. Only these 256 channel spectra are discussed below. In one instance, which is discussed in Section 3.5.7, the consideration of fitting the Fe/DZ-1 spectrum in the presence of an unexpected absorber texture, i.e., a non-random powder absorber, was also considered.

3.2.2. Support Preparation

Delaminated zeolite DZ-1 was synthesized from borosilicate precursor ERB-1(P) following previously developed synthesis protocols.[23] ERB-1(P) was crystallized in PTFE autoclaves at 448

K for 7 days without tumbling, from a synthesis gel with molar composition 1 SiO_2 (Aerosil 200):18.9 H_2O:1.4 piperidine:1.3 H_3BO_3, and subsequently washed with copious amount of H_2O. In a typical synthesis of DZ-1, 1.0 g of ERB-1(P) zeolite precursor was treated with 4.0 g of $Zn(NO_3)_2 \cdot 6H_2O$ and 35 g of pH 1 HNO_3 in a 125 mL sealed thick-walled glass reactor, under vigorous stirring at 135 °C for 48 h. The solid product was collected on a filter, washed thoroughly with water, and calcined in air at 823 K for 6 h after a 1 K/min ramp.

Aerosil 200 (Evonik) was chosen as a representative amorphous silica support. It was pretreated by first surface-hydroxylating a slurry in refluxing water at 393 K for 16 h, drying, sieving, followed by dehydroxylation under Ar at 823 K for 6 h. The pretreated support was kept under an inert Ar atmosphere until further handling.

3.2.3. Fe^{3+} Incorporation onto Siliceous Supports

In a 150 mL glass high pressure vessel, 300 mg of the solid was stirred with 30 mL of a 0.1 M solution of NaFeEDTA at 373 K for 60 hours. The resulting powder was filtered and washed with water and calcined in air at 823 K (1 K/min ramp) for 6 h. Materials thus prepared were labeled Fe/SiO_2 and Fe/DZ-1. Select samples were not calcined, as indicated in the text. Iron contents were measured by ICP-AES at Galbraith Laboratories.

Control materials were prepared by incipient wetness impregnation of a solution of NaFeEDTA to achieve Fe^{3+} contents resembling those on Fe/SiO_2 and Fe/DZ-1. An aqueous NaFeEDTA solution of appropriate concentration was added dropwise until the minimum wetting volume was reached, and the materials were subsequently vacuum dried at room temperature.

3.2.4. Catalytic Oxidation of Adamantane

35 mg of adamantane and 70 mg of octafluoronapthalene (internal standard) were dissolved in 20 mL of acetonitrile and added to 100 mg of catalyst in a 25 mL multi-necked round-bottom flask fitted with a condenser, heated to a reaction temperature of 333 K. Oxidation was initiated by the addition of 1 mL of 30 wt % aqueous H_2O_2 and 0.1 mL samples were periodically withdrawn and filtered, to remove catalyst, using a 0.2 μm syringe filter packed with silver powder, to decompose unreacted hydrogen peroxide.[4] Analysis of samples by gas chromatography (Agilent 6890 Gas Chromatography System) and comparison of peak areas to standards was used to quantify the progress of the reaction. Turnover numbers (TON) were calculated as the ratios of 1-adamantanol, 2-adamantanol, and 2-adamantanone produced to that of the iron present, and are thus a measure of specific activity of the Fe^{3+} active site. Spent catalyst samples were recovered by filtration and washing with copious acetonitrile, and were subsequently analyzed by diffuse reflectance UV-vis spectroscopy.

3.3. Results and Discussion

3.3.1. Support Synthesis and Characterization of Sites for Cation Grafting

Textural properties as determined from N_2 physisorption at 77 K are summarized in Table 3.1 for the delaminated zeolite DZ-1, its non-delaminated counterpart ERB-1, and amorphous SiO_2. Delamination of the borosilicate precursor ERB-1(P) yielded the material DZ-1, and resulted in doubling of the external surface area (Table 3.1) to values approaching those of amorphous SiO_2. Exfoliation of non-covalently bound zeolite layers into a disordered arrangement is consistent with the observed decrease in micropore volume (Table 3.1). This can be explained by internal voids in 3-dimenstional ERB-1 being instead exposed as external surfaces in DZ-1. The increase in total pore volume results from additional mesoporosity in the region between disordered stacking of zeolite layers, as confirmed by the hysteresis in N_2 physisorption isotherms (Figure A3.1).[40] While the extent of delamination is incomplete (i.e. not all zeolite layers in the precursor material become exfoliated as single sheets), the results here are consistent with previous results of ERB-1(P) delamination,[23] showing an approximate doubling of the external surface area when compared with conventional ERB-1. This enhancement in accessible external surface area allows the use DZ-1 as a support with accessibility similar to SiO_2 but with properties intrinsic to crystalline zeolitic materials.[20,23]

Table 3.1. Textural Properties of Supports and Support Precursors.

Material	S_{acc} (m^2/g)[a]	V_{tot} (cm^3/g)[c]	V_{micro} (cm^3/g)[d]
ERB-1[b]	62	0.27	0.15
DZ-1	134	0.34	0.13
SiO_2	190	1.2	< 0.01

[a]Accessible surface area, determined by the BET method for SiO_2, and from the t-plot external surface area for microporous ERB-1 and DZ-1. [b]Corresponds to calcined version of ERB-1(P). [c]Total pore volume. [d]Micropore volume, determined from t-plot method; SiO_2 is non-porous fumed silica with no microporosity. Full N_2 physisorption isotherms at 77 K can be found in Figure A3.1.

Support grafting sites consist of silanol groups (Si-OH), and are pre-organized into neighboring tetrahedral arrangements or "silanol nests" in DZ-1, as depicted in Scheme 3.1. It is likely that calcination treatment of DZ-1, required for full removal of the organics from as-prepared DZ-1 (structure-directing agents used in the synthesis of ERB-1), may result in condensation of SiOH groups in silanol nests into siloxane species.[41] Thus, we performed control experiments in which DZ-1 was treated with water at conditions identical to those that were used for Fe^{3+} incorporation, but in the absence of NaFeEDTA precursor. The resulting material exhibited strong infrared ν(OH) stretching frequencies centered about 3500 cm^{-1} (Figure A3.2), consistent with the presence of extensively hydrogen-bonded silanol defects, such as those found in silanol nests,[42-44] under aqueous conditions that occur during grafting.

3.3.2. Incorporation of Fe^{3+} into Siliceous Supports

Grafting of Fe^{3+} onto both SiO_2 and DZ-1 was achieved by a simple thermal treatment of the support with an aqueous solution of NaFeEDTA, washing, and calcination, as depicted in Scheme 3.1. The properties of the resulting Fe^{3+} containing materials, Fe/DZ-1 and Fe/SiO_2, are summarized in Table 3.2. No changes in accessible surface area are detected after Fe^{3+} grafting, indicating that this treatment does not structurally affect the support. Under identical synthesis conditions, the 0.45 Fe/nm^2 surface-density of Fe/DZ-1 is ~6 times higher than the 0.08 Fe/nm^2 in Fe/SiO_2, when normalized by the accessible surface area. We posit that all Fe^{3+} is located on the external surface area of the DZ-1 support, and not inside of micropores, where it would be inaccessible for activation of bulky reactive substrates relevant to catalytic applications. We assert this location because the molecular dimensions of the NaFeEDTA complex of more than 7 Å (see Figure A3.3)[45] preclude diffusion of this complex along zeolitic channels of the MWW framework of DZ-1, which have a limiting cross-section ~4 Å.[46-48] Similarly, as a result of the chelating nature and large complexation constant of EDTA, the possibility of unbound hydrated Fe^{3+} diffusing into these channels is also precluded. As a result, we conclude that all grafted Fe^{3+} is located only on the external surface of DZ-1, thereby allowing for a direct catalytic comparison to equally-accessible sites on Fe/SiO_2, where Fe^{3+} incorporation can occur on silanols anywhere on its freely accessible mesoporous surface.

Table 3.2. Physicochemical Characterization of Fe^{3+} Containing Materials.

Material	S_{acc} (m^2/g)[a]	Fe content (wt. %)	Grafting density (Fe/nm^2)[b]
Fe/DZ-1	138	0.57	0.45
Fe/SiO_2	191	0.14	0.08

[a]Accessible surface area, determined by the BET method for Fe/SiO_2, and from the t-plot external surface area for Fe/DZ-1. [b]Determined by normalizing Fe content, as measured by ICP-AES, by the accessible surface area.

We performed control experiments to determine whether Fe^{3+} incorporation occurs via a full EDTA ligand dissociation/exchange (Scheme 3.2, top), or whether both support and EDTA can act as ligands after Fe^{3+} grafting (Scheme 3.2, center). Thermogravimetric analysis (TGA) of as-synthesized (non-calcined) materials after aqueous NaFeEDTA treatment is sensitive to the presence of the EDTA ligand, which is known to combust at 450-650 K, resulting in a sharp mass loss.[4,5] The results of TGA, shown in Figure 3.1, demonstrate the absence of any combustible ligands (i.e. EDTA) in both Fe/DZ-1 and Fe/SiO_2 (solid lines). Mass-loss profiles for these two materials closely resemble those for DZ-1 and SiO_2 supports that were treated under the same conditions but in the absence of NaFeEDTA (dotted lines in Figure 3.1). This comparison confirms that the observed mass losses reflect only to condensation of surface silanols, and not combustion of organics. The more significant mass loss for Fe/DZ-1 than for Fe/SiO_2 reflects higher silanol content in the former, consistent with its high density of hydroxyl-rich silanol nests throughout the internal porosity of the zeolite framework.

For comparison, we synthesized control materials via incipient wetness impregnation of

supports with aqueous solutions of NaFeEDTA, a method that was elegantly studied by Prieto-Centurion *et al.*[4,5] These control materials achieve similar Fe^{3+} loadings to those in Fe/DZ-1 and Fe/SiO_2, but exhibit a sharp loss of mass at 450-650 K due to EDTA combustion (dashed lines in Figure 3.1), which is not observed in either Fe/DZ-1 or Fe/SiO_2. Furthermore, diffuse-reflectance UV-visible spectroscopy of Fe/DZ-1 before calcination displays two absorbance bands, as in the final calcined material, in contrast to a single, broader absorbance band for the material prepared by incipient wetness impregnation (Figure A3.4, *vide infra* for further discussion), where Fe^{3+} remains bound by EDTA (Scheme 3.2, bottom).[4,5] This confirms the incorporation of Fe^{3+} into its grafted environment after aqueous NaFeEDTA treatment of the support, and full dissociation of EDTA. Taken together, the comparison of the materials prepared by our ligand-exchange method with control materials prepared by incipient wetness impregnation conclusively demonstrates that Fe^{3+} incorporation into Fe/DZ-1 and Fe/SiO_2 occurs by complete displacement of EDTA ligand and condensation of the cation with silanol ligands on the support.

Such an exchange requires a high degree of silanol cooperativity in order to compete with strong chelation of Fe^{3+} by EDTA. We note that the high binding constant of Fe^{3+} (aq) + H_2EDTA^{2-} (aq) ⇌ $FeEDTA^-$ (aq) + $2H^+$ (aq), log K = 8.6 measured at pH of 6-7,[49] reflects the six-fold chelating coordination of EDTA to Fe^{3+}, and not that of individual carboxylate or amine Lewis base substituents of the EDTA ligand. Furthermore, silanol–Fe^{3+} interactions have been previously determined to be highly-favorable thermodynamically with an interaction free energy, ΔG, of *ca.* –2 kcal/mol.[50] Considering that the aqueous NaFeEDTA complex consists of a 7-coordinate Fe^{3+} center, with 6-fold coordination by EDTA expanded by additional coordination of H_2O,[45,49] we propose that this labile H_2O may be initially displaced by interaction with a surface silanol. The resulting coordination to a support silanol would facilitate subsequent reaction of surface silanols with the Fe^{3+} center, with the eventual full displacement of EDTA by a new chelating ligand environment, now defined by the support.

For such an EDTA-for-silanol ligand-exchange process to occur at all, the support must provide a favorable grafted environment for Fe^{3+}. Hence, we attribute the ~six-fold higher Fe^{3+} uptake by DZ-1 relative to SiO_2 to be the result of the more favorable grafting environment provided by the spatial arrangement of hydroxyls in silanol nests, as compared to chemically identical but more randomly distributed silanols on SiO_2, where few hydroxyl arrangements with the required spatial organization for grafting exist (see Scheme 3.4 **I**). The pre-organized tetrahedral arrangement of silanol defects in DZ-1 ensures that Fe^{3+} quickly reacts to become fully connected to the support after initial displacement of EDTA, in effect becoming chelated by the zeolite framework (see Scheme 3.4 I→**II**). Thus, zeolitic silanol nests act as uniform chelating grafting sites with favorable molecular recognition properties for Fe^{3+}, thereby leading to successful EDTA-for-silanol exchange. Indeed, Fe contents of 0.57 wt% in Fe/DZ-1 are close to the maximum number of available grafting sites calculated from the Si/B ratio and the external surface area, assuming only T-sites directly on the external surface to be available for exchange (maximum loading of ~0.7 wt% Fe, see section 3.5.1). This indicates nearly full occupancy of accessible silanol nests in DZ-1 with Fe^{3+}, confirming the high-affinity of silanol nests as grafting sites for Fe^{3+}.

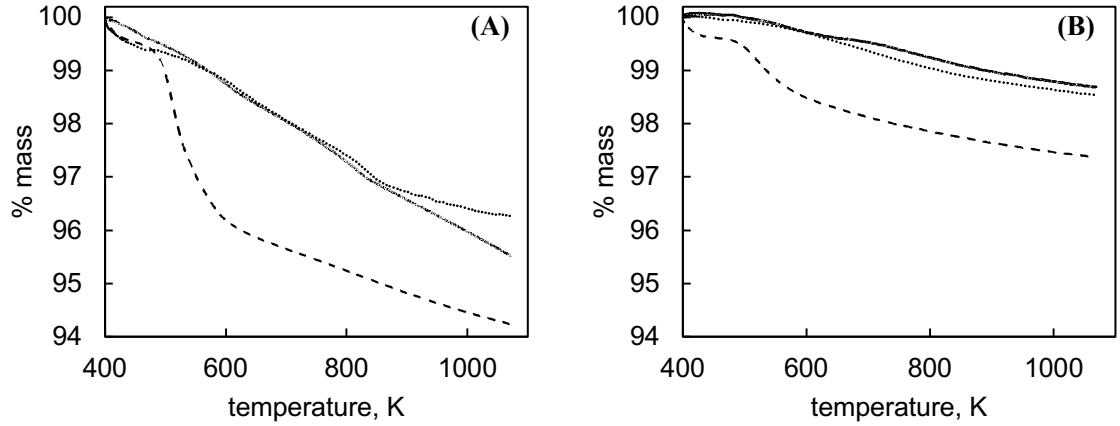

Figure 3.1. Thermogravimetric analysis for materials prepared on DZ-1 **(A)** and SiO_2 **(B)**. Solid lines correspond materials prepared as Fe/SiO_2 and Fe/DZ-1, before calcination. Dotted lines correspond to bare supports treated under the same conditions as for Fe^{3+} incorporation but in the absence of the dissolved NaFeEDTA precursor complex. Control materials synthesized by incipient wetness impregnation of the support with solutions of NaFeEDTA consist of materials with Fe^{3+} loadings of 0.57 wt% **(A)** and 0.17 wt% **(B)**, and are shown as dashed lines. EDTA ligand loadings calculated from combustive losses correspond to within **(A)** 10% and **(B)** 27% of those expected from the Fe^{3+} metal loadings; differences are due to experimental uncertainties in the amount of NaFeEDTA added and the small differences being quantified thermogravimetricaly.

Taken together, the above results demonstrate that when presented with the competing chelating environments of EDTA or silanol nests, Fe^{3+} incorporation only occurs via full exchange of chelation by EDTA for chelation by a silicate network (Scheme 3.2, top; Scheme 3.4 I→**II**). This exchange provides a route towards isolated Fe^{3+} grafted sites that avoids the need for removal of protecting ligands by oxidative heat treatment, a treatment that may result in formation of deleterious FeO_x aggregates.[4,5] More fundamentally, these observations evidence how pre-organization of silanols in nests enables cooperativity, leading to successful displacement of a chelating organic ligands and grafting onto a siliceous surface. This ability to control denticity of support to a grafted cation by silanol cooperativity expands on previous work in which surface silanol density affects mono- vs. bidentate attachment of silica as a ligand to grafted cations (see Chapter 4).[9,51]

3.3.3. Characterization of Fe^{3+} Sites in Fe/DZ-1 vs. Fe/SiO_2 by UV-Visible Spectroscopy

Fe^{3+} sites in Fe/DZ-1 and Fe/SiO_2 were investigated spectroscopically to determine how the coordination environment of Fe^{3+} is influenced by the support. Diffuse-reflectance absorption spectroscopy in the UV-visible region (UV-vis), shown in Figure 3.2, reveals (support)O-Fe(III) ligand-to-metal charge-transfer electronic transitions, transitions which are sensitive to the coordination state of transition metal ions.[52] In both materials, spectral absorption occurs almost entirely below 300 nm (solid lines, Figure 3.2), a wavelength range which is indicative of highly dispersed/monomeric Fe^{3+}. Fe-O-Fe oligomers and bulk Fe_2O_3 are known to absorb above 300 nm, but no strong absorbance in this region is observed,[4,5,12,53,54] indicating that although small

aggregates may exist in both materials, their population is negligible compared to the predominance of isolated species absorbing strongly below 300 nm. The presence of isolated species demonstrates the effectiveness of EDTA in protecting Fe^{3+} cations from mutually reacting to form aggregates, a problem that is commonly encountered with traditional methods of cation incorporation, especially on SiO_2 supports.[4,5,17,55] Control experiments, in which non-chelated $Fe(NO_3)_3$ was used as a precursor for Fe^{3+} incorporation on amorphous SiO_2, indeed showed extensive formation of FeO_x aggregates, as detected by diffuse reflectance UV-vis spectroscopy shown in Figure A3.5, thus confirming the importance of EDTA chelation in maintaining Fe^{3+} isolation during cation deposition.

While Fe^{3+} is present as a highly-dispersed species on both supports, the UV-vis spectra of calcined materials (solid lines in Figure 3.2) exhibit different absorption bands, indicating distinct coordination environments for isolated cations in these two supports. Fe/SiO_2 absorbs as a single band centered at 260 nm, whereas Fe/DZ-1 absorbs with two distinct higher-energy bands centered at 220 and 257 nm, consistent with previous studies of isolated Fe^{3+} sites grafted onto SiO_2 [4,5,12] and zeolites.[53,56] The strong absorbance band at 260 nm for Fe/SiO_2 (Figure 3.2B) has been previously assigned to isolated Fe^{3+} within an octahedral coordination on the surface of silica, a coordination sphere defined by both siloxy SiO^- ligands from the support and coordinated ambient water.[4,18] In contrast, two distinct charge-transfer transitions are observed in the spectrum of Fe/DZ-1 in Figure 3.2A. These bands are consistent with pseudo-tetrahedral coordination of Fe^{3+} to SiO^- in the zeolite framework, but overall octahedral coordination is possible in these materials, given their exposure to ambient water, which coordinates to Fe^{3+} to complete the octahedral coordination.[4,18] UV-vis spectroscopy alone, however, cannot conclusively discern between tetrahedral and octahedral coordination of the Fe^{3+}.[53,56]

UV-vis spectra of Fe/DZ-1 and Fe/SiO_2 materials before calcination were also measured and studied to understand the effect of high temperature treatment on Fe^{3+}, and are included as dashed lines in Figure 3.2. These spectra resemble those of their calcined versions, and not those of materials prepared by incipient wetness impregnation where Fe^{3+} remains coordinated to EDTA (Figure A3.4), again confirming ligand-exchange of EDTA for surface silanols. Calcination, performed as the final synthetic step, does not significantly alter UV-vis absorption spectra for Fe^{3+} in Fe/DZ-1, indicating that Fe^{3+} is already incorporated directly into silanol nests in its final coordination environment, and is stable to heat treatment (Scheme 3.4 **III**). For Fe/SiO_2, the two absorbance bands before calcination resembles that of Fe/DZ-1, suggesting that Fe^{3+} binds to sites resembling silanol nests on amorphous silica. Such nest-like features can occur on the surface of SiO_2 given its random distribution of silanols, and may behave similarly to those on defective zeolites, as represented in Scheme 3.4 **I**.[57] Given the solid-trace curve in Figure 3.2B, they do not appear to be stable to calcination on SiO_2, however, leading to a change in coordination for Fe^{3+} in the calcined material (Scheme 3.4 **III**). The lack of any long-range crystalline order in amorphous silica may account for why such a structure is not mechanically rigid and instead rearranges for Fe/SiO_2 but remains stable during calcination for Fe/DZ-1. This is again consistent with Fe^{3+} condensation to the support being more difficult on SiO_2, due to a very low abundance of sites with favorable geometry, in contrast to uniform silanol nest pre-organization in DZ-1.

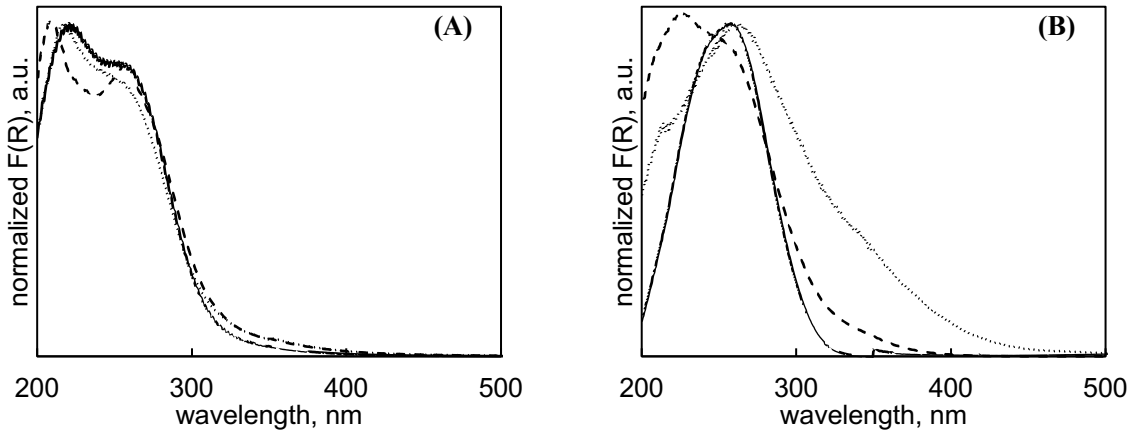

Figure 3.2. Diffuse-reflectance UV-visible spectra for Fe/DZ-1 **(A)** and Fe/SiO_2 **(B)** catalysts. Fe/DZ-1 and Fe/SiO_2 are shown as solid lines, whereas their non-calcined versions are shown as dashed lines. The materials recovered after catalytic oxidation of adamantane are shown as dotted lines.

3.3.4. Characterization of Fe^{3+} Sites in Fe/DZ-1 vs. Fe/SiO_2 by ^{57}Fe Mössbauer Spectroscopy

Iron-57 Mössbauer spectra, measured at 5 K, were acquired to help provide additional detailed information on grafted Fe^{3+}, and are shown in Figure 3.3. The low absorbance of the samples makes spectral deconvolution difficult, but because of both the asymmetric nature of the spectra and the possibility of octahedral or tetrahedral coordination of Fe^{3+} as noted above, the spectra have both been fit with two symmetric quadrupole doublets (see solid and dashed components in Figure 3.3); the corresponding best fit parameters to these spectra are given in Table 3.3. Other possible fits for the Fe/DZ-1 spectrum, based on a single quadrupole doublet fits with the presence of texture or preferential crystalline orientation (Figure A3.6, Table A3.1) but are not considered here, because texture is unlikely to be actually present in the absorber.

No ordered Fe_2O_3 domains, which would be expected to give rise to a sextet spectral component at 5 K,[55,58,59] are observed. This confirms that all high-spin Fe^{3+} occurs as isolated species. It is immediately apparent that the total spectral areas, even at 5 K, are very small at 0.46(1) and 0.14(1) (%ε)(mm/s), values that indicate that the Fe^{3+} recoil free fraction in both samples is low and suggest that much of the Fe^{3+} in the samples may be attached close to or essentially on the surfaces of the support, rather than in the bulk of the support. The significantly higher total areas for Fe/DZ-1 than for Fe/SiO_2 are also in agreement with the larger Fe contents in the former, as expected from the Fe contents in Table 3.2.

It is well established that, in an oxidic pseudooctahedral (O_h) coordination environment, high-spin Fe^{3+} typically exhibits a 5 K isomer shift, δ, of *ca.* 0.5 mm/s. In contrast, in a zeolite-like oxidic pseudotetrahedral (T_d) coordination environment lower isomer shifts of between *ca.* 0.05 to 0.25 mm/s are typically observed.[55] This difference in isomer shifts forms the basis for the assignment of the two quadrupole doublets found in Table 3.3. Further, in general in such coordination environments, values of quadrupole splitting, ΔE_Q, are found to be smaller in a pseudotetrahedral environment than in a pseudooctahedral environment,[60-62] as is also consistent

with the assignment given in Table 3.3. Though spectral parameters assigned to O_h in DZ-1 (Table 3.3) have also been attributed to Fe^{3+} sites in the vicinity of Brønsted acidic protons,[63] the lack of an IR band at 3630 cm^{-1}, characteristic of such Brønsted acid protons in ferrosilicates[53] (Figure A3.7), leads us to conclude that these parameters do not originate from Fe^{3+} sites in the vicinity of Brønsted acidic protons. The Mössbauer spectra linewidths, Γ, are rather larger than the typical 0.24 to 0.3 mm/s, and the smaller linewidths observed in Fe/SiO_2, as compared with Fe/DZ-1, are indicative of a narrower distribution of Fe^{3+} environments assigned to each component in the former.

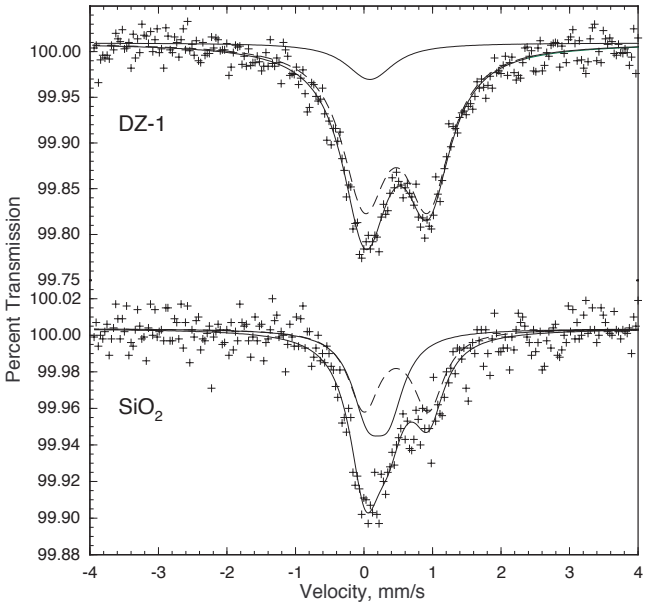

Figure 3.3. ^{57}Fe Mössbauer spectra of Fe/DZ-1, upper spectrum, and Fe/SiO_2, lower spectrum, obtained at 5 K. The dashed and solid line spectral components correspond to Fe^{3+} in pseudooctahedral and pseudotetrahedral environments, respectively. + represent the experimental data points and the solid line through these data points corresponds to the total spectral fits, summarized in Table 3.3.

The values of spectral parameters in Table 3.3 suggest that while Fe/DZ-1 contains some pseudotetrahedral high-spin Fe^{3+}, the vast majority lies in a pseudooctahedral environment. While pseudotetrahedral coordination to SiO^- ligands is expected for Fe^{3+} sites incorporated into the zeolite framework, the predominance of octahedral coordination observed herein is not inconsistent with such framework incorporation. We attribute this octahedral coordination to hydration during ambient storage leading to coordination from both the zeolite framework and adsorbed ambient water. Indeed, ambient water has been found to strongly affect Fe^{3+} coordination environment and its Mössbauer spectra.[4,18,55,56,64,65] We thus attribute the O_h assignment in Table 3.3 to isolated framework Fe^{3+} sites grafted in silanol nests. The spectral parameters in Fe/SiO_2 have very similar hyperfine parameters to Fe/DZ-1, but correspond to *ca.* 50 percent area for each coordination environment.

Most Fe^{3+} is present mostly in a single pseudo-O_h environment (88%) in Fe/DZ-1, in contrast to an equal abundance of pseudo-O_h (52%) and pseudo-T_d (48%) Fe^{3+} sites in Fe/SiO_2, confirming a different distribution of grafting environments in DZ-1 and SiO_2 supports for otherwise isolated

high-spin Fe^{3+} in calcined materials. This single pseudo-O_h environment evidences that silanol nests in DZ-1 provide a uniform grafting environment for Fe^{3+}, which is maintained even after calcination. In contrast, a mixture of coordination environments is present for Fe^{3+} grafted on SiO_2, both because of the heterogeneous array of available grafting sites and the greater mechanical flexibility of the amorphous silica network, which may lead to changes in the cation coordination upon calcination. Such a conclusion is fully consistent with the UV-visible absorption bands in Figure 3.2, which demonstrate significant differences in coordination of Fe^{3+} in calcined Fe/DZ-1 vs. Fe/SiO_2, the latter which changes upon calcination. This difference, depicted in Scheme 3.4 **II→III**, highlights the importance of pre-organized silanol nests as uniform grafting sites capable of achieving structural homogeneity of the grafted cation and stability to calcination, demonstrating the unique advantages of using crystalline over amorphous siliceous frameworks in the synthesis of supported metal oxides.

Table 3.3. Mössbauer Spectral Parameters Obtained at 5 K[a].

Material	δ [b] (mm/s)	ΔE_Q [c] (mm/s)	Γ [d] (mm/s)	*Area* (%)	*Total Area* (%ε) (mm/s)	High-Spin Fe^{3+} Assignment[e]
Fe/ DZ-1	0.10(9)	0.1(4)	0.79(4)	11(3)	0.46(1)	T_d
	0.47(3)	0.9(8)	0.79(4)	88(3)		O_h
Fe/ SiO_2	0.20(7)	0.3(1)	0.55(6)	48(4)	0.14(1)	T_d
	0.47(7)	0.9(1)	0.55(6)	52(4)		O_h

[a]The statistical fitting uncertainties are given in parenthesis; the actual uncertainties are probably twice as large. [b]The isomer shifts, δ, are given relative to α-iron foil measured at 295 K. [c]Quadrupole splitting. [d]Spectral linewidth. [e]T_d, pseudo-tetrahedral; O_h, pseudo-octahedral.

3.3.5. Stability of Fe^{3+} Sites During the Catalytic Oxidation of Adamantane with H_2O_2

Fe/DZ-1 and Fe/SiO_2 were studied for the catalytic oxidation of adamantane with H_2O_2, depicted in Scheme 3.3. TON values, shown in Figure 3.4A as a function of time, are similar between Fe/DZ-1 and Fe/SiO_2 within the measured uncertainty, and reflect the intrinsic reactivities of these sites because their location on the external surface ensures equal accessibility to reactants. While similarity in TON indicates comparable specific activity of the active sites on both supports, the higher Fe^{3+} contents in Fe/DZ-1 make this material significantly more active than Fe/SiO_2 as an oxidation catalyst on a per catalyst-mass basis. The product selectivity was calculated as the ratio of measured tertiary (1-adamentanol) to secondary (2-adamenanol and 2-adamentanone) oxidation products normalized by the number of hydrogens, and depends on the radical nature of the oxidation process, because C-H dissociation energies are lower at 3° carbons relative to 2° carbons. The average selectivity of ~2.5 measured for both catalysts (Figure 3.4B) is indicative of sites more reactive than molecular catalysts but more selective than indiscriminate •OH radicals, and agrees with values for other supported Fe^{3+} oxide catalysts.[4,5,12]

Given the tendency of supported Fe^{3+} sites to form mobile and possibly soluble species under oxidation conditions,[7] we performed hot filtration tests, which confirm that soluble Fe^{3+} species

were not responsible for any observed oxidation activity (Figure A3.8). The lack of significant differences in catalytic properties between Fe/DZ-1 and Fe/SiO_2, despite differing Fe^{3+} coordination environments, is not unexpected, as previous work has concluded that adamantane oxidation is catalyzed not only by isolated Fe^{3+} sites but also by small oxide clusters, when the same precursor is used for deposition.[5]

Alkane oxidation catalysts are subject to chemical degradation under corrosive catalytic conditions such as those caused by the presence of aqueous H_2O_2. For example, during catalytic oxidation of phenol by H_2O_2 catalyzed by Fe/SiO_2, migration of mobile Fe^{3+} species results in formation of less active bulk Fe^{3+} oxide phases.[7] We thus recovered catalyst samples and characterized them by diffuse reflectance UV-vis spectroscopy to assess changes to the state of Fe^{3+} that may occur due to exposure to catalytic conditions; the results are shown as dotted spectra in Figure 3.2, for direct comparison with freshly prepared materials. Significant differences in the spectra of Fe/DZ-1 and Fe/SiO_2 are observed. When compared to the freshly prepared catalyst, a significant broadening of the absorption band is seen for Fe/SiO_2, with notable contributions from species absorbing above 300 nm that were absent in the fresh catalyst. These newly formed species that absorb > 300 nm are indicative of formation of oligomeric FeO_x agglomerates in Fe/SiO_2, which likely arise from the reaction of mobile Fe species generated by the corrosive conditions encountered during catalytic testing. In stark contrast, absorption bands remain unchanged for Fe/DZ-1, indicating that its Fe^{3+} sites remain stable and in the same coordination as in freshly prepared samples.

Scheme 3.3. Fe^{3+} catalyzed oxidation of adamantane.

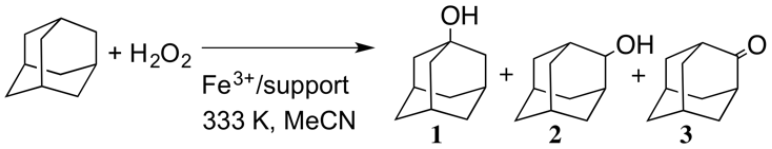

Oxidation products are alcohols (1-adamantanol **1**, 2-adamantanol **2**) and ketones (2-adamantanone **3**). **1** corresponds to tertiary, and **2** and **3** to secondary products.

In order to obtain further evidence of the stability of Fe^{3+} sites in Fe/DZ-1, vs. leaching and agglomeration in Fe/SiO_2, we further performed stress tests in which the materials were treated with 30 wt% H_2O_2 in water at 333 K. The results, shown in Figure A3.9, conclusively demonstrate that corrosive H_2O_2 causes agglomeration of Fe^{3+} on Fe/SiO_2 into oxides, but does not affect analogous sites on Fe/DZ-1. The Fe/SiO_2 sample was calcined after stress-testing to remove any coordinated species, yet the same broad absorbance pattern is observed (Figure A3.9), confirming that the absorbance is indeed related to the formation of FeO_x agglomerates (and not due to new charge-transfer bands arising from coordination of hydroperoxo species to Fe^{3+}). It should be noted that elemental analysis showed very similar Na^+/Fe^{3+} ratios of 0.20 and 0.25 for Fe/DZ-1 and Fe/SiO_2, respectively, eliminating the possibility that NaFeEDTA precursor counter cations may be playing a role in the properties of grafted species, as has been observed to occur in related systems.[4,5] In addition, with a ~6-fold higher concentration of Fe^{3+} on the external surface area for DZ-1 as compared to SiO_2, a significantly higher surface Fe^{3+} concentration is available for migration and agglomeration in Fe/DZ-1, but no such behavior is observed in the crystalline catalyst. These considerations demonstrate fundamentally different behaviors under catalytic conditions for Fe/DZ-1 and Fe/SiO_2 that affect the stability of active species to leaching and

formation of agglomerates, as depicted in Scheme 3.4 **III→IV**.

Given that no nominal compositional differences exist between amorphous SiO_2 and crystalline DZ-1, as both consist of SiO_2 networks that differ only in the arrangement of atoms, we conclude that the coordination environment of grafted Fe^{3+} is directly responsible for the exceptional stability of the Fe^{3+} sites in Fe/DZ-1 when compared to those in Fe/SiO_2. Simple surface grafting on an amorphous support is insufficient to prevent the formation of mobile species that migrate on the support surface to form agglomerates during catalytic oxidation. In contrast, environments arising from Fe^{3+} incorporation into pre-organized defect sites in zeolite frameworks are capable of stabilizing against active-site leaching, migration, and agglomeration. We hypothesize that this stabilization is due to stronger interaction of Fe^{3+} with the support when incorporated into the geometrically favored tetrahedral environment of the silanol nest, in essence being chelated and held in place by the stable, extended crystalline framework. Indeed, prior work has shown that Al^{3+} heteroatoms, responsible for acidity in aluminosilicates, are more stable and acidic when found as part of ordered crystalline aluminosilicate frameworks, as compared to analogous sites on amorphous phases.[66–70] Based on these observations, we hypothesize that cations rigidly held within silicate frameworks are more stable than those simply grafted on the surfaces, providing a general basis for the preparation of robust grafted cations on solid supports as catalysts.

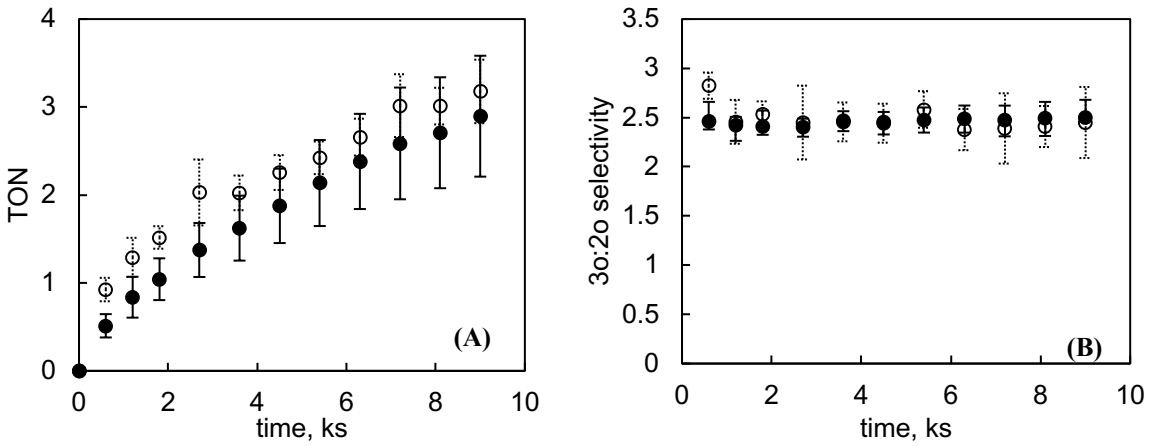

Figure 3.4. Turnover number **(A)** and tertiary to secondary (3^o:2^o) selectivity **(B)** as a function of time for Fe/DZ-1 (•, solid uncertainties) and Fe/SiO_2 (o, dashed uncertainties) in the batch catalytic oxidation of adamantane with H_2O_2. The uncertainties represent standard deviation of measured values in replicate experiments.

3.4. Conclusions

We have developed a novel approach to the incorporation of Fe^{3+} onto siliceous supports, consisting of an exchange of chelating EDTA ligand in solution for chelating silicate ligand environments on the support. The protection of Fe^{3+} cations by EDTA during grafting results in Fe^{3+} sites that are isolated from each other and located on the external surface of the supports. This enabled a rigorous comparison of amorphous SiO_2 vs. crystalline DZ-1 as supports for Fe^{3+}, which comes to the following conclusions, schematically depicted as numbered steps in Scheme

3.4.

(**I**) Silanol nests, consisting of framework vacancies within a delaminated zeolitic support, act as pre-organized silicate grafting sites. Such sites are uniformly abundant in DZ-1, resulting in a high degree of framework incorporation of Fe^{3+} in DZ-1, approaching the theoretical maximum cation loading. In contrast, the random distribution of silanol on amorphous SiO_2 severely limits the availability of grafting sites with the correct spatial arrangement to promote full exchange of EDTA for support silanols.

(**II**) Fe^{3+} fully dissociates from EDTA upon grafting, and is not partially bound by EDTA ligand (top vs. center of Scheme 3.2). This observation demonstrates how this spatial pre-organization of silanols within nests facilitates cooperativity, allowing the chelating EDTA to be completely displaced into solution and replaced by a new chelating environment, that of the silicate network.

(**III**) The Fe^{3+} framework sites in DZ-1 are more structurally homogenous and thermally stable than their surface-grafted analogues on amorphous SiO_2, demonstrating how the pre-organization of silanols within nests is essential in ensuring the selective synthesis of uniform and stable grafted structures.

(**IV**) The importance of such stability for functional applications is apparent during the oxidation of adamantane with H_2O_2, where Fe^{3+} active sites are stable to leaching and agglomeration only when incorporated into the framework of Fe/DZ-1, and not when surface grafted in Fe/SiO_2. This difference demonstrates how the silicate framework in DZ-1 can act as a robust chelating ligand, maintaining the active sites intact during harsh application conditions.

Our work unequivocally demonstrates how the silicate grafting environment on the support, and not just the chemical identity of the silanols, is capable of enforcing a specific coordination for a grafted cation, thereby controlling its materials properties akin to the way in which the ligand sphere impacts homogeneous catalysts. Synthetic control in the preparation of functional materials based on grafted cations is typically achieved by tailored syntheses of molecular precursors for grafting onto supports; in contrast, in our materials such synthetic control is achieved by tuning silanol grafting sites, enforcing a pre-defined spatial arrangement and allowing cooperativity of silanol ligands within nests, thereby influencing the synthesis, speciation, and stability of grafted sites. This approach may aid in future selective synthesis of uniform supported oxide structures that are relevant to both fundamental and practical applications, and generally expands our understanding of amorphous versus crystalline supports as ligands for grafted cation sites.[34-36]

We anticipate our findings will help guide future work on the synthesis of functional materials based on grafted cations and supported metal oxides, where amorphous silica supports are routinely employed to overcome diffusion limitations of microporous zeolites without consideration of impact of crystallinity on the active structures. Instead, zeolitic materials with high external surface areas, achievable by delamination or other novel synthetic techniques, can be used as accessible crystalline catalyst supports.[71–73] By combining their high accessibility with the properties of silanol nests as grafting environments for transition metal cations, we are beginning to develop novel functional materials which can significantly expand the catalytic uses of zeolites beyond the traditional realm of gas-phase small-molecule activation, to those involving

transition metal active sites and/or bulky substrates in liquid phase reactions.

Scheme 3.4. Comparative summary of grafted Fe^{3+} sites in crystalline DZ-1 vs. amorphous SiO_2.

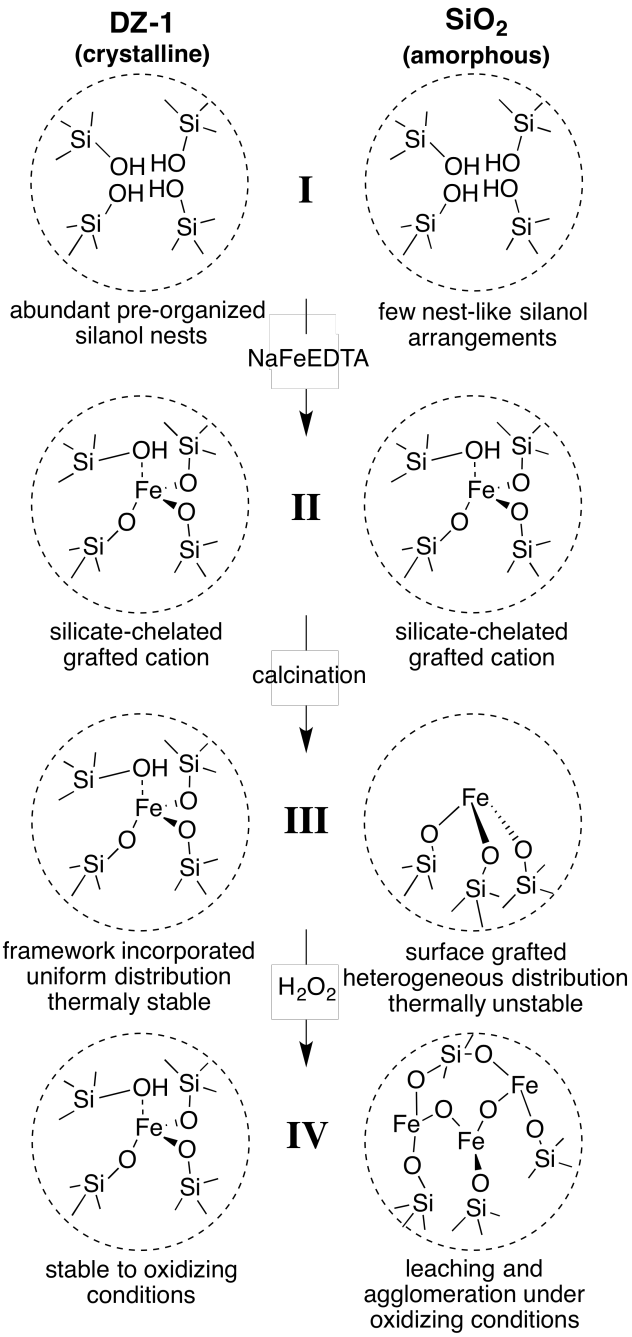

I, **II**, **III**, and **IV** are schematic representations of the different steps in the material synthesis process, referenced in the text. They represent the properties of DZ-1 vs. SiO_2 as supports and of Fe^{3+} cations grafted onto them.

3.5. Appendices

3.5.1. Calculation of Density of Grafting Sites

The unit cell of MWW consists of 14 face atoms exposed on the external surface.[47,48] The area per unit cell of this surface is given by $\frac{\text{unit cell volume}}{\text{length of c-axis}} = \frac{4518\text{Å}^3}{25.2\text{Å}} = 179\text{Å}^2$, or taking the reciprocal of this, there are 0.558 unit cells/nm^2 of surface. Given the external surface area of 134 m^2/g (Table 3.1), and with appropriate unit conversions, 0.558 unit cells/nm^2 x 134 m^2/g = 7.46x10^{19} surface unit cells per g. A Si/B ratio of 13 (determined from elemental analysis) gives 1 B atom per 14 atoms of the surface unit cell, so 1 B/unit cell * 7.46x10^{19} surface unit cells / g * 6.022x10^{23} mol^{-1} = 124 μmol/g of B. Since each leached B acts as a grafting site, this gives a maximum loading of 124 μmol/g of Fe^{3+}, equivalent to 0.69 wt% Fe.

3.5.2. N_2 physisorption isotherms at 77 K

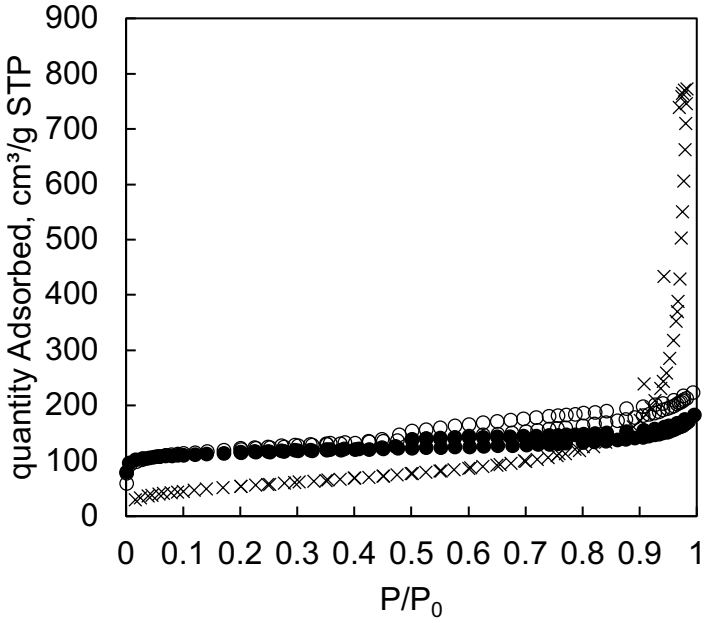

Figure A3.1. N_2 physisorption isotherms at 77K for materials described in Table 3.1: ERB-1 (●), DZ-1 (o), SiO_2 (x). ERB-1 corresponds to ERB-1(P) calcined as per DZ-1 treatment protocols.

3.5.3. Fourier-Transform Infrared Spectra of DZ-1 Support

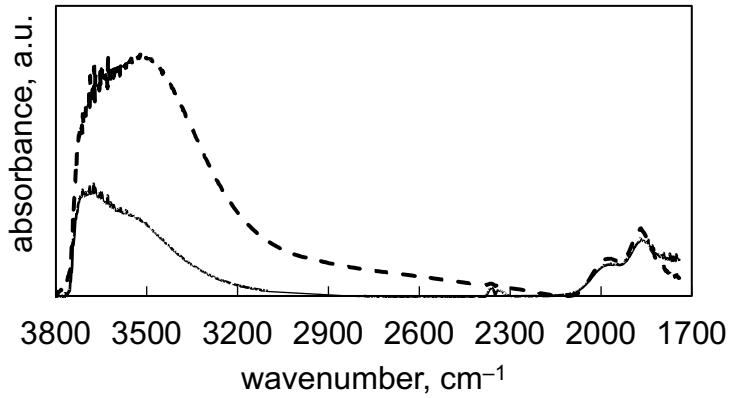

Figure A3.2. Fourier-transform infrared spectra (FTIR) of calcined DZ-1 support (solid line) and its rehydroxylated counterpart (dashed line), consisting of calcined DZ-1 treated under the same conditions as for Fe^{3+} incorporation but in the absence of the dissolved NaFeEDTA precursor. The growth of the band centered at *ca.* 3500 cm^{-1} is indicative of the re-synthesis of silanol nests that may have been removed during calcination.[43] FTIR spectra of self-supporting wafers were acquired under in-situ He purge at 393 K to remove physisorbed water, and were normalized to integrated intensities of skeleton Si-O-Si overtones in the range 1740 – 2080 cm^{-1}.[28]

3.5.4. Molecular Modeling of NaFeEDTA

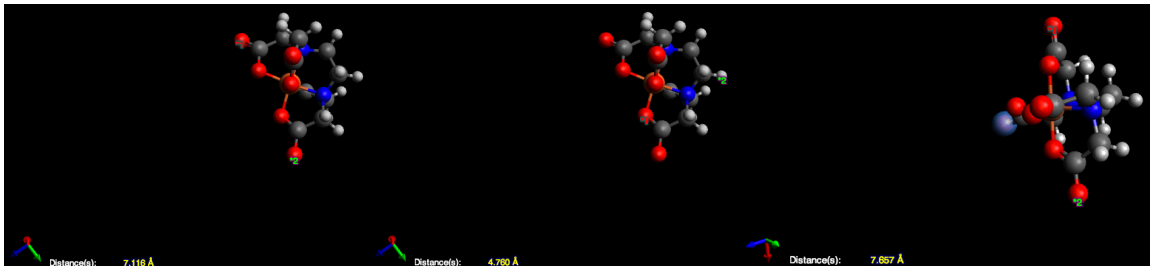

Figure A3.3. Molecular model of the $FeEDTA^-$ complex used to investigate inter-nuclear distances, prepared using Avogadro: an open-source molecular builder and visualization tool. Version 1.1.1 (http://avogadro.cc/),[74] and structurally optimized using the UFF force field. Carbon is shown as black, oxygen as red, hydrogen as white, and iron as orange. Distances shown correspond to shortest inter-nuclear distances between outermost atoms along the three axes. The shortest interatomic distances measured was 4.76 Å (right figure), but diffusion along this axis would require a channel accommodating the complex along axes measuring 7.1 Å (left figure) or 7.7 Å (right figure). Additionally, van der Walls radii are ~1 Å larger than atomic nuclei, and both water – known to coordinate to $FeEDTA^-$ –[45] and counteractions are not shown. Overall, this results in a molecule significantly larger than the diffusion allowed radius of 4.92 Å in 10-membered rings of MWW.[47] Indeed, Al^{3+}, only complexed by its hydration sphere, has been shown to be too large for diffusion into 10-member ring channels in a variety of zeolite framework topologies.[75]

3.5.5. Diffuse-Reflectance UV-visible Spectroscopy of Materials Prepared by Incipient Wetness Impregnation

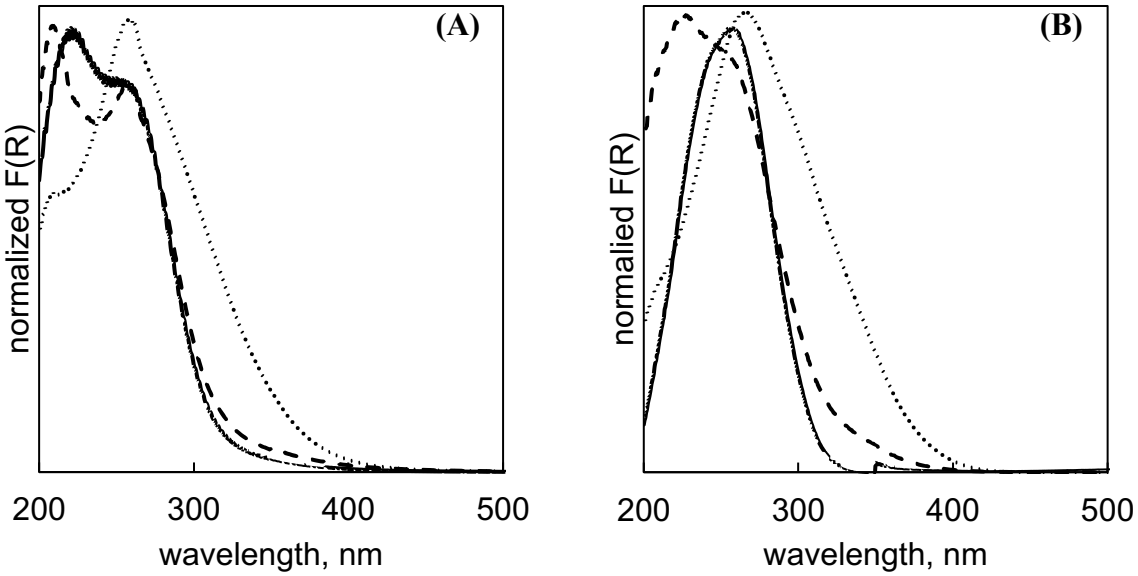

Figure A3.4. Diffuse reflectance UV-visible spectra for materials prepared on DZ-1 **(A)** and SiO_2 **(B)**. Solid lines correspond to Fe/SiO_2 and Fe/DZ-1, while dashed lines correspond to the same materials before calcination treatment. For Fe/DZ-1, the environment of Fe^{3+} before calcination is similar to that of the calcined material, while for Fe/SiO_2, a slight narrowing of the absorbance bands observed. As a control, as-made (non-calcined) materials were prepared by incipient wetness impregnation on the same supports, and their spectra shown in dotted lines. These spectra exhibit a maximum ~255-265 nm and a broad absorbance band, consistent with Fe^{3+} being bound to EDTA even after impregnation.[4] This comparison confirms that Fe^{3+} is bound to the support, and not to the EDTA ligand, in the as-prepared Fe/SiO_2 and Fe/DZ-1 materials, consistent with a ligand exchange process during Fe^{3+} incorporation.

3.5.6. Diffuse-Reflectance UV-visible Spectroscopy of Material Prepared by Non-Chelated Iron(III) Precursor

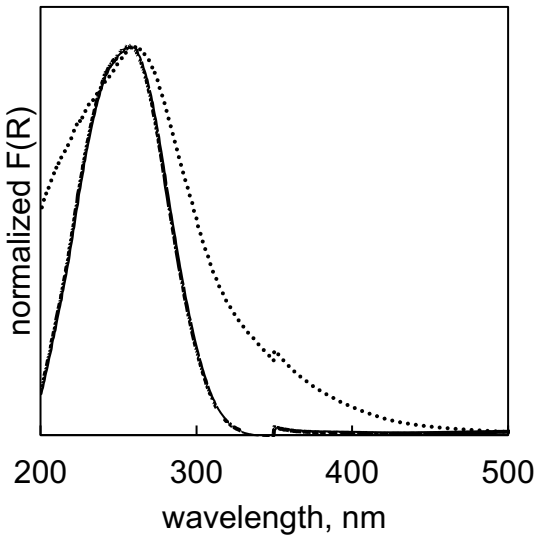

Figure A3.5. Diffuse reflectance UV-visible spectra for Fe/SiO_2 (solid line), prepared by treatment with NaFeEDTA as detailed in the experimental section, contrasted to a material prepared with the same conditions but with $Fe(NO_3)_3$ as a precursor (dotted line). The latter shows extensive absorbance above 300 nm, indicating formation of oligomeric Fe-O-Fe species when a non-chelating Fe^{3+} precursor is used.

3.5.7. Alternative Mössbauer Spectral Fits

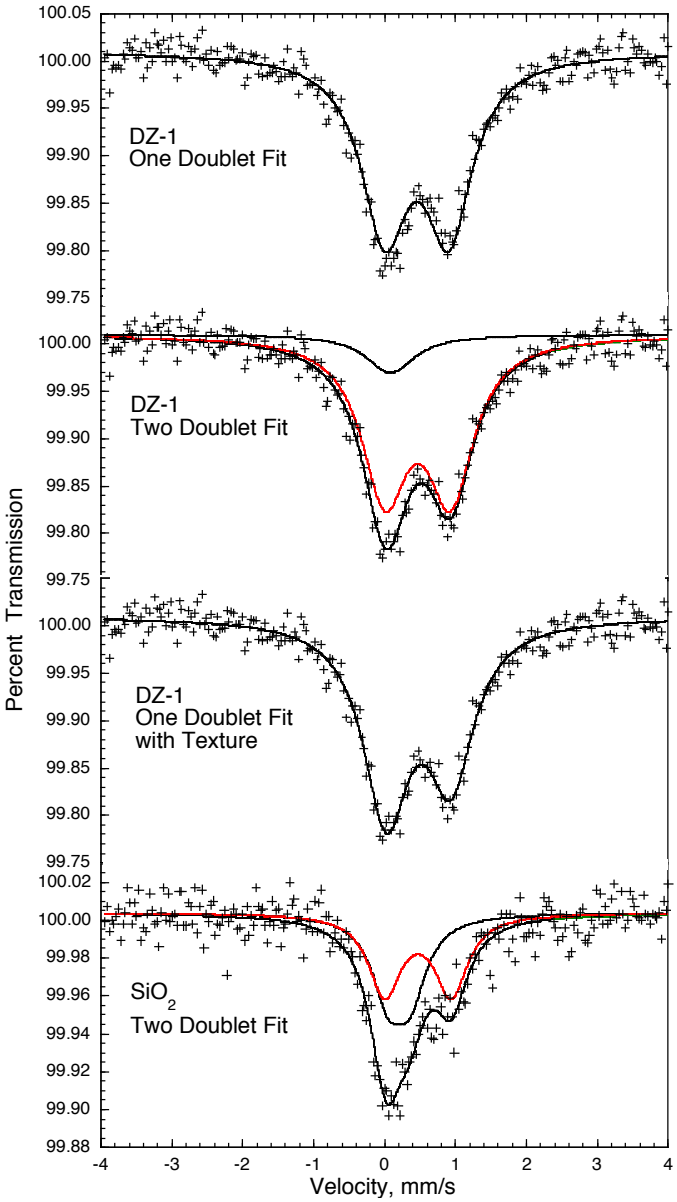

Figure A3.6. Mössbauer spectra for Fe/DZ-1 and Fe/SiO_2 at 5 K and fit with three different models for Fe/DZ-1, the three top spectral fits, and for Fe/SiO_2, the bottom spectrum. + represent raw data and the solid line indicates spectral fits, summarized below in Table A3.1. The 512 channel spectrum was converted to 256 channel spectrum by addition of adjacent channels for improvement of S/N ratio. Similar fits (not shown) were obtained for spectra that were not-added. Values of $\chi^2 < 1$ indicate over-parametrization, so three different spectral fits were considered for Fe/DZ-1 in order to ensure rigorous assignment of species. A one-doublet fit, with a single symmetric quadrupole doublet (top), yielding an acceptable $\chi^2 = 0.93$, indicating most Fe^{3+} is pseudo-O_h. However, the obvious asymmetry of the spectrum made us consider a two-doublet fit, resulting in two doublets with different isomer shifts and/or quadrupole splittings (second from top), which confirms most Fe^{3+} occurs as pseudo-O_h species. We also considered the presence of

texture (textured-doublet, third fit from top), which can occur if the crystallites show preferential orientation or a non-random orientation. The texture function is at a reasonable value of 2.8(1), but non-random crystallite orientation is highly unlikely in these materials. Given the nature of our materials and the asymmetric nature of the spectra, we consider the two-doublet fit as the most appropriate (see main text). The bottom fit, shown in Figure 3.3, is for Fe/SiO_2 at 5 K and is discussed in the full paper and is shown here for comparison.

Table A3.1. Mössbauer Spectral Parameters Obtained at 5 K for Different Fits [a].

Material	Fit	δ, mm/s[b]	ΔE_Q, mm/s	Γ, mm/s	Texture [c]	Area, %	High-Spin Iron(III) Assignment	χ^2
Fe/DZ-1	One-doublet	0.45(1)	0.91(1)	0.80(2)	2.00	100	pseudo-O_h	0.9340
Fe/DZ-1	Two-doublet	0.10(9) 0.47(3)	0.1(4.0) 0.9(8)	0.79(4) 0.79(4)	2.00 2.00	11(3) 88(3)	pseudo-T_d pseudo-O_h	0.8015 -
Fe/DZ-1	Textured doublet	0.48(1)	0.91(1)	0.80(3)	2.8(1)	100	pseudo-O_h	0.7941
Fe/SiO_2	Two-doublet	0.20(7) 0.47(7)	0.3(1) 0.9(1)	0.55(6) 0.55(6)	2.00 2.00	48(4) 52(4)	pseudo-T_d pseudo-O_h	0.8780

[a]All added channel fits. The statistical fitting uncertainties are given in parenthesis. The true uncertainties are probably twice as large. [b]The isomer shifts are given relative to α-iron foil measured at 295 K. [c]If the texture is 2.00 the quadrupole doublet components have the same area and there is no texture present; a value greater than 2.00 indicates the low-velocity component of a doublet has a larger area than the high-velocity component.

3.5.8. Fourier-Transform Infrared Spectrum of Fe/DZ-1

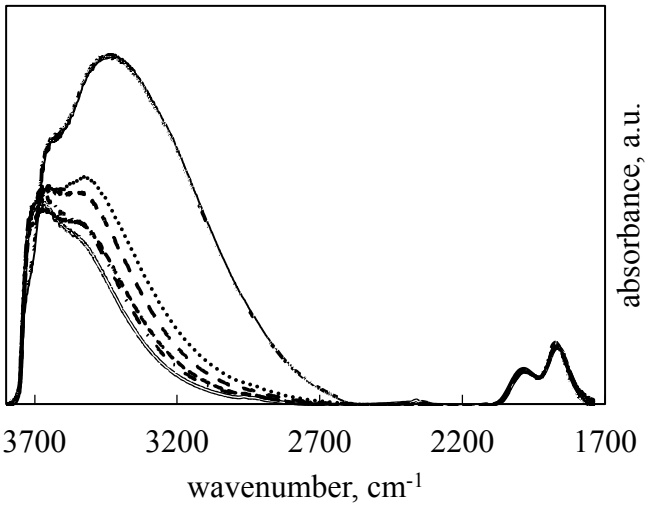

Figure A3.7. Fourier-transform infrared (FTIR) spectrum of self-supporting wafer of Fe/DZ-1 acquired under He purge at increasing temperatures of 313 K (solid lines), 353 K (dotted lines), 393 K (long dashed lines), 413 K (short dashed lines), 433 K (dot dashed lines), and 453 K (double parallel lines) to remove water interference. No evidence of Brønsted acidic Fe(O-H)Si hydroxyl stretching, expected at 3630 cm^{-1},[53] is seen.

3.5.9. Catalytic Hot Filtration Tests

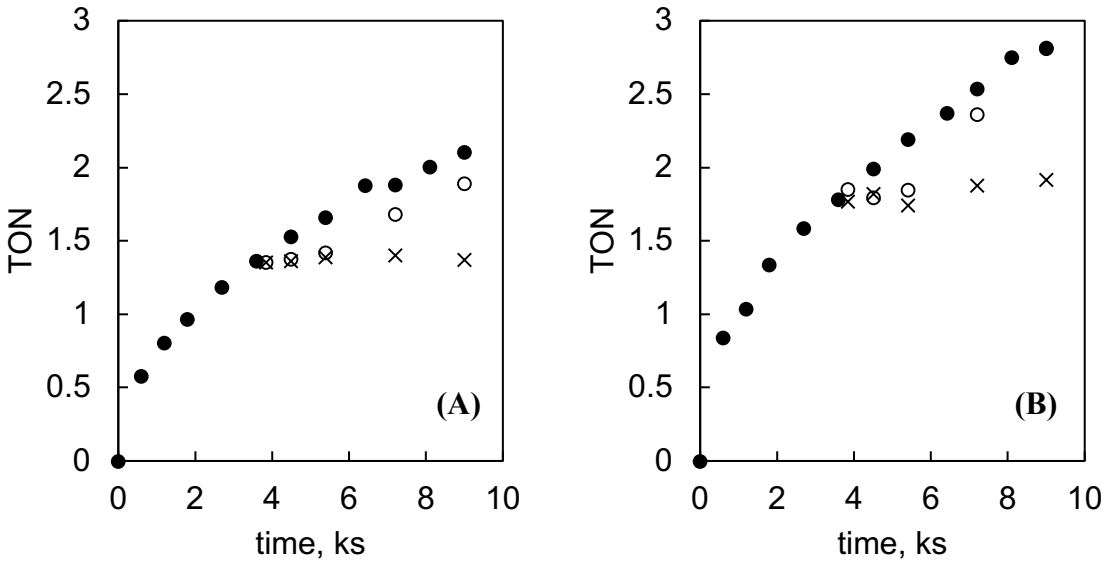

Figure A3.8. Hot filtration test to confirm that homogeneous Fe^{3+} species are not responsible for catalytic activity,[4] for Fe/DZ-1 **(A)** and Fe/SiO_2 **(B)**. Results under typical catalytic testing conditions (Section 3.2.4) are shown as solid circles (•). After 60 min of reaction, a portion of the reaction mixture was removed and transferred using a preheated syringe to an identical flask at the reaction temperature and the reaction was monitored (hollow circles, o). A different portion was transferred to an identical reaction flask at the reaction temperature using a preheated filtration setup, and was filtered to remove the catalyst, and the reaction products were monitored (cross markers, x). Results show that hot transfer to a different reaction flask preserved activity, but that filtration to remove the heterogeneous catalyst resulted in complete loss of catalytic activity. If homogeneous Fe species, which are not removed by filtration, were active, oxidation products would be expected after catalyst removal. This is not seen in these results, confirming that only heterogeneous species are responsible for oxidation.

3.5.10. Diffuse-Reflectance UV-visible Spectroscopy of Stress-Tested Materials

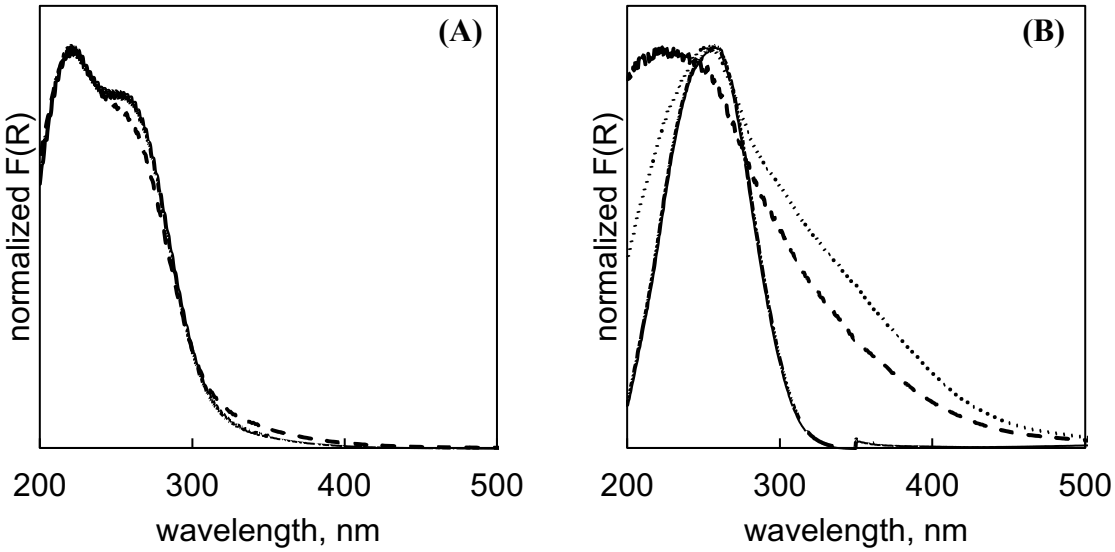

Figure A3.9. Stress testing results of Fe/DZ-1 **(A)** and Fe/SiO_2 **(B)**. The spectrum for the as-made material is shown as a solid line, while that of the stress-tested material is shown as a dashed line. Stress-testing consisted in treating 50 mg of material at 333 K for 2 h with 1.5 mL of 30 wt% H_2O_2, followed by filtration, washing with acetonitrile, and drying. Results show that no significant change in coordination state occurs for Fe/DZ-1, while significant absorption broadening occurs for Fe/SiO_2, indicating agglomeration of Fe species into FeO_x agglomerates, similar to the behavior of these materials under catalytic conditions. To confirm that this additional absorbance is not due to charge transfer band originating from the coordination of other species present during stress testing, the spectrum for stress-tested Fe/SiO_2 was acquired after calcination of the tested material (dotted line right), confirming that this broadness in absorption persists and is solely due to absorption by supported oxide species.

3.6. References

(1) Bell, A. T.; Gates, B. C.; Ray, D. *Basic Research Needs: Catalysis for Energy*; Bethesda, Maryland, 2007.

(2) van Dillen, A. J.; Terörde, R. J. A. M.; Lensveld, D. J.; Geus, J. W.; de Jong, K. P. Synthesis of Supported Catalysts by Impregnation and Drying Using Aqueous Chelated Metal Complexes. *J. Catal.* **2003**, *216*, 257–264.

(3) Zhu, Y.; Tang, W.; Zhao, B.; Cai, X.; Xie, Y. Spontaneous Dispersion of Salts and Oxides onto Surfaces of Zeolites and Its Applications. In *Recent Advances in the Science and Technology of Zeolites and Related Materials, Proceedings of the 14th International Zeolite Conference*; 2004; Vol. 154, pp 3021–3027.

(4) Prieto-Centurion, D.; Notestein, J. M. Surface Speciation and Alkane Oxidation with Highly Dispersed Fe(III) Sites on Silica. *J. Catal.* **2011**, *279*, 103–110.

(5) Prieto-Centurion, D.; Boston, A. M.; Notestein, J. M. Structural and Electronic Promotion with Alkali Cations of Silica-Supported Fe(III) Sites for Alkane Oxidation. *J. Catal.* **2012**, *296*, 77–85.

(6) Oyama, S. T. *Mechanisms in Homogeneous and Heterogeneous Epoxidation Catalysis*; Elsevier: Amsterdam, 2011.

(7) Satishkumar, G.; Landau, M. V.; Buzaglo, T.; Frimet, L.; Ferentz, M.; Vidruk, R.; Wagner, F.; Gal, Y.; Herskowitz, M. Fe/SiO_2 Heterogeneous Fenton Catalyst for Continuous Catalytic Wet Peroxide Oxidation Prepared in Situ by Grafting of Iron Released from $LaFeO_3$. *Appl. Catal. B Environ.* **2013**, *138–139*, 276–284.

(8) Soled, S. Silica-Supported Catalysts Get a New Breath of Life. *Science* **2015**, *350*, 1171–1172.

(9) Bouh, A. O.; Rice, G. L.; Scott, S. L. Mono- and Dinuclear Silica-Supported Titanium(IV) Complexes and the Effect of TiOTi Connectivity on Reactivity. *J. Am. Chem. Soc.* **1999**, *121*, 7201–7210.

(10) Roukoss, C.; Fiddy, S.; de Mallmann, A.; Rendón, N.; Basset, J.-M.; Kuntz, E.; Copéret, C. Access to Well-Defined Isolated Fe(II) Centers on Silica and Their Use in Oxidation. *Dalton Trans.* **2007**, No. 47, 5546–5548.

(11) Roukoss, C.; Basset, J.-M.; Copéret, C.; Lucas, C.; Kuntz, E. Effect of the Nuclearity of Perhydrocarbyl Fe(II) Complexes on the Grafting on Oxide Supports. *Comptes Rendus Chim.* **2008**, *11*, 620–627.

(12) Nozaki, C.; Lugmair, C. G.; Bell, A. T.; Tilley, T. D. Synthesis, Characterization, and Catalytic Performance of Single-Site Iron(III) Centers on the Surface of SBA-15 Silica. *J. Am. Chem. Soc.* **2002**, *124*, 13194–13203.

(13) Holland, A. W.; Li, G.; Shahin, A. M.; Long, G. J.; Bell, A. T.; Tilley, T. D. New Fe/SiO_2 Materials Prepared Using Diiron Molecular Precursors: Synthesis, Characterization and Catalysis. *J. Catal.* **2005**, *235*, 150–163.

(14) Thomas, J. M.; Raja, R.; Lewis, D. W. Single-Site Heterogeneous Catalysts. *Angew. Chem. Int. Ed.* **2005**, *44*, 6456–6482.

(15) Argo, A. M.; Odzak, J. F.; Lai, F. S.; Gates, B. C. Observation of Ligand Effects during Alkene Hydrogenation Catalysed by Supported Metal Clusters. *Nature* **2002**, *415*, 623–626.

(16) Gervasini, A.; Messi, C.; Carniti, P.; Ponti, A.; Ravasio, N.; Zaccheria, F. Insight into the Properties of Fe Oxide Present in High Concentrations on Mesoporous Silica. *J. Catal.* **2009**, *262*, 224–234.

(17) Parmaliana, A.; Arena, F.; Frusteri, F.; Martínez-Arias, A.; López Granados, M.; Fierro, J. L. G. Effect of Fe-Addition on the Catalytic Activity of Silicas in the Partial Oxidation of Methane to Formaldehyde. *Appl. Catal. A Gen.* **2002**, *226*, 163–174.
(18) Arena, F.; Gatti, G.; Martra, G.; Coluccia, S.; Stievano, L.; Spadaro, L.; Famulari, P.; Parmaliana, A. Structure and Reactivity in the Selective Oxidation of Methane to Formaldehyde of Low-Loaded FeOx/SiO_2 Catalysts. *J. Catal.* **2005**, *231*, 365–380.
(19) Runnebaum, R. C.; Ouyang, X.; Edsinga, J. A.; Rea, T.; Arslan, I.; Hwang, S.-J. J.; Zones, S. I.; Katz, A. Role of Delamination in Zeolite-Catalyzed Aromatic Alkylation: UCB-3 versus 3-D Al-SSZ-70. *ACS Catal.* **2014**, *4*, 2364–2368.
(20) Roth, W. J.; Čejka, J. Two-Dimensional Zeolites: Dream or Reality? *Catal. Sci. Technol.* **2011**, *1*, 43.
(21) Maheshwari, S.; Jordan, E.; Kumar, S.; Bates, F. S.; Penn, R. L.; Shantz, D. F.; Tsapatsis, M. Layer Structure Preservation during Swelling, Pillaring, and Exfoliation of a Zeolite Precursor. *J. Am. Chem. Soc.* **2008**, *130*, 1507–1516.
(22) Maheshwari, S.; Martínez, C.; Teresa Portilla, M.; Llopis, F. J.; Corma, A.; Tsapatsis, M. Influence of Layer Structure Preservation on the Catalytic Properties of the Pillared Zeolite MCM-36. *J. Catal.* **2010**, *272*, 298–308.
(23) Ouyang, X.; Wanglee, Y.-J.; Hwang, S.-J.; Xie, D.; Rea, T.; Zones, S. I.; Katz, A. Novel Surfactant-Free Route to Delaminated All-Silica and Titanosilicate Zeolites Derived from a Layered Borosilicate MWW Precursor. *Dalton Trans.* **2014**, *43*, 10417–10429.
(24) Flytzani-Stephanopoulos, M.; Gates, B. C. Atomically Dispersed Supported Metal Catalysts. *Annu. Rev. Chem. Biomol. Eng.* **2012**, *3*, 545–574.
(25) Smith, G. V.; Notheisz, F. *Heterogeneous Catalysis in Organic Chemistry*; Academic Press, 1999.
(26) Copéret, C.; Chabanas, M.; Petroff Saint-Arroman, R.; Basset, J.-M. Homogeneous and Heterogeneous Catalysis: Bridging the Gap through Surface Organometallic Chemistry. *Angew. Chem. Int. Ed.* **2003**, *42*, 156–181.
(27) Zhuravlev, L. T. The Surface Chemistry of Amorphous Silica. Zhuravlev Model. *Colloids Surfaces A Physicochem. Eng. Asp.* **2000**, *173*, 1–38.
(28) Vansant, E. F.; Voort, P. Van Der; Vrancken, K. C. *Characterization and Chemical Modification of the Silica Surface*, 1st ed.; Elsevier, 1995; Vol. 93.
(29) Shantz, D. F.; Schmedt Auf Der Günne, J.; Koller, H.; Lobo, R. F. Multiple-Quantum ^{1}H MAS NMR Studies of Defect Sites in as-Made All- Silica ZSM-12 Zeolite. *J. Am. Chem. Soc.* **2000**, *122*, 6659–6663.
(30) Baerlocher, C.; Xie, D.; McCusker, L. B.; Hwang, S.-J.; Chan, I. Y.; Ong, K.; Burton, A. W.; Zones, S. I. Ordered Silicon Vacancies in the Framework Structure of the Zeolite Catalyst SSZ-74. *Nat. Mater.* **2008**, *7*, 631–635.
(31) Ouyang, X.; Hwang, S.-J.; Xie, D.; Rea, T.; Zones, S. I.; Katz, A. Heteroatom-Substituted Delaminated Zeolites as Solid Lewis Acid Catalysts. *ACS Catal.* **2015**, *5*, 3108–3119.
(32) Koller, H.; Chen, C. Y.; Zones, S. I. Selectivities in Post-Synthetic Modification of Borosilicate Zeolites. *Top. Catal.* **2015**, *58*, 451–479.
(33) Hwang, S.-J.; Chen, C. Y.; Zones, S. I. Boron Sites in Borosilicate Zeolites at Various Stages of Hydration Studied by Solid State NMR Spectroscopy. *J. Phys. Chem. B* **2004**, *108*, 18535–18546.
(34) Ehresmann, J. O.; Kletnieks, P. W.; Liang, A.; Bhirud, V. A.; Bagatchenko, O. P.; Lee, E.

J.; Klaric, M.; Gates, B. C.; Haw, J. F. Evidence from NMR and EXAFS Studies of a Dynamically Uniform Mononuclear Single-Site Zeolite-Supported Rhodium Catalyst. *Angew. Chem. Int. Ed.* **2006**, *45*, 574–576.
(35) Ogino, I.; Gates, B. C. Molecular Chemistry in a Zeolite: Genesis of a Zeolite Y-Supported Ruthenium Complex Catalyst. *J. Am. Chem. Soc.* **2008**, *130*, 13338–13346.
(36) Hoffman, A. S.; Fang, C. Y.; Gates, B. C. Homogeneity of Surface Sites in Supported Single-Site Metal Catalysts: Assessment with Band Widths of Metal Carbonyl Infrared Spectra. *J. Phys. Chem. Lett.* **2016**, *7*, 3854–3860.
(37) Bell, A. T. The Impact of Nanoscience on Heterogeneous Catalysis. *Science* **2003**, *299*, 1688–1691.
(38) Ertl, G.; Knözinger, H.; Weitkamp, J. *Handbook of Heterogeneous Catalysis*; Wiley: Weinheim, Germany, 1997.
(39) Prisecaru, I. WMOSS4 Mössbauer Spectral Analysis Software.
(40) Ogino, I.; Nigra, M. M.; Hwang, S.-J.; Ha, J. M.; Rea, T.; Zones, S. I.; Katz, A. Delamination of Layered Zeolite Precursors under Mild Conditions: Synthesis of UCB-1 via Fluoride/Chloride Anion-Promoted Exfoliation. *J. Am. Chem. Soc.* **2011**, *133*, 3288–3291.
(41) Senderov, E.; Halasz, I.; Olson, D. H. On Existence of Hydroxyl Nests in Acid Dealuminated Zeolite Y. *Microporous Mesoporous Mater.* **2014**, *186*, 94–100.
(42) Bordiga, S.; Roggero, I.; Ugliengo, P.; Zecchina, A.; Bolis, V.; Artioli, G.; Buzzoni, R.; Marra, G.; Rivetti, F.; Spanò, G.; Lamberti, C. Characterisation of Defective Silicalites. *J. Chem. Soc. Dalt. Trans.* **2000**, No. 21, 3921–3929.
(43) de Ruiter, R.; Kentgens, A. P. M.; Grootendorst, J.; Jansen, J. C.; van Bekkum, H. Calcination and Deboronation of [B]-MFI Single Crystals. *Zeolites* **1993**, *13*, 128–138.
(44) Woolery, G. L.; Alemany, L. B.; Dessau, R. M.; Chester, A. W. Spectroscopic Evidence for the Presence of Internal Silanols in Highly Siliceous ZSM-5. *Zeolites* **1986**, *6*, 14–16.
(45) Szilágyi, P. Á.; Madarász, J.; Kuzmann, E.; Vértes, A.; Molnár, G.; Bousseksou, A.; Sharma, V. K.; Homonnay, Z. Thermal Stability of the Fe^{III}EDTA Complex in Its Monomeric Form. *Thermochim. Acta* **2008**, *479*, 53–58.
(46) Cheng, J. C.; Degnan, T. F.; Beck, J. S.; Huang, Y. Y.; Kalyanaraman, M.; Kowalski, J. A.; Loehr, C. A.; Mazzone, D. N. A Comparison of Zeolites MCM-22, Beta, and Usy for Liquid Phase Alkylation of Benzene with Ethylene. *Stud. Surf. Sci. Catal.* **1999**, *121*, 53–60.
(47) Baerlocher, C.; McCusker, L.; Olson, D. *Atlas of Zeolite Framework Types*, 6th ed.; Elsevier: Amsterdam, 2007.
(48) Lawton, S. L.; Leonowicz, M. E.; Partridge, R. D.; Chu, P.; Rubin, M. K. Twelve-Ring Pockets on the External Surface of MCM-22 Crystals. *Microporous Mesoporous Mater.* **1998**, *23*, 109–117.
(49) Hovey, J. K.; Tremaine, P. R. Thermodynamics of the Complexes of Aqueous Iron(III), Aluminum, and Several Divalent Cations with EDTA: Heat Capacities, Volumes, and Variations in Stability with Temperature. *J. Phys. Chem.* **1985**, *89*, 5541–5549.
(50) Das, U.; Zhang, G.; Hu, B.; Hock, A. S.; Redfern, P. C.; Miller, J. T.; Curtiss, L. A. Effect of Siloxane Ring Strain and Cation Charge Density on the Formation of Coordinately Unsaturated Metal Sites on Silica: Insights from Density Functional Theory (DFT) Studies. *ACS Catal.* **2015**, *5*, 7177–7185.
(51) Grosso-Giordano, N. A.; Solovyov, A.; Hwang, S.-J.; Katz, A. Effect of Coordination Environment in Grafted Single-Site Ti-SiO_2 Olefin Epoxidation Catalysis. *Top. Catal.* **2016**, *59*,

1110–1122.
(52) Tippins, H. H. Charge-Transfer Spectra of Transition-Metal Ions in Corundum. *Phys. Rev. B* **1970**, *1*, 126–135.
(53) Bordiga, S.; Buzzoni, R.; Geobaldo, F.; Lamberti, C.; Giamello, E.; Zecchina, A.; Leofanti, G.; Petrini, G.; Tozzola, G.; Vlaic, G. Structure and Reactivity of Framework and Extraframework Iron in Fe-Silicalite as Investigated by Spectroscopic and Physicochemical Methods. *J. Catal.* **1996**, *158*, 486–501.
(54) Schwidder, M.; Kumar, M. S.; Klementiev, K.; Pohl, M. M.; Brückner, A.; Grünert, W. Selective Reduction of NO with Fe-ZSM-5 Catalysts of Low Fe Content: I. Relations between Active Site Structure and Catalytic Performance. *J. Catal.* **2005**, *231*, 314–330.
(55) Maier, S. M.; Jentys, A.; Metwalli, E.; Müller-Buschbaum, P.; Lercher, J. A. Determination of the Redox Processes in FeBEA Catalysts in NH_3−SCR Reaction by Mössbauer and X-Ray Absorption Spectroscopy. *J. Phys. Chem. Lett.* **2011**, *2*, 950–955.
(56) Pérez-Ramírez, J.; Groen, J. C.; Brückner, A.; Kumar, M. S.; Bentrup, U.; Debbagh, M. N.; Villaescusa, L. A. Evolution of Isomorphously Substituted Iron Zeolites during Activation: Comparison of Fe-Beta and Fe-ZSM-5. *J. Catal.* **2005**, *232*, 318–334.
(57) Heitmann, G. P.; Dahlhoff, G.; Hölderich, W. F. Catalytically Active Sites for the Beckmann Rearrangement of Cyclohexanone Oxime to ε-Caprolactam. *J. Catal.* **1999**, *186*, 12–19.
(58) Tuel, A.; Arcon, I.; Millet, J. M. M. Investigation of Structural Iron Species in Fe-Mesoporous Silicas by Spectroscopic Techniques. *J. Chem. Soc. Faraday Trans.* **1998**, *94*, 3501–3510.
(59) Connell, G.; Dumesic, J. A. Acidic Properties of Binary Oxide Catalysts. I. Mössbauer Spectroscopy and Pyridine Adsorption for Iron Supported on Silica. *J. Catal.* **1986**, *101*, 103–113.
(60) Dubkov, K. A.; Ovanesyan, N. S.; Shteinman, A. A.; Starokon, E. V; Panov, G. I. Evolution of Iron States and Formation of α-Sites upon Activation of FeZSM-5 Zeolites. *J. Catal.* **2002**, *207*, 341–352.
(61) Kumar, R.; Date, S. K.; Bill, E.; Trautwein, A. Mössbauer Spectroscopic Study of Ferrisilicate Analog of Zeolite BETA. *Zeolites* **1991**, *11*, 211–213.
(62) Meagher, A.; Nair, V.; Szostak, R. A Mössbauer Study of ZSM-5-Type Ferrisilicates. *Zeolites* **1988**, *8*, 3–11.
(63) Gurgul, J.; Łątka, K.; Hnat, I.; Rynkowski, J.; Dzwigaj, S. Identification of Iron Species in FeSiBEA by DR UV-Vis, XPS and Mössbauer Spectroscopy: Influence of Fe Content. *Microporous Mesoporous Mater.* **2013**, *168*, 1–6.
(64) Morice, J. A.; Rees, L. V. C. Mössbauer Studies of ^{57}Fe in Zeolites. *Trans. Faraday Soc.* **1968**, *64*, 1388–1395.
(65) Pérez-Ramírez, J.; Mul, G.; Kapteijn, F.; Moulijn, J. A.; Overweg, A. R.; Doménech, A.; Ribera, A.; Arends, I. W. C. E. Physicochemical Characterization of Isomorphously Substituted FeZSM-5 during Activation. *J. Catal.* **2002**, *207*, 113–126.
(66) Liu, Y.; Zhang, W.; Pinnavaia, T. J. Steam-Stable Aluminosilicate Mesostructures Assembled from Zeolite Type Y Seeds. *J. Am. Chem. Soc.* **2000**, *122*, 8791–8792.
(67) Liu, Y.; Zhang, W.; Pinnavaia, T. J. Steam-Stable MSU-S Aluminosilicate Mesostructures Assembled from Zeolite ZSM-5 and Zeolite Beta Seeds. *Angew. Chem. Int. Ed.* **2001**, *40*, 1255–1258.

(68) Corma, A.; Grande, M. S. S.; Gonzalez-Alfaro, V.; Orchilles, A. V. V. Cracking Activity and Hydrothermal Stability of MCM-41 and Its Comparison with Amorphous Silica-Alumina and a USY Zeolite. *J. Catal.* **1996**, *159*, 375–382.
(69) Vogt, E. T. C.; Whiting, G. T.; Dutta Chowdhury, A.; Weckhuysen, B. M. Chapter Two – Zeolites and Zeotypes for Oil and Gas Conversion. In *Advances in Catalysis: Zeolites and Zeotypes for Oil and Gas Conversion*; 2015; Vol. 58, pp 143–314.
(70) Ali, M. A.; Tatsumi, T.; Masuda, T. Development of Heavy Oil Hydrocracking Catalysts Using Amorphous Silica-Alumina and Zeolites as Catalyst Supports. *Appl. Catal. A Gen.* **2002**, *233*, 77–90.
(71) Roth, W. J.; Nachtigall, P.; Morris, R. E.; Čejka, J. Two-Dimensional Zeolites: Current Status and Perspectives. *Chem. Rev.* **2014**, *114*, 4807–4837.
(72) Zhang, X.; Liu, D.; Xu, D.; Asahina, S.; Cychosz, K. A.; Agrawal, K. V.; Al Wahedi, Y.; Bhan, A.; Al Hashimi, S.; Terasaki, O.; Thommes, M.; Tsapatsis, M. Synthesis of Self-Pillared Zeolite Nanosheets by Repetitive Branching. *Science* **2012**, *336*, 1684–1687.
(73) Luo, H. Y.; Michaelis, V. K.; Hodges, S.; Griffin, R. G.; Román-Leshkov, Y.; Roman-Leshkov, Y. One-Pot Synthesis of MWW Zeolite Nanosheets Using a Rationally Designed Organic Structure-Directing Agent. *Chem. Sci.* **2015**, *6*, 6320–6324.
(74) Hanwell, M. D.; Curtis, D. E.; Lonie, D. C.; Vandermeerschd, T.; Zurek, E.; Hutchison, G. R. Avogadro: An Advanced Semantic Chemical Editor, Visualization, and Analysis Platform. *J. Cheminform.* **2012**, *4*.
(75) Zones, S. I.; Benin, A.; Hwang, S.-J.; Xie, D.; Elomari, S.; Hsieh, M.-F. Studies of Aluminum Reinsertion into Borosilicate Zeolites with Intersecting Channels of 10- and 12-Ring Channel Systems. *J. Am. Chem. Soc.* **2014**, *136*, 1462–1471.

Chapter 4

Effect of Coordination Environment in Grafted Single-Site Ti/SiO_2 Olefin Epoxidation Catalysis

Reprinted and adapted by permission from Springer Nature: *Topics in Catalysis*, Grosso-Giordano, N. A.; Solovyov, A.; Hwang, S.-J.; Katz, A. Effect of Coordination Environment in Grafted Single-Site Ti-SiO_2 Olefin Epoxidation Catalysis, *59* (13), 1110–1122, copyright **2016**.

The effect of calix[4]arene ligand symmetry, as dictated by lower-rim substitution pattern, on its coordination to a Ti^{IV} cation is assessed in solution and when grafted on silica (SiO_2), and its effect on epoxidation catalysis by calix[4]arene-Ti^{IV} grafted on SiO_2 is investigated. C_{2v} symmetric *tert*-butylcalix[4]arene-Ti complexes that are 1,3-alkyl disubstituted at the lower rim (**di-R-Ti**) are compared to previously reported C_s symmetric complexes, which are singly substituted at the lower rim (**mono-R-Ti**). ^{13}C MAS NMR spectra of complexes isotopically enriched at the lower-rim alkyl position indicate that **di-R-Ti** predominantly grafts onto silica as the conformation found in solution, exhibiting a deshielded alkyl resonance compared to the grafted **mono-R-Ti** complexes, which is consistent with stronger (alkyl ether)→Ti dative interactions in the former. Moreover, ^{13}C MAS NMR spectroscopy detects an additional contribution from an "endo" conformer for grafted **di-R-Ti**, which is not observed in solution. Based on prior molecular modeling studies and on ^{13}C MAS NMR spectroscopy chemical shifts, this "endo" conformer is proposed to have similar (alkyl ether)→Ti distances at the lower-rim and electron density at the Ti center relative to grafted **mono-R-Ti** complexes. Different ligand-to-metal charge transfer edge-energies, calculated from diffuse-reflectance UV-visible spectra, are observed between grafted **mono-R-Ti** and **di-R-Ti** complexes, with respective values o 2.24 ± 0.02 eV and 2.16 ± 0.02 eV. Despite these differences, rates of *tert*-butyl hydroperoxide consumption during the epoxidation of 1-octene are found to be largely insensitive to ligand symmetry, with average rate constants of ~1.5 $M^{-2}s^{-1}$ and initial TOF of ~4 ks^{-1} at 50 °C for grafted **mono-R-Ti** and **di-R-Ti**. Grafted **di-C_1-Ti** complexes are nonetheless more selective than **mono-C_1-Ti** complexes (45% vs 34 % respectively at a 50% conversion at 65-80 °C), illustrating the importance of the Ti^{IV} coordination environment on epoxidation catalysis.

4.1. Introduction

Heterogeneous catalysts often present non-uniform active surfaces which are difficult to characterize at the molecular level. The understanding of structure-function relationships in heterogeneous catalysts continues to be a challenging and rewarding pursuit, since these relationships enable catalyst optimization in a way that is rooted in rational molecular-level understanding, at the state of the art of the field. This understanding benefits from being able to precisely control the synthesis of uniform catalytic active sites, such that specific molecular features can be correlated to catalytic performance,[1] and in a way that leverages on characterization of soluble catalyst precursors in solution.[2–4]

Ti^{IV} on silica is a well-known active and selective Lewis acid catalyst for olefin epoxidation, particularly when found as isolated, tetrahedrally coordinated active sites embedded or grafted on a heterogeneous support.[5–7] Indeed, titanosilicates represent a class of materials broadly used in epoxidation but only understood at the atomic level in a limited way.[3,8–13] For example, while there is agreement that six-coordinate, coordinatively saturated Ti^{IV} sites, as found in bulk TiO_2, are inactive, it remains unobvious whether the ideal site for catalysis is an isolated Ti^{IV} or slightly oligomeric species with Ti-O-Ti connectivity.[14]

Our research group has pioneered the use of grafted metallocalixarene complexes as a strategy to synthesize isolated Ti^{IV} active sites with controllable molecular environments,[15] which maintain site isolation and provide a precise model system to study heterogeneous catalysts.[16–19] Using titanocalixarene model systems, we correlated 3d-orbital occupancy at grafted Ti^{IV} centers on SiO_2 to Lewis acidity and catalytic activity for olefin epoxidation using an organic hydroperoxide as the oxidant.[17] This was a demonstration that the connectivity and coordination of a Ti^{IV} center, as enforced by an organic ligand, could be synthetically tailored to control the molecular environment of a working catalyst active site on a surface.

The strong difference between the two titanocalixarene complexes used in this prior study,[17] however, led us to look for opportunities to alter Ti^{IV} coordination in subtler ways; therefore, we continue our studies here, with calixarene ligands where only differences in dative interactions to Ti^{IV} are possible. Based on studies of vanadocalixarenes, we hypothesized that the lower-rim symmetry of p-*t*-butylcalix[4]arene complexes should influence dative interactions and 3d occupancy at the Ti^{IV} center, and thus could have a measurable impact on catalytic activity.[20] In particular, we hypothesized that C_{2v} symmetric calixarene ligands (**di-R** in Scheme 4.1) should impart a higher 3d-orbital electron density on the Ti^{IV} center than C_s symmetric ligands (**mono-R** in Scheme 4.1), based on the shorter alkoxy ether oxygen – titanium dative distances in **di-R** relative to **mono-R** complexes. We thus predicted depressed epoxidation rates for Ti^{IV} complexes of the **di-R** ligand.

In this work, we tested this hypothesis by synthesizing four titanocalixarene complexes, consisting of two different symmetries controlled by different lower-rim substituents, which we immobilized onto dehydroxylated silica supports. These catalysts were tested for the epoxidation of 1-octene using *tert*-butyl hydroperoxide (TBHP), an oxidant widely used in the industrial epoxidation of olefins.[21] Catalytic activity and selectivity were used to investigate the influence of coordination environment on catalysis. The main difference between the synthesized titanocalixarenes was dictated by ligand coordination of **mono-R** versus **di-R** ligands (see Scheme 4.1, where R=alkyl chain). **Mono-C_1-Ti** has been previously synthesized,

characterized,[22] grafted, and studied for alkene epoxidation;[15–17] it is stable when grafted, has C_s symmetry, displays one weak methoxy oxygen-Ti dative interaction, and is an active epoxidation catalyst. The **di-C_1-Ti** complex has been synthesized,[23,24] but to our knowledge it has never been grafted on a surface or tested in olefin epoxidation. It is stable at room temperature, has C_{2v} symmetry, and displays two stronger methoxy oxygen-Ti interactions as a result of shorter RO-Ti distances. Analogous **mono-C_5** and **di-C_5**, with pentoxy replacing methoxy alkyl ether substituents were also synthesized to investigate lower-rim substituent effects. These four ligands were used to synthesize metallocalixarenes complexes, which were grafted onto SiO_2 resulting in active epoxidation catalysts with varying inner-sphere coordination environments. In addition, outer-sphere effects were studied by varying the hydroxyl density of the SiO_2 support surface by pre-treating SiO_2 at different temperatures.

We first describe the synthesis of grafted titanocalixarene materials and confirm the intact grafting of complexes onto SiO_2 by a combination of elemental analysis and solid-state ^{13}C NMR spectroscopy. Using calixarene ligands isotopically enriched at the methoxy position (O-R positions in Scheme 4.1) and ^{13}C MAS NMR spectroscopy, we demonstrate that **di-C_1-Ti** grafts in two different conformations, consistent with previously published molecular modeling results of solution-phase conformations of Ti-calixarene complexes.[24] Diffuse reflectance UV-visible spectroscopy is used as a probe for measuring ligand-to-metal-charge-transfer (LMCT) edge energies in complexes with different symmetries. We then use these materials to investigate the postulated hypothesis on the influence that dative interactions to Ti^{IV} have on catalytic performance in olefin epoxidation, when using TBHP as oxidant.

Scheme 4.1. Synthesis of Grafted Calixarene-Ti Materials.

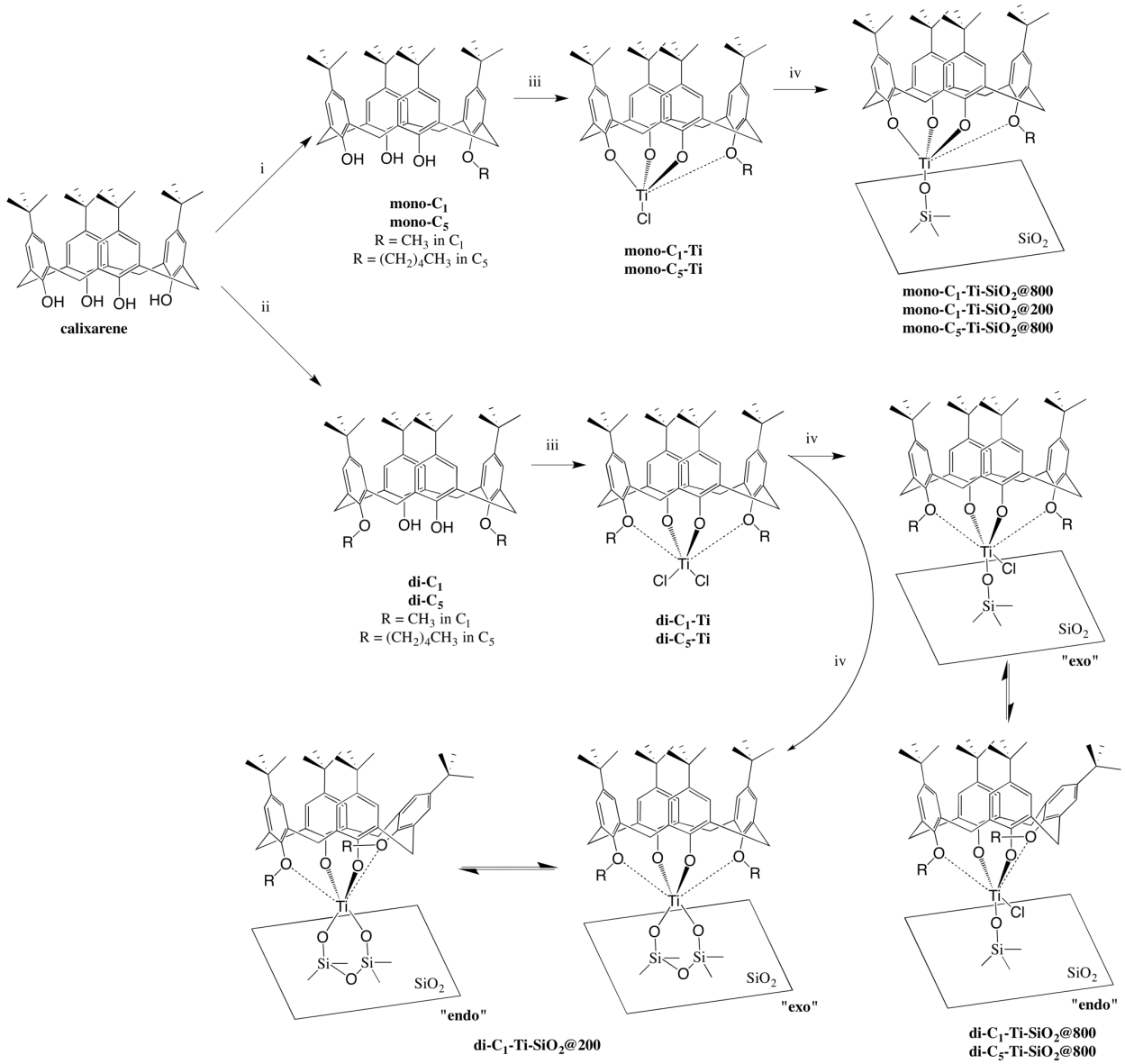

(i) 1.1 equiv CsF, 2 equiv of iodomethane or 1-bromopentane, DMF, 60 °C, 18 h; (ii) 3 equiv K_2CO_3, 3 equiv iodomethane or 1-brompentane, DMF, 60 °C, 48 h; (iii) 0.9 equiv $TiCl_4$, anhydrous toluene, 40 °C, 1.5 h; (iv) SiO_2 surface, toluene, ambient temperature, 24 h. O-Ti dative interactions are shown in with dashed lines. **di-C_1-Ti-SiO_2@800**, **di-C_5-Ti-SiO_2@800**, **di-C_1-Ti-SiO_2@200 are** hypothesized structures. Reversible arrows indicate the two proposed conformations for the complex on the surface.

4.2. Experimental

4.2.1. General Experimental

tert-Butylcalix[4]arene was purchased from Aldrich. Chemical reagents were purchased at reagent grade quality and were used without further purification unless otherwise noted. Toluene was freshly distilled over sodium / benzophenone. Benzene-d6 was distilled over sodium and stored over pretreated molecular sieves. DMF was used as received. Reactions were monitored with TLC on Selecto 60 plates. Silica gel chromatography purification of calixarene ligands was performed using Selecto 60 silica gel (0.32-0.64 mm particle size). Synthesis of titanocalixarenes was performed under Ar using Schlenk techniques. $TiCl_4$ was used as 1.0 M solution in toluene (Aldrich).

4.2.2. General Analytical

Carbon-hydrogen-nitrogen analysis was performed at UC Berkeley Microanalytical facility using a Perkin Elmer 2400 Series II combustion analyzer, and grafted calixarene loadings were estimated by assuming that carbon contents were entirely due to the presence of calixarenes **mono-C_1**, **mono-C_5**, **di-C_1**, and **di-C_5**. Ti contents were measured by ICP-AES at Galbraith Laboratories. Cl contents were measured by Suppressed Ion Chromatography at Galbraith Laboratories.

Support surface areas were determined by the BET method from N_2 physisorption measurements performed with a Micromeritics ASAP 2020 instrument at 77 K after sample evacuation at 623 K for 4h.

Diffuse reflectance UV-visible (DR UV-vis) spectra were measured at ambient conditions using a Varian Cary 4000 Specrophotometer fitted with a Praying Mantis attachment from Harrick Scientific Instruments. Compacted poly-(tetrafluroethylene) powder was used as a perfect reflector standard for baseline corrections, and all spectra are reported using Kublka-Munk pseudo-absorbance. Ligand-to-metal charge-transer (LMCT) edge energies of the materials were calculated following methods previously used for titanocalixarenes.[16] Slopes of tangent lines as shown in Figure 4.3 were calculated from the first derivative of the transformed spectra, and were drawn tangent to the spectra at their point of inflection.

Solid-state ^{13}C magic-angle spinning (MAS) NMR signals were collected using a Bruker DSX-500 spectrometer and a Bruker 4 mm MAS probe at the Caltech Solid-State NMR Facility. Solution NMR spectra were measured using a Bruker AM-400 spectrometer at the UC-Berkeley NMR Facility. ES mass spectra were recorded at the UC Berkeley Mass Spectrometry Facility.

4.2.3. Calixarene Ligand, Titanocalixarene, and Grafted Material Synthesis

The synthesis of ligands, titanocalixarene complexes, and grafted materials are summarized in Scheme 4.1.

4.2.3.1. Calixarene Ligands

Regioselective functionalization of calixarenes is well known.[25] Using a weak base in alkylation of calixarenes affords distal-1,3-dialkylated product with good yield.[26] By reaction of *tert*-butylcalixarene with 3 equivalents of potassium carbonate and excess haloalkane, we synthesized distal dialkylated calixarene with good yield. For the selective synthesis of monoalkyl-calixarene, a protection-deprotection strategy,[27] using a weaker base like cesium fluoride,[28] or lower loadings of potassium carbonate and reaction condition variation have been reported.[29] In our study, we used a direct monoalkylation method based on reaction of *tert*-butylcalixarene with 1.1 equavelent of cesium fluoride with moderate yields.

4.2.3.1.1. General Procedure for Synthesis of mono-C_1, mono-C_5

To a mixture of *tert*-butylcalix[4]arene (2.88 mmol) and CsF (3.17 mmol) in 30 ml of dry DMF, methyl iodide or 1-bromopentane (5.76 mmol) was added at 40 °C. The resulting mixture was heated at 50 °C for 18 h. The solvent was evaporated and the residue was re-dissolved in chloroform. This solution was washed with water, and the organic layer was dried over sodium sulfate and evaporated to dryness. The white product was purified using column chromatography.

5,11,17,23-Tetra-*tert*-butyl- 25-(^{13}C-methoxy)-26,27,28-trihydroxy-calix[4]arene (**mono-C_1**): After purification via column chromatography (eluent DCM/n-hexane 1:1 v/v, R_f 0.9), a white powder was obtained in 43 % yield; ^{1}H NMR ($CDCl_3$): δ 10.20 (s, 1H, O*H*), 9.60 (s, 2H, O*H*), 7.13 (m, 2H, Ar*H*), 7.09 (d, 2H, ^4J = 2.0 Hz, Ar*H*), 7.08 (s, 2H, Ar*H*), 7.02 (d, 2H, ^4J = 2.0 Hz, Ar*H*), 4.39 (d, 2H, ^2J = 12.5 Hz, ArCH_2Ar), 4.30 (d, 2H, ^2J = 12.5 Hz, ArCH_2Ar), 4.16 (d, 3H, ^1J = 144.9 Hz, ^{13}CH_3), 3.47 (d, 4H, ^2J = 14.0 Hz, ArCH_2Ar), 1.26 (s, 9H, t-C$_4H_9$), 1.24 (s, 18H, t-C$_4H_9$), 1.23 (s, 9H, t-C$_4H_9$); ^{13}C NMR($CDCl_3$): δ 148.32, 147.83, 143.61, 143.22, 133.43, 128.20, 127.90, 126.51, 125.80, 125.73, 125.69, 63.28, 34.28, 34.03, 33.96, 33.02, 32.12, 31.51, 31.28; HR ESI MS calcd for $^{12}C_{44}{}^{13}C_1H_{57}O_4$ 662.4296, found 662.4280.

5,11,17,23-Tetra-*tert*-butyl-25-(1-pentyloxy)-26,27,28-trihydroxy-calix[4]arene (**mono-C_5**): After purification via column chromatography (eluent DCM/n-hexane 1:1 v/v, R_f 1.0), a white powder was obtained in 49 % yield; ^{1}H NMR ($CDCl_3$): δ 10.29 (s, 1H, O*H*), 9.69 (s, 2H, O*H*), 7.17 (s, 2H, Ar*H*), 7.14 (d, 2H, ^4J = 2.4 Hz, Ar*H*), 7.13 (s, 2H, Ar*H*), 7.06 (d, 2H, ^4J = 2.4 Hz, Ar*H*), 4.44 (d, 2H, ^2J = 12.8 Hz, ArCH_2Ar), 4.36 (d, 2H, ^2J = 13.6 Hz, ArCH_2Ar), 4.21 (t, 2H, ^3J = 7.2 Hz, OCH_2), 3.52 (d, ^2J = 13.6 Hz, ArCH_2Ar), 3.50 (d, ^2J = 12.8 Hz, ArCH_2Ar), 2.24 (m, 2H, CH_2), 1.69 (m, 2H, CH_2), 1.60 (m, 2H, CH_2), 1.30 (s, 9H, t-C$_4H_9$), 1.29 (s, 18H, t-C$_4H_9$), 1.27 (s, 9H, t-C$_4H_9$), 1.08 (t, 3H, ^3J = 7.2 Hz, CH_3); ^{13}C NMR($CDCl_3$): δ 149.47, 148.54, 148.07, 147.87, 143.63, 143.12, 133.58, 128.40, 128.22, 127.73, 126.44, 125.99, 125.78, 125.75, 125.69, 76.76, 34.28, 34.06, 33.97, 33.08, 32.31, 31.56, 31.54, 31.47, 31.32, 29.53, 28.05, 22.59, 14.15; HR ESI MS calcd for $^{12}C_{49}H_{65}O_4$ 717.4888, found 717.4872.

4.2.3.1.2. General Procedure for Synthesis of di-C_1, di-C_5

To a mixture of tert-butylcalix[4]arene (1.54 mmol) and potassium carbonate (4.60 mmol) in 25 ml of dry DMF, methyl iodide or 1-bromopentane (4.60 mmol) was added at 40 °C. The resulting mixture was heated at 50 °C for 48 h. The solvent was evaporated and the residue was

re-dissolved in chloroform. This solution was washed with water, and the organic layer was dried over sodium sulfate and evaporated to dryness. The white product was purified using column chromatography.

5,11,17,23-Tetra-*tert*-butyl- 25, 27(di-^{13}C-methoxy)-26, 28-dihydroxy-calix[4]arene (**di-C_1**): After purification via column chromatography (eluent DCM/n-hexane 1:1.5 v/v, R_f 0.7), a white powder was obtained in 39 % yield; ^{1}H NMR ($CDCl_3$): δ 7.29 (s, 2H, O*H*), 7.10 (s, 4H, Ar*H*), 6.80 (s, 4H, Ar*H*), 4.31 (d, 4H, ^2J = 13.0 Hz, ArC*H*$_2$Ar), 3.98 (d, 6H, ^1J = 144.4 Hz, ^{13}C*H*$_3$), 3.36 (d, 4H, ^2J = 13.0 Hz, ArC*H*$_2$Ar), 1.33 (s, 18H, t-C$_4$*H*$_9$), 0.97 (s, 18H, t-C$_4$*H*$_9$); ^{13}C NMR($CDCl_3$): δ 151.19, 150.51, 146.86, 141.53, 132.32, 127.90, 125.56, 125.09, 63.52, 60.88, 33.94, 33.88, 31.75, 31.42, 31.04; HR ESI MS calcd for $^{12}C_{44}{}^{13}C_2H_{60}O_4Na_1$ 701.4451, found 701.4444.

5,11,17,23-Tetra-*tert*-butyl- 25, 27-dipentyloxy-26, 28-dihydroxy-calix[4]arene (**di-C_5**): After purification via column chromatography (eluent DCM/n-hexane 1:1.5 v/v, R_f 0.8), a white powder was obtained in 56 % yield; ^{1}H NMR ($CDCl_3$): δ 7.89 (s, 2H, O*H*), 7.12 (s, 4H, Ar*H*), 6.92 (s, 4H, Ar*H*), 4.39 (d, 4H, ^2J = 12.8 Hz, ArC*H*$_2$Ar), 4.05 (t, 4H, ^3J = 6.8 Hz, OC*H*$_2$), 3.39 (d, 4H, ^2J = 12.8 Hz, ArC*H*$_2$Ar), 2.11 (m, 4H, C*H*$_2$), 1.74 (m, 4H, C*H*$_2$), 1.56 (m, 4H, C*H*$_2$), 1.36 (s, 18H, t-C$_4$*H*$_9$), 1.08 (s, 18H, t-C$_4$*H*$_9$), 1.07 (t, 6H, ^3J = 7.2 Hz, C*H*$_3$); ^{13}C NMR($CDCl_3$): δ 150.93, 150.13, 146.68, 141.25, 132.90, 127.87, 125.50, 125.09, 76.60, 34.02, 33.86, 31.91, 31.78, 31.15, 29.79, 28.25, 22.63, 14.21; HR ESI MS calcd for $^{12}C_{54}H_{76}O_4Na_1$ 811.5636, found 811.5633.

4.2.3.2. General Procedure for Synthesis calix[4]arne-Ti Complexes

Complexes **mono-C_1-Ti**, **mono-C_5-Ti**, **di-C_1-Ti**, and **di-C_5-Ti** were synthesized by adding to 0.9 equiv of $TiCl_4$ (1.0 M solution in toluene, Aldrich) to a 0.04 M solution of the corresponding calixarene ligand in toluene and stirring at 40 °C for 1.5 h. $TiCl_4$ was used as a limiting reagent to prevent formation of polymeric TiO_x species.

di-C_1-Ti: After evaporation of solvent and dissolution in C_6D_6, ^{1}H NMR (C_6D_6) δ 7.17 (s, 4 H, Ar*H*), 6.82 (s, 4 H, Ar*H*), 4.60 (d, 4 H, $^2J_{HH}$ = 13.4 Hz, C*H*$_2$), 4.19 (d, 6 H, OC*H*$_3$, $^1J_{C,H}$ = 146 Hz), 3.19 (d, 4 H, $^2J_{HH}$ = 13.6 Hz, C*H*$_2$), 1.38 (s, 18 H, C(C*H*$_3$)$_3$), 0.68 (s, 18 H, C(C*H*$_3$)$_3$), ^{13}C NMR (C_6D_6) δ 70.9 (O*C*H$_3$) observed due to ^{13}C enrichment at OCH_3 position. In agreement with literature.[24]

di-C_5-Ti: After evaporation of solvent and dissolution in C_6D_6, ^{1}H NMR (C_6D_6) δ 7.12 (s, 4 H, Ar*H*), 6.89 (s, 4 H, Ar*H*), 4.60 (d, 4 H, $^2J_{HH}$ = 13.4 Hz, C*H*$_2$), 5.04 (tt, 4 H, OC*H*$_2$-), 4.87 (d, 4H, C*H*$_2$, $^2J_{HH}$ = 13.2 Hz), 3.24 (d, 4 H, $^2J_{HH}$ = 13.6 Hz, C*H*$_2$), 2.03 (tt , 4 H, C*H*$_2$ alkyl), 1.42 (s, 18 H, C(C*H*$_3$)$_3$), 1.01 (tt , 4 H, C*H*$_2$ alkyl), 0.70 (m, 28 H, C(C*H*$_3$)$_3$ and C*H*$_2$C*H*$_3$ alkyl).

mono-C_1-Ti: After evaporation of solvent and dissolution in C_6D_6, ^{1}H NMR (C_6D_6): *δ* 7.14 (s, 4 H, Ar*H*), 6.82 (s, 2 H, Ar*H*), 6.78 (s, 2 H, Ar*H*), 4.97 (d, $^2J_{H,H}$ = 12.8 Hz, 2 H, C*H*$_2$), 4.31 (d, $^2J_{H,H}$ = 12.8 Hz, 2 H, C*H*$_2$), 3.84 (d, 3 H, OC*H*$_3$, $^1J_{C,H}$ = 146 Hz), 3.22 (d, $^2J_{H,H}$ = 12.8 Hz, 2 H, C*H*$_2$), 3.13 (d, $^2J_{H,H}$ = 12.8 Hz, 2 H, C*H*$_2$), 1.37 [s, 18 H, C(C*H*$_3$)$_3$], 0.77 [s, 9 H, C(C*H*$_3$)$_3$], 0.68 [s, 9 H, C(C*H*$_3$)$_3$] ppm. ^{13}C NMR (C_6D_6): *δ* 65.4 (O*C*H$_3$) observed due to ^{13}C enrichment at OCH_3 position. In agreement with literature.[22]

mono-C_5-Ti: After evaporation of solvent and dissolution in C_6D_6, ^{1}H NMR (C_6D_6) δ aromatics overlap with residual toluene solvent, 5.03 (d, 2 H, $^2J_{HH}$ = 12.8 Hz, CH_2), 4.58 (d, 2 H, $^2J_{HH}$ = 12.4 Hz, CH_2), 4.48 (t, 2H, $^2J_{HH}$ = 6.4 Hz, OCH_2-alkyl), 3.33 (d, 2H, $^2J_{HH}$ =13.2 Hz, CH_2), 3.29 (d, 2H, $^2J_{HH}$ =12.6 Hz, CH_2), 1.94 (tt , 2 H, CH_2 alkyl), 1.48 (s, 18 H, C(CH_3)$_3$), 0.91 (m , 2 H, CH_2 alkyl), 0.82 (m, 23 H, C(CH_3)$_3$ and CH_2CH_3 alkyl).

4.2.3.3. General procedure for grafting of calix-4]arene-Ti complexes onto SiO_2

Selecto Scientific Silica Gel SiO_2 (32-63 particle size) was treated under dry air and Ar for 4 h at 200 °C and 800 °C to prepare SiO_2@200 and SiO_2@800 supports, respectively, and transferred to an Ar glovebox under air-free conditions. 1 g of SiO_2 support was degassed under vacuum at 200 °C for 2 h, cooled, and suspended in 10 mL of toluene. To this, 4 mL of the dissolved titanocalixarene complex was added, and stirred at room temperature for 18 h. The solids were decanted, the supernatant removed, and the solids washed with 5x40 mL of anhydrous toluene by subsequent decantation and supernatant removals, until the supernatant was colorless indicating all excess complex had been removed. The materials were dried under dynamic vacuum at 120 °C for 1 h and stored in an Ar glovebox.

4.2.4. Catalysis

1-octene epoxidation rates and selectivity were measured by combining, in a 25 mL Schlenk flask, ~30 mg of catalyst (weighed under Ar) and ~300 mg of 4A molecular sieves (previously dehydrated at 573K for 6 h) and treating the contents under dynamic vacuum at 393 K for 1h. To this, 20 mL of a 0.18 M solution of 1-octene (distilled from CaH_2) in octane (distilled from Sodium / benzophenone) were added, and the contents equilibrated under stirring to 323 K for 0.5 h. The reaction was started by addition of 0.125 mL of a 6.5 M solution of *tert*-butyl-hydroperoxide (TBHP) in nonane (Aldrich, concentration measured by iodometric titration)[30], and aliquots were removed every 1 h and analyzed by gas chromatography using an Agilent 6890A gas chromatograph. As discussed elsewhere,[15] epoxidation rates are proportional to catalyst, alkene, and oxidant concentrations:

$$\text{rate} = \frac{d[\text{TBHP}]}{dt} = k[\text{Ti}][\text{alkene}][\text{TBHP}] \qquad (4.1)$$

where quantities in square brackets [] represent concentration in the reactor in mol L^{-1}. Selectivity was calculated based on the limiting reagent, TBHP, and is a measure of the efficiency with which oxidant consumption produces the desired epoxide product. It was calculated as the ratio of epoxide yield to TBHP conversion, with yield given by the ratio of epoxide produced to TBHP initially present, and conversion given by the ratio of TBHP consumed to TBHP initially present. TBHP and epoxide present in the reaction mixture were quantified by comparing gas chromatograph peak areas in aliquots of the reaction mixture to peak areas of external references prepared with known concentration of TBHP and epoxide within the range observed in the reaction mixture. Initial turnover frequencies (TOF_0) were calculated by extrapolating the TOF measured at each data point to initial time using a second order polynomial fit. TOF at each time point were calculated as the ratio of epoxide produced per Ti^{IV} site per time.

4.3. Results and Discussion

4.3.1. Physicochemical Characterization of Titanocalixarene Grafting on SiO_2

Three distinct synthetic handles control the Ti^{IV} coordination environment of materials in Scheme 4.1: (i) the choice of calixarene ligand, which controls the surface complex symmetry and the oxygen–titanium dative interactions (see Scheme 4.1); (ii) the choice of alkyl ether (methoxy C_1 or pentoxy C_5) substituent on the lower-rim phenolic oxygen; and (iii) the choice of SiO_2 support pre-treatment temperature, which controls hydroxyl group surface density (low in **SiO_2@800**, high in **SiO_2@200**).

The coordination environment and corresponding physicochemical characterization for each grafted titanocalixarene material is summarized in Table 4.1. All materials show successful grafting of the intact titanocalixarene complex onto the support, as indicated by a nearly ~1:1 calixarene to titanium ratio. Observed deviations from this 1:1 ratio are attributed to experimental uncertainty in elemental analysis due to the lower site loading compared to previous work.[15,31]

Grafting resulted in submonolayer surface coverages of the titanocalixarene complex,[15] which we attribute to grafting being performed at mild, room temperature conditions here as opposed to reflux conditions of prior work, as well as the higher degree of silica-support dehydroxylation for the SiO_2@800 used here.[15,16] This implies that only the most reactive surface hydroxyl groups successfully form covalent attachment to the titanocalixarene at milder conditions, which were chosen to be gentle so as to avoid conversion of **di-C_1-Ti** and **di-C_5-Ti** to **mono-C_1-Ti** and **mono-C_5-Ti** through lower-rim alkyl ether bond cleavage, which occurs in solution at higher temperatures.[17] The **SiO_2@200** support, which consist of a near-maximum surface hydroxyl group coverage (expected to be ~5 OH/nm^2), accommodates a higher grafted site density when compared to **SiO_2@800**, with only about 15% of the maximum hydroxyl group surface coverage (expected to be ~0.7 OH/nm^2).[32] The higher abundance of potential hydroxyl grafting sites, and the higher surface acidity due to weak silanol acid sites on **SiO_2@200** facilitates Ti-Cl bond cleavage to form the Ti-O-Si connectivity in grafted species.

Grafted **mono-C_1-Ti-SiO_2** sites consist of pseudo-tetrahedral Ti^{IV} with three bonds to calix[4]arene and one bond to the silica surface (Scheme 4.1),[15] and should contain no Cl from synthesis. However, despite our best efforts to remove HCl byproduct by washing and drying during synthesis, some Cl remains, as evidenced by measurable Cl content shown in Table 4.1 for **mono-C_1-Ti-SiO_2@800**. This is presumably the result of Si-Cl bond formation and/or physisorbed HCl. We note that a maximum 4 Cl:Ti ratio would be possible from $TiCl_4$ if no HCl were removed during washing of the grafted material. Notwithstanding this background Cl content, which introduces some experimental uncertainty to the analysis below, we attempt to use Cl elemental analysis as data that informs as to the number of silica attachment points for the **di-R-Ti** complexes.

Table 4.1. Physicochemical and Spectroscopic Data for Grafted Materials

Material[a]	Coordination environment			Site density (nm^{-2})[b]		Calix:Ti ratio	Cl^{e}:Ti ratio	LMCT edge-energy (eV)
	oxygen dative interaction	support	O-R substituent	Calix[c]	Ti[d]			
di-C_1-Ti-SiO_2@800	di	SiO_2@800	O-CH_3	0.067	0.073	0.91	3.2	2.16[f]
mono-C_1-Ti-SiO_2@800	mono	SiO_2@800	O-CH_3	0.068	0.079	0.86	1.3	2.26[f]
di-C_1-Ti-SiO_2@200	di	SiO_2@200	O-CH_3	0.113	0.098	1.15	2.0	2.18
mono-C_1-Ti-SiO_2@200	mono	SiO_2@200	O-CH_3	0.098	0.092	1.07	-	2.23
di-C_5-Ti-SiO_2@800	di	SiO_2@800	O-$(CH_2)_4CH_3$	0.059	0.079	0.75	-	2.14
mono-C_5-Ti-SiO_2@800	mono	SiO_2@800	O-$(CH_2)_4CH_3$	0.083	0.098	0.85	-	2.24

[a] Labeled as on Scheme 4.1.
[b] Based on a measured BET surface area of 402 m^2/g.
[c] Based on combustion analysis.
[d] Based on ICP-AES.
[e] Cl content based on suppressed ion chromatography. Handled under air-free conditions to prevent Ti-Cl hydrolysis.
[f] Measured at ± 0.01eV

di-R-Ti complexes will lose a Cl ligand upon grafting but have yet a second labile Cl ligand coordinated to the Ti^{IV} center. When grafting on a highly hydroxylated surface, we observe the Cl:Ti ratio of **di-C_1-Ti-SiO_2@200** (2.0) to be similar to that of **mono-C_1-Ti-SiO_2@800** (1.3) (the slightly higher Cl content on **SiO_2@200** is attributable to the higher HCl adsorption capacity of the more polar hydroxyl-rich silica surface). The similarity of Cl:Ti ratio between **di-C_1-Ti-SiO_2@200** (2.0) and **mono-C_1-Ti-SiO_2@800** (1.3) is consistent with bipodal attachment of **di-C_1-Ti** to adjacent silanols, as shown in Scheme 4.1, in agreement with previous demonstrations of bipodal grafting of Ti precursors with labile ligands onto SiO_2 at full surface hydroxyl coverages.[14] In contrast, the Cl:Ti ratio for the case of **di-C_1-Ti-SiO_2@800** (3.2) increases by ~1 Cl when compared to **di-C_1-Ti-SiO_2@200** (2.0). This is consistent with monopodal bonding of **di-C_1-Ti** to the **SiO_2@800** surface and retention of a Ti-Cl bond as hypothesized in Scheme 4.1 for di-**C_1-Ti-SiO_2@800**. Under catalytic conditions, this Ti-Cl bond would presumably be converted to –OR (R = oxidant fragment O-*t*-butyl or R = alcohol fragment *t*-butyl) ligand.

Further confirmation of intact grafting of **mono-C_1-Ti** and **di-C_1-Ti** complexes comes from solid-state ^{13}C MAS NMR spectroscopy. For this, we synthesized ^{13}C isotopically enriched versions of **mono-C_1** and **di-C_1** ligands, at the methoxy lower-rim substituent (denoted R in Scheme 4.1). Enrichment at this position is evidenced by ^1H solution-phase NMR spectroscopy, showing a doublet for O-CH_3 with very strong coupling (^1J = 144-145 Hz), due to direct coupling with the ^{13}C nucleus. In contrast, a singlet is observed at this position for a regular ^{12}C nucleus due to the absence of coupling.[22,24] As shown in Figure 4.1A, the ^{13}C MAS NMR spectrum of **mono-C_1-Ti-SiO_2@800** exhibits a single broad resonance centered about 64 ppm, which is near the 65 ppm resonance of the **mono-C_1-Ti** complex in solution. The principal ^{13}C MAS NMR resonance for **di-C_1-Ti-SiO_2@800** is centered about 69 ppm in Figure 4.1B, again at slightly higher field from the 71 ppm observed in solution for **di-C_1-Ti**. Upon integrating the total area under the methoxy resonance, a 1.9-fold higher integrated area per Ti is observed for **di-C_1-Ti-SiO_2@800** relative to **mono-C_1-Ti-SiO_2@800** (Figure A4.1, Table A4.1). This ratio being so nearly equal to 2.0 suggests that both methoxy substituents on the **di-C_1-Ti-SiO_2@800** precursor survive our gentle grafting conditions, and further support the structures shown in Scheme 4.1.

In solution-phase ^{13}C NMR spectroscopy (see section 4.2.3), a downfield shift of ~6 ppm in the principal methoxy resonance of **di-C_1-Ti** is observed when compared to **mono-C_1-Ti**, which we attribute to stronger methoxy coordination to the Ti^{IV} center in **di-C_1-Ti**. In addition, the ^1H chemical shift of **mono-C_1-Ti** O-CH_3 resonance is 3.84 ppm, in contrast to **di-C_1-Ti** O-CH_3 resonance at 4.18 ppm. The same result is independent of alkoxy substituent, as **mono-C_5-Ti** and **di-C_5-Ti** also exhibit this effect, with **di-C_5-Ti** O-CH_2- resonances at 5.05 ppm while **mono-C_5-Ti** O-CH_2- at 4.48 ppm. Such deshielded alkoxy ether resonances for the **di-R-Ti** complexes are indicative of stronger dative bonding and shorter Ti-OCH_3 bond distances in the **di-R-Ti** complex relative to **mono-R-Ti**, consistent with previously reported single-crystal X-ray diffraction data, in which Ti-OCH_3 bond distances were measured for **mono-C_1-Ti** and **di-C_1-Ti** at 2.4 Å[22] and 2.1 Å,[24] respectively. These distances suggest stronger dative methoxy coordination to the Ti^{IV} Lewis acid site in **di-C_1-Ti** compared to **mono-C_1-Ti** and support the observed downfield shift in the grafted sites described above. This effect of stronger coordination due to shorter RO-Ti distances was previously predicted based on simple geometric models using both data from electronic-structure calculations and single-crystal X-ray diffraction. It was further hypothesized that this stronger RO-Ti interaction would lead to higher 3d-orbital occupancy at the Ti^{IV} center,[20]

which in turn was predicted to lead to suppressed catalytic activity, based on previous studies correlating higher d-orbital occupancy to decreases activity for olefin epoxidation.[17]

It is important to note the information about titanocalixarene complex symmetry from ^{1}H solution-phase NMR spectroscopy of the precursor complexes (see section 4.2.3). Both **di-C_1-Ti** and **di-C_5-Ti** present only 2 distinct C*H*$_2$ methylene bridge resonances in the calix[4]arene, while **mono-C_1-Ti** and **mono-C_5-Ti** present four distinct resonances at this position, indicating the expected different symmetry of coordination (C_{2v} in **di-R-Ti**[24] vs C_s for **mono-R-Ti**).[22] Similarly, only one resonance is observed in ^{13}C solution-phase NMR at the –O*C*H$_3$ position because only one such carbon is present in **mono-C_1-Ti** and because of C_{2v} symmetry in **di-C_1-Ti**. These symmetry assignments further support the reasoning in the paragraph above. However, unlike the solution-phase ^{13}C NMR spectrum of **di-C_1-Ti**, the ^{13}C solid-state NMR spectrum for **di-C_1-Ti-SiO_2@800** and for **di-C_1-Ti-SiO2@200** exhibits a second upfield resonance centered around 63-65 ppm, as shown in Figures 1B and 1C. This second resonance indicates an additional chemical environment surrounding Ti^{IV} centers in **di-C_1-Ti-SiO_2**, which is not present in solution, and which may arise from the heterogeneity inherent in the silica surface. This heterogeneity presumably leads to the flexible calixarene ligand adopting a different conformation in the grafted form of the complex, different from that in solution.

Previous elegant studies by Radius have analyzed the different conformations that the **di-C_1-Ti** complex can adopt via molecular modeling.[24] While the most energetically favorable conformation corresponds to both methoxy substituents being "exo", the second lowest energy contributor involves a conformation in which one of the methoxy substituents is "endo", as represented in Scheme 4.1. This "endo" conformation results in Ti-OCH$_3$ distances of 2.4 Å - 2.5 Å (Figure A4.2, LiTCl2_"endo"), significantly longer than for the "exo" conformation (2.1 Å)[24] and similar to distances in mono-C_1-Ti (2.4 Å)[22]. The similarity of the measured bond distances between **mono-C_1-Ti** and those calculated for the "endo" conformation of the **di-C_1-Ti** suggests a similar chemical shift for methoxy resonances. This is consistent with the observed similarity of the chemical shifts for the shoulder resonance described above (63-65 ppm) and the methoxy resonance of **mono-C_1-Ti-SiO_2@800** (64 ppm), suggesting that the upfield resonance in grafted **di-C_1-Ti** may correspond to the "endo" conformer of **di-C_1-Ti-SiO_2**. While this conformation is energetically less favored according to calculations,[24] and is not detected in solution for **di-C_1-Ti**, it presumably becomes favorable in the grafted complexes due to the impinging proximity of the silica surface in a certain fraction of sites. Further evidence for the existence of the "endo" conformation is seen when comparing Figures 1B and 1C of the same complex, **di-C_1-Ti**, grafted on supports of different hydroxyl density, **SiO_2@800** and **SiO_2@200**, respectively. On **SiO_2@200**, the upfield "endo" resonance becomes more prominent (64% of integrated area on **di-C_1-Ti-SiO_2@200**, only 31% on **di-C_1-Ti-SiO_2@800**, Table A4.2) than the "exo" resonance, implying that **di-C_1-Ti** is grafts predominantly as the "endo" conformer. This is consistent with the conformational change from "exo" to "endo" being induced by the proximity of the SiO_2 surface, which is presumably closer for complexes grafted on **SiO_2@200** due to the bipodal attachment of **di-C_1-Ti**, as opposed to monopodal attachment on **SiO_2@800**, as outlined above (Scheme 4.1). We further expect that upon adsorption of the oxidant during catalysis, steric crowding may lead to more grafted sites being in the "endo" conformation.

Altogether, these results cumulatively suggest that the materials prepared display at least three molecularly distinct active sites with different Ti^{IV} coordination environments, as summarized in

Scheme 4.1: tripodal connectivity to the calixarene with monopodal attachment to the silica surface (all **mono-R** ligand materials), dipodal attachment to both the calixarene and the silica surface (di-**C_1-Ti-SiO_2@200**), and dipodal attachment to calixarene with monopodal attachment to the silica surface and a free (-Cl) coordination site (**di-R-Ti-SiO_2@800**), with both "endo" and "exo" conformers for the latter two.

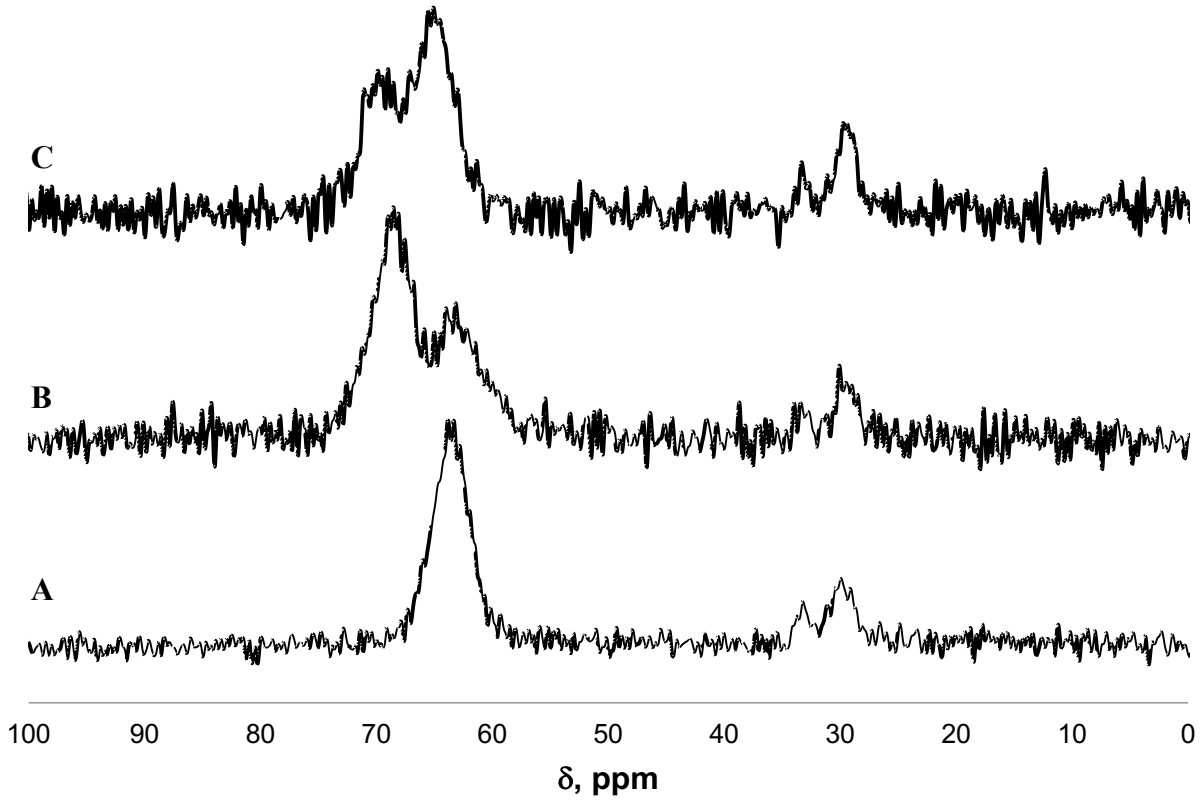

Figure 4.1. ^{13}C MAS solid-state NMR spectrum of **(A) mono-C_1-SiO_2@800**, **(B) di-C_1-SiO_2@800**, **(C) di-C_1-SiO_2@200**. The strongest resonances correspond to ^{13}C enriched methoxy lower-rim substituents. Resonances between 20-40 ppm arise due to upper-rim tert-butyl substituents, which are not isotopically enriched.

4.3.2. Spectroscopic Comparison of the Ti^{IV} Coordination Environment in Grafted Materials

Evidence of differing electronic environments in **di-R-Ti** compared to the **mono-R-Ti** grafted complexes comes from diffuse reflectance UV-vis spectra and calculated ligand-to-metal-charge-transfer (LMCT) edge energies. As shown in Figure 4.2, all materials display the absorption centered at 230 nm that is indicative isolated Ti^{IV} sites,[33] a 270-290 nm band arising from π-π^* aromatic transitions, and a broad absorption feature at 290-500 nm, previously assigned to Ti^{IV}-calixarene charge transfer (LMCT) transitions.[15] A higher intensity of this latter band in materials with **di-R** calixarene ligands is observed and is independent of the SiO_2 support used (traces b

and c in Figure 4.2). This is visually apparent due to a strong, opaque, red coloring of **di-R-Ti** complexes in solution compared to the more translucid, lighter red coloring of **mono-R-Ti** complexes, a visible difference which persists in the grafted materials.

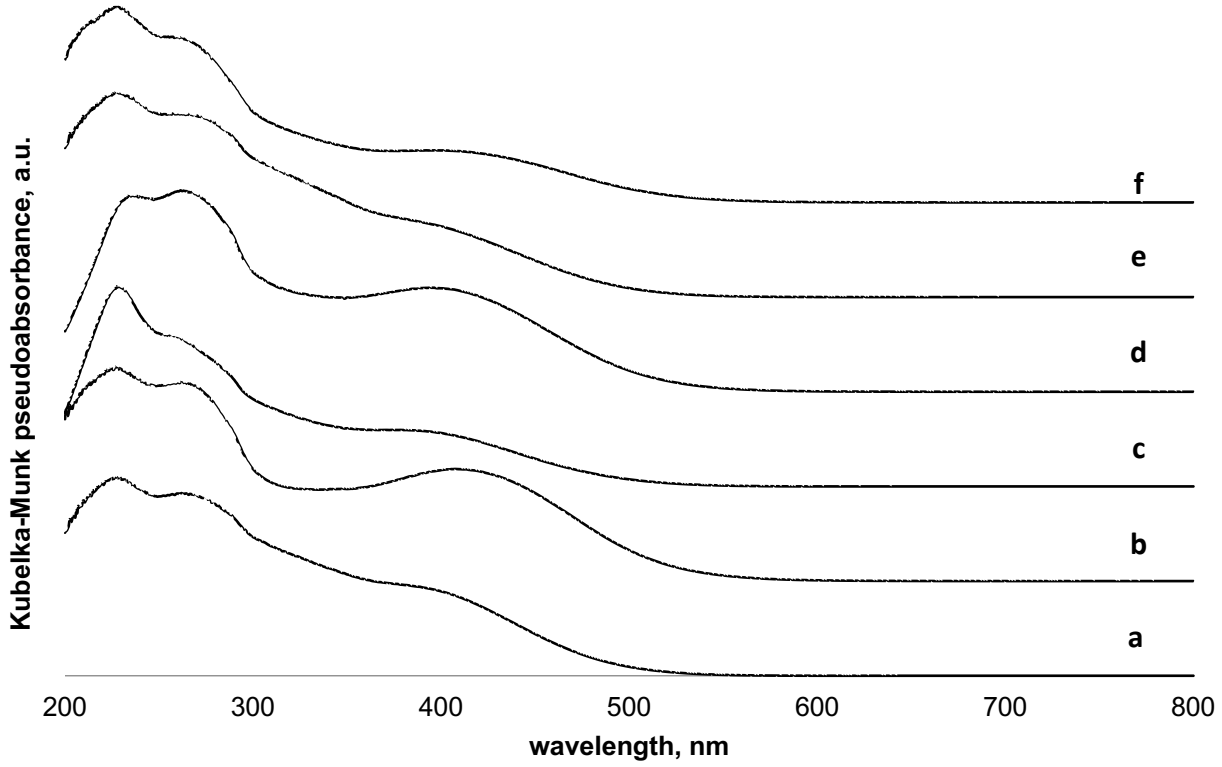

Figure 4.2. DR-UV spectra for all grafted materials. (a) **mono-C_1-SiO_2@800**, (b) **di-C_1-SiO_2@800**, (c) **mono-C_1-SiO_2@200**, (d) **di-C_1-SiO_2@200**, (e) **mono-C_5-SiO_2@800**, (f) **di-C_1-SiO_2@800**.

All **mono-R-Ti-SiO_2** complexes have LMCT edge energies at 2.24 ± 0.02 eV, in agreement with previous work.[16] No influence of lower-rim alkyl-ether substituent is observed, as indicated by similar LMCT energies for **mono-C_1-Ti-SiO_2@800** and **mono-C_5-Ti-SiO_2@800**, as well as **di-C_1-Ti-SiO_2@800** and **di-C_5-Ti-SiO_2@800**. However, a decrease in LMCT energy to 2.16 ± 0.02 eV for **di-R-Ti@SiO_2** materials is observed, as illustrated by differing intercepts for selected materials in Figure 4.3. Previous studies have demonstrated that LMCT energies are insensitive to a large number of substituents on the calixarene upper rim[16,34] and even strong oxygen coordination to the Ti^{IV} center.[17] This leads us to conclude that the different coordination geometry surrounding the Ti^{IV} center is responsible for the variation in LMCT energy. Extended Hückel calculations of the two geometries have shown that geometry does affect the energetics of frontier orbitals responsible for LMCT transitions[35] and lowers Ti LUMO by ~0.1 eV in **di-C_1-Ti** when compared to **mono-C_1-Ti**,[23] consistent with the measured differences in LMCT edge energies in these materials.

These results provide a well-defined molecular system to test the structure of ligand coordination to Ti^{IV}. In particular, the LMCT edge energies provide a useful fingerprint that differentiates **mono-R-Ti** and **di-R-Ti** grafted surface complexes, which is important in understanding Ti^{IV} coordination in calix[4]arene-Ti complexes in the remainder of this thesis.

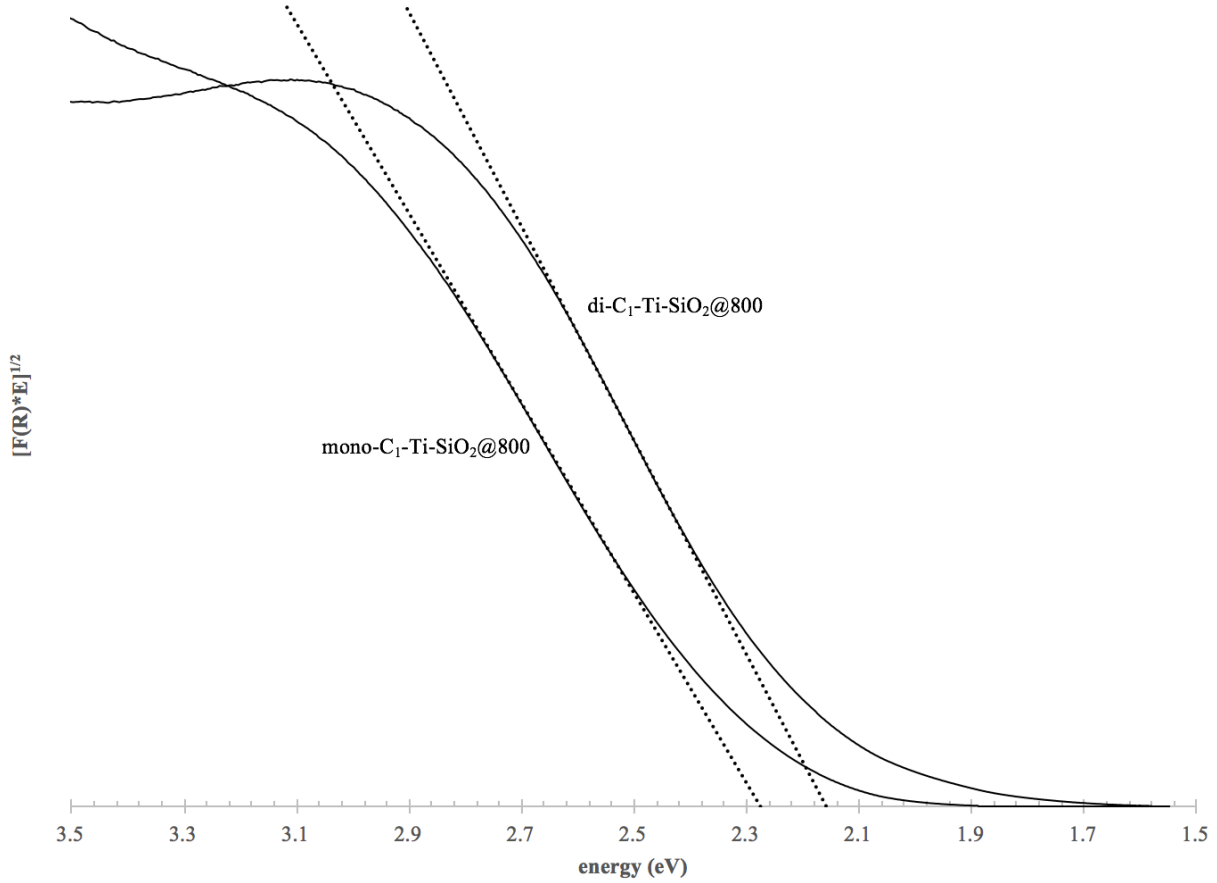

Figure 4.3. Diffuse-reflectance UV-visible spectra of representative grafted complexes **mono-C_1-SiO_2@800** and **di-C_1-SiO_2@800**. Both spectra use the Kubelka-Munk formalism (denoted as F(R)) and assume indirect LMCT transitions. LMCT edge energies are defined as the intercept of the shown (dotted) tangent lines calculated from the 1st derivative of the transformed spectra. E denotes energy.

4.3.3. Catalysis

All grafted titanocalixarene materials are active catalysts for the epoxidation of 1-octene in octane at 50 °C using *tert*-butyl hydroperoxide (TBHP) as the oxidant, as summarized in Table 4.2. The catalytic activity of different materials was used as a probe for the influence of the Ti^{IV} coordination environment on catalysis. Catalytic activity was compared in terms of (i) TOF extrapolated to initial time using a second order polynomial fit, as shown in Figure 4.4; (ii) a pseudo 1st order rate for TBHP decomposition, as shown in Figure A4.3; (iii) selectivity at ~30% conversion, defined as the ratio of epoxide produced to oxidant consumed. These values of initial TOF at 50 °C are similar to those previously observed for titanocalixarene materials for this

reaction,[31] and are indicative of persistent grafting of titanocalixarene complexes onto SiO_2, since homogeneous titanocalixarenes from potentially leached sites have been demonstrated to be inactive for epoxidation.[15,16] We performed a hot filtration experiment,[36] in which the solid catalyst was filtered out of solution at catalytic conditions and epoxidation activity ceased, in order to confirm that surface grafted **di-R-Ti** complexes do not leach into solution as active catalysts (Figure A4.4). The results of this indicate that novel grafted **di-R-Ti-SiO_2** catalysts described in this work are truly heterogeneous in nature just as their previously described **mono-R-Ti-SiO_2**.[15]

Materials supported on **SiO_2@200** showed ~40% slower rates of consumption of TBHP for both **mono-C_1-Ti** and **di-C_1-Ti** grafted complexes. Given that the decrease is similar for both complexes, we can exclude the possibility that bipodal attachment to silica in **di-C_1-Ti-SiO_2@200** when compared to di-**C_1-Ti-SiO_2@800** is responsible for decreased activity, since **mono-C_1-Ti** grafts through a single Ti-OSi in both SiO_2 supports. This leads us to conclude that the outer-sphere slightly affects TBHP consumption rates.

At these conditions, all materials reached ~30-40% conversion of TBHP and <3% conversion of 1-octene at 50 °C after 6 h with 40 – 43 % selectivity, indicating that 40-43% of TBHP is consumed towards epoxide formation as opposed to unproductive decomposition to *tert*-butyl alcohol (TBOH). Along with TBHP consumption, a concomitant increase in TBOH in solution was observed, but no significant olefin oxidation byproducts were detected. This low selectivity has been previously attributed to the relative difficulty of epoxidation for terminal alkenes such as 1-octene.[15]

When comparing grafted **mono-R-Ti** to **di-R-Ti** complexes on the same support and with the same lower-rim alkyl ether substituent, rate constants are within 13% of each other for all temperatures (Table 4.2). This indicates that the catalytic activity is virtually unaffected by the inner-coordination sphere for Ti^{IV} as enforced by the calix[4]arene ligand. This outcome is an unexpected and surprising result given the stronger dative coordination expected and observed by NMR spectroscopy in **di-R-Ti** relative to **mono-R-Ti** in the resting state (i.e. prior to catalytic testing), as well as the previously observed correlation between decreased Lewis acidity and epoxidation activity with increased dative coordination.[17]

One possible interpretation for this unexpected outcome, consistent with these and all previous results, is that the grafted **di-R-Ti** site undergoes a further conformational change to the "endo" conformer (Scheme 4.1) under catalysis conditions. Indeed, calixarene ligands are known to be prone to undergoing conformational changes.[37] While ^{13}C solid-state NMR spectroscopy showed only 31% of sites in **di-C_1-Ti-SiO_2@800** and 64% of sites in **di-C_1-Ti-SiO_2@200** were in the "endo" conformation in the catalyst "resting state" (Table A4.2), the flexibility of the calix[4]arene means that under catalytic conditions, where bulky TBHP is expected to be bound to the Ti^{IV} center,[16] more sites may adopt this conformation, similar to the observed trend favoring the "endo" conformer when comparing **di-C_1-Ti-SiO_2@200** and **-SiO_2@800** (see section 4.3.1). This "endo" conformation, with longer RO-Ti distances, is expected to have a similar 3d-electron occupancy to grafted **mono-C_1-Ti** sites and thus a similar catalytic activity, which could explain the small differences in initial TOF and k_{TBHP} when comparing grafted **mono-R-Ti** to **di-R-Ti** sites.

Table 4.2. Epoxidation Rates and Selectivities for Different Grafted Titanocalixarene Sites

Material	Coordination Environment			Temp. (°C)	k_{TBHP} ($M^{-2}s^{-1}$)[a]	TOF_0 (ks^{-1})[b]	Selectivity[c]
	Oxygen dative interaction	Support	O-R substituent				
di-C_1-Ti-SiO_2@800	di	SiO_2@800	O-CH_3	50	1.6	4.4	0.43
				65	4.4	15	0.47
				80	5.5	24	0.47
mono-C_1-Ti-SiO_2@800	mono	SiO_2@800	O-CH_3	50	1.5	4.2	0.43
				65	4.0	10	0.38
				80	5.5	20	0.39
di-C_1-Ti-SiO_2@200	di	SiO_2@200	O-CH_3	50	0.98	2.0	0.40
mono-C_1-Ti-SiO_2@200	mono	SiO_2@200	O-CH_3	50	0.97	2.2	0.43
di-C_5-Ti-SiO_2@800	di	SiO_2@800	O-$(CH_2)_4CH_3$	50	1.7	4.2	0.43
mono-C_5-Ti-SiO_2@800	mono	SiO_2@800	O-$(CH_2)_4CH_3$	50	1.5	3.2	0.40

[a]Pseudo 1st order rate constant based on the consumption of TBHP, according to equation 4.1. Reaction was carried out in excess olefin (<3% olefin conversion at 30-40% TBHP conversion).

[b]Initial turnover frequency, defined as amount of epoxide produced per Ti site per time (measured in kiloseconds), extrapolated to initial time.

[c]Ratio of epoxide yield with respect to initial TBHP present to TBHP conversion after 6 h of reaction. ~30% conversion at 50°C, ~75% conversion at 65°C, ~85% conversion at 80°C.

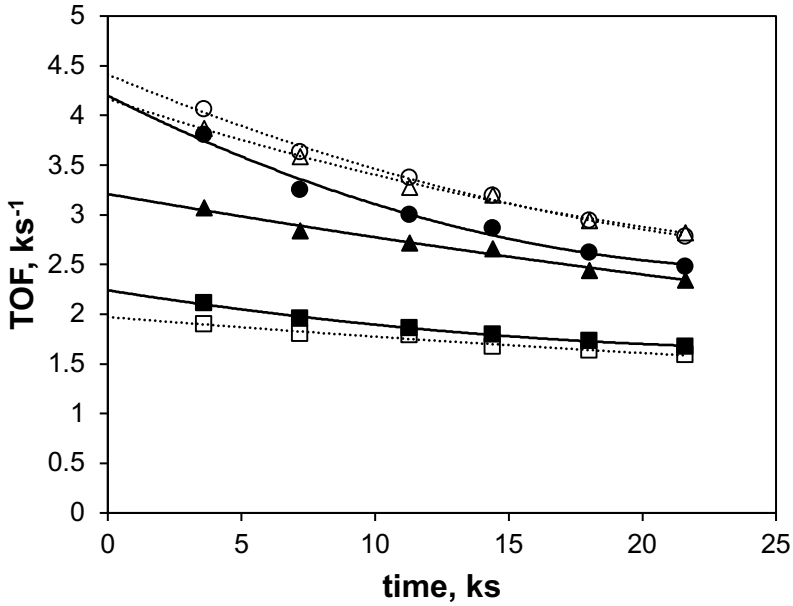

Figure 4.4. Catalytic turnover frequency (TOF) as a function of time for grafted titanocalixarene catalysts. 2nd order polynomial fits used for extrapolation are shown. **mono-C_1-Ti-SiO_2@800** (•, solid line), **di-C_1-Ti-SiO_2@800** (o, dotted line), **mono-C_5-Ti-SiO_2@800** (▲ , solid line), **di-C_5-Ti-SiO_2@800** (Δ, dotted line), **mono-C_1-Ti-SiO_2@200** (■, solid line), **di-C_1-Ti-SiO_2@200** (□, dotted line).

There is one additional possibility, besides a predominant "endo" conformation during catalysis, that may account for the observed similarity of rates between grafted **mono-R-Ti** and **di-R-Ti** sites, which is discussed below. Recovery of **di-C_1-Ti-SiO_2** catalysts isotopically enriched at the methoxy ether position used for epoxidation and subsequent MAS ^{13}C solid-state NMR spectroscopy showed only a single, broad, upfield resonance at 63-65 ppm when compared to materials in the resting state (see Figure A4.5). While this shift is consistent with the "endo" conformer prevailing after catalysis, a 40-50% decrease in methoxy resonance, without concomitant loss of calixarene ligand, is observed (see Table A4.2). The similarity in chemical shift of this upfield resonance to the chemical shift of grafted **mono-C_1-Ti** suggests that it is possible that after catalyst recovery, cleavage of the methoxy ether may result in the transformation of **di-C_1-Ti** into **mono-C_1-Ti**. While this transformation is known to occur in solution through lower-rim alkyl ether bond cleavage,[17] it is unexpected for surface grafted species which were stable upon drying at 120 °C. This transformation would imply that two catalysts with different inner coordination environments in the resting state may adopt a similar coordination environment in the active state, and thus display similar epoxidation activities as observed here. It is important to note, however, that catalyst recovery involved reaction under deactivating conditions (without molecular sieves), washing, drying, and storage (see Figure A4.5) which are not representative of the state of the calixarene ligand under reaction conditions and add uncertainty to this analysis. In-situ ^{13}C MAS solid-state NMR spectroscopy experiments would be needed in the future to asses the state of the calixarene ligand under reaction conditions.

Studies for **mono-C_1-Ti-SiO_2@800** and **di-C_1-Ti-SiO_2@800** were extended to higher

temperatures and demonstrate differences in selectivity between the two symmetries, as shown in Figure 4.5. This observation argues for a lack of methoxy cleavage under catalysis conditions, which cannot be decisively ruled out given the discussion above. Catalyst **di-C_1-Ti-SiO_2@800** is consistently more selective than **mono-C_1-Ti-SiO_2@800** despite rate constants (Table 4.2, maximum 13% difference at a given temperature) and activation energies (Figure A4.6, 11% difference) for TBHP consumption at all temperatures being almost indistinguishable between the two symmetries. Altogether, this data illustrates the importance of tuning the inner-sphere Ti^{IV} coordination environment in epoxidation catalysis.

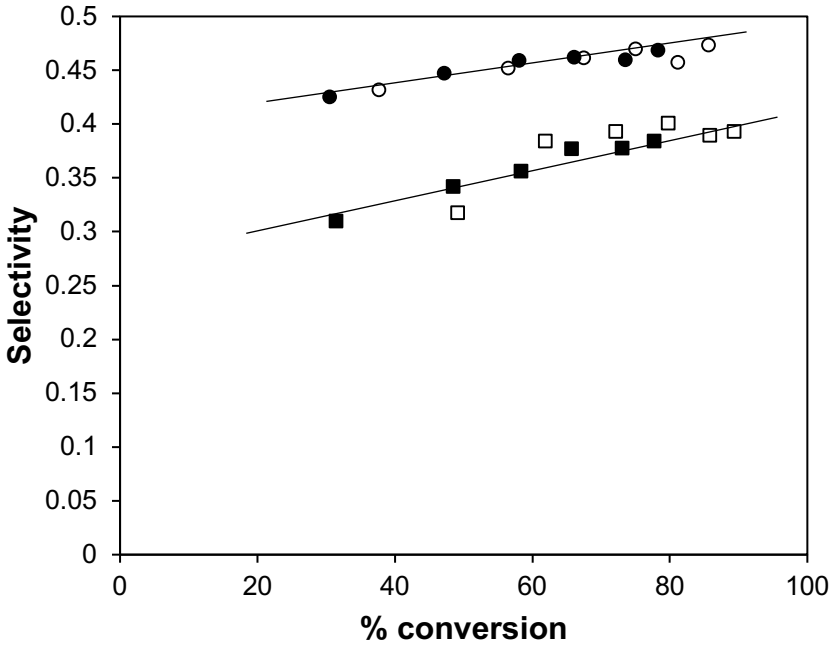

Figure 4.5. Plot of conversion vs. selectivity of TBHP towards epoxide, showing scatter in the results but an overall increase of selectivity with conversion, and better selectivity of grafted **di-C_1-Ti** when compared to **mono-C_1-Ti** materials at higher temperatures. Lines shown are interned as a guide to the eye. Each data point corresponds to a different time point during the reaction. Circles correspond to **di-C_1-Ti-SiO_2@800** while squares correspond to **mono-C_1-Ti-SiO_2@800**; filled markers correspond to measurements at 65 °C, while hollow markers correspond to measurements at 80 °C.

4.4. Conclusions

In this study, we have sought to gain a greater understanding of the influence that the organic ligand coordination sphere surrounding a grafted Ti^{IV} cation has on its catalytic activity. We investigated this question by enforcing different Ti^{IV} coordination environments using calix[4]arene ligands, providing unique synthetic controls to prepare uniform, well-defined catalytic sites, and probed how this environment affects epoxidation activity, when using an organic hydroperoxide as the oxidant.

The symmetry of the Ti^{IV} site, as enforced by grafting either a **mono-R-Ti** (C_s symmetry) or a **di-R-Ti** (C_{2v} symmetry) complex, is found to have significant effects on the nature of the grafted site. ^{13}C MAS NMR spectroscopy demonstrates the same single methoxy resonance for grafted **mono-C_1-Ti** as the complex in solution, indicating intact titanocalixarene grafting. The upfield resonance of the methoxy carbon in **mono-C_1-Ti-SiO_2@800** (64 ppm) when compared to **di-C_1-Ti-SiO_2@800** (69 ppm) indicates stronger electronic deshielding at the methoxy position in the latter, confirming our hypothesis that RO→Ti dative interactions are stronger in the grafted **di-C_1-Ti** complex due to shorter RO-Ti distances. LMCT edge energies of 2.24 ± 0.02 eV for **mono-R-Ti@SiO_2** and 2.16 ± 0.02 eV for **di-R-Ti@SiO_2** materials demonstrate differences in the electronic properties of the Ti^{IV} center as enforced by the coordination geometry of the organic ligand. However, the ^{13}C MAS NMR spectrum of **di-C_1-Ti-SiO_2@800** and **di-C_1-Ti-SiO_2@200** also shows an upfield-shifted shoulder resonance, which we attribute to an unexpected "endo" conformer of the grafted complex. This "endo" conformer, brought about by the steric constraints of the impinging SiO_2 surface, has longer Ti-OR distances (i.e. weaker dative interactions) than the "exo" conformer according to prior molecular modeling studies – something that is consistent with its observed upfield shift.

It had been previously hypothesized that stronger RO→Ti dative interactions in grafted **di-R-Ti** complexes would lead to lower Lewis acidity of Ti^{IV} and lower epoxidation rates;[20] however, in this work, epoxidation activity as measured by rates of TBHP consumption is found to be largely unaffected by the symmetry of the grafted titanocalixarene. We thus propose two hypotheses: (a) under catalytic conditions, in the working state, grafted **di-R-Ti** sites exist in their "endo" conformation, which exhibits a similar RO-Ti distance and predicted 3d-electron occupancy based on this distance as **mono-R-Ti**; (b) that under catalytic conditions **di-R-Ti** undergoes a rearrangement to **mono-R-Ti**. Both possibilities are consistent with the similar rates of epoxidation observed and illustrate the need to assess the state of grafted catalytic sites in the active state, as they may, when grafted on a surface, exhibit additional complexities not seen in solution. Despite limited effects of ligand coordination symmetry on TBHP consumption rates, measurable improvements in selectivity (45 vs 34 % at a 50% conversion) for **di-C_1-Ti-SiO_2@800** when compared to **mono-C_1-Ti-SiO_2@800** demonstrates the importance that coordination environment plays in determining catalytic activity, and illustrates the importance of precisely controlling the molecular environment of catalytic active sites in formulating the most effective catalyst.

The spectroscopic probes (in particular LMCT edge-energies) developed here lay a foundation to understand Ti^{IV} coordination in grafted calix[4]arne-Ti^{IV} catalysts. This, together with the observation of different conformations of these complexes when grafted on silica, which may undergo structural rearrangements under reaction conditions, are important in understanding epoxidation reactivity by these complexes that is discussed in the remainder of this thesis.

4.5. Appendices

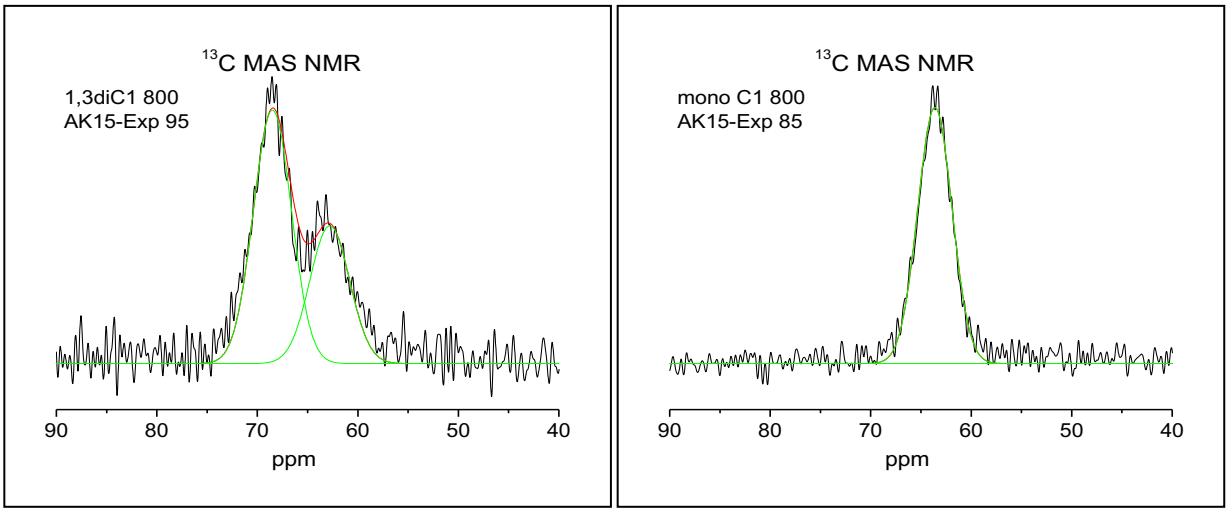

Figure A4.1. Gaussian fits to the ^{13}C MAS solid-state NMR spectra shown in Figure 4.1.

Table A4.1. ^{13}C MAS solid-state NMR spectra peak quantifications in Figure A4.1.

mono-C_1-Ti-SiO_2@800			**di-C_1-Ti-SiO_2@800**		
ppm	**width**	**intensity**	**ppm**	**width**	**intensity**
63.6	425	475.6	68.5	472.5	522.5
			62.8	493.75	296.3
Ti loading (umol/g)	52		**Ti loading (umol/g)**	49	
intensity/umol	9.0		**intensity/umol**	16.7	

The observed ratio of intensity **di-C_1-Ti-SiO_2@800** : **mono-C_1-Ti-SiO_2@800** = 1.86 ~ 2 (~7% error). About 36% of intensity comes from resonance centered at 62.8 for **di-C_1-Ti-SiO_2@800**. If we would consider that the resonance at 62.8 ppm in **di-C_1-Ti-SiO_2@800** is due to **di-C_1-Ti** complex that decomposed to **mono-C_1-Ti**, assuming the expected 2:1 ratio of methoxy resonances, then it follows that the fraction of sites with grafted **mono-C_1-Ti** is 53%, and the intensity per methoxy group is of 10.6, which is a 17% error. Since this is twice the error than assuming the calixarene is intact, we conclude that **di-C_1-Ti** is grafted intact and that it is present in two different chemical environments.

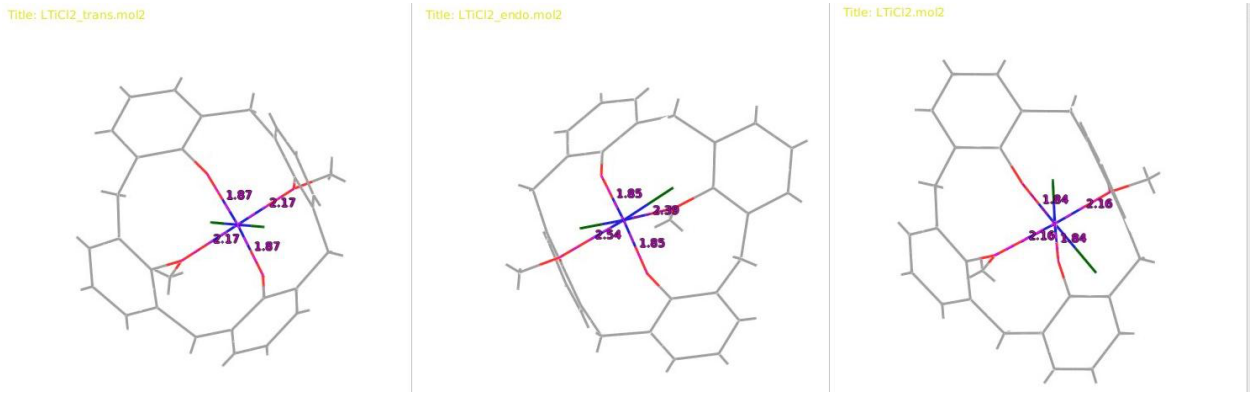

Figure A4.2. Conformations of di-C_1-Ti in solution. Data generously provided by Prof. Dr. Udo Radius from reference.[24]

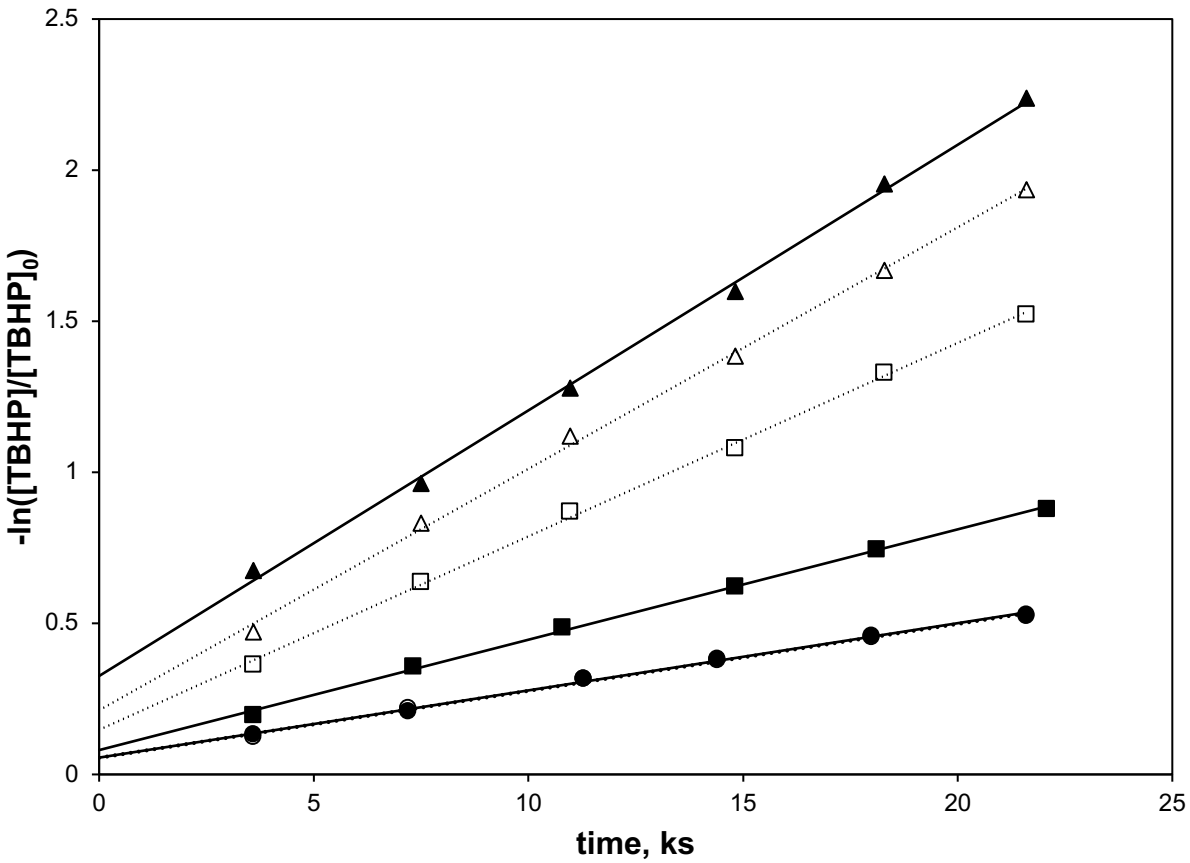

Figure A4.3. Natural logarithm of ratio of TBHP oxidant concentration to initial TBHP concentration ($[TBHP]_0$) as a function of time for representative grafted titanocalixarene catalysts at different temperatures. Linear trend confirm that kinetics can be described as pseudo 1st order in TBHP. Data for **mono-C_1-Ti-SiO_2@800** catalyst is shown as filled markers with solid trendlines, while that for **di-C_1-Ti-SiO2@800** catalysts is shown as hollow markers with dotted trendlines. Temperatures: 50 °C (•,o), 65 °C (■,□), 80 °C (▲,Δ). Slopes are not normalized by Ti reactor contents and thus not represent the relative value of rates in Table 4.1. Data points at 50 °C (•,o) overlap, making hollow markers not visible behind filled markers.

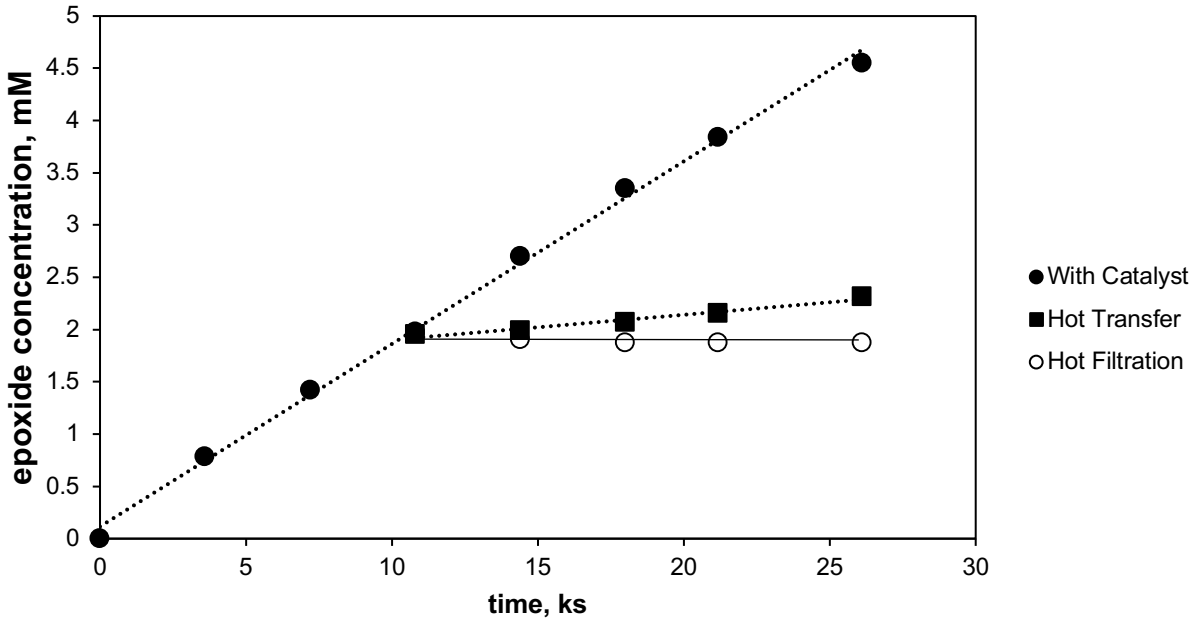

Figure A4.4. Results of hot-filtration test. Epoxidation was carried out with **di-C_1-Ti-SiO_2@800** at 50ºC as described in section 4.2.4, with 20 mL of solution. After 3 h of reaction time, 5 mL of the solution were transferred to an empty flask, preheated at 50 ºC and containing molecular sieves, using a syringe preheated at 50 ºC; this "hot transfer" solution contained some suspended catalyst and thus showed epoxidation activity as indicated by continued epoxide production. Separately, after 3 h of reaction time, 5 mL of the solution were transferred to an empty flask, preheated at 50ºC and containing molecular sieves, using a syringe that was fitted with a filter preheated at 50ºC; this "hot filtration" solution contained no catalyst and displayed no epoxidation activity, indicating that homogeneous species, if at all present, are inactive for epoxidation. This confirms the heterogeneous nature of **di-C_1-Ti-SiO_2@800** catalyst. Data series "with catalyst" corresponds to solution in original reaction flask, where epoxidation activity continued as expected, and is intended as a control.

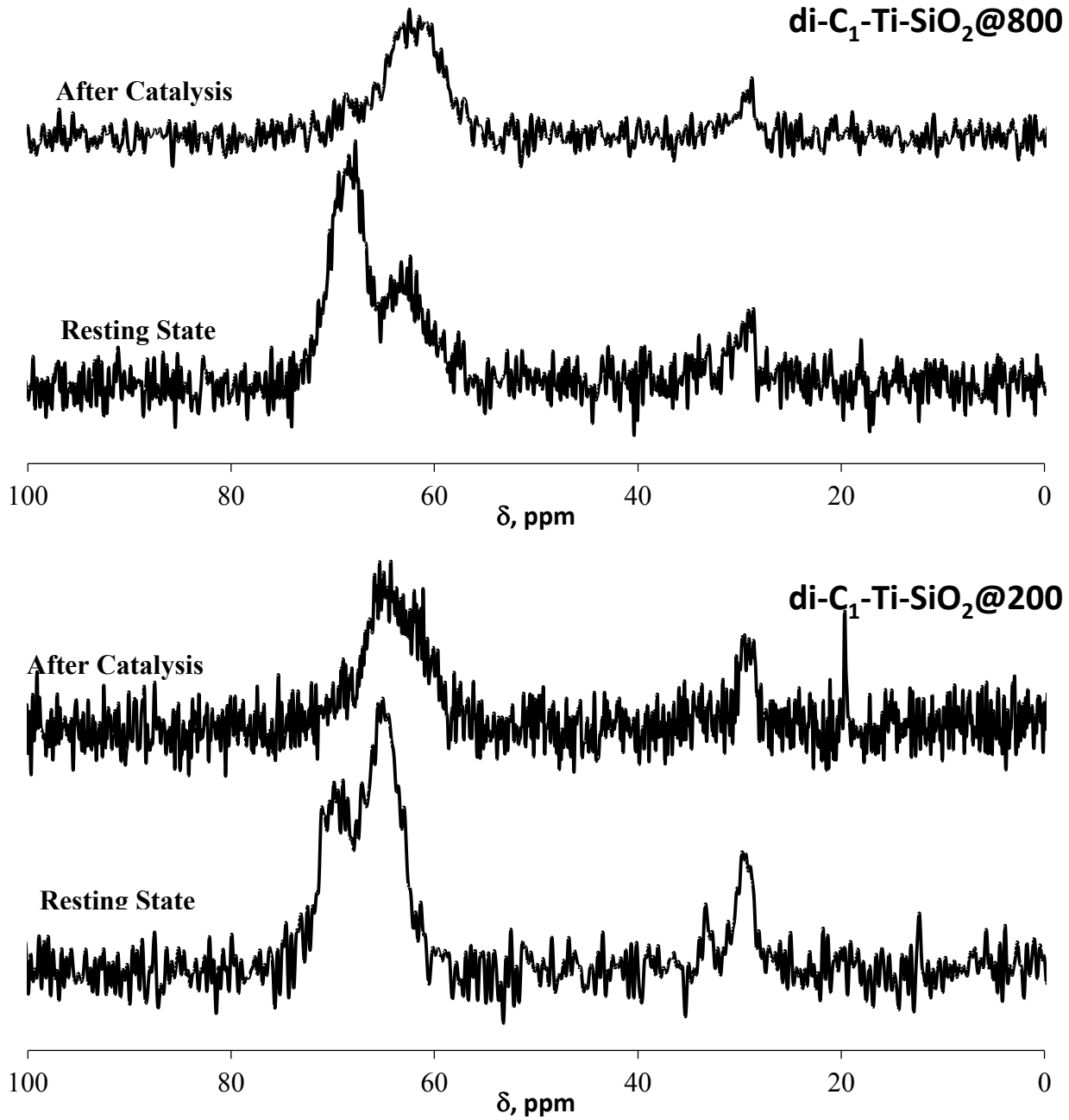

Figure A4.5. MAS ^{13}C solid-state NMR spectrum of **mono-C_1-SiO_2@800** (top figure) and **di-C_1-SiO_2@200** (bottom figure) as-made ("Resting State", shown at the bottom of each figure) and recovered after 1 h of epoxidation activity ("After Catalysis", show at the top of each figure). All catalysts are ^{13}C isotope enriched at the methoxy ether position. The Resting State catalyst was treated as per epoxidation conditions described in section 4.2.4, in the absence of molecular sieves, for 1 h. After this, it was decanted, the supernatant removed, washed with 3 x 50 mL of toluene by subsequent decantation, dried for 1h at 65 ºC, and handled and stored under Ar. For both catalysts, a single, broad, upfield resonance remains after catalytic activity.

Table A4.2. ^{13}C MAS solid-state NMR spectra peak quantifications for data shown in Figure A4.5.

	di-C_1-Ti-SiO_2@800			di-C_1-Ti-SiO_2@200		
	Resting State	**After Catalysis**	**% change**	**Resting State**	**After Catalysis**	**% change**
Normalized peak area (a.u.)	7.9 (69% "exo", 31% "endo")*	4.8	-40	10.1 (36% "exo", 64% "endo")*	5.3	-48
Calixarene ligand loading (umol/g)	36	34	-6	67	54	-18

*Percentage of total area corresponding to "exo" conformer (lower field ~68-70 ppm ppm) and "endo" conformers (higher field ~63-65 ppm)

Peak area is the total integrated intensity determined by fitting methoxy resonances in the 65-75 ppm region to Gaussian curves. Normalized peak areas (by weight and number of scans) are comparable for each catalyst before and after catalysis, but not across both catalysts due to changes in the NMR probe sensitivity. Calix[4]arene ligand loadings estimated by assuming the mass loss between 473 and 1073 K under air treatment monitored by thermogravimetric analysis, when compared to the bare support, is entirely due to combustion of calixarene ligand. A 40 – 50 % decrease in methoxy resonance but only 6-18% loss of calixarene ligand implies that the methoxy ether may be lost from grafted **di-C_1-Ti**. Methoxy ether loss close to 50% is suggestive of transformation of **di-C_1-Ti** to **mono-C_1-Ti**, which only has one (as opposed to two) ^{13}C enriched methoxy ether positions.

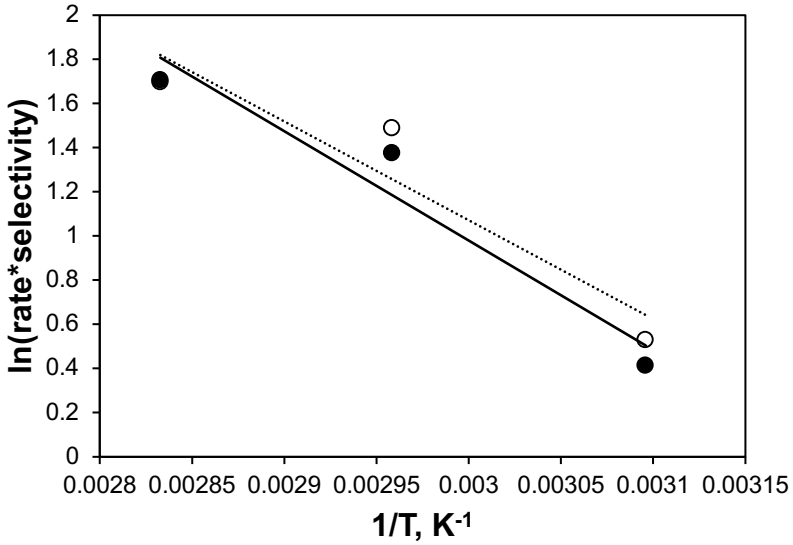

Figure A4.6. Arrhenius plot for **mono-C_1-Ti-SiO_2@800** (•) and for **di-C_1-Ti-SiO_2@800** (o) showing similar exponential dependence of rates with temperature. Calculated activation energies are 41 and 37 kJ/ mol for **mono-C_1-Ti-SiO_2@800** and **di-C_1-Ti-SiO_2@800** respectively.

4.6. References

(1) Bell, A. T. The Impact of Nanoscience on Heterogeneous Catalysis. *Science* **2003**, *299*, 1688–1691.

(2) Copéret, C.; Chabanas, M.; Petroff Saint-Arroman, R.; Basset, J.-M. Homogeneous and Heterogeneous Catalysis: Bridging the Gap through Surface Organometallic Chemistry. *Angew. Chem. Int. Ed.* **2003**, *42*, 156–181.

(3) Corma, A.; García, H. Lewis Acids as Catalysts in Oxidation Reactions: From Homogeneous to Heterogeneous Systems. *Chem. Rev.* **2002**, *102*, 3837–3892.

(4) Corma, A. Attempts to Fill the Gap Between Enzymatic, Homogeneous, and Heterogeneous Catalysis. *Catal. Rev.* **2004**, *46*, 369–417.

(5) Dusi, M.; Mallat, T.; Baiker, A. Epoxidation of Functionalized Olefins Over Solid Catalysts. *Catal. Rev.* **2000**, *42*, 213–278.

(6) Marchese, L.; Gianotti, E.; Dellarocca, V.; Maschmeyer, T.; Rey, F.; Coluccia, S.; Thomas, J. M. Structure–Functionality Relationships of Grafted Ti-MCM41 Silicas. Spectroscopic and Catalytic Studies. *Phys. Chem. Chem. Phys.* **1999**, *1*, 585–592.

(7) Thomas, J. M.; Sankar, G. The Role of Synchrotron-Based Studies in the Elucidation and Design of Active Sites in Titanium−Silica Epoxidation Catalysts. *Acc. Chem. Res.* **2001**, *34*, 571–581.

(8) Corma, A. State of the Art and Future Challenges of Zeolites as Catalysts. *J. Catal.* **2003**, *216*, 298–312.

(9) Saxton, R. J. Crystalline Microporous Titanium Silicates. *Top. Catal. 9*, 43–57.

(10) Clerici, M. Epoxidation of Lower Olefins with Hydrogen Peroxide and Titanium Silicalite. *J. Catal.* **1993**, *140*, 71–83.

(11) Maschmeyer, T.; Rey, F.; Sankar, G.; Thomas, J. M. Heterogeneous Catalysts Obtained by Grafting Metallocene Complexes onto Mesoporous Silica. *Nature* **1995**, *378*, 159–162.

(12) Guidotti, M.; Ravasio, N.; Psaro, R.; Ferraris, G.; Moretti, G. Epoxidation on Titanium-Containing Silicates: Do Structural Features Really Affect the Catalytic Performance? *J. Catal.* **2003**, *214*, 242–250.

(13) Jarupatrakorn, J.; Tilley, T. D. Silica-Supported, Single-Site Titanium Catalysts for Olefin Epoxidation. A Molecular Precursor Strategy for Control of Catalyst Structure. *J. Am. Chem. Soc.* **2002**, *124*, 8380–8388.

(14) Bouh, A. O.; Rice, G. L.; Scott, S. L. Mono- and Dinuclear Silica-Supported Titanium(IV) Complexes and the Effect of TiOTi Connectivity on Reactivity. *J. Am. Chem. Soc.* **1999**, *121*, 7201–7210.

(15) Notestein, J. M.; Iglesia, E.; Katz, A. Grafted Metallocalixarenes as Single-Site Surface Organometallic Catalysts. *J. Am. Chem. Soc.* **2004**, *126*, 16478–16486.

(16) Notestein, J. M.; Solovyov, A.; Andrini, L. R.; Requejo, F. G.; Katz, A.; Iglesia, E. The Role of Outer-Sphere Surface Acidity in Alkene Epoxidation Catalyzed by Calixarene-Ti(IV) Complexes. *J. Am. Chem. Soc.* **2007**, *129*, 15585–15595.

(17) Notestein, J. M.; Andrini, L. R.; Kalchenko, V. I.; Requejo, F. G.; Katz, A.; Iglesia, E. Structural Assessment and Catalytic Consequences of the Oxygen Coordination Environment in Grafted Ti-Calixarenes. *J. Am. Chem. Soc.* **2007**, *129*, 1122–1131.

(18) Nandi, P.; Tang, W.; Okrut, A.; Kong, X.; Hwang, S.-J.; Neurock, M.; Katz, A. Catalytic Consequences of Open and Closed Grafted Al(III)-Calix[4]Arene Complexes for Hydride and Oxo Transfer Reactions. *Proc. Natl. Acad. Sci. U. S. A.* **2013**, *110*, 2484–2489.

(19) Nandi, P.; Solovyov, A.; Okrut, A.; Katz, A. Al III –Calix[4]Arene Catalysts for Asymmetric Meerwein–Ponndorf–Verley Reduction. *ACS Catal.* **2014**, *4*, 2492–2495.
(20) de Silva, N.; Hwang, S.-J.; Durkin, K. A.; Katz, A. Vanadocalixarenes on Silica: Requirements for Permanent Anchoring and Electronic Communication. *Chem. Mater.* **2009**, *21*, 1852–1860.
(21) *Kirk-Othmer Encyclopedia of Chemical Technology*; John Wiley & Sons, Inc.: Hoboken, NJ, USA, 2000.
(22) Friedrich, A.; Radius, U. A Calix[4]Arene Monoalkyl Ether as a Model of a Tris(Phenolate) Ligand with a Hemilabile Anisole Moiety: Syntheses, Molecular Structures and Bonding of Calix[4]Arene Ether Supported Titanium Complexes and Their Catalytic Activity in Epoxidation Reactions. *Eur. J. Inorg. Chem.* **2004**, *2004*, 4300–4316.
(23) Zanotti-Gerosa, A.; Solari, E.; Giannini, L.; Floriani, C.; Re, N.; Chiesi-Villa, A.; Rizzoli, C. Titanium-Carbon Functionalities on an Oxo Surface Defined by a Calix [4] Arene Moiety and Its Redox Chemistry. *Inorganica Chim. Acta* **1998**, *270*, 298–311.
(24) Radius, U. Shaping the Cavity of the Macrocyclic Ligand in Metallocalix[4]Arenes: The Role of the Ligand Sphere. *Inorg. Chem.* **2001**, *40*, 6637–6642.
(25) Böhmer, V. Calixarene – Makrocyclen Mit (Fast) Unbegrenzten Möglichkeiten. *Angew. Chemie* **1995**, *107*, 785–818.
(26) Dijkstra, P. J.; Brunink, J. A. J.; Bugge, K. E.; Reinhoudt, D. N.; Harkema, S.; Ungaro, R.; Ugozzoli, F.; Ghidini, E. Kinetically Stable Complexes of Alkali Cations with Rigidified Calix[4]Arenes: Synthesis, x-Ray Structures, and Complexation of Calixcrowns and Calixspherands. *J. Am. Chem. Soc.* **1989**, *111*, 7567–7575.
(27) Shang, S.; Khasnis, D. V.; Burton, J. M.; Santini, C. J.; Fan, M.; Small, A. C.; Lattman, M. From a Novel Silyl P-Tert-Butylcalix[4]Arene Triether to Mono-O-Alkyl Substitution: A Unique, Efficient, and Selective Route to Mono-O-Substituted Calix[4]Arenes. *Organometallics* **1994**, *13*, 5157–5159.
(28) Groenen, L. C.; Ruël, B. H. M.; Casnati, A.; Verboom, W.; Pochini, A.; Ungaro, R.; Reinhoudt, D. N. Synthesis of Monoalkylated Calix[4]Arenes via Direct Alkylation. *Tetrahedron* **1991**, *47*, 8379–8384.
(29) van Loon, J.-D.; Verboom, W.; Reinhoudt, D. N. Selective Functionalization and Conformational Properties of Calix[4]Arenes, a Review. *Org. Prep. Proced. Int.* **1992**, *24*, 437–462.
(30) Zawadiak, J.; Gilner, D.; Kulicki, Z.; Baj, S. Concurrent Iodimetric Determination of Cumene Hydroperoxide and Dicumenyl Peroxide Used for Reaction Control in Dicumenyl Peroxide Synthesis. *Analyst* **1993**, *118*, 1081.
(31) Winner, L.; Daniloff, G.; Nichiporuk, R. V.; Solovyov, A.; Katz, A. Patterned Grafted Lewis-Acid Sites on Surfaces: Olefin Epoxidation Catalysis Using Tetrameric Ti(IV)–Calix[4]Arene Complexes. *Top. Catal.* **2015**, *58*, 441–450.
(32) Zhuravlev, L. T. Concentration of Hydroxyl Groups on the Surface of Amorphous Silicas. *Langmuir* **1987**, *3*, 316–318.
(33) Marchese, L.; Maschmeyer, T.; Gianotti, E.; Coluccia, S.; Thomas, J. M. Probing the Titanium Sites in Ti−MCM41 by Diffuse Reflectance and Photoluminescence UV−Vis Spectroscopies. *J. Phys. Chem. B* **1997**, *101*, 8836–8838.
(34) Notestein, J. M.; Iglesia, E.; Katz, A. Photoluminescence and Charge-Transfer Complexes of Calixarenes Grafted on TiO_2 Nanoparticles. *Chem. Mater.* **2007**, *19*, 4998–5005.

(35) Fantacci, S.; Sgamellotti, A.; Re, N.; Floriani, C. Density Functional Study of Tetraphenolate and Calix[4]Arene Complexes of Early Transition Metals. *Inorg. Chem.* **2001**, *40*, 1544–1549.
(36) Prieto-Centurion, D.; Notestein, J. M. Surface Speciation and Alkane Oxidation with Highly Dispersed Fe(III) Sites on Silica. *J. Catal.* **2011**, *279*, 103–110.
(37) Böhmer, V. Calixarenes, Macrocycles with(Almost) Unlimited Possibilities. *Angew. Chemie* **1995**, *34*, 785–818.

Chapter 5

Outer-Sphere Control of Catalysis on Surfaces: A Comparative Study of Ti(IV) Single-Sites Grafted on Amorphous versus Crystalline Silicates for Alkene Epoxidation

Adapted with permission from Grosso-Giordano, N. A.; Schroeder, C.; Okrut, A.; Solovyov, A.; Schöttle, C.; Chassé, W.; Marinković, N.; Koller, H.; Zones, S. I.; Katz, A. Outer-Sphere Control of Catalysis on Surfaces: A Comparative Study of Ti(IV) Single-Sites Grafted on Amorphous versus Crystalline Silicates for Alkene Epoxidation. *J. Am. Chem. Soc.* **2018**, *140* (15), 4956–4960.

The effect of outer-sphere environment on alkene epoxidation catalysis using an organic hydroperoxide oxidant is demonstrated for calix[4]arene-Ti^{IV} single-sites grafted on amorphous vs. crystalline delaminated zeotype (UCB-4) silicates as supports. A chelating calix[4]arene macrocycle ligand enforces a constant Ti^{IV} inner-sphere, as characterized by UV-visible and X-ray absorption spectroscopies, thus enabling the rigorous comparison of outer-sphere environments across different siliceous supports. These outer-sphere environments are characterized by solid-state ^{1}H NMR spectroscopy to comprise proximally organized silanols confined within 12-membered-ring cups in crystalline UCB-4, and are responsible for up to 5-fold enhancements in rates of epoxidation by Ti^{IV} centers.

5.1. Introduction

Supported catalytic active sites comprising isolated cations are ubiquitous;[1,2] however, their rational molecular design is currently hampered by a lack of understanding of how outer-sphere effects control their reactivity. Outer-sphere effects are controlled by surface moieties that are vicinal (non-coordinating) to the active centers,[3,4] as opposed to coordinating ligands of the inner-sphere,[5–9] and are commonly invoked in the reactivity of soluble molecular catalysts[10] and metalloenzymes.[11] Their experimental observation on supported molecular catalysts has been elusive, however, because of the challenges associated with modifying the outer-sphere without significantly affecting other aspects – such as inner-sphere or steric accessibility – of the active site.[12-18] Here, we demonstrate that outer-sphere environments have profound consequences on the reactivity of Ti^{IV} sites supported on siliceous surfaces, the same type of active sites used in industrial propylene epoxidation catalysts.[19-21] Our approach enforces a constant inner-sphere environment for grafted Ti^{IV} single-sites with a chelating macrocyclic calix[4]arene ligand, while maintaining active-site accessibility across crystalline zeolitic versus amorphous outer-sphere environments of identical composition. This enables us to unequivocally determine that outer-sphere effects are responsible for rate enhancements of up to 5-fold per Ti^{IV} site in crystalline zeolitic supports during the catalytic epoxidation of cyclohexene with *t*-butyl hydroperoxide. NMR characterization reveals that these effects arise from differences in the proximal organization of surface silanol groups and their framework location relative to Ti^{IV} active centers, demonstrating the importance of precisely designing outer-sphere structures for active sites on surfaces.

5.2. Experimental

Our approach is shown in Scheme 5.1, and is based on a calix[4]arene-Ti surface complex (highlighted in brown) as a Lewis-acid catalytic Ti^{IV} center. This is grafted onto a silanol (SiOH) group on the surface of three different siliceous supports, consisting of a crystalline delaminated zeotype UCB-4,[22] and two amorphous silicas, which comprise Aerosil® 200 fumed silica particles (denoted SiO_2) and MCM-41,[23] a hexagonally ordered silicate with uniform 2.6 nm mesopores (see sections 5.5.1.1 and 5.5.2).[24] The resulting catalysts comprising grafted calix[4]arene-Ti complexes are denoted **calix-Ti/SUP**, where **SUP** = **UCB-4**, **SiO_2**, or **MCM-41** indicates the support in Scheme 5.1. Further experimental details are included in appendix 5.5.1.

Scheme 5.1. Grafted calix[4]arene-Ti^{IV} materials.

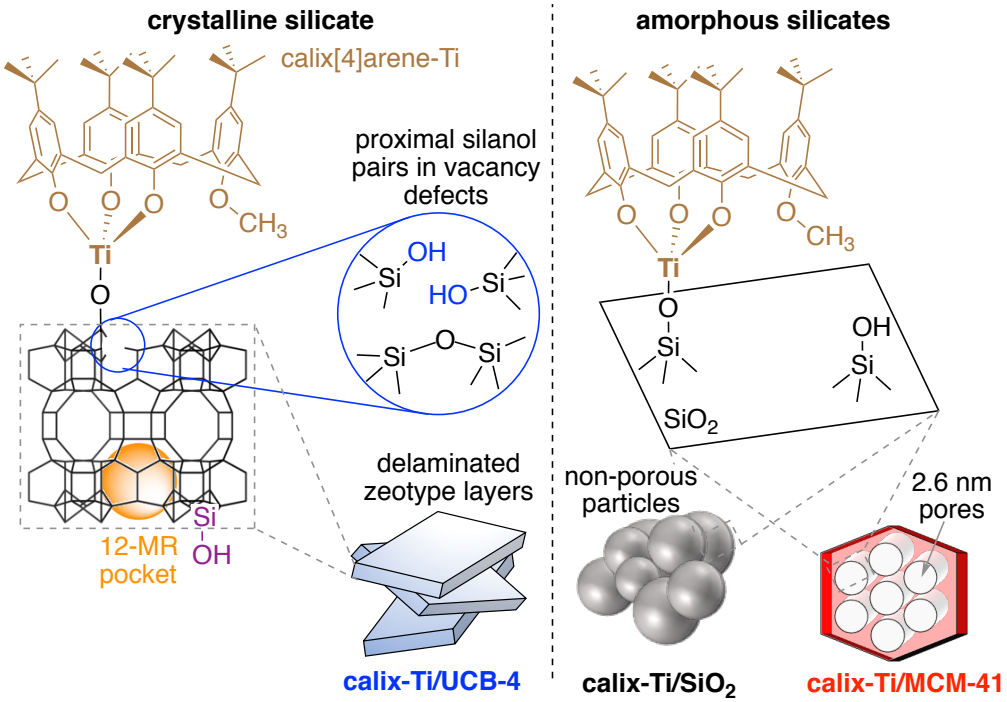

Schematic representation of grafted calix[4]arene-Ti^{IV} structures (brown). Details of the crystalline SSZ-70 (MWW-type) zeotype framework of UCB-4 (left panel) are shown along the a-c plane, with vertices representing $SiO_{4/2}$ tetrahedra connected by Si-O-Si bonds. Silanol (SiOH) species characterized by NMR on SSZ-70 are represented as a proximal silanol pair in blue, and a crystal-terminating isolated silanol in purple.

5.3. Results and Discussion

The physicochemical properties of all catalysts are summarized in Table 5.1. Upon grafting, calix[4]arene-to-Ti ratios in all catalysts were measured to be near unity (calix:Ti in Table 5.1), confirming that the surface complex is intact and that the calix[4]arene ligand remains bound to Ti^{IV},[25] as depicted in Scheme 5.1. The macrocyclic dimensions of the calix[4]arene-Ti^{IV} precursor prevents its diffusion into zeotype micropores during grafting, ensuring that grafting occurs on the external surface only, as also indicated by analysis of grafting densities (Sction 5.5.3). The location of all active sites on the external surface ensures their equal accessibility for activation of organic hydroperoxides in the absence of steric limitations imposed by zeolitic micropores,[26,27] enabling a direct and rigorous comparison of intrinsic calix[4]arene-Ti^{IV} reactivity across all materials.

Table 5.1. Physicochemical properties of supports and Ti^{IV}-containing materials.

Support	wt.% Ti	Calix: Ti	LMCT edge (eV)	A_{rel}[a]	k_{eff}[b]
SiO_2	0.35	1.0	2.29	0.92	8
MCM-41	0.70	1.0	2.21	0.89	10
UCB-4	0.37	1.1	2.24	0.93	42

[a]Ratio of Ti K-edge XANES pre-edge area features, ±0.07 (Sections 5.5.1.3 and 5.5.6). [b]Effective epoxidation rate constant, $M^{-2}s^{-1}$, ±1 (Sections 5.5.1.4 and 5.5.7).

The outer-sphere environment as controlled by the support surface surrounding the grafted calix[4]arene-Ti^{IV} complex is compositionally identical in all siliceous supports. However, it contrasts in (i) the ordered crystalline versus random amorphous arrangement of silicate framework, and (ii) the organization of surface silanol (Si-OH) onto which calix[4]arene-Ti is grafted.[28] This is respectively illustrated by (i) the presence of twelve membered-ring pockets (12-MR pocket in Scheme 5.1) on the external surface of crystalline UCB-4,[29] which are absent in amorphous SiO_2 and MCM-41;[24] and (ii) the random distribution of isolated silanol groups on the surface of these partially dehydroxylated amorphous silicates, in contrast to silanol organization into cooperative proximal arrangements in crystalline UCB-4 (Scheme 5.1).[28] These arrangements are synthesized by the post-synthetic hydrolysis and removal of B^{III} from zeolitic frameworks such as SSZ-70 studied here, exposing a vacancy defect terminated by silanols.

Given the role that silanol groups have on the grafting and outer-sphere environments of calix[4]arene-Ti^{IV} sites, we investigated their nature and local organization in both crystalline and amorphous supports by solid-state ^1H NMR spectroscopy, prior to calix[4]arene-Ti^{IV} grafting (in order to reduce interference of ^1H signals from organics). We chose to examine the non-delaminated B-SSZ-70, the calcined variant of the layered zeotype precursor that leads to UCB-4 (Sections 5.5.1.1 and 5.5.2), because delamination does not affect calix[4]arene-Ti^{IV} grafting densities or catalytic activity (Table A5.2 and Figure A5.5). After B^{III} removal from the borosilicate framework of B-SSZ-70 there is an appearance of resonances corresponding to silanols in the ^1H MAS NMR spectrum at 2-8 ppm (Figure A5.2A). The ^1H single-quantum double-quantum (SQ-DQ) MAS NMR dipolar correlation spectrum shows two well-resolved cross-correlation peaks (Figure 5.1A) for hydrogen-bonded silanols, at 3.3 and 4.0 ppm. This cross-correlation rigorously confirms two silanols comprising different chemical shifts to be

adjacent in space, indicative of a well-ordered paired silanol arrangement being formed in vacancies exposed by B^{III} removal, as depicted in blue in Scheme 5.1. Corresponding data for B-SSZ-70 where B^{III} remains part of the crystalline framework (Figure A5.2Ca) confirms that this arrangement does not exist prior to B^{III} removal. Such deboronation treatments are generally believed to synthesize vacancy defect structures termed "silanol nests" in zeotype frameworks, consisting of four hydrogen-bonded silanols; however, no rigorous study has determined the actual number of silanols involved in such structures.[30] Our 2Q NMR data unequivocally demonstrates the existence of at least two such paired silanols in SSZ-70, and all attempts by ^{1}H NMR to show the presence of more than two silanols employing 3Q or 4Q excitation have been unsuccessful. In contrast, the amorphous SiO_2 support (dehydroxylated at 823 K) shows no signal for hydrogen-bonded silanols, and its SQ-DQ MAS NMR spectrum shows only a weak autocorrelation signal at 1.8 ppm (Figure 5.1B), corresponding to randomly paired surface silanols, whose abundance is insignificant when compared to the paired silanols in SSZ-70 (Section 5.5.4).

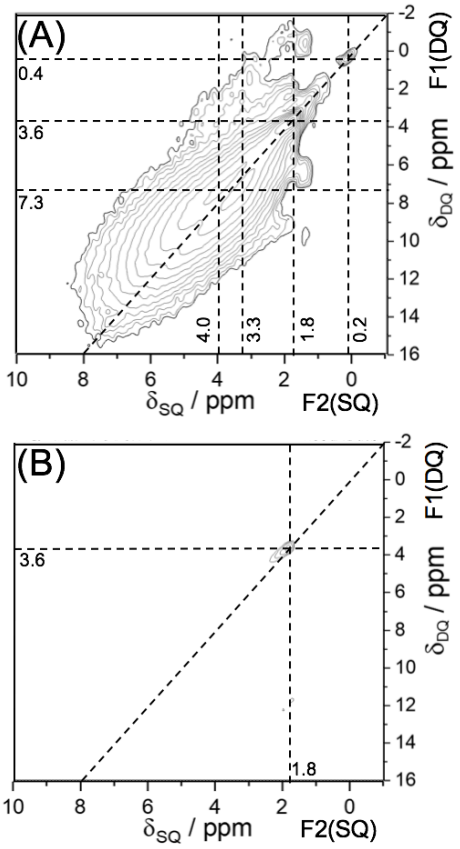

Figure 5.1. ^{1}H SQ DQ MAS NMR spectra acquired at a magnetic field strength of 9.74 T and a MAS rate of 9000 Hz of **(A)** B-SSZ-70 after B^{III} removal, and **(B)** SiO_2.

In order to quantify the pairing and distances between silanol groups, ^{1}H DQ build-up curves were measured.[31] These data on SSZ-70 reveal that 34% of silanols are found within well-ordered pairs, with a ^{1}H-^{1}H distance of 2.5 Å (Figure A5.2Db and section 5.5.4). This distance indicates that considerable rearrangement of the local structure is necessary upon B^{III} removal, as the

average edge length (between oxygen atoms) of a tetrahedral center is 2.6 Å. A minority silanols in SSZ-70 are isolated species on its external crystal-terminating surface, with signal at 1.8 ppm,[32] depicted in purple in Scheme 5.1. In amorphous SiO_2, the vast majority (82%) of silanols are isolated, while the remaining protons exhibit an instant rise to maximum double-quantum intensity at early evolution times (Figure A5.2Da), with an extremely large dipolar coupling constant of at least 15 kHz (indicating a H-H distance below 2.0 Å), unlikely to represent paired silanols and instead typical of rigidly adsorbed water (H-H distance of 1.6 Å).

Because of the close proximity of silanol pairs in UCB-4, multidentate support Si-O-Ti^{IV} connectivity is possible in principle, at the expense of breaking some Ti-O(calix) bonds. To address this, we measured calix[4]arene-Ti ligand-to-metal charge-transfer (LMCT) edge-energies, since this energy has been previously reported to be sensitive to the number of covalent connections between calix[4]arene oxygens and grafted Ti^{IV} cations (see Chapter 4).[33] These values are all measured to be 2.25 ± 0.05 eV for all **calix-Ti/SUP** materials (Table 5.1), consistent with tridentate calix[4]arene connectivity and single-point attachment to support, as two-point attachment of the calix[4]arene would have resulted in a lower edge energy of 2.14 eV (see Section 5.5.5).[33] This confirms the equivalent inner-sphere coordination for Ti^{IV} in all catalysts, as depicted in Scheme 5.1.

To investigate possible variations in electronic environment of Ti^{IV} centers grafted on different supports, we performed Ti K-edge XANES,[34,35] with results shown in Figure 5.2. Pre-edge features, highlighted in the insert of Figure 5.2, arise from electronic transitions of core electrons into empty 3d orbitals of d^0 Ti^{IV}, and are thus a descriptor of 3d orbital availability and Lewis-acid strength.[35] This descriptor is quantified by the value of A_{rel} in Table 5.1 (Sections 5.5.1.3 and 5.6), and its value of 0.9 together with pre-edge positions at 4970 eV is consistent with site-isolated 4-coordinate Ti^{IV} centers within grafted calix[4]arene-Ti surface complexes.[3,35,36] The lack of changes in these values and pre-edge peak heights across all materials (Figure 5.2 and Table 5.1), within experimental uncertainty, confirms the identical 3d orbital occupancy and inner-sphere of Ti^{IV} centers across all catalysts.

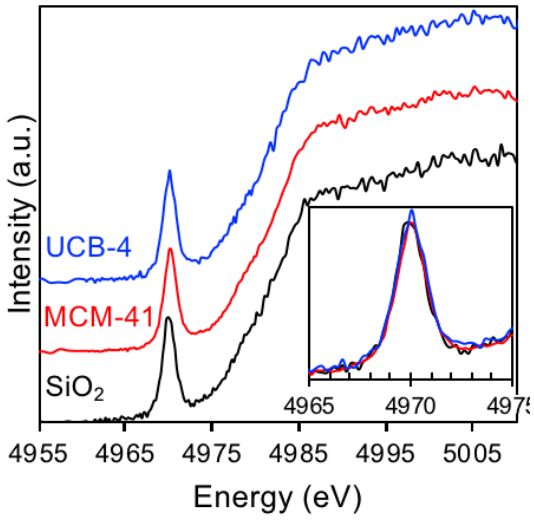

Figure 5.2. Normalized Ti K-edge XANES spectra, with insert detailing the pre-edge region, for calix[4]arene-Ti^{IV} sites on the labeled support.

Rate constants normalized by Ti^{IV} contents (k_{eff}) for the epoxidation of cyclohexene with *tert*-butyl hydroperoxide (Scheme A5.3), a common probe reaction for epoxidation activity, are summarized in Table 5.1 for all **calix-Ti/SUP** catalysts, with epoxide yields uniformly high (Figure A5.6B). Values of k_{eff} are observed to be 4- and 5-fold higher in crystalline **calix-Ti/UCB-4**, as compared to amorphous **calix-Ti/MCM-41** and **calix-Ti/SiO_2**, respectively. Similar enhancements favoring **calix-Ti/UCB-4** are also observed when quantifying turnover numbers for epoxide production (Figure 5.3), irrespective of whether the amorphous support contains a well-ordered porous system in MCM-41 or not (SiO_2). We surmise that, on a single-site basis, all Ti^{IV} centers behave similarly when grafted on amorphous supports, as described previously,[26] but with distinctly lower activity than on crystalline **calix-Ti/UCB-4**. Control experiments were performed to confirm that the high-activity in **calix-Ti/UCB-4** relative to the amorphous catalysts is not due to artifacts of the delamination, acid washing treatment, presence of B^{III}, or diffusional constraints, is independent of calix[4]arene-Ti^{IV} surface density (Section 5.5.3), and is generalizable to other olefins and oxidants (Section 5.5.7). Significantly, calix[4]arene-Ti^{IV} sites grafted on fully hydroxylated SiO_2 (**calix-Ti/SiO_2-AW** in Section 5.5.3) exhibit rates equivalent to those of **calix-Ti/SiO_2** (k_{eff} = 8 $M^{-2}s^{-1}$), indicating that silanol pairing as achieved by high local silanol densities on amorphous silicates is alone insufficient for enhancing reactivity.

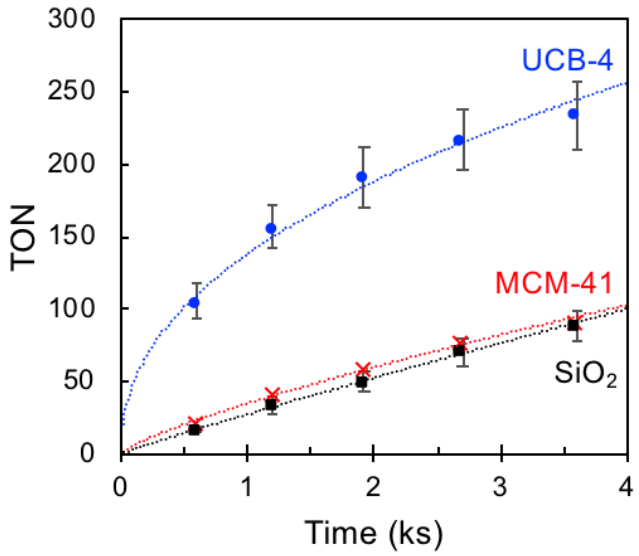

Figure 5.3. Catalytic turnover numbers (TON) for epoxide production as a function of time, for calix[4]arene-Ti^{IV} sites on the labeled support.

Based on the identical electronic and inner-sphere environments of grafted Ti^{IV} for all catalysts, active sites would be expected to display similar epoxidation rates in the absence of outer-sphere effects; however, they are instead observed to be up to 5-fold more active when grafted on the crystalline framework of UCB-4, in comparison to amorphous supports. We conclude that these enhancements in rate are brought about by outer-sphere effects intrinsic to the support in **calix-Ti/UCB-4**. These effects specifically involve paired silanols located within 12-MR pockets in UCB-4, distinct from those present in fully hydroxylated amorphous SiO_2, where surface heterogeneity precludes a precise location of silanol pairs with respect to active centers. Calix[4]arene-Ti^{IV} grafting on UCB-4 may occur one of the two silanols in the organized pair –

thereby leaving one silanol in close proximity to the site –, or on the exterior surface, adjacent to the silanol pair. In either scenario, the existence of a neighboring silanol may facilitate the activation of bound intermediates (e.g. for hydroperoxide binding or subsequent transfer of oxygen to epoxide),[37,38] giving rise to the observed outer-sphere effects. While these effects have long been hypothesized,[39] challenges in controlling Ti^{IV} inner-spheres[40] and steric accessibility across supports have precluded their observation,[26,27] despite decades of seminal work.[41,42] Our synthetic approach overcomes these challenges, providing the first rigorous experimental demonstration of outer-sphere effects on per-site activity in titanosilicates.

5.4. Conclusions

Our findings evidence the role of organization and location of outer-sphere functionalities for catalysis on surfaces, analogous to outer-sphere residue cooperativity within active sites of certain protease enzymes.[43] By exploiting delaminated zeotypes as accessible crystalline supports with well-defined surface environments, optimal active sites that incorporate outer-sphere functionalities can be rationally designed. Such approaches may lead to improvements in olefin epoxidation catalysts,[44,45] where state-of-the-art technologies still rely on amorphous supports when using organic hydroperoxides as oxidants,[19-21] and in catalysis on surfaces in general, where the control over the organization of structural environments surrounding active centers is only beginning to emerge.

5.5. Appendices

5.5.1. Experimental Methods

5.1.1.1. Support Preparation

Aerosil® 200 (Evonik) was used as a representative amorphous silica support. It was hydroxylated in refluxing water at 393 K for 16 h, dried, and sieved, followed by dehydroxylation under Ar at 823 K for 6 h to achieve a surface dominated by isolated hydroxyl groups (~1 /nm^2).[46] MCM-41 was chosen as comparative amorphous support with ordered porosity (see section 5.5.2), and was obtained from Sigma-Aldrich; it was pretreated by high temperature treatment under Ar at 823 K for 6 h. Both pretreated supports were kept under an inert Ar atmosphere until further handling. These supports are represented by SiO_2 and MCM-41 in Scheme A5.1. A select SiO_2 sample, denoted as SiO_2-AW was treated with 2 M HNO_3 for 18 h at 373 K, filtered, washed with copious water, and dried at 120˚C.

The delaminated zeotype studied is UCB-4,[22] synthesized by delamination of borosilicate precursor B-SSZ-70(P), followed by B^{3+} removal, as depicted in Scheme A5.1 (i). B-SSZ-70(P) was crystallized in PTFE autoclaves at 423 K for 8 days, from a synthesis gel with molar composition 1 SiO_2 (Aerosil 200): 30 H_2O: 0.175 1,3-diisobutylimidazolium hydroxide: 0.1 H_3BO_3; it was washed with copious amount of H_2O, and its identity was confirmed by comparison of its powder X-ray diffraction (PXRD) pattern with literature precedent.[47] Calcination treatment of B-SSZ-70(P) would result in 3-D zeolite B-SSZ-70. Instead, B-SSZ-70(P) was delaminated into UCB-4 via modified previously developed protocols:[22] a mixture of 5.0 g of B-SSZ-70(P) per 5.5 g of cetyltrimethylammonium bromide (CTAB) (Sigma-Aldrich, ≥99.0%), 8.5 g of tetrabutylammonium fluoride trihydrate (TBAF) (Sigma-Aldrich, ≥97%), and 8.5 g of tetrabutylammonium chloride (TBACl) (Sigma-Aldrich, ≥97%) and 20 mL of DMF (Fisher Scientific) was placed in a screw-capped 500 mL PFA tube, and stirred at 373 K for 72 h. After cooling, the slurry was sonicated for 1 h in an ice bath, using a Branson digital sonifier 450 operating under pulse mode (1.0 s on and 0.1 s off). The sonicated slurry was centrifuged to separate the solid, and washed with DMF (1x50 mL) and 1,4-dioxane (3x50 mL) under centrifugation, dried at 323 K overnight, and treated in air at 823 K for 6 h after a 1 K/min ramp. Framework B^{3+} was removed to generate vacancy defects, by treatment of 500 mg of delaminated zeolite with 50 mL of 2N HNO_3 at 373 K for 18 h, followed by filtration and washing with copious amounts of H_2O. This resulted in material **UCB-4**, depicted in Scheme A5.1.

Scheme A5.1. Summary of materials synthesis strategy.

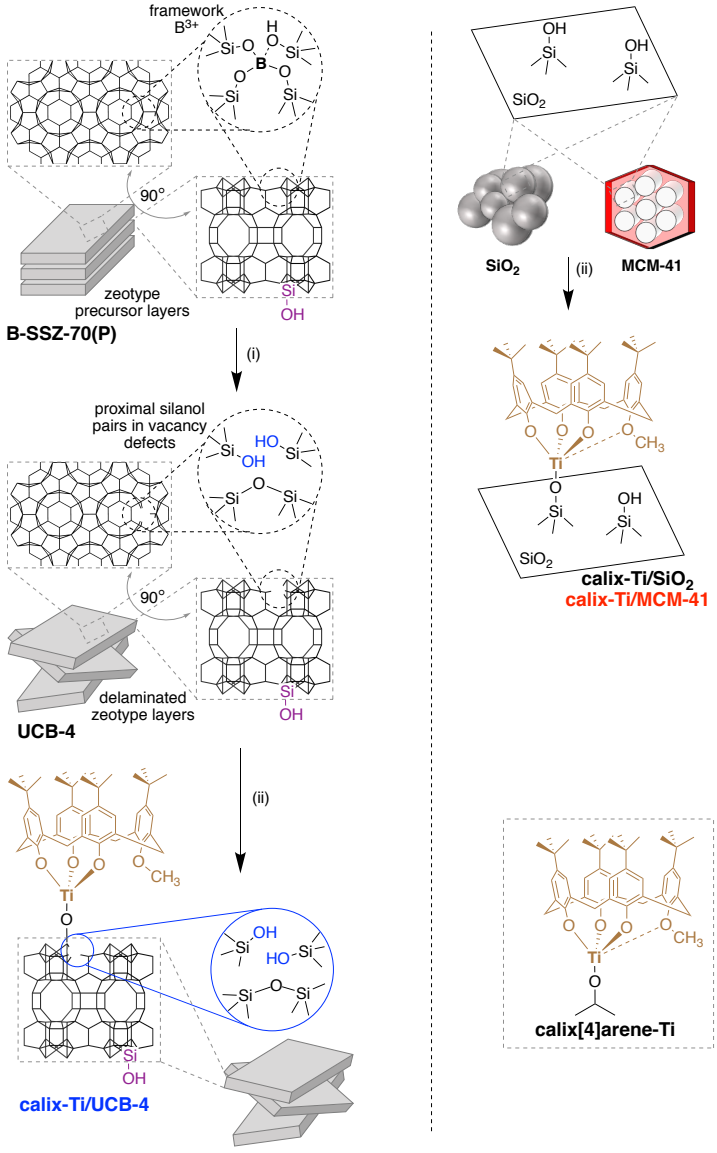

Schematic representation of materials synthesis procedure. Details of the crystalline zeotype framework of SSZ-70 and UCB-4 are shown along the a-c plane and rotated 90° along the a-b plane (top left), with vertices representing $SiO_{4/2}$ tetrahedra centers and lines Si-O-Si bonds. (i) Delamination of B-SSZ-70(P) into UCB-4 is achieved by heating in the presence of surfactant and ammonium halide salts, followed by sonication, washing, calcination, followed by acid washing (see section 5.5.1.1). This final step removes B^{3+} exposing a framework vacancy consisting proximal silanol pairs. Zeotype layers are schematically shown as rectangles; delamination causes extensive disordering of these layers, thereby increasing the accessible external surface of the support. (ii) Ti^{IV} incorporation onto supports is achieved by treatment of the dehydrated support in the presence of the calix[4]arene-Ti^{IV} precursor (shown bottom right) in refluxing toluene, which results in its condensation with a support silanols. These silanols are randomly distributed on the surface of amorphous SiO_2 and MCM-41 (right), or pre-organized into pairs within vacancies (left).

5.5.1.2. Ti^{IV} Incorporation onto Siliceous Supports

Ti^{IV} incorporation was achieved by grafting of calix[4]arene-Ti^{IV} complex (Scheme A5.1, bottom right) on supports through condensation of precursor with support silanols, as depicted in Scheme A5.1 (ii). The choice of this precursor complex leads to deposition of site-isolated Ti^{IV}, as opposed to ill-defined oligomeric TiO_2 oxides formed by self-condensation of commonly used alkoxide or halide Ti^{IV} precursors, and prevents Ti^{IV} incorporation into micropores which are too small to accommodate diffusion of the precursor complex.[48] This limits Ti^{IV} deposition to the external surface of all supports, ensuring its uniform coordinative unsaturation and reactant accessibility, thus enabling catalytic comparison of all materials under similar reactant diffusion regimes.

The calix[4]arene-Ti^{IV} complex was prepared by following previous synthesis protocols,[49,50] and successful synthesis was confirmed by liquid-phase ^1H NMR spectroscopy. Covalent attachment of calix[4]arene-Ti^{IV} to the support (grafting) was achieved by suspending moisture-free supports in toluene, adding the calix[4]arene-Ti^{IV} complex dissolved in toluene, refluxing the suspension for 18 h, followed by washing with copious amount of hot toluene, resulting in materials **calix-Ti/SiO_2**, **calix-Ti/MCM-41**, and **calix-Ti/UCB-4**. Control materials based on other supports detailed in section 5.5.3 were prepared in the same manner, with **calix-Ti/UCB-4(low)** being prepared by limiting the amount of calix[4]arene-Ti^{IV} complex dissolved in toluene during grafting.

5.5.1.3. General Analytical Methods

Support surface areas were determined by the BET method from N_2 physisorption measurements performed with a Micromeritics ASAP 2020 instrument at 77 K after sample evacuation at 623 K for 4 h. External surface areas and micropore volumes were calculated by the t-plot method.[51]

Carbon-hydrogen-nitrogen analysis was performed at UC Berkeley Microanalytical facility using a Perkin Elmer 2400 Series II combustion analyzer, and grafted calix[4]arene loadings were estimated by assuming that carbon contents were entirely due to the presence of calixarenes. Ti contents were measured by ICP-AES at Galbraith Laboratories, unless otherwise noted.

Select noted samples were analyzed by thermogravimetric analysis (TGA), performed with a Netzsch 449C Jupiter TGA instrument by treating a sample in a mixed gas flow consisting of 20% O_2 and 80% Ar from room temperature to 1073 K at a ramp rate of 5 K/min. Calix[4]arene contents in these grafted materials were determined by assuming that during treatment in air up to 1073 K, any additional mass loss when compared to the bare support was due to combustion of the calix[4]arene ligand. Ti^{IV} contents were measured in these grafted materials by spectrophotometric quantification of products formed by aqueous H_2O_2 treatment of Ti^{IV} extracted from materials by neat sulfuric acid (1 mL per 20 mg of material).[5]

Diffuse reflectance UV-visible spectra were measured at ambient conditions by using a Varian Cary 4000 Spectrophotometer fitted with a Praying Mantis attachment from Harrick Scientific Instruments. Compacted poly-(tetrafluroethylene) powder was used as a standard perfect reflector for the baseline corrections, and all spectra are reported using Kubelka-Munk pseudoabsorbance, F(R), and normalized to the maximum value of absorbance. Ligand-to-metal charge-transfer

(LMCT) edge-energies of calix[4]arene-Ti^{IV} containing materials were calculated following methods previously used for titanocalixarenes.[3] See Figure A5.3 for example of calculation: slopes of tangent lines as shown were calculated from the first derivative of the transformed spectra, and were drawn tangent to the spectra at their point of inflection. The intersection of this line with the horizontal axis was taken as the LMCT edge-energy, denoting onset of absorption.

Ti K-edge spectra were acquired using a fluorescence detector and a Si(111) monochromator at beamline 2-2 of SSRL (Stanford Synchrotron Radiation Lightsource, SLAC National Accelerator Laboratory, Menlo Park, California, USA). Energies were calibrated in transmission mode against a Ti^0 foil standard with known absorption edge energy (4966 eV), with edge energies determined as the first inflection point of normalized spectra. X-ray adsorption spectra were acquired between 4766 eV and 5200 eV, with a maximum resolution in the pre-edge of 0.2 eV. Multiple spectra were acquired and coadded to improve signal-to-noise ratios due to low Ti^{IV} contents in materials being studied. Spectra were measured while samples were treated at 453 K under 20 mL/min He flow in a Nashner-Adler reaction cell, in order to remove moisture. Pre-edge features are known to be affected by ambient moisture,[35] and preliminary measurements were done to determine that no changes in spectral features occur with treatment above this temperatures (i.e. 453 K is sufficient to remove any coordinating water). Athena XAS analysis software was used to perform quantitative data analysis. Spectra were normalized to a pre-edge straight line fit in the range 4905-4950 below the edge, and to 2^{nd} order polynomial fit between 4985 and 5200 eV above the edge. As in previous studies, the normalized Ti K-edge was fit to an arctan function, while the pre-edge features were fit to four Gaussian peaks, labeled A1, A2, A3, and B, in order of ascending energy, with centers constrained to lie within, respectively, 4968–4969 eV, 4969–4971 eV, 4971–4972, and 4973–4974 eV.[3,35,36] Details of spectral fits are included in Section 5.5.6.

^1H MAS NMR and ^1H SQ-DQ MAS NMR experiments were performed using a Bruker Avance DSX 400 spectrometer at a ^1H Larmor frequency of 400 MHz, utilizing the software Topspin 1.3. The MAS NMR measurements were carried out with the EASY pulse sequence to remove a background from the NMR.[52] Chemical shifts were referenced with adamantane ($\delta(^1H)$=1.78 ppm) and the rf power on the ^1H channel was 62.5 kHz. The samples were packed in a 4 mm ZrO_2 with a Kel-F cap under dry nitrogen atmosphere to prevent the samples from rehydration. The samples were measured with a MAS rate of 9000 Hz. For the excitation and reconversion blocks of the DQ experiments, the BABA pulse sequence (one rotor period each) was used.[53]

The ^1H double quantum build-up curves were acquired with a Bruker Minispec under static conditions (^1H Larmor frequency of 19.56 MHz). The samples were packed in a glass tube under dry nitrogen atmosphere, then the tube was sealed. The analysis of raw data was performed with Origin 2017, the simulations of the curves and were performed with the program ftikreg.[31]

NMR experiments were performed on SSZ-70, the non-delaminated variant of UCB-4. For these studies, B-SSZ-70(P) was synthesized in fluoride media to obtain defect free zeolite crystals, per the following procedure: into a tared reactor were added 2.08 g of tetraethyl orthosililicate (10 mM of SiO_2), 11.11 g of an aqueous 0.45 M solution diisobutyl imidazolium hydroxide (5 mM), and 0.062 grams of boric acid. The reactor was closed and the TEOS allowed to hydrolyze at room temperature for 2 days, after which the reactors were opened and water and

ethanol were evaporated by air flow in a fume hood. Once evaporation caused the reactant masses in the reactors to reach 1.70 g, (H_2O:SIO_2 ~7), 0.185 grams of 50% HF (~ 5 mM) were added. The reactors were closed and heated to 423 K while being tumbled at 43 rpm, for 8 days. The products were washed with copious water before drying and then assessed as SSZ-70 by PXRD. The resulting B-SSZ-70(P) was calcined as for UCB-4 to obtain B-SSZ-70, and subsequently acid-treated as for B^{3+} removal of UCB-4 (above) to result in SSZ-70. Prior to NMR experiments, zeolite samples were treated under dynamic vacuum at 393 K for 1 h to remove atmospheric water.

5.5.1.4. Catalytic Characterization.

Rates of cyclohexene epoxidation with *tert*-butyl-hydroperoxide (TBHP), shown in scheme A5.3, were measured in batch reactors with external temperature control. ~25 mg of catalyst and ~300 mg of molecular sieves were evacuated at 393 K (1h) to remove moisture, a known catalyst poison,[54] followed by cooling to 323 K and addition of 20 mL of octane (distilled from Na) and 0.3 mL of cyclohexene (distilled from CaH_2). Addition of 0.1 mL of TBHP in n-decane (concentration 5.9 M measured by iodometric titration)[55] initiated epoxidation, the progress of which was monitored by comparing gas chromatograph peak areas of aliquots removed from the reactor to external references prepared with known concentration of reactants and products, while reproducible injection volumes were ensured by the n-decane internal standard. Select experiments were performed with 1-octene and cis-stilbene as olefins, and ethylbenzene hydroperoxide as oxidants. Reactant concentrations and temperature were kept unchanged with respect to the above conditions used for cyclohexene oxidation with TBHP.

Epoxidation rates are known to be proportional to catalyst, alkene, and oxidant concentrations:[25]

$$\text{rate} = \frac{d[\text{TBHP}]}{dt} = k_{eff}[\text{Ti}][\text{alkene}][\text{TBHP}] \qquad \text{(A5.1)}$$

In all reactions, initial [alkene]:[TBHP] ratios were in excess of 5, allowing the determination of a pseudo first-order rate constant, k_{eff}, as the slope of the linear plot of -ln(1-X)/[cyclohexene]/[Ti] vs. time, where conversion X = 1- [TBHP]/$[\text{TBHP}]_0$, and $[\text{TBHP}]_0$ is initial oxidant concentration. Turnover numbers were measured as TON = [epoxide]/[Ti] at any given time, and denote the per-active site productivity towards the desired product. Note that square brackets [] denote concentration, while initial concentrations are noted by a $_0$ subscript, $[]_0$.

5.5.2. Support Textural Properties

Table A5.1 summarizes all textural properties for supports under study, for amorphous materials and the delaminated zeolite. The former, SiO_2 and MCM-41, have very different surface areas (S_{BET}) and porosity, with MCM-41 consisting in uniform mesopores, as indicated by sharp increase in gas uptakes at P/P_0 ~0.35 in Figure A5.1. These mesopores are 2.1-2.7 nm wide (manufacturer specification, Sigma-Aldrich) and were measured to have an average width of 2.6 nm after analysis of the data in the isotherm of Figure A5.1 by the BJH method.[56] In contrast, SiO_2 has no well-defined pore system. This enables a comparison into the effect of pore structure on catalytic activity for amorphous materials.

When comparing non-delaminated B-SSZ-70 to delaminated B-UCB-4, external surface area increases by a factor of ~2 (Table A5.1) due to exfoliation of precursor layers, and total pore volume increases due to porosity generated between disorderly stacked layers up. Micropore volume decreases upon delamination, consistent exposure of surface in the inter-layer space that would be found inside inaccessible micropores. Acid washing of B-UCB-4 to remove B^{3+} and synthesize UCB-4 does not significantly affect external surface areas but somewhat decreases micropore volumes because additional mesoporosity created by extensive defect formation within zeolitic frameworks. Properties of B-UCB-4 used for grafting density calculations in main text.

Table A5.1. Full support textural properties.

Support	S_{BET} (m^2/g)[a]	S_{ext} (m^2/g)[b]	V_{micro} (m^2/g)[b]	V_{tot} (m^2/g)[c]
B-SSZ-70	-	68.9	0.197	0.32
B-UCB-4	-	136	0.166	0.47
UCB-4	-	129	0.144	0.46
SiO_2	190	175	n/a	1.19
MCM-41	913	955	n/a	0.90

B-UCB-4 corresponds to support before acid washing for removal of framework B^{3+}. B-SSZ-70 corresponds to B-SSZ-70(P) calcined in air at 823 K for 6 h after a 1 K/min ramp. [a]Determined from the BET method, and used to quantify accessible surface area for amorphous, non-microprous silica materials (Table 5.1); not a valid analysis for microporous materials, thus omitted. [b]External surface (S_{ext}) area and micropore volumes (V_{micro}) determined from the t-pot method; S_{ext} used to quantify the accessible surface area of microporous materials. [c]Determined from total analysis gas uptakes.

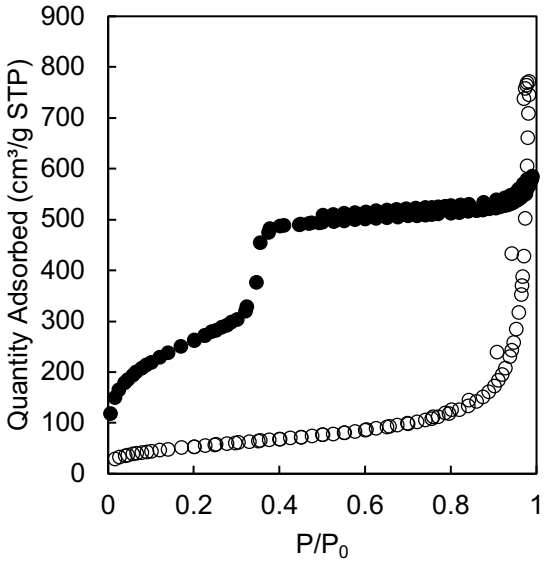

Figure A5.1. N_2 physisorption isotherms at 77K for amorphous materials described in Table A5.1: MCM-41 (●), Aerosil SiO_2 (o).

5.5.3. Physicochemical and Catalytic Properties of Control Materials and Evaluation of Grafting Densities

Several control materials were prepared: (i) non-delaminated, acid-washed SSZ-70 from B-SSZ-70; (ii) acid-washed Aerosil, SiO_2-AW; (iii) UCB-4(low), where the amount of calix[4]arene-Ti^{IV} in solution during grafting on UCB-4 was limited to result in sub-monolayer coverages, (iv) Ti^{IV}-free B-UCB-4, where B^{III} sites are not removed, and (v) MCM-41(high), with higher calix[4]arene-Ti^{IV} loading than the material reported in the main text. These materials serve to assess whether (i) (SSZ-70) delamination treatment, (ii) (SiO_2-AW) acid-washing, (iii) (UCB-4(low)) surface density of calix[4]arene-Ti^{IV}, (iv) (B-UCB-4) presence of B^{III} centers, and (v) (MCM-41(high)) diffusional constraints affect catalytic properties. Acid-washing subjects SiO_2-AW to full hydroxylation relative to silica supports pretreated at 823 K in the main text, and serves as a control to evaluate the effect of hydroxylation and silanol pairing/association on an amorphous support. Note also that acid-washing fully removes B^{III} from the zeolitic framework,[57] and no B^{III} sites are expected to remain or contribute to catalysis, which is confirmed experimentally below. Grafted materials on these supports are denoted **calix-Ti/SSZ-70** and **calix-Ti/SiO_2-AW**, and **calix-Ti/UCB-4(low)**, and **calix-Ti/MCM-41(high)**. Note that **B-UCB-4** consists of the bare support and does not contain Ti^{IV}.

The physicochemical properties of grafted materials and those in the main text are summarized in Table A5.2. Calix[4]arene:Ti ratios of ~ 1 indicate intact grafting of the complex, as for other materials discussed in the main text. Calix[4]arene-Ti^{IV} grafting densities (Table A5.2, normalized per external SiO_2 surface area) of 0.38 Ti/nm^2 for **calix-Ti/UCB-4** reflect a higher density of silanols relative to partially dehydroxylated amorphous supports in **calix-Ti/SiO_2** (0.25 Ti/nm^2) and **calix-Ti/MCM-41** (0.11 Ti/nm^2). The external surface of **MCM-41** includes that

within its mesopores, which are wide enough to accommodate diffusion of calix[4]arene-Ti^{IV}, and we thus expect grafting to occur mainly inside these mesopores; the higher specific surface area of **MCM-41** (Table A5.1) provides a higher surface for grafting and results in substantially higher Ti contents in these materials (Table A5.2). Grafting densities are lower than what would be expected form a 14 x 14 Å footprint of *t*-butyl-calix[4]arene (0.51 /nm^2), and reflect grafting by random irreversible chemisorption, which prevents equilibration into full monolayer coverage. By limiting the amount of calix[4]arene-Ti^{IV} in solution during grafting, converges in **calix-Ti/UCB-4(low)** are only of 0.17 Ti/nm^2. Delamination of SSZ-70 layered zeolite precursor to synthesize UCB-4 increases accessible external surface area two-fold (Table A5.1), but grafting densities remain constant at 0.37 Ti/nm^2 (Table A5.2) when excess calix[4]arene-Ti^{IV} is used in synthesis, and are similar to that observed on fully hydroxylated SiO_2-AW (0.38 Ti/nm^2), which suggests this may be the maximum grafting density on a fully hydroxylated siliceous surface. This implies that grafting occurs exclusively on the external surface of the zeolite support; otherwise, if any grafting occurred in micropores, densities normalized on an external surface basis as in Table A5.2 would be considerably higher than the maximum on fully hydroxylated SiO_2, and would change upon delamination.

We note that silanol densities on amorphous SiO_2 are expected to be ~ 1/nm^2,[46] and higher for SiO_2-AW. Comparison of NMR intensities in Figure 5.1 of the main text makes it evident that deboronated SSZ-70 exhibits much higher silanol contents than SiO_2. Thus, all materials examined by NMR spectroscopy exhibit silanol densities much higher than calix[4]arene-Ti^{IV} grafting densities listed in Table A5.2, implying that grafting would not result in significant consumption of silanol groups, and would therefore not affect the conclusions drawn from NMR spectra in Figure 5.1, which consists of bare support and do not contain grafted calix[4]arene-Ti^{IV}.

Rates of epoxidation for control materials are summarized as rate constants Table A5.2 (k_{eff}) and as turnover numbers as function of time in Figure A5.5. k_{eff} (Table A5.2) and turnover numbers (Figure A5.5) as a function of time for **calix-Ti/SSZ-70** and **calix-Ti/UCB-4(low)** are similar to those of **calix-Ti/UCB-4** (Figure A5.5 green and purple vs. blue), and significantly higher than those on any amorphous material. When comparing these three crystalline materials, rate constants are within 30%, a small difference when compared to the to the five-fold difference in rates when comparing **calix-Ti/UCB-4** to **calix-Ti/SiO_2**. The comparison of **calix-Ti/SSZ-70** and **calix-Ti/UCB-4** indicates that delamination treatment does not affect catalytic activity. In addition, the comparison of **calix-Ti/UCB-4** and **calix-Ti/UCB-4(low)** indicates that the reactivity does not depend on surface grafting density in UCB-4, and that these grafted species behave as "single-sites" that react independent of each other, as previously observed when grafted on amorphous SiO_2.[25] Finally, a negligible amount of epoxide production is found when using B-UCB-4, the bare B^{III}-containing support without calix[4]arene-Ti^{IV}, as catalyst (<0.5 % yield after 2 h, compared to yields up to 80% within 1 h in Figure A5.6B), indicating that B^{III} centers are inactive for epoxidation.

Separately, turnover numbers are similar between **calix-Ti/SiO_2** and **calix-Ti/SiO_2-AW** (black vs. orange traces in Figure A5.5), and k_{eff} epoxidation rates are also within the ±1 uncertainty of each other. This indicates that acid-washing does not affect epoxidation rates normalized by Ti^{IV} contents for amorphous supports, even if grafting densities are significantly higher on SiO_2-AW than on SiO_2. Therefore, acid-washing, necessary in the preparation of UCB-4, is not responsible

for any catalytic enhancement. More importantly, calix[4]arene-Ti^{IV} sites grafted on fully hydroxylated calix-**Ti/SiO_2-AW**, which consists of similar silanol densities as UCB-4 as explained above, exhibit rates equivalent to those of **calix-Ti/SiO_2** (k_{eff} = 8 $M^{-2}s^{-1}$). We surmise that silanol pairing as achieved by high local densities on amorphous silica is therefore insufficient for optimal activity: location of these paired silanols within the crystalline framework cups of UCB-4 also plays a decisive role in catalysis.

Finally, control material **calix-Ti/MCM-41(high)** exhibits 20% higher calix[4]arene-Ti^{IV} loadings and grafting densities compared to **calix-Ti/MCM-41**. This implies that calix[4]arene-Ti^{IV} in **calix-Ti/MCM-41(high)** will graft deeper in the 1-D mesopores of MCM-41 compared to **calix-Ti/MCM-41**, and would be under more severe diffusional constraints if these constraints are present under this experimental regime. Rate constants are, however, within 10% of each other on a per site basis (Table A5.2) and turnover numbers are similar between these two materials (Figure A5.5), excluding any significant impact of diffusional constraints on the activity of calix[4]arene-Ti^{IV} sites inside the pores of MCM-41, compared to the unhindered surface of SiO_2. These two amorphous surfaces thus behave similarly to each other.

Table A5.2. Physicochemical and catalytic properties of control materials.

Support	wt. % Ti	Calix:Ti	Ti/nm^2	k_{eff} ($M^{-2}s^{-1}$)
SSZ-70	0.19	1.4	0.37	33
SiO_2-AW	0.51	1.0	0.38	8
B-UCB-4[b]	n/a[c]	n/a	n/a	n/a[d]
UCB-4(low)	0.13	0.9	0.17	32
UCB-4[a]	0.37	1.1	0.38	42
SiO_2[a]	0.35	1.0	0.25	8
MCM-41[a]	0.70	1.0	0.11	10
MCM-41(high)	0.84	0.9	0.14	9

[a]Corresponds to materials in the main text. Calixarene and Ti contents for control materials were determined from thermogravimetric analysis and UV-visible Ti assay (see Section 5.5.1.3). [b]Corresponds to a B-UCB-4 material that was not subject to B^{III} removal and onto which no Ti was incorporated. [c] ~0.5 wt% B. [d] Less than 0.5 % yield of epoxide after 2 h of reaction, with ~ 5% conversion of oxidant.

5.5.4. ^{1}H SQ-DQ MAS NMR Experiments

We investigated changes accompanying deboronation of SSZ-70 zeolite by following this on a calcined sample (same conditions as used for catalyst synthesis in Scheme A5.1) using solid-state NMR spectroscopy. The ^{1}H MAS NMR spectrum of calcined B-SSZ-70 shows low intensity between 2 ppm – 8 ppm, where resonances corresponding to hydrogen-bound BOH and silanols of not fully anchored boron sites, as they were found previously for calcination temperatures below 823 K.[58,59] Additionally, there is a sharp line at 1.8 ppm, which is mainly due to silanols on the crystal-terminating external surface (see Figure A5.2Aa). After deboronation of this sample, substantial intensity is generated in the region expected for hydrogen-bound silanols. Deconvolution of the same spectral region for the deboronated sample shows a decrease in the

sharp resonance at 3.2 ppm in the projection of the ^{1}H SQ-DQ MAS NMR spectrum (Figure A5.2Bb) compared to the single-quantum ^{1}H MAS NMR spectrum (Figure A5.2Ba). This decrease in intensity allows greater resolution of resonances associated with hydrogen-bound silanols in the double-quantum spectrum, and may in principle be due to the 3.2 ppm resonance being represented by either an isolated silanol group or adventitious mobile water.

The double quantum spectra show clear differences in the homonuclear coupling between the sample before and after deboronation. The calcined B-SSZ-70 exhibits a weak autocorrelation signal for hydrogen-bound BOH and SiOH in Figure A5.2Ca. In contrast, the spectrum of the deboronated sample in Figure A5.2Cb consists of two well-resolved cross-correlation peaks, which represent two silanols that comprise different chemical shifts.

The measurement of double quantum build-up curves reveals the strength of the dipolar coupling of ^{1}H-^{1}H coupled pairs contributing to the double quantum spectrum. Intensities of the double-quantum and single-quantum reference signals were obtained by averaging the initial part of the free induction decay (15 μs for SSZ-70 and 40 μs for SiO_2 and normalized with respect to the highest reference intensity). Since the dipolar coupling is proportional to $1/r^3$ (r: ^{1}H-^{1}H distance), distributions of ^{1}H-^{1}H distances are obtained. This method is pair-selective which means that a derived dipolar coupling constant reflects the distance between two protons, irrespective of a possibly higher number of protons adjacent to the pair. This method provides quantitative information on the relative abundance of silanol pairing, whereas the high-resolution DQ spectral intensities (such as shown in Figs. 1 and A5.2C) cannot be directly compared in a quantitative manner. Double quantum build-up curves were measured for deboronated SSZ-70 and SiO_2. The resulting dipolar coupling constants needed to be scaled with a conversion factor of 2/3, as the program ftikreg assumes the Baum-Pines pulse sequence to be used, while the experiments had to be carried out with a 3 pulse sequence.

The normalized DQ build up curve along with the derived distance distribution of deboronated SSZ-70 is shown in Figure A5.2Da. Two maxima are found in the distribution of dipolar couplings at 1.5 kHz and 7.5 kHz, which correspond to distances of 4.3 Å and 2.5 Å, respectively (see Figure A5.2Db). The distance of 2.5 Å is assigned to the silanols generated by boron extraction (broad signals at 3.3 ppm and 4.0 ppm). The distance of 4.3 Å on the other hand can be interpreted as the average ^{1}H-^{1}H distance of the external SiOH on the crystal-terminating surface (narrow signal at 1.8 ppm), depicted in purple in Scheme 5.1 of the main text.

On the other hand, the normalized DQ build up curve for the calcined SiO_2 cannot be simulated in a physically meaningful way (Figure A5.2Da), as it instantly jumps at the expected plateau at 0.5. This hints at a very large dipolar coupling constant present in the sample with at least 15 kHz, possibly due to rigid water. An exact measurement is not possible with the used setup. Protons with such a strong dipolar coupling are not detectable with the spinning speeds (9 kHz) applied in the 2D high-resolution DQ spectrum. Therefore, these rigid water molecules are not visible in the high-resolution spectrum of Fig 1B. Vice-versa, the sharp autocorrelation signal shown in Figure 5.1B must be of extremely low abundance, because such a sharp DQ signal is below detection limit in the DQ build-up measurements.

The amount of isotropic mobile ^{1}H (meaning isolated ^{1}H) can be obtained by fitting of different evolution time regions of the functions of the function $I_{ref} - I_{DQ}$ with monoexponential functions in the form of ω*exp(-x/t) with I_{ref} = normalized reference intensity and I_{DQ} = normalized double

quantum intensity for each given evolution time τ_{DQ}. ω denotes the fraction of corresponding ^1H. For the deboronated SSZ-70 (see Figure A5.2Ea), the amount of isolated ^1H ω_{iso} is found to be 30%, while the amount of weakly coupled silanols $\omega_{dd,weak}$ is 36% (4.3 Å apart). This leaves 34% of the observed ^1H for the "paired silanols" (2.5 Å apart). In the same way, the amount of isolated ^1H in SiO_2 is found to be $\omega_{iso,1} + \omega_{iso,2} = 82\%$ (Figure A5.2Eb), while 18% of ^1H are very strongly dipolar coupled, most likely as rigid water molecules captured in the bulk volume of the SiO_2. Figure A5.2Eb also shows that the signal intensity for the deboronated SSZ-70 decreases much faster with increasing evolution time than for SiO_2. There are far more silanols, whose ^1H are dipolar coupled in SSZ-70.

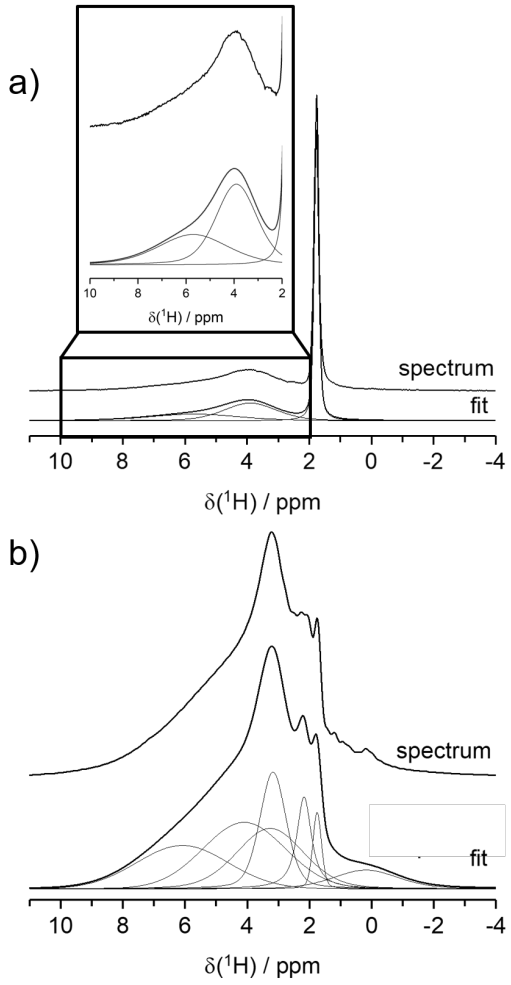

Figure A5.2A. ^1H MAS NMR spectra of the a) calcined B-SSZ-70 and b) the deboronated SSZ-70.

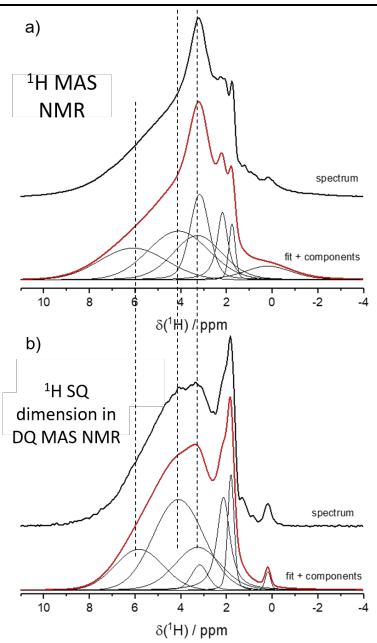

Figure A5.2B. a) ^{1}H MAS NMR spectra and deconvolution and b) projection of the SQ dimension from the ^{1}H SQ-DQ MAS NMR spectra in Figure A5.2Cb of the deboronated SSZ-70.

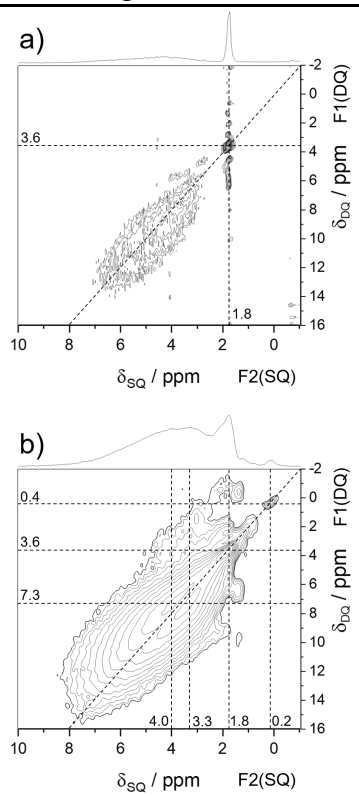

Figure A5.2C. ^{1}H SQ-DQ MAS NMR spectra of the a) calcined B-SSZ-70 and b) the deboronated SSZ-70.

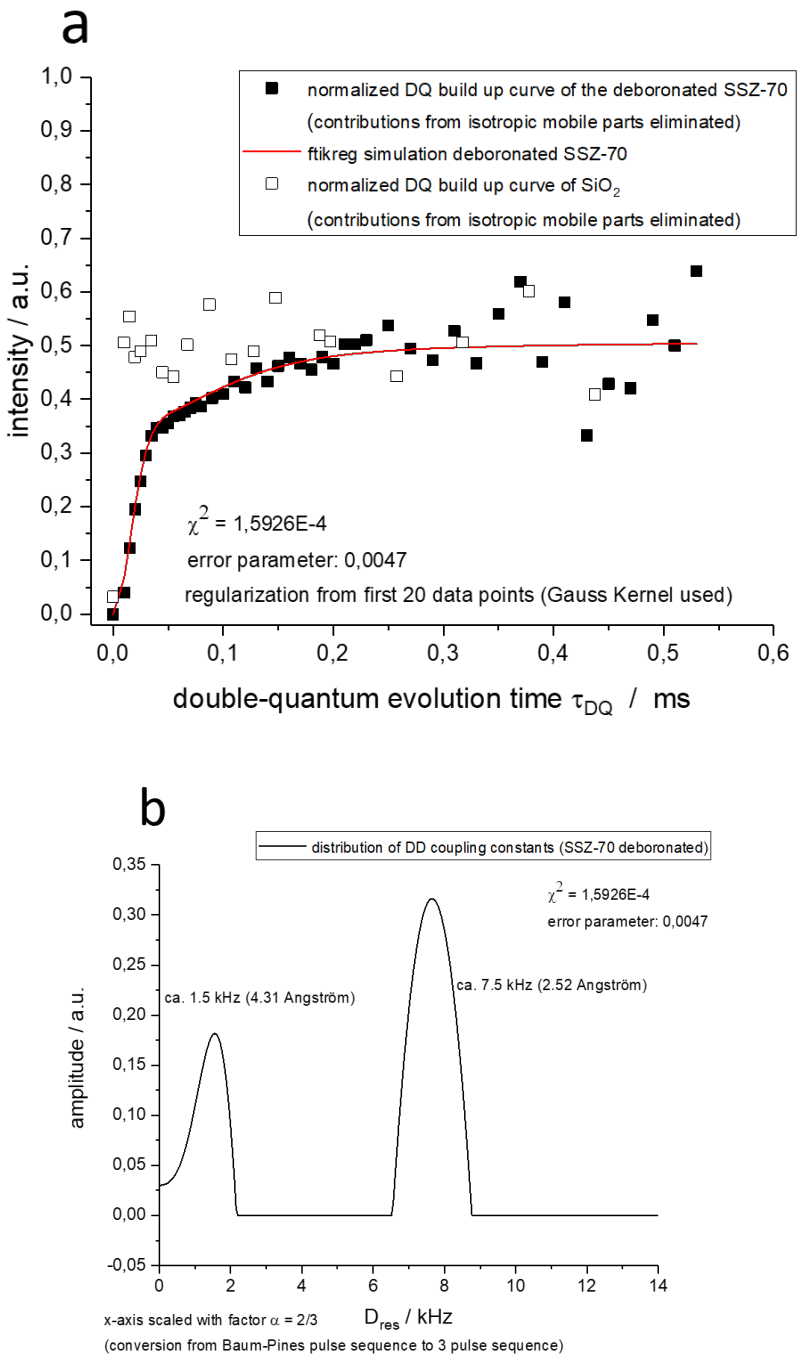

Figure A5.2D. a) Normalized ^{1}H double quantum build up curves of the deboronated SSZ-70 and SiO_2 and ftikreg simulation. b) Corresponding distribution of ^{1}H-^{1}H dipolar coupling constants in the deboronated SSZ-70.

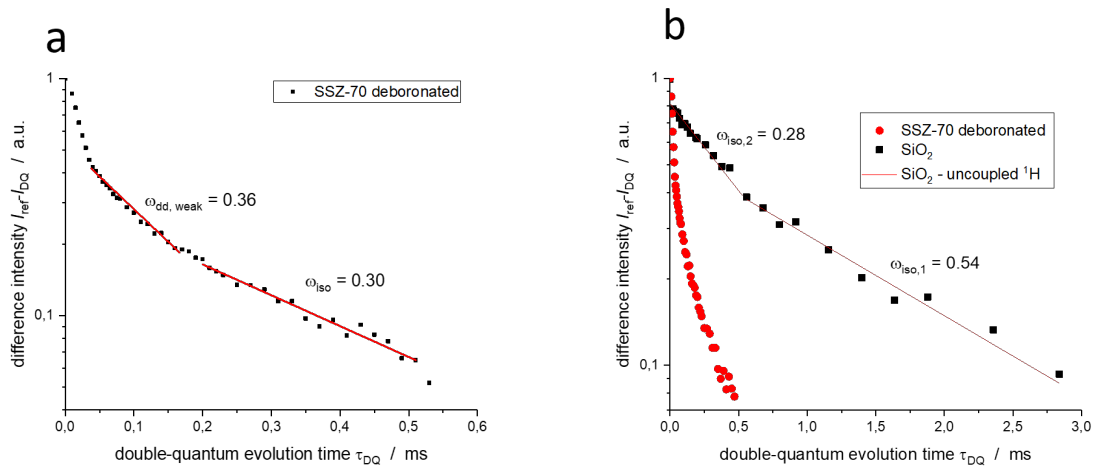

Figure A5.2E. a) Function of $I_{ref} - I_{DQ}$ for the deboronated SSZ-70 and exponential fits for the isotropic mobile parts and the weakly dipolar coupled hydrogens. b) Function of $I_{ref} - I_{DQ}$ for SiO_2 and the deboronated SSZ-70 and exponential fits for the isotropic mobile parts

5.5.5. Detailed analysis of Ligand-to-Metal Charge-Transfer (LMCT) Edge Energies

Ligand-to-metal charge-transfer edge energies represent the minimum energy required to excite electron from the highest occupied molecular orbital to the lower unoccupied molecular orbital.[60] These transitions are assumed to be indirect for calix[4]arene-Ti^{IV} complexes.[3] Figure A5.3 shows diffuse-reflectance UV-visible spectrum for all **calix-Ti/SUP** materials, expressed in Kubelka-Munk pseudoabsorbance units, F(R). The absorption features correspond to Si(O)-Ti LMCT (200-230 nm), π–π* aromatic transitions of calix[4]arene (270-290 nm), and calix[4]arene(O)-Ti^{IV} LMCT (~400-550 nm). Edge-energies for this last transition can be calculated from Tauc plots: absorbance is transformed into $[F(R)*E]^{1/2}$ units (inserts in Figure A5.3), where E denotes photon energy, and the onset of absorption is determined, defined as the intercept of the tangent line with the horizontal axis (Figure A5.3 inserts, tangent lines highlighted in green). These were drawn by determining the point of inflection and slope from 1st derivative of the transformed spectra. The values of the intercept can be found in Table 5.1 (LMCT edge) of the main text.

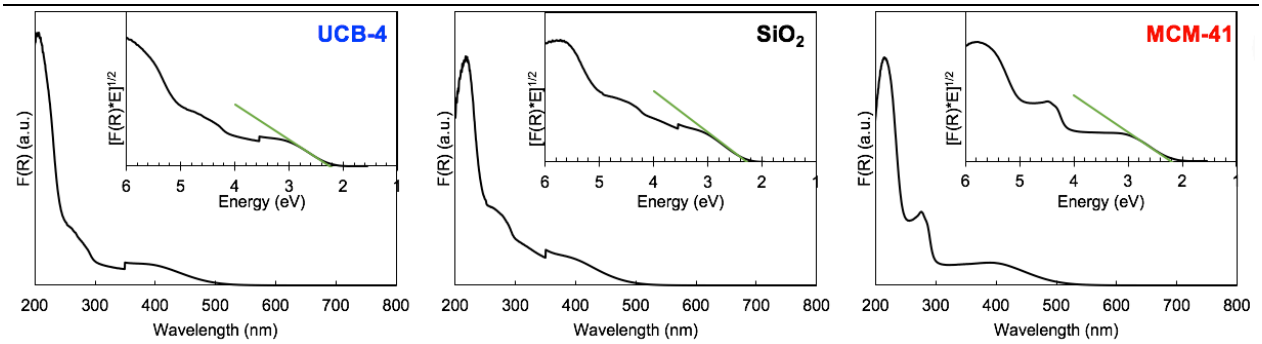

Figure A5.3. Diffuse-reflectance UV-visible spectrum of **calix-Ti/SUP** materials (**SUP** material noted in each figure) and corresponding Tauc plot (insert), with transformed absorbance units and tangent line (green) used in calculation of LMCT edge-energy.

Edge-energies are useful in determining calix[4]arene(O)-Ti^{IV} connectivity, because they arise from charge-transfer transitions from the calix[4]arene to Ti^{IV} cations. We have recently reported a variety of grafted calix[4]arene-Ti^{IV} structures and their corresponding edge-energies, shown in Scheme A5.2 (Chapter 4).[33] On dehydroxylated SiO_2, consisting of a surface dominated by isolated hydroxyl groups, only monopodal attachment to the support, as in Scheme A5.2(I) is possible, with reported LMCT edge-energies of 2.23-2.26 eV. The values of LMCT edge-energy reported in Table 5.1 for **calix-Ti/SiO_2** and **calix-Ti/MCM-41** of 2.29 and 2.21 eV, respectively, agree within an experimental error of 0.03 eV with those reported for structure (**I**) in Scheme A5.2, confirming the monodentate attachment of calix[4]arene-Ti^{IV} to the amorphous SiO_2 and MCM-41 supports. In **calix-Ti/UCB-4**, however, silanol nests provide grafting environments where multimodal attachment of a grafted cation is possible, with possible partial displacement of chelating ligands,[28] as would happen if a calix[4]arene(O)-Ti^{IV} attachment is displaced by a SiO-Ti attachment. If this were the case, it would be possible to obtain grafted structures as in Scheme A5.2B(**II**) and (**III**), with only bidentate connectivity to the calix[4]arene and bidentate connectivity to the support. These grafted structures, however, were reported to have a LMCT edge energies of 2.16 – 2.18 eV, ~ 0.10 eV lower than those where monopodal attachment to the support occurs. Thus, the LMCT edge energy of 2.24 eV for **calix-Ti/UCB-4** in consistent with monopodal attachment of the calix[4]arene-Ti^{IV} to the support, as in Scheme A5.2(**I**), indicating a grafted structure as shown in Scheme 5.1 of the main text: connected to the support by a single point of attachment and chelated by tridentate attachment to the calix[4]arene.

Scheme A5.2. Values of edge-energy for representative grafted calix[4]arene-Ti^{IV} structures.[33]

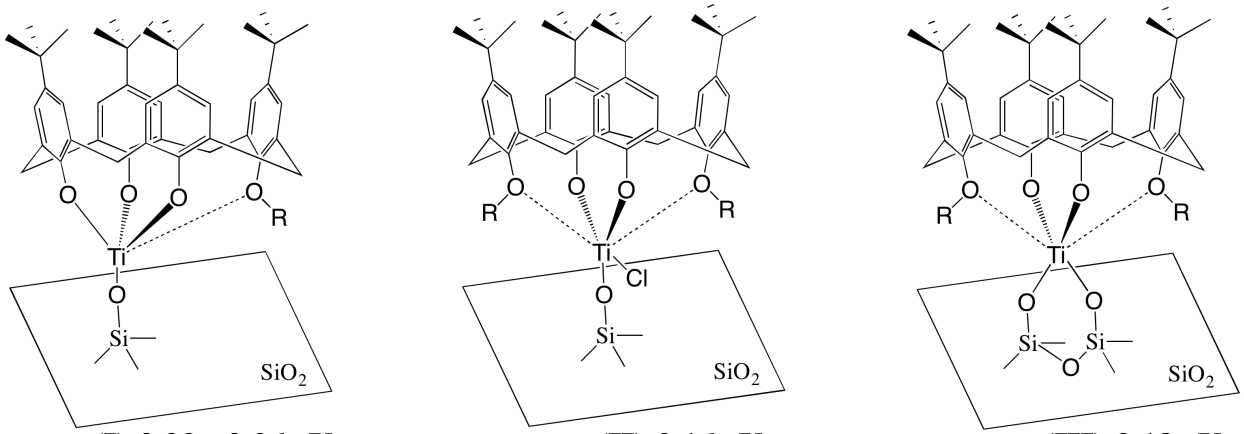

(I) 2.23 - 2.26 eV **(II) 2.16 eV** **(III) 2.18 eV**

Values of LMCT edge-energies for calix[4]arene-Ti^{IV} grafted structures with different coordination as reported in Chapter 4.[33] Possible grafted structures are (**I**) tripodal chelation by calix[4]arene, monopodal grafting to support (as in the case of **calix-Ti/SiO_2** in this work); (**II**) bipodal attachment to calix[4]arene with monopodal attachment to the support; and (**III**) bipodal attachment to both support and calix[4]arene.

5.5.6. Ti K-edge XANES Peak-Fitting Details

Ti K-edge XANES pre-edge feature deconvolution for all materials is shown in Figure A5.4. Reference TiO_2 shows four clearly defined A1, A2, A3 and B areas. All four of these features occur on **calix-Ti/SUP** materials, but with much different relative areas. The ratio of areas (A2+A3) to total pre-edge area (A1+A2+A3+B) is an established measure of 3d orbital availability and Lewis acidity,[3,35,36] and is tabulated in Table 5.1 of the main text. The uncertainty in these values is estimated at ±0.07,[35] implying that all A_{rel} values in Table 5.1 are equal for these materials within uncertainty. The positions of pre-edge features for all materials are also indistinguishable being within the 0.2 eV resolution with which spectra were acquired. Pre-edge heights are also indistinguishable from each other, ranging from 0.45 – 0.49 for all materials, within the uncertainty of ±0.02 estimated from spectral noise for features 5000-5010 eV in Figure 5.1B of the main text. This indicates identical structural and electronic inner-spheres for Ti^{IV} in all **calix-Ti/SUP** materials.

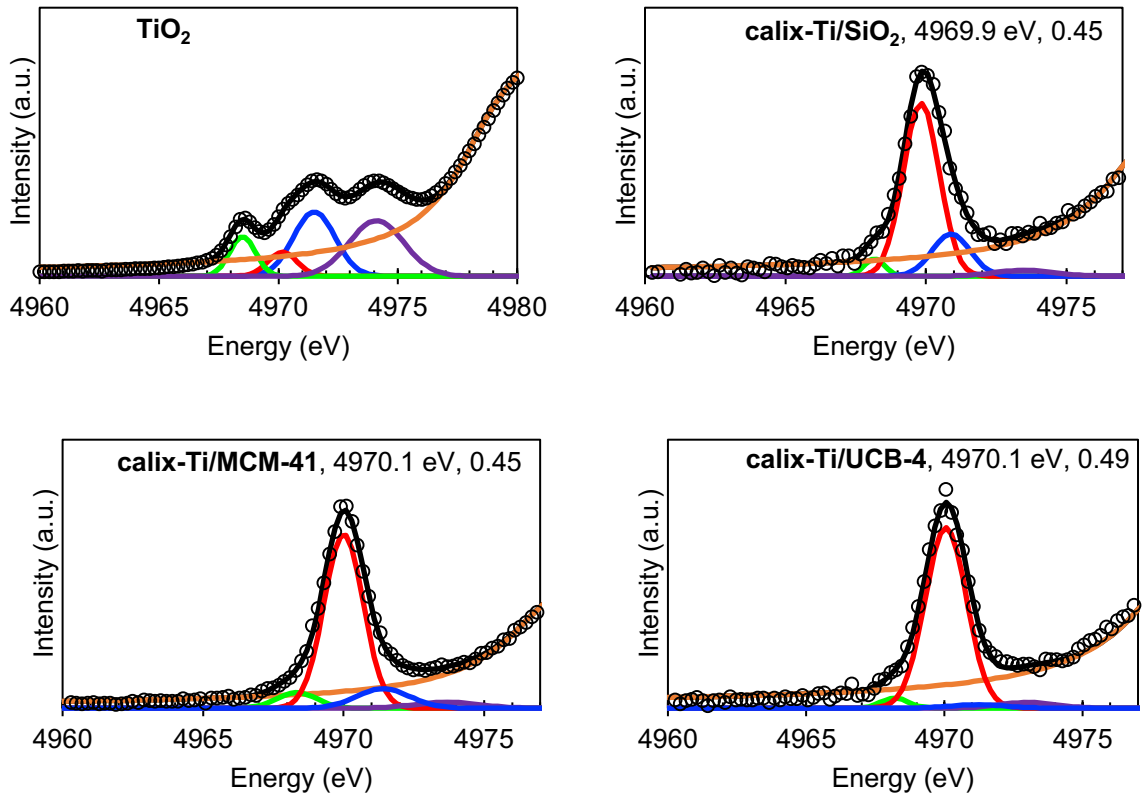

Figure A5.4. Detail of pre-edge features for a reference TiO_2 sample acquired in transmission mode and the three **calix-Ti/SUP** materials acquired in fluorescence mode. Material corresponding to each spectrum is indicated above in each figure, followed by the maximum pre-edge position and normalized intensity value. Experimental data are indicated by circles (o), while fits are indicated by a black line. Deconvolution of pre-edge features into area components are also shown: arctangent of step edge (orange), A1 (green), A2 (red), A3 (blue), A4 (purple).

5.5.7. Olefin Epoxidation Reaction Kinetics; Testing of Different Olefins and Oxidants

Rates of epoxidation were measured for the Ti^{IV}-catalyzed epoxidation of cyclohexene with *tert*-butyl hydroperoxide (TBHP), shown in Scheme A5.3. Kinetic measurements were performed under pseudo-1st order conditions in TBHP, by conducting experiments in >5 excess of olefin to TBHP oxidant. 1st order plots used in calculation of rate constants listed in Table 5.1 and Table A5.2 are shown in Figure A5.6A. Linear fits describe the data well and intercept the y-axis close to the origin, indicating the appropriateness of a 1st order consumption of [TBHP] in describing rate data, as per equation A5.1. Because TBHP decomposition can also occur as a reaction competing with epoxidation, both TBHP conversions (used in Figure A5.6A to determine rate constants) and epoxide yields (defined as ratio of [epoxide] to $[TBHP]_0$) were investigated, and are plotted on a parity plot in Figure A5.6B. All data points lie close to the parity line, indicating almost full conversion of TBHP to epoxide, and justifying the analysis of rates in terms of TBHP consumption. Epoxide conversions that are slightly lower than yields are indicative of a small amount of TBHP decomposition, typically less than 10%, which does not affect our interpretation of trends in reactivity. This is also seen by the fact that trends in oxidant consumption in Figure A5.6 follow trends in epoxide production in Figure A5.5, when comparing slopes in Figure A5.6A and k_{eff} values in Table 5.1 and Table A5.2 to TON ($mol_{epoxide}/mol_{Ti}$) differences in the Figure A5.5.

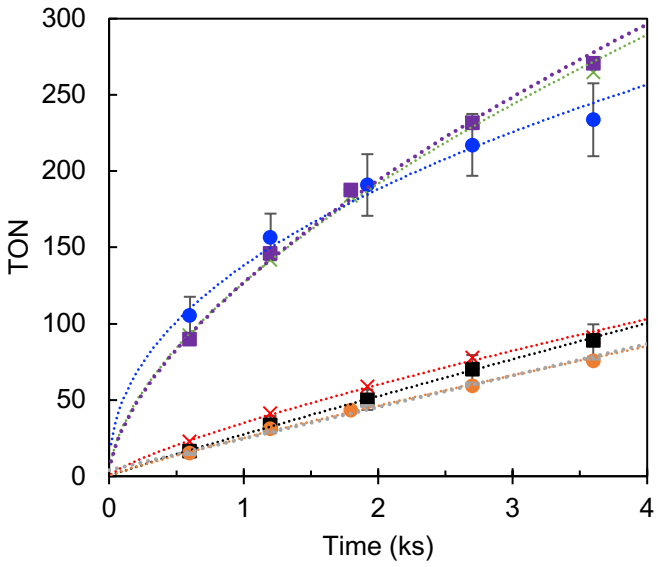

Figure A5.5. Rates of epoxidation of cyclohexene with TBHP quantified as turnover numbers as a function of time. Calix[4]arene-Ti^{IV} supported on UCB-4 (blue circles, •), MCM-41 (red crosses, x), MCM-41(high) (grey dashes, -), SiO_2 (black square, ■), SSZ-70 (green crosses, x), and UCB-4(low) (purple squares, ■), and SiO_2-AW (orange circles, •). Uncertainties calculated from standard deviation of duplicate experiments for **calix-Ti/UCB-4** and **calix-Ti/SiO_2**. Lines are intended as a guide to the eye and do not represent any model fits. Turnover numbers for **calix-Ti/SSZ-70** and **calix-Ti/UCB-4(low)** are in line with those of **calix-Ti/UCB-4**, while those for **calix-Ti/SiO_2-AW** are in line with those for **calix-Ti/SiO_2**, indicating that delamination and acid-washing do not affect catalytic activity.

Scheme A5.3. Ti^{IV}-catalyzed epoxidation of cyclohexene with *tert*-butyl hydroperoxide.

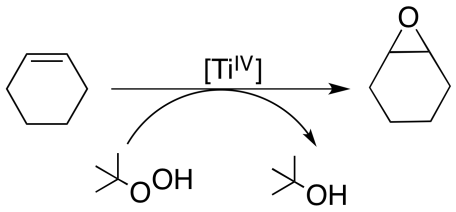

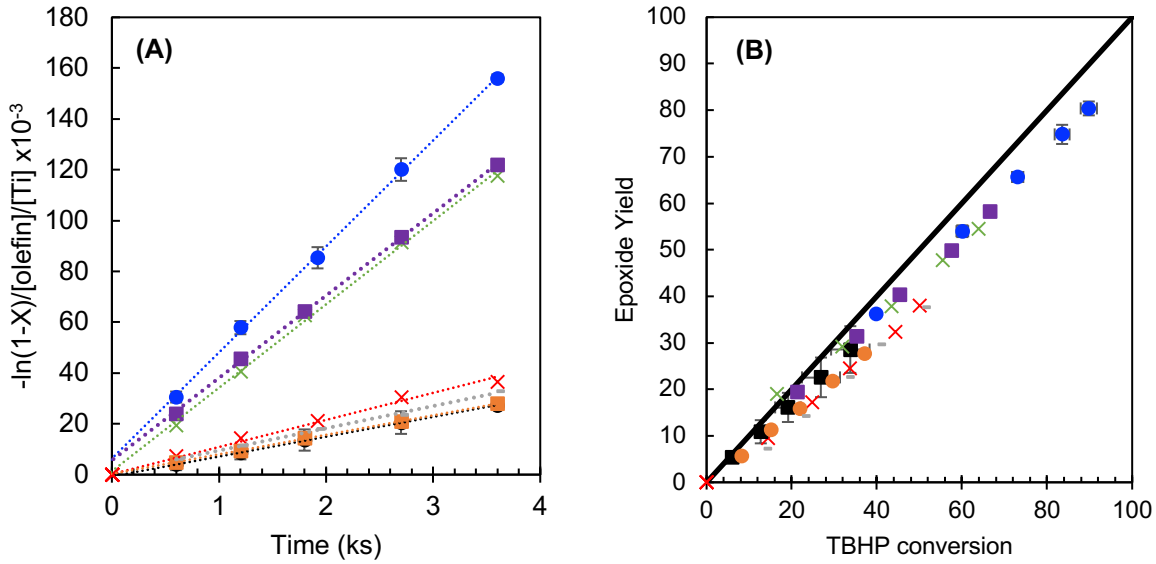

Figure A5.6. (A) Kinetic plots used for determination of pseudo-1st order rate constants for epoxidation based on TBHP consumption; on y-axis, -ln(1-X), where conversion X = 1-[TBHP]/[TBHP]$_0$, is normalized by olefin [olefin] and Ti [Ti] concentrations, to yield a straight line with slope = k_{eff}. **(B)** Parity plot (parity line indicated as 1:1 slope black line) of TBHP conversion (=1-[TBHP]/[TBHP]$_0$) and Epoxide yield (=[epoxide]/[TBHP]$_0$) for all data points in Figure A5.5 and A5.6A; near parity of conversion and yield are seen, indicating high selectivity of conversion of TBHP oxidant to epoxide. Data for calix[4]arene-Ti^{IV} supported on UCB-4 (blue circles, •), MCM-41 (red crosses, x), MCM-41(high) (grey dashes, -), SiO_2 (black square, ■), SSZ-70 (green crosses, x), and UCB-4(low) (purple squares, ■), and SiO_2-AW (orange circles, •), are shown. Uncertainties calculated from standard deviation of duplicate experiments for **calix-Ti/UCB-4** and **calix-Ti/SiO_2**.

Additionally, we tested two other olefins, 1-octene (terminal olefin) and cis-stilbene (bulky internal olefin) as well as an additional organic hydroperoxide oxidant (ethylbenzene hydroperoxide). Results in Figure A5.7 shows that, while absolute rates depend on the type of olefin or oxidant, **calix-Ti/UCB-4** is consistently significantly more reactive than **calix-Ti/SiO_2**, confirming the generalizability of outer-sphere catalytic enhancements to other olefins even when using other organic hydroperoxides as oxidants. We include conversion-yield data in for 1-octene in Figure A5.7(D) to show that epoxidation of this terminal olefin deviates from parity, when

compared to almost full conversion of olefin to epoxide in Figure A5.6(B). This is because it is more difficult to selectively oxidize of the more electron deficient terminal 1-octene, and some decomposition of hydroperoxide inevitably occurs.

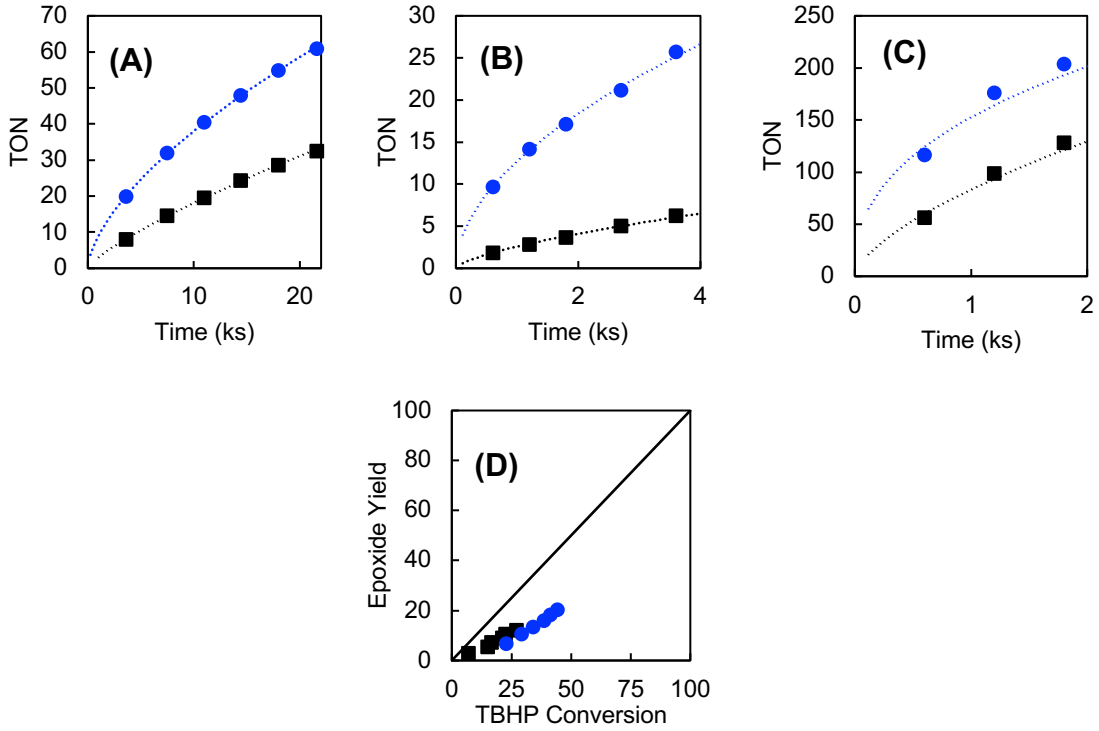

Figure A5.7. Rates of epoxidation quantified as turnover numbers as a function of time for Calix[4]arene-Ti^{IV} supported on UCB-4 (blue circles, •) and SiO_2 (black square, ■) for **(A)** 1-octene as olefin and TBHP as oxidant**, (B)** cis-stilbene as olefin and TBHP as oxidant, and **(C)** cyclohexene as olefin and ethylbenzene hydroperoxide as oxidant. Lines are intended as a guide to the eye and do not represent any model fits. **(D)** Parity plot (parity line indicated as 1:1 slope black line) of TBHP conversion (=1-[TBHP]/$[TBHP]_0$) and Epoxide yield (=[epoxide]/$[TBHP]_0$) for data for 1-octene epoxidation in Figure A5.7(A).

5.6. References

(1) Pelletier, J. D. A.; Basset, J. M. Catalysis by Design: Well-Defined Single-Site Heterogeneous Catalysts. *Acc. Chem. Res.* **2016**, *49*, 664–677.

(2) Thomas, J. M. *Design and Applications of Single-Site Heterogeneous Catalysts : Contributions to Green Chemistry, Clean Technology and Sustainability*; Imperial College Press: London, 2012.

(3) Notestein, J. M.; Solovyov, A.; Andrini, L. R.; Requejo, F. G.; Katz, A.; Iglesia, E. The Role of Outer-Sphere Surface Acidity in Alkene Epoxidation Catalyzed by Calixarene-Ti(IV) Complexes. *J. Am. Chem. Soc.* **2007**, *129*, 15585–15595.

(4) Bass, J. D.; Anderson, S. L.; Katz, A. The Effect of Outer-Sphere Acidity on Chemical Reactivity in a Synthetic Heterogeneous Base Catalyst. *Angew. Chem. Int. Ed.* **2003**, *42*, 5219–5222.

(5) Bouh, A. O.; Rice, G. L.; Scott, S. L. Mono- and Dinuclear Silica-Supported Titanium(IV) Complexes and the Effect of TiOTi Connectivity on Reactivity. *J. Am. Chem. Soc.* **1999**, *121*, 7201–7210.

(6) Lu, J.; Aydin, C.; Liang, A. J.; Chen, C. Y.; Browning, N. D.; Gates, B. C. Site-Isolated Molecular Iridium Complex Catalyst Supported in the 1-Dimensional Channels of Zeolite Hssz-53: Characterization by Spectroscopy and Aberration-Corrected Scanning Transmission Electron Microscopy. *ACS Catal.* **2012**, *2*, 1002–1012.

(7) Nandi, P.; Tang, W.; Okrut, A.; Kong, X.; Hwang, S.-J.; Neurock, M.; Katz, A. Catalytic Consequences of Open and Closed Grafted Al(III)-Calix[4]Arene Complexes for Hydride and Oxo Transfer Reactions. *Proc. Natl. Acad. Sci. U. S. A.* **2013**, *110*, 2484–2489.

(8) Bordiga, S.; Bonino, F.; Damin, A.; Lamberti, C. Reactivity of Ti(IV) Species Hosted in TS-1 towards H2O2-H2O Solutions Investigated by Ab Initio Cluster and Periodic Approaches Combined with Experimental XANES and EXAFS Data: A Review and New Highlights. *Phys. Chem. Chem. Phys.* **2007**, *9*, 4854–4878.

(9) Radhakrishnan, R.; Oyama, S. T.; Chen, J. G.; Asakura, K. Electron Transfer Effects in Ozone Decomposition on Supported Manganese Oxide. *J. Phys. Chem. B* **2001**, *105*, 4245–4253.

(10) Comas-Vives, A.; Ujaque, G.; Lledós, A. *Inner- and Outer-Sphere Hydrogenation Mechanisms: A Computational Perspective*; Academic Press, 2010; Vol. 62.

(11) Edwards, R. A.; Whittaker, M. M.; Whittaker, J. W.; Baker, E. N.; Jameson, G. B. Outer Sphere Mutations Perturb Metal Reactivity in Manganese Superoxide Dismutase. *Biochemistry* **2001**, *40*, 15–27.

(12) Bermejo-Deval, R.; Orazov, M.; Gounder, R.; Hwang, S. J.; Davis, M. E. Active Sites in Sn-Beta for Glucose Isomerization to Fructose and Epimerization to Mannose. *ACS Catal.* **2014**, *4*, 2288–2297.

(13) Comotti, M.; Li, W.-C. C.; Spliethoff, B.; Schüth, F.; Schuth, F. Support Effect in High Activity Gold Catalysts for CO Oxidation. *J. Am. Chem. Soc.* **2006**, *128*, 917–924.

(14) Grosso-Giordano, N. A.; Eaton, T. R.; Bo, Z.; Yacob, S.; Yang, C. C.; Notestein, J. M. Silica Support Modifications to Enhance Pd-Catalyzed Deoxygenation of Stearic Acid. *Appl. Catal. B Environ.* **2016**, *192*, 93–100.

(15) Lu, J.; Serna, P.; Aydin, C.; Browning, N. D.; Gates, B. C. Supported Molecular Iridium Catalysts: Resolving Effects of Metal Nuclearity and Supports as Ligands. *J. Am. Chem. Soc.* **2011**, *133*, 16186–16195.

(16) Liu, J.; Lucci, F. R.; Yang, M.; Lee, S.; Marcinkowski, M. D.; Therrien, A. J.; Williams,

C. T.; Sykes, E. C. H.; Flytzani-Stephanopoulos, M. Tackling CO Poisoning with Single-Atom Alloy Catalysts. *J. Am. Chem. Soc.* **2016**, *138*, 6396–6399.
(17) Park, J. W.; Thomas, K.; Van Gestel, J.; Gilson, J. P.; Collet, C.; Dath, J. P.; Houalla, M. Study of Ir/WO_3/Al_2O_3 Ring Opening Catalysts. *Appl. Catal. A Gen.* **2010**, *388*, 37–44.
(18) Dijkmans, J.; Dusselier, M.; Janssens, W.; Trekels, M.; Vantomme, A.; Breynaert, E.; Kirschhock, C.; Sels, B. F. An Inner-/Outer-Sphere Stabilized Sn Active Site in ??-Zeolite: Spectroscopic Evidence and Kinetic Consequences. *ACS Catal.* **2016**, *6*, 31–46.
(19) Oyama, S. T. *Mechanisms in Homogeneous and Heterogeneous Epoxidation Catalysis*; Elsevier: Amsterdam, 2011.
(20) Sheldon, R. A.; Van Doorn, J. A. Metal-Catalyzed Epoxidation of Olefins with Organic Hydroperoxides. I. A Comparison of Various Metal Catalysts. *J. Catal.* **1973**, *31*, 427–437.
(21) Sheldon, R. A. Synthetic and Mechanistic Aspects of Metal-Catalysed Epoxidations with Hydroperoxides. *J. Mol. Catal.* **1980**, *7*, 107–126.
(22) Ogino, I.; Eilertsen, E. A.; Hwang, S.-J.; Rea, T.; Xie, D.; Ouyang, X.; Zones, S. I.; Katz, A. Heteroatom-Tolerant Delamination of Layered Zeolite Precursor Materials. *Chem. Mater.* **2013**, *25*, 1502–1509.
(23) Sever, R. R.; Alcala, R.; Dumesic, J. A.; Root, T. W. Vapor-Phase Silylation of MCM-41 and Ti-MCM-41. *Microporous Mesoporous Mater.* **2003**, *66*, 53–67.
(24) Chen, C.-Y.; Li, H.-X.; Davis, M. E. Studies on Mesoporous Materials I. Synthesis and Characterization of MCM-41. *Microporous Mater.* **1993**, *2*, 17–26.
(25) Notestein, J. M.; Iglesia, E.; Katz, A. Grafted Metallocalixarenes as Single-Site Surface Organometallic Catalysts. *J. Am. Chem. Soc.* **2004**, *126*, 16478–16486.
(26) Blasco, T.; Corma, A.; Navarro, M. T.; Pérez Pariente, J. Synthesis, Characterization, and Catalytic Activity of Ti-MCM-41 Structures. *J. Catal.* **1995**, *156*, 65–74.
(27) Khouw, C.; Dartt, C. B.; Labinger, J. A.; Davis, M. E. Studies on the Catalytic-Oxidation of Alkanes and Alkenes by Titanium Silicates. *J. Catal.* **1994**, *149*, 195–205.
(28) Grosso-Giordano, N. A.; Yeh, A. J.; Okrut, A.; Xiao, D. J.; Grandjean, F.; Long, G. J.; Zones, S. I.; Katz, A. Effect of Defect Site Preorganization on Fe(III) Grafting and Stability: A Comparative Study of Delaminated Zeolite vs Amorphous Silica Supports. *Chem. Mater.* **2017**, *29*, 6480–6492.
(29) Hsieh, M.-F. Ph.D. Dissertation, University of California, Santa Barbara, CA, 2014.
(30) Senderov, E.; Halasz, I.; Olson, D. H. On Existence of Hydroxyl Nests in Acid Dealuminated Zeolite Y. *Microporous Mesoporous Mater.* **2014**, *186*, 94–100.
(31) Chassé, W.; Valentín, J. L.; Genesky, G. D.; Cohen, C.; Saalwächter, K. Precise Dipolar Coupling Constant Distribution Analysis in Proton Multiple-Quantum NMR of Elastomers. *J. Chem. Phys.* **2011**, *134*.
(32) Shantz, D. F.; Schmedt Auf Der Günne, J.; Koller, H.; Lobo, R. F. Multiple-Quantum ^{1}H MAS NMR Studies of Defect Sites in as-Made All- Silica ZSM-12 Zeolite. *J. Am. Chem. Soc.* **2000**, *122*, 6659–6663.
(33) Grosso-Giordano, N. A.; Solovyov, A.; Hwang, S.-J.; Katz, A. Effect of Coordination Environment in Grafted Single-Site Ti-SiO_2 Olefin Epoxidation Catalysis. *Top. Catal.* **2016**, *59*, 1110–1122.
(34) Thomas, J. M.; Sankar, G. The Role of Synchrotron-Based Studies in the Elucidation and Design of Active Sites in Titanium−Silica Epoxidation Catalysts. *Acc. Chem. Res.* **2001**, *34*, 571–581.

(35) Notestein, J. M.; Andrini, L. R.; Kalchenko, V. I.; Requejo, F. G.; Katz, A.; Iglesia, E. Structural Assessment and Catalytic Consequences of the Oxygen Coordination Environment in Grafted Ti-Calixarenes. *J. Am. Chem. Soc.* **2007**, *129*, 1122–1131.
(36) Eaton, T. R.; Campos, M. P.; Gray, K. A.; Notestein, J. M. Quantifying Accessible Sites and Reactivity on Titania-Silica (Photo)Catalysts: Refining TOF Calculations. *J. Catal.* **2014**, *309*, 156–165.
(37) Khouw, C. B.; Davis, M. E. Catalytic Activity of Titanium Silicates Synthesized in the Presence of Alkali-Metal and Alkaline-Earth Ions. *J. Catal.* **1995**, *151*, 77–86.
(38) Wells, D. H.; Joshi, A. M.; Delgass, W. N.; Thomson, K. T. A Quantum Chemical Study of Comparison of Various Propylene Epoxidation Mechanisms Using H_2O_2 and TS-1 Catalyst. *J. Phys. Chem. B* **2006**, *110*, 14627–14639.
(39) Wells, D. H.; Delgass, W. N.; Thomson, K. T. Evidence of Defect-Promoted Reactivity for Epoxidation of Propylene in Titanosilicate (TS-1) Catalysts: A DFT Study. *J. Am. Chem. Soc.* **2004**, *126*, 2956–2962.
(40) Eaton, T. R.; Boston, A. M.; Thompson, A. B.; Gray, K. A.; Notestein, J. M. Counting Active Sites on Titanium Oxide-Silica Catalysts for Hydrogen Peroxide Activation through In Situ Poisoning with Phenylphosphonic Acid. *ChemCatChem* **2014**, *6*, 3215–3222.
(41) Ratnasamy, P.; Srinivas, D.; Knözinger, H. Active Sites and Reactive Intermediates in Titanium Silicate Molecular Sieves. *Adv. Catal.* **2004**, *48*, 1–169.
(42) *See Supporting Information Section 8*.
(43) Carter, P.; Wells, J. A. Dissecting the Catalytic Triad of a Serine Protease. *Nature* **1988**, *332*, 564–568.
(44) Aigner, M.; Grosso-Giordano, N. A.; Schottle, C.; Okrut, A.; Zones, S.; Katz, A. Epoxidation of 1-Octene under Harsh Tail-End Conditions in a Flow Reactor II: Impact of Delaminated-Zeolite Catalyst Surface Area and Structural Integrity on Catalytic Performance. *React. Chem. Eng.* **2017**, *2*, 852–861.
(45) Aigner, M.; Grosso-Giordano, N. A.; Okrut, A.; Zones, S. I.; Katz, A. Epoxidation of 1-Octene under Harsh Tail-End Conditions in a Flow Reactor I: A Comparative Study of Crystalline vs. Amorphous Catalysts. *React. Chem. Eng.* **2017**, *2*, 842–851.
(46) Ek, S.; Root, A.; Peussa, M.; Niinistö, L. Determination of the Hydroxyl Group Content in Silica by Thermogravimetry and a Comparison with ^{1}H MAS NMR Results. *Thermochim. Acta* **2001**, *379*, 201–212.
(47) Archer, R. H.; Zones, S. I.; Davis, M. E. Imidazolium Structure Directing Agents in Zeolite Synthesis: Exploring Guest/Host Relationships in the Synthesis of SSZ-70. *Microporous Mesoporous Mater.* **2010**, *130*, 255–265.
(48) Thomas, J. M.; Raja, R.; Lewis, D. W. Single-Site Heterogeneous Catalysts. *Angew. Chem. Int. Ed.* **2005**, *44*, 6456–6482.
(49) Groenen, L. C.; Ruël, B. H. M.; Casnati, A.; Verboom, W.; Pochini, A.; Ungaro, R.; Reinhoudt, D. N. Synthesis of Monoalkylated Calix[4]Arenes via Direct Alkylation. *Tetrahedron* **1991**, *47*, 8379–8384.
(50) Friedrich, A.; Radius, U. A Calix[4]Arene Monoalkyl Ether as a Model of a Tris(Phenolate) Ligand with a Hemilabile Anisole Moiety: Syntheses, Molecular Structures and Bonding of Calix[4]Arene Ether Supported Titanium Complexes and Their Catalytic Activity in Epoxidation Reactions. *Eur. J. Inorg. Chem.* **2004**, *2004*, 4300–4316.
(51) Ertl, G.; Knözinger, H.; Weitkamp, J. *Handbook of Heterogeneous Catalysis*; Wiley:

Weinheim, Germany, 1997.
(52) Jaeger, C.; Hemmann, F. EASY: A Simple Tool for Simultaneously Removing Background, Deadtime and Acoustic Ringing in Quantitative NMR Spectroscopy. Part II: Improved Ringing Suppression, Application to Quadrupolar Nuclei, Cross Polarisation and 2D NMR. *Solid State Nucl. Magn. Reson.* **2014**, *63*, 13–19.
(53) Schnell, I.; Spiess, H. W. High-Resolution 1H NMR Spectroscopy in the Solid State: Very Fast Sample Rotation and Multiple-Quantum Coherences. *J. Magn. Reson.* **2001**, *151*, 153–227.
(54) Corma, A.; Domine, M.; Gaona, J. A.; Jordá, J. L.; Navarro, M. T.; Rey, F.; Pérez-Pariente, J.; Tsuji, J.; McCulloch, B.; Nemeth, L. T. Strategies to Improve the Epoxidation Activity and Selectivity of Ti-MCM-41. *Chem. Commun.* **1998**, No. 20, 2211–2212.
(55) Zawadiak, J.; Gilner, D.; Kulicki, Z.; Baj, S. Concurrent Iodimetric Determination of Cumene Hydroperoxide and Dicumenyl Peroxide Used for Reaction Control in Dicumenyl Peroxide Synthesis. *Analyst* **1993**, *118*, 1081.
(56) Barrett, E. P.; Joyner, L. G.; Halenda, P. P. The Determination of Pore Volume and Area Distributions in Porous Substances. I. Computations from Nitrogen Isotherms. *J. Am. Chem. Soc.* **1951**, *73*, 373–380.
(57) Ouyang, X.; Hwang, S.-J.; Xie, D.; Rea, T.; Zones, S. I.; Katz, A. Heteroatom-Substituted Delaminated Zeolites as Solid Lewis Acid Catalysts. *ACS Catal.* **2015**, *5*, 3108–3119.
(58) Koller, H.; Fild, C.; Lobo, R. F. Variable Anchoring of Boron in Zeolite Beta. *Microporous Mesoporous Mater.* **2005**, *79*, 215–224.
(59) Koller, H.; Chen, C. Y.; Zones, S. I. Selectivities in Post-Synthetic Modification of Borosilicate Zeolites. *Top. Catal.* **2015**, *58*, 451–479.
(60) Barton, D. G.; Shtein, M.; Wilson, R. D.; Soled, S. L.; Iglesia, E. Structure and Electronic Properties of Solid Acids Based on Tungsten Oxide Nanostructures. *J. Phys. Chem. B* **1999**, *103*, 630–640.

Chapter 6

Orientation and Conformation of a Chemisorbed Molecule at the Interface of Microporous Cavities and a Crystalline Surface

We investigate how surface environment influences the conformation of a grafted macrocyclic calix[4]arene-Ti^{IV} complex (**cTi**) on the external surface of a silicates, including zeotype *-SVY. Elemental analysis and UV-visible spectroscopies indicate intact grafting of **cTi**; however, X-ray absorption and $^{13}C\{^{1}H\}$ CPMAS NMR spectroscopies detect a unique conformation of **cTi** when it is grafted at crystallographically equivalent locations adjacent to sub-nanometer surface cavities (7.1 Å in diameter). Electronic structure calculations (DFT) reveal that this conformation involves a specific orientation of **cTi**, stabilized by attractive Van der Waals interactions between the hydrocarbon units of the calix[4]arene and the siloxane walls of surface cavities. These observations provide a rare "snapshot" of the resting state of a partially confined molecule at the interface of a surface and micropores thereon.

6.1. Introduction

The non-elementary process of how a molecule transitions from a bulk fluid phase into an intra-crystalline micropore is currently unknown, despite its importance to understanding porous materials and their applications, including adsorption,[1–3] catalysis[4–6] (especially at the pore mouths)[7,8], separations,[9] and sensing.[10] The kinetic nature and extremely low probability of this transition,[1,2] together with lack of uniformity of surface structures,[9,11–15] makes its experimental study challenging.

Here, we investigate how surface location of a chemisorbed macrocyclic molecule affects its ability to interact with a nearby microporous cavity. Primary evidence for this interaction comes from conformational changes to the macrocycle detected by a combination of UV-visible, X-ray absorption, and solid-state NMR spectroscopies, which are consistent with predictions by electronic-structure calculations. Our data specifically demonstrate how Van der Waals interactions control the conformation and orientation of the chemisorbed molecules, providing a rare molecular "snapshot" of the resting state of a molecule in transition as it penetrates a micropore on a surface.

Our approach is shown in Scheme 6.1, and is based on a macrocyclic calix[4]arene-Ti^{IV} complex, which is grafted (i.e. chemisorbed) onto a silanol group (SiOH) on the surface of a silicate that is either a crystalline zeotype or amorphous.[16] This complex, which is grafted intact on the silicate surface (see 6.5.2), consists of a cyclic tetramer of phenols, three of which chelate to the Ti^{IV} center (blue), and a fourth which is substituted at the lower-rim with a methoxy group (red). These phenols are substituted at the upper rim by R = *t*-butyl groups in **cTi** or R = H in **HcTi**. We first focus our study on **cTi** to establish how surface environments affects its conformation.

Scheme 6.1. Grafting of calix[4]arene-Ti complexes (cTi) onto surface silanols

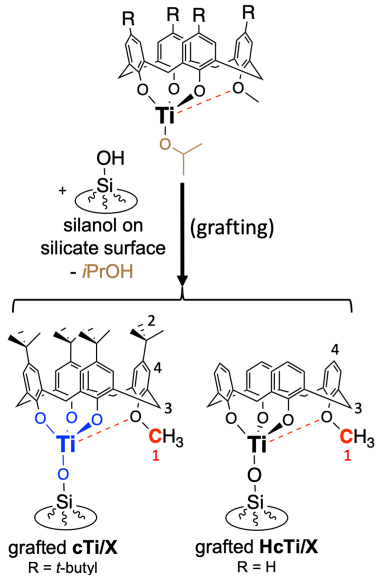

calix[4]arene-Ti^{IV} structures with upper-rim substituents R = *t*-butyl (**cTi**) and R = H (**HcTi**). Grafting of isopropoxide precursor occurs *via* condensation with silanol groups on the silicate surface. Colors, numbers, and insets highlight regions of the molecules referenced in the text.

The possible molecular environments experienced by the grafted **cTi** are shown in Scheme 6.2. These environments depend on the type of surface framework structures surrounding the silanol onto which **cTi** grafts, which depend on the type of silicate. All zeotypes examined exhibit a high external surface (Table A6.2) and have *-SVY topology,[17,18] which have been synthetically manipulated to control the location of silanols by a recently reported synthetic approach.[6] There are two possible locations for silanols on the external surface of these zeotypes, highlighted in Scheme 6.2:[6] (**i**) terminal T-atom positions (purple) and (**ii**) confining 12-membered-ring (12-MR) cavities[19] (orange). Terminal T-atom positions (**i**) are the only crystallographic locations where silanols occur in **2**, because it is the only location where the $SiO_{4/2}$ four-connected network is interrupted in its defect-free framework. These terminal T-atom positions are all crystallographically equivalent (T_6 sites of MWW)[20] and uniformly separated by 8.3 Å. Instead, 12-MR cavities (**ii**) comprise shallow hemispherical cavities 7.1 Å wide and 7.0 Å deep,[21] which are partially-confining,[6,19] and can be thought of as pore mouths of zeolites. The location of silanols within each of these two features, summarized in Scheme 6.2, consists of only (**i**) in **2**, only (**ii**) in **3-b,** and both (**i**) and (**ii**) in **2-a** and **3-a**. In contrast to these ordered crystalline zeotype frameworks, **1** is a non-microporous dehydroxylated amorphous silica (Aerosil 200 treated at 823 K), and serves as a comparison of a non-uniform surface environment.

Scheme 6.2. Schematic representation of silanol locations in surface framework environments

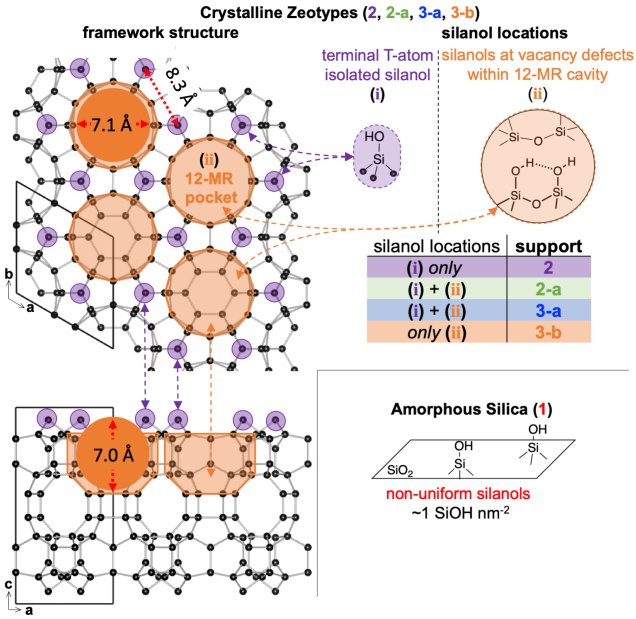

The crystalline framework layers of delaminated SSZ-70 zeotypes (*-SVY topology) is shown along two crystallographic planes, and its unit cell indicated within black parallelograms. Vertices correspond to tetrahedrally coordinated T-atoms that make up the zeotype framework; they are connected through oxygen bridges shown as grey lines. The external zeotype surface is dominated by features on the a-b plane. Silanols (and by extension grafted **cTi**) can be located within two district molecular environments on this surface: terminal T-atom positions (**i**), and confining 12-MR cavities (**ii**). The presence of silanols in each of these environments, as controlled by the type of silicate, is summarized in the table. Synthetic details are in Scheme 7.1.

Samples with **cTi** grafted onto them are denoted **cTi/X**, where **X** indicates the support **1**, **2**, **2-a**, **3-a**, or **3-b**. **cTi** grafts only where silanols are present;[6] in zeotypes, it grafts only on the external surface, because its large dimensions preclude its diffusion into micropores.[6,16] Therefore, **cTi** is grafted only at terminal T-atom positions (**i**) in **cTi/2**, only within 12-MR cavities (**ii**) in **cTi/3-b**, within a mixture of these in **cTi/2-a** and **cTi/3-a**, and on a non-uniform surface in amorphous **cTi/1**.[6] Below, our data demonstrate that the crystallographically equivalent location of **cTi** in **cTi/2** leads to a unique conformation, in which a *t*-butyl phenol substituent orients itself to interact with the 12-MR cavity.

6.2. Experimental

6.2.1 Material Synthesis and Characterization

Synthesis of support **1**, **1-a**, **2**, **3-a**, and **3-b** is described in 7.2.1. **2-a** was synthesized by treatment of 500 mg of delaminated zeolite **2** with 50 mL of 2N HNO_3 at 373 K for 18 h, followed by filtration and washing with copious amounts of H_2O. Incorporation of cTi was achieved as described in 7.2.2, but using a *t*-butyl-calix[4]arene ligand with ^{13}C enrichment at the lower-rim methoxy position (Scheme 6.1). **HcTi/X** was synthesized by identical protocols to **cTi/X** materials, but starting with an H-calix[4]arene ligand purchased from Life Chemicals. Analytical methods are described in 7.2.3.

^{1}H MAS NMR and $^{13}C\{^{1}H\}$ CPMAS experiments were conducted on a Bruker Avance I spectrometer operating at 9.4 T. Spectra were acquired and processed with the software Topspin 1.3 and a Bruker HX double resonance probehead was used. The samples were filled in 4 mm ZrO_2 rotors with Kel-F end caps and spun at 9 kHz MAS during acquisition. $\pi/2$ pulses of 4 μs were employed on the ^{1}H channel (ν_{RF} = 62.5 kHz) and the rf field strength on the ^{13}C channel was 50.0 kHz ($\pi/2$ = 5 μs). Contact time for ^{1}H-^{13}C magnetization transfer was 1 ms, utilizing a 70%-100% ramp on ^{1}H. All spectra were referenced against adamantane ($\delta(^{1}H)$ = 1.78 ppm, $\delta(^{13}C)$ = 29.47 ppm). For $^{13}C\{^{1}H\}$ CPMAS, a recycle delay of 10s was used, while 20s were used for ^{1}H MAS NMR.

6.2.2 Electronic Structure Calculations

Electronic structure calculations were performed with the Gaussian 16 revision A03 software,[22] by DFT methods using a spin-symmetry-restricted B3LYP functional.[23,24] Dispersion interactions were incorporated into the energies of B3LYP calculations using DFT-D3(0) methods.[25] Chemical shift were calculated with Gauge-Independent Atomic Orbital (GIAO) method.[26] Active site models were constructed based on the SSZ-70 framework structure,[17] shown schematically in Scheme 6.2. A full 12-MR pocket structure and next-nearest Si^{IV} neighbors were used as the basis of the cluster model, and the position of the atoms was frozen based on crystallographic information unless otherwise noted. This cluster model **I** can be seen in Figure A6.10, where the location of the 12-MR pocket is highlighted; six silanol groups surrounding this pocket, which constitute terminal T-atom positions (**i**), and are also highlighted in purple. To model the presence of a silanol, a vacancy defect was introduced at a T-site known to be preferentially occupied by B^{III} at the upper-rim of 12-MR pockets;[27] this is an *in-silico* mimic of removal of B^{III} during the synthesis of **3-a** via deboronation of **3**. This vacancy is nominally terminated by four silanols, in a so called "silanol nest";[28,29] however, we have recently shown that only two silanols are involved in such vacancy structures,[30] because hydroxyl groups in such proximity would likely spontaneously condense.[31] Based on these experimental observations, hydroxyls with shortest O---O distances in the T-atom vacancies where connected via a single -O- link (i.e. "condensed"), and the next-nearest neighbor Si^{IV} T-atoms and associated oxygen atoms were allowed to fully optimize while freezing all other framework atoms. This is shown in structure **II** in Figure A6.10. Si and O atoms that were allowed to relax during optimization, together with their next-nearest neighbors, were treated with 6-31G(d) basis sets; fully frozen Si centers were treated with a reduced basis set 6-31G to minimize computational

costs.

Grafted **cTi** sites were modeled either with truncated version of the support, or with the SSZ-70 surface model. The entire calix[4]arene-Ti complex core was modeled in both cases, the only difference being the Ti-O-Si connectivity to the support. The Ti^{IV} core and associated O bridges and next-nearest C and Si centers were modeled with the 6-311+G(d,p) basis set, while the rest of the calix[4]arene ligand was modelled with a 6-31G(d) basis set. In the truncated model, connectivity to the support was modeled by attachment of the Ti^{IV} core, through an oxygen bridge, to a single Si^{IV} center truncated by hydrides (i.e. $-OSiH_3$), as done for related systems.[32] This $-OSiH_3$ ligand is a sufficiently large cluster to result in accurate Ti-O bond distances, as indicated by comparison to a larger cluster with Si-O-Si connectivity in Figure A6.9. In the full SSZ-70 structural model, the $-OSiH_3$ was replaced by connectivity to the SSZ-70 framework at a X_3SiO^- ligand (X is the rest of the SSZ-70 framework) originating from support, either in the model for terminal T-atom positions **I** or a defect silanol inside a 12-MR pocket **II** (Figure A6.10).

6.3. Results and Discussion

To characterize the Ti^{IV} coordination sphere, we examined **cTi/X** samples by Ti K-edge X-ray absorption (XAS) near edge spectra (XANES), with results shown in Figure 6.1A and Table 6.1. Prominent pre-edge features are observed for all materials, manifested as a peak at energies lower than the rising edge. These pre-edge features are known to be sensitive to changes in the symmetry of the oxygen coordination environment of Ti^{IV}.[33] With the exception of **cTi/2**, values of pre-edge position at 4970.0 eV and pre-edge height 0.50 ± 0.03 are observed for all materials, consistent with previous reports of calix[4]arene-Ti^{IV} grafted on silicate surfaces.[30,33,34] In contrast, for **cTi/2**, we observed a lower pre-edge height of 0.38 and shifted pre-edge position of 4970.2 eV, which indicate deviations from ideal tetrahedral symmetry,[35] and longer Ti-O bond lengths,[36] respectively. Such changes suggest that a different coordination environment of Ti^{IV} occurs in **cTi/2**, relative to all other **cTi/X** samples.

Table 6.1. Physicochemical characterization of cTi grafted on different silicate supports

Sample	Ti K-edge XANES pre-edge [a]		EXAFS fit parameters [b]		observed methoxy
	position (eV)	height (a.u.)	*R* (Å)	σ^2 x10^3 (Å^2)	^{13}C NMR δ (p.p.m) [c]
cTi/1	4970.0	0.47	1.82	3(1)	64.1
cTi/2	4970.2	0.38	1.86	5(2)	63.5
cTi/2-a	4970.0	0.49	1.82	3(1)	64.2
cTi/3-a	4970.0	0.51	1.82	3(1)	64.3
cTi/3-b	4970.0	0.54	1.82	3(1)	64.2
HcTi/1	-	-	-	-	64.4
HcTi/2	-	-	-	-	64.0

[a]From analysis of Ti K-edge XANES pre-edge features shown in Figures 1(A) and S1; these data correspond to materials without methoxy ^{13}C isotopic enrichment, with physicochemical properties in Table A6.2.[b] EXAFS fit parameters for data in Figure 6.1(B); amplitude reduction factor S_0^2 is 0.76 ± 0.04 for all samples; coordination number *N* is 4 for all samples; energy correction term ΔE_0 is -3.3 ± 0.8 for all samples; σ^2 is the disorder term, where the number in parenthesis denotes uncertainty in last significant digit; *R* is distance between absorber and backscatter, ± 0.01. EXAFS fits for **1** and **3-a** correspond to previously published materials.[6] [c] From Figure 6.3A.

We also examined Ti K-edge EXAFS, shown in Figure 6.1B. EXAFS best-fit parameters (Table 6.1) indicate 4 oxygen scatterers located at a distance of 1.82 Å for all materials except **cTi/2**, in agreement with the Ti-O distances observed in calix[4]arene-Ti^{IV} complexes by single-crystal X-ray diffraction.[37,38] In contrast, in **cTi/2**, a scattering distance of 1.86 Å and an increase in σ^2 are observed. This increased σ^2 indicates greater variability in the Ti-O bond distances surrounding Ti^{IV} in **cTi/2**, and is reflected in its diminished EXAFS intensities. These observations support data from Ti K-edge XANES, where increased geometric distortion and longer Ti-O distance were detected for **cTi/2**.

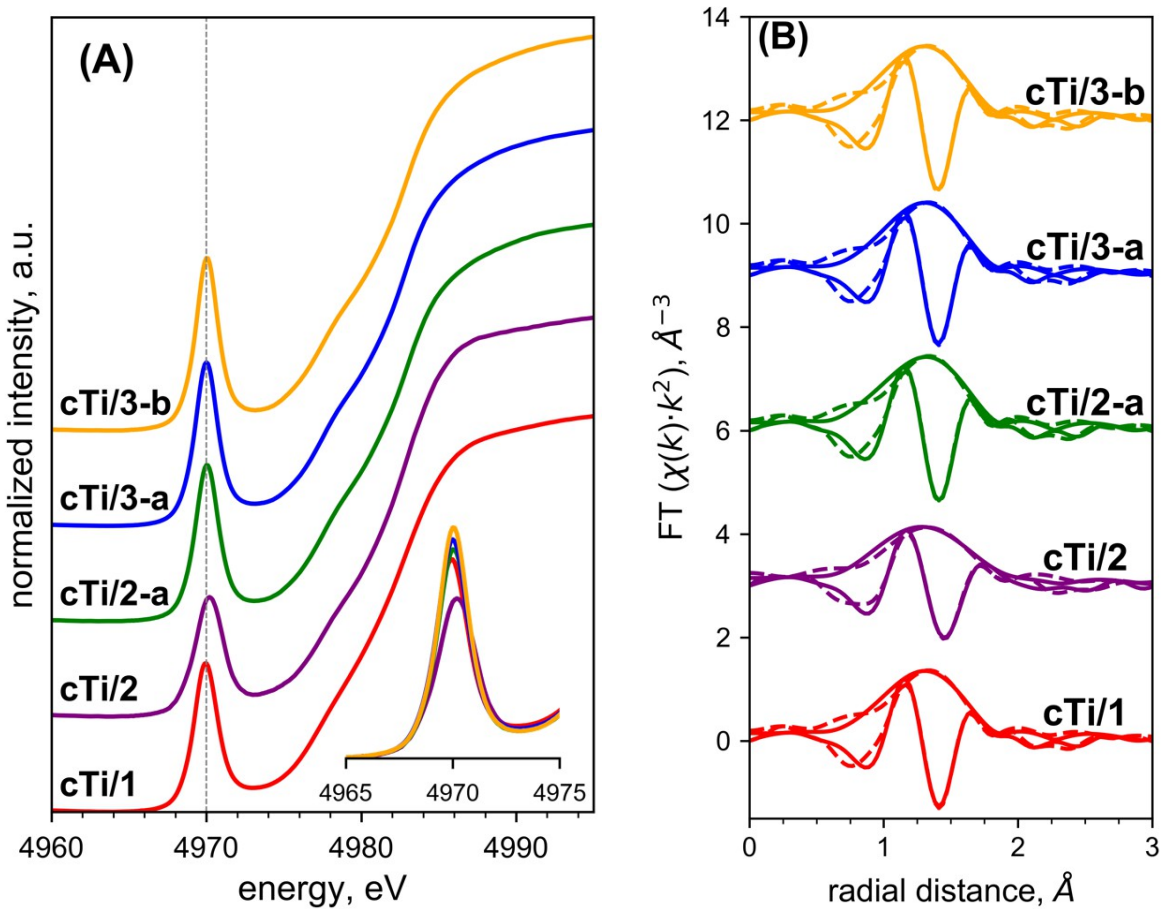

Figure 6.1. (A) Normalized Ti K-edge XANES spectra of **cTi/X** samples; the position of prominent pre-edge features is highlighted by a dashed line at 4970.0 eV. Pre-edge features are overlaid at the bottom right for visual comparison; detail in Figure A6.1. **(B)** Magnitude and Imaginary parts of Fourier transforms (FT) of EXAFS spectra (solid lines), together with best-fits to the data resulting from calculated parameters in Table 6.1 (dashed lines); see Figure A6.2 for $\chi(k)$. All spectra are staggered for clarity, and the material is indicated beside each dataset.

Given that **cTi** is grafted intact in **cTi/2** (calix:Ti ~ 1), and has an identical connectivity as in all other materials (UV-vis edge energies, *vide supra*), the different oxygen coordination sphere detected by XAS in **cTi/2** must originate from changes in the conformation of grafted **cTi**, rather than in the types or numbers of ligands bound to the Ti^{IV} center.[33] Such conformational change is not entirely unexpected, because the calix[4]arene scaffold is conformationally flexible.[39–42]

To further probe the conformation of **cTi**, we ^{13}C isotopically enriched the lower-rim methoxy position of **cTi** (red in Scheme 6.1) and characterized all samples via ^{13}C-{^{1}H}-CPMAS NMR spectroscopy. We did this because $\delta(^{13}C)$ of this substituent is known to be affected by the distance of dative interactions between the methoxy oxygen and Ti^{IV} center (red dashed line in Scheme 6.1),[16] which is expected to change with the calix[4]arene conformation.[40,41,43] Figure 6.3A shows ^{13}C-{^{1}H}-CPMAS NMR spectra, with resonance positions summarized in Table 6.1. All **cTi/X** samples except **cTi/2** exhibit a resonance of 64.2 ± 0.2 ppm, in reasonable agreement with the chemical shift of ~65 ppm measured at the lower-rim methoxy substituent (position 1 in

Scheme 6.1) in solution complexes.[37] In contrast, this chemical shift for **cTi/2** is measured at 63.5 ppm, 0.7 ppm upfield. As a control of the accuracy of these measurements, no shift is detected for *t*-butyl groups (2 in Scheme 6.1) at ~30 ppm, and the $\delta(^{13}C)$ for the lower-rim methoxy substituent is not affected by **cTi** surface density (Figure A6.4). Therefore, the 0.7 ppm upfield shift for **cTi/2** indicates a distinct chemical environment for the lower-rim methoxy group. Together with data from XAS, these results provide strong evidence of a different conformation of **cTi** in **cTi/2**.

To further understand the possible conformations of grafted **cTi**, we performed density functional theory calculations (DFT). We tested the accuracy of such an approach by comparing experimental single-crystal X-ray diffraction data and DFT results for **cTi-Cl**, a **cTi** analog, in Table A6.3.[37] Based on this comparison, we conclude that DFT accurately predicts $<d_{Ti\text{-}O}>$, the average distance of the four Ti-O covalent bonds that comprise the inner-coordination sphere of Ti^{IV}.

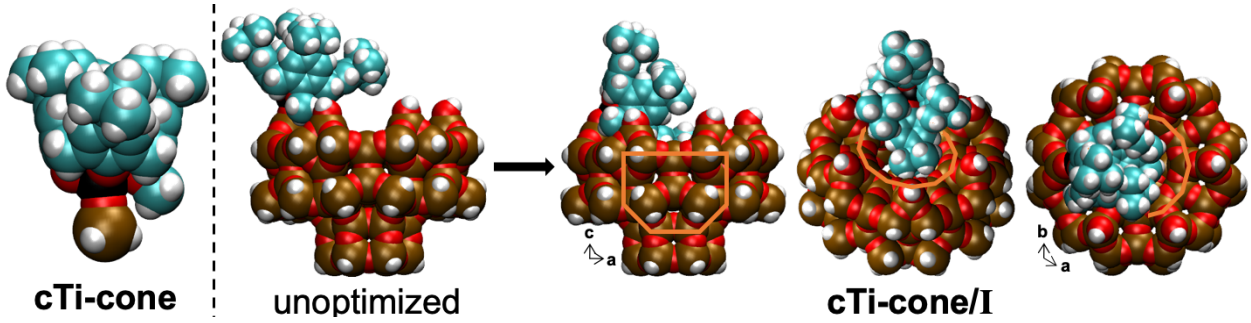

Figure 6.2. Van-der-Waals representations of the DFT-optimized structure **cTi-cone** (left) and **cTi-cone/I** (three different views), compared to an unoptimized structure derived from **cTi-cone/I**, where all internal geometric parameters remain unchanged, but where the (calix)Ti-O-Si angle was set to 180° (this is the approximate angle of this bond in cTi-cone) without any further optimization. An overlay of 12-MR cavities is shown in orange for direct comparison with Scheme 6.2. The average Ti-O distance $<d_{Ti\text{-}O}>$ is 1.83 ± 0.04 Å, where ± indicates standard deviation of distances (see Table A6.3). Red: O; white: H; black: Ti; brown: Si; cyan: C.

We first used a $-OSiH_3$ ligand as a surrogate for connectivity to the silicate support, resulting in DFT-optimized structure, **cTi-cone** in Figure 6.2 (see 6.5.3.2 for higher-energy conformations than "cone"). In order to understand how the surface environment affects this conformation, we constructed structure **I**, a model of the zeotype surface of **2** based on the crystallographic structure shown in Scheme 6.2 (Figure A6.10). We subsequently grafted **cTi-cone** to a terminal T-atom positions (**i**) in model **I**, the only possible location in **2** (note that all (**i**) are crystallographically equivalent). The resulting structure **cTi-cone/I** (Figure 6.2) is an *in-silico* model of **cTi/2**.

We observe **cTi-cone/I** to exhibit an unusual conformation in Figure 6.2: the calix[4]arene scaffold is tilted into the 12-MR cavity, with one *t*-butyl group (diameter ~7 Å, Figure A6.12) fitting precisely within and spanning the entire diameter of the 12-MR cavity (~7.1 Å).[21] The calculated average Ti-O distance in **cTi-cone/I** is $<d_{Ti\text{-}O}>$ = 1.83 ± 0.04 Å, where ± indicates standard deviation of the four Ti-O bonds within complex. This is longer and less symmetric than the $<d_{Ti\text{-}O}>$ = 1.82 ± 0.01 Å calculated in **cTi-cone**. In particular, the Ti-O(support) lengthens to 1.88 Å in **cTi-cone/I**, compared to 1.82 Å of the Ti-$OSiH_3$ bond in **cTi-cone** (Table A6.3). These

calculated trends mirror experimental observations by XANES and EXAFS, which determined that Ti-O distances are lengthened and exhibit stronger distortion from an ideal tetrahedron in **cTi/2** relative to other samples. We surmise that **cTi-cone/I** is an accurate model of the state of **cTi** in **cTi/2**, indicating that the surface environment in **cTi/2** causes **cTi** to adopt an unusual conformation, responsible for the spectroscopic (XAS and MAS NMR) particularities of this sample.

To understand the origin of the unique conformation predicted by DFT in **cTi-cone/I**, we consider an unoptimized structure derived from **cTi-cone/I**, but where the entirety of the calix[4]arene scaffold is forced to lie outside of the 12-MR cavity (Figure 6.2). Unoptimized and optimized structures differ by 194 kJ mol^{-1}, of which 158 kJ mol^{-1} are due to non-covalent dispersion (i.e. Van der Waals) interactions, as calculated by DFT-D3(0) methods.[25] The stabilization of the conformation **cTi-cone/I** is therefore associated with Van der Waals interactions – between hydrocarbon fragments on the calix[4]arene and siloxane on the silicate – which are maximized when a phenolic sub-unit of **cTi** orients itself onto the rim of the 12-MR cavity and a *t*-butyl group interacts directly with the walls of this cavity. This spatial orientation is enabled by the specific grafting location at terminal T-atom positions (**i**) and its relative distance to the 12-MR cavity (**ii**). If, instead, grafting occurs within the 12-MR cavity (as in **cTi/3-b**), no reorientation of the *t*-butyl group is possible because of steric crowding within the confines of the cavity (see Figure A6.11). These conclusions are summarized in Scheme 6.3.

The presence of **cTi** in a unique conformation (**cTi-cone/I**) is consistent with the uniqueness of the spectroscopic features of **cTi/2** in XAS (Figure 6.1), ^{13}C-{^{1}H}-CPMAS NMR (Figure 6.3), and ^{1}H MAS NMR (Figure A6.5). This conformation (**cTi-cone/I**) requires **cTi** be connected to terminal T-atom positions (**i**), which are known to act as the only location where **cTi** is grafted in **cTi/2**.[6] We therefore surmise that the structural uniformity in **cTi/2**, where the crystallographically equivalent terminal T-atom positions (**i**) act as the only grafting locations, leads to **cTi-cone/I** being observed uniquely in **cTi/2**. This contrasts with the inherently non-uniform environments in amorphous **cTi/1**, or at a variety of possible grafting T-sites locations (and resulting environments/conformations) in zeotype vacancies of **cTi/2-a**, **cTi/3-a**, **cTi/3-b**, as summarized in Scheme 6.3.

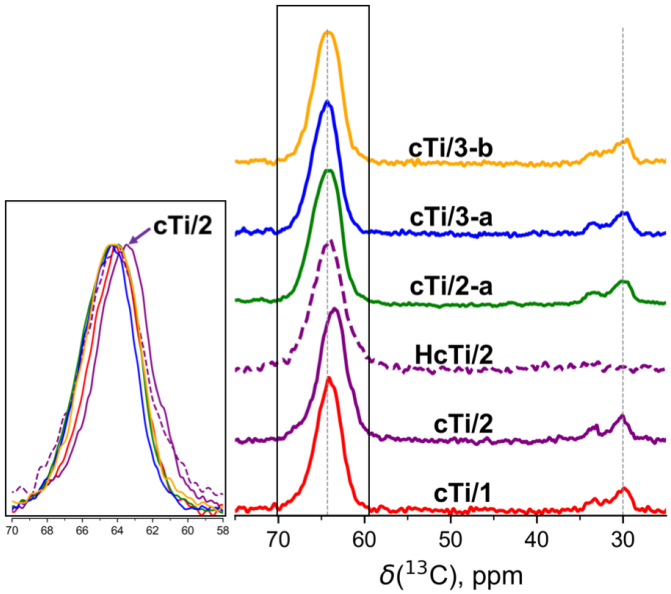

Figure 6.3. ^{13}C-{^{1}H}-CPMAS NMR spectra, staggered and normalized to maximum value, for samples indicated. Vertical lines and numbers indicate principal resonances discussed in the text. The inset shows an overlay off all spectra with the different maximum for **cTi/2** highlighted. Associated ^{1}H MAS NMR spectra are shown in Figure A.6.5.

Given the interaction between the *t*-butyl substituent and 12-MR cavity observed in Figure 6.2 for **cTi-cone/I** (the unique conformation observed in **cTi/2**), we decided to examine **HcTi/2**, where this upper-rim *t*-butyl substituent is absent (Scheme 6.1). DFT calculations (Figure A6.13) predict that the phenolic sub-unit of **HcTi** lies flat onto the rim of the 12-MR cavity, but no part of the molecule fills the 12-MR cavity. The ^{13}C-{^{1}H}-CPMAS NMR spectrum of **HcTi/2** isotopically enriched at the lower-rim methoxy position is shown in Figure 6.3, and exhibits a peak position (Table 6.1) that overlays with those of all other **cTi/X** samples, except **cTi/2**, as well as with a control sample **HcTi/1** (Figure A6.6). This result suggests that the unique conformation involving a reoriented calix[4]arene scaffold that occurs in **cTi/2** does not occur in **HcTi/2**, despite the structural uniformity of both samples. This in turn means that the interactions between a *t*-butyl substituent and the 12-MR cavity are essential to achieving a unique conformation in **cTi/2**, which cannot occur in the absence of this interaction in **HcTi/2**.

Scheme 6.3. Summary of calix[4]arene-Ti^{IV} conformations in zeotype structures.

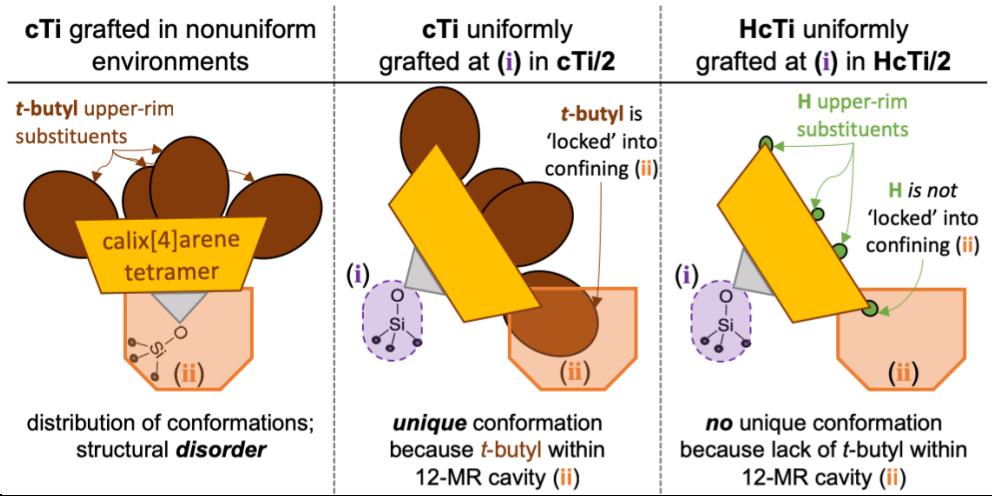

6.4. Conclusions

This comparison of **cTi/2** to **HcTi/2** provides strong evidence that one of the *t*-butyl substituents of the grafted macrocycle in **cTi/2** is located within the microporous cavity, with the remainder outside of it (Scheme 6.3). This demonstrates that even a 'partial penetration' of an adsorbate into a pore can bring about a unique conformation, controlled by the Van der Waals interactions between the adsorbate and pore walls. Such non-covalent interactions of adsorbates with pore walls have been previously reported when molecules are fully confined within the micropores of zeolites.[44,45] Our observations here point to the prevalence of these interactions even for molecules that are only partially confined, at an interface between a less sterically hindered ('unconfined') site and an adjacent 'more confining' cavity.

We view this data as highly relevant to understanding how molecules transition into confining environments in porous materials. Many studies have suggested that the state of a molecule at the interface of a surface and confining micropore controls the kinetics of adsorption and reaction. For example, Lercher and co-workers[1,2] postulated the orientations of aromatic molecules controls sticking and trapping coefficients on an external crystal surface.[1] Separately, several reports have observed that more confining voids exposed to a less spatially constrained environment in zeolites – such as 12-MR cavities,[6] micropore openings,[7,8] or side-pockets exposed to a larger micropore –[46] provide molecular specificity that controls reaction rates even when reactants are only partially confined. The kinetic nature of these phenomena, however, has precluded a direct observation of partially confined molecules. Our observations here constitute a "snapshot" of such molecules, and provide direct evidence that partial confinement brings about a unique molecular orientation of an adsorbate, at the interface of a surface and confining micropore.

6.5. Appendices

6.5.1. Physicochemical Properties of Grafted Materials

Physicochemical characterization, with results in Table A6.1, was performed in order to confirm the integrity of the grafted calix[4]arene-Ti^{IV} complex. Grafting densities are comparable (within a factor of 2) for all samples, and are higher for **HcTi/X** than for **cTi/X**, because the smaller surface footprint of the former (which lacks large *t*-butyl substituent) enables a higher surface packing density. Measured calix[4]arene-to-Ti ratios (calix:Ti) are ~1.0, indicating intact grafting of the molecular **cTi** complex across all samples. calix:Ti > 1 for **HcTi/X** are attributed to measurement errors due to the very low loading of this complex on the surface. UV-visible spectra (Figure A6.3) exhibit broad absorption features at 290-500 nm, arising from calix[4]arene(O)-Ti^{IV} ligand-to-metal charge transfer transitions (LMCT),[16] consistent with calix[4]arene coordination to Ti^{IV} after grafting. The measured edge-energies associated with these LMCT are known to be sensitive to the number of covalent connections between calix[4]arene oxygens and grafted Ti^{IV} cations,[41] and are shown in Table 6.1. Their uniform value of 2.27 ± 0.02 eV for all **cTi/X** samples is indicative of identical connectivity within grafted **cTi** centers across all materials. This result is expected, given uniform chelation of Ti^{IV} centers by calix[4]arene macrocycles, irrespective of the support.

A higher value of this edge energy for **HcTi/X** (2.43 ± 0.02 eV), is agreement with prior reports,[34] indicates a different macrocyclic ligand. In particular, the higher energy transition of this LMCT suggest that electron donating *t*-butyl groups increase the energy of the highest-occupied-molecular-orbitals of the calix[4]arene ligand in **cTi**, compared to H ligand in **HcTi**, resulting in a smaller energy gap for transition into the lowest-unoccupied-molecular-orbitals of the d^0 Ti^{IV} center.

Table A6.1. Physicochemical characterization of calix[4]arene-Ti grafted on different silicates, with ^{13}C enrichment at the lower-rim methoxy substituent

Sample	calix:Ti [a]	Ti nm^{-2} [b]	wt% Ti	UV-vis LMCT edge (eV) [c]
cTi/1	0.8	0.25	0.38	2.32
cTi/2	1.0	0.14	0.15	2.27
cTi/2-a	1.1	0.34	0.24	2.25
cTi/3-a	0.8	0.32	0.37	2.27
cTi/3-b	0.9	0.21	0.17	2.26
cTi/3-a-lim[d]	0.8	0.18	0.20	2.29
HcTi/1	1.9	0.44	0.55	2.41
HcTi/2	1.5	0.23	0.15	2.44

[a]Ratio of measured calix[4]arene to Ti content. [b]Ti content normalized to accessible surface area of the silicate (t-plot external surface area for zeotypes; BET surface area for amorphous SiO_2). [c]UV-visible calixarene-to-Ti metal-to-ligand charge-transfer edge-energy; see Figure A6.3A. [d] Material analogous to **cTi/3-a**, but with a lower grafting density.

Table A6.2. Physicochemical characterization of cTi grafted on different supports for XAS absorption measurements. [a]

Support	S_{ext} ($m^2\ g^{-1}$)[b]	Calix:Ti	Ti nm^{-2}	wt% Ti	UV-vis LMCT Edge (eV)
1	190	1.0	0.24	0.35	2.29
2	89	0.9	0.16	0.11	2.30
2-a	-	1.0	0.28	0.19	2.23
3-a	135	0.9	0.31	0.32	2.27
3-b	-	1.0	0.14	0.13	2.28

[a] All materials, with the exception of **2-a**, corresponds materials in Chapter 7. They were synthesized by identical synthetic procedures to those shown in Table A6.1, but lack ^{13}C enrichment at the lower-rim of the calixarene (1 in Scheme 6.1). Note the similarity in physicochemical properties to materials in Table A6.1.

[b] Accessible surface area, determined by the BET method for SiO_2, and from the t-plot external surface area for microporous zeotypes.

6.5.2. Electronic Spectra

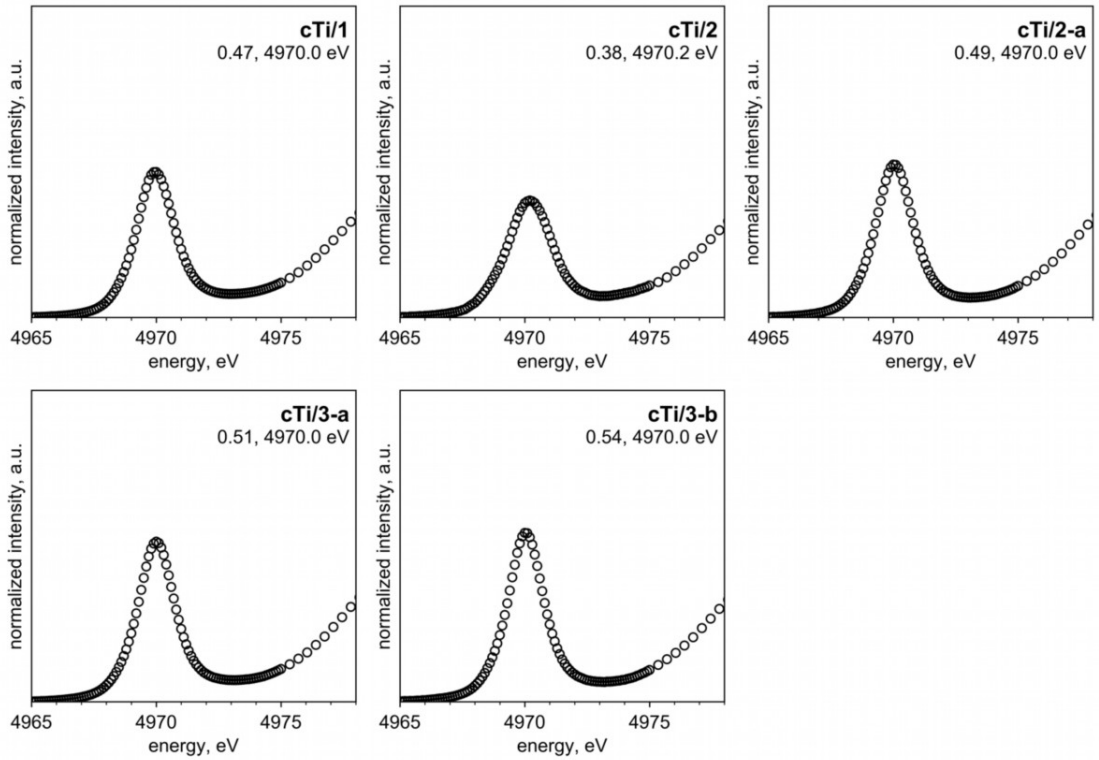

Figure A6.1. Detail of Ti K-edge XANES pre-edge features. Normalized peak height and pre-edge peak position, defined as the energy of maximum intensity, are shown for each spectrum.

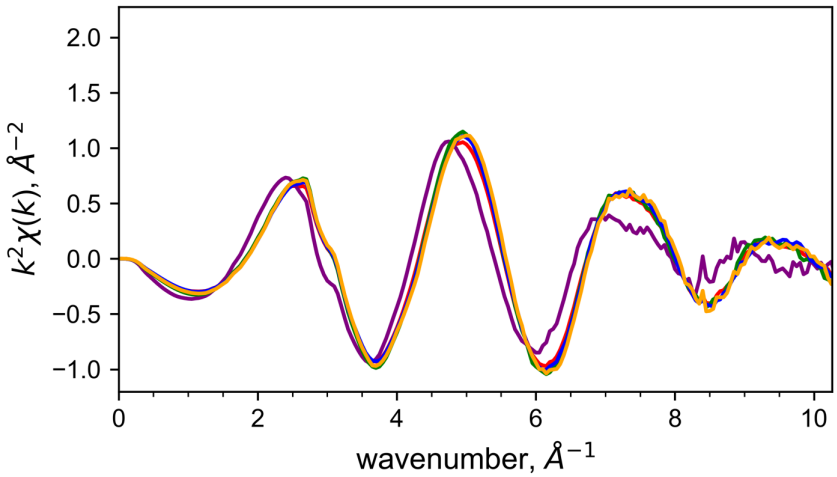

Figure A6.2. EXAFS $\chi(k)$ used in Fourier transforms of the spectra characterizing in Figure 6.1B. Colors correspond to colors in Figure 6.1B: **cTi/1** in red, **cTi/2** in purple, **cTi/2-a** in green, **cTi/3-a** in blue, **cTi/3-b** in orange. Fourier transform windows were 2.84 Å^{-1} to 8.76 Å^{-1} for **cTi/2-a**, and 3.12 Å^{-1} to 10.26 Å^{-1} in all others.

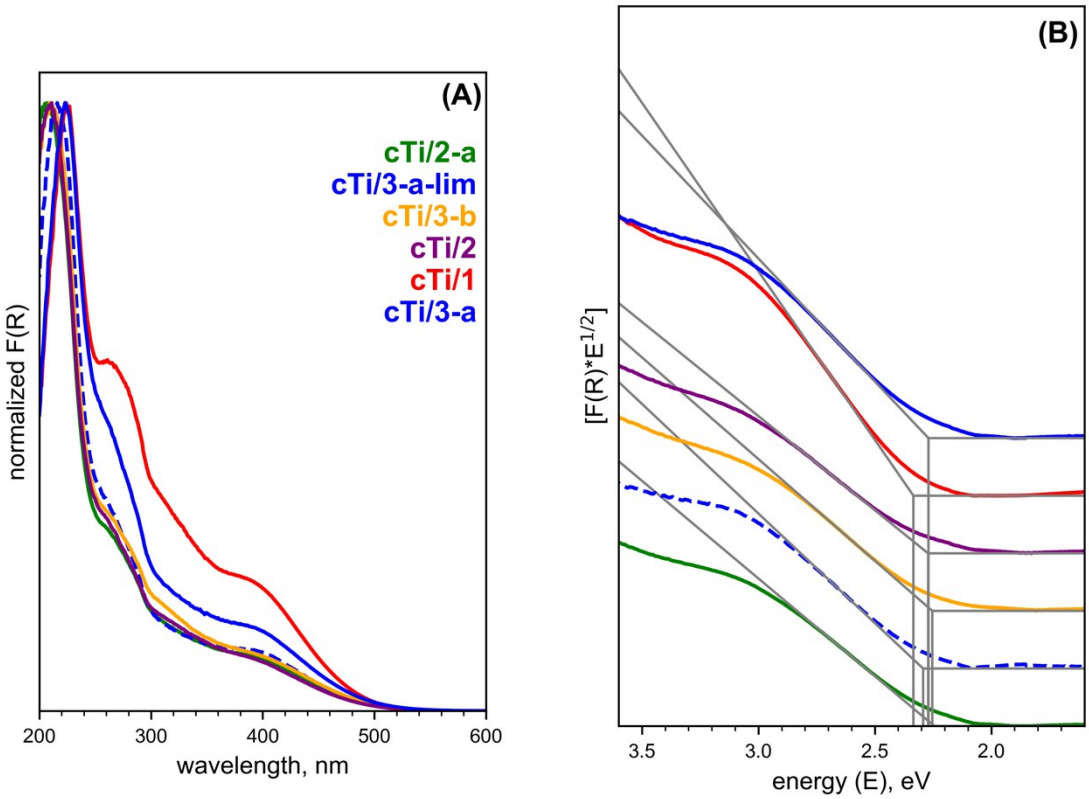

Figure A6.3. (A) Diffuse-reflectance UV-visible spectra and **(B)** Tauc plots used to calculate UV-visible LMCT edge-energies for materials color-coded as indicated in **(A)**. Dashed blue indicates **cTi/3-a-lim**. Grey lines are tangents in calculation of the edge-energies, which correspond to the intercept indicated by the grey vertical line.

6.5.3. NMR Measurements

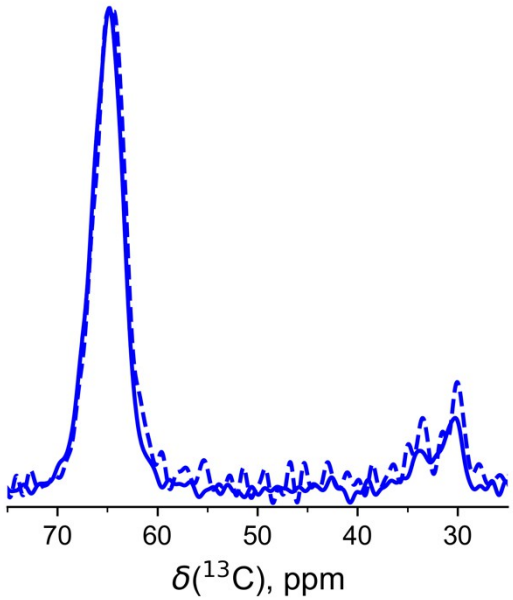

Figure A6.4. Normalized $^{13}C\{^{1}H\}$ CPMAS NMR comparing of **cTi** grafted on **3-a** at low (dashed) vs. high (solid) loadings of **cTi** (see **3-a-lim** in Table A6.1 for physicochemical properties of material prepared at low loading). Surface grafting density does not affect the observed chemical shifts, as evident by the overlay of the spectra. Without minimum-maximum normalization, the spectra differ in intensity of their maxima by 2.57.

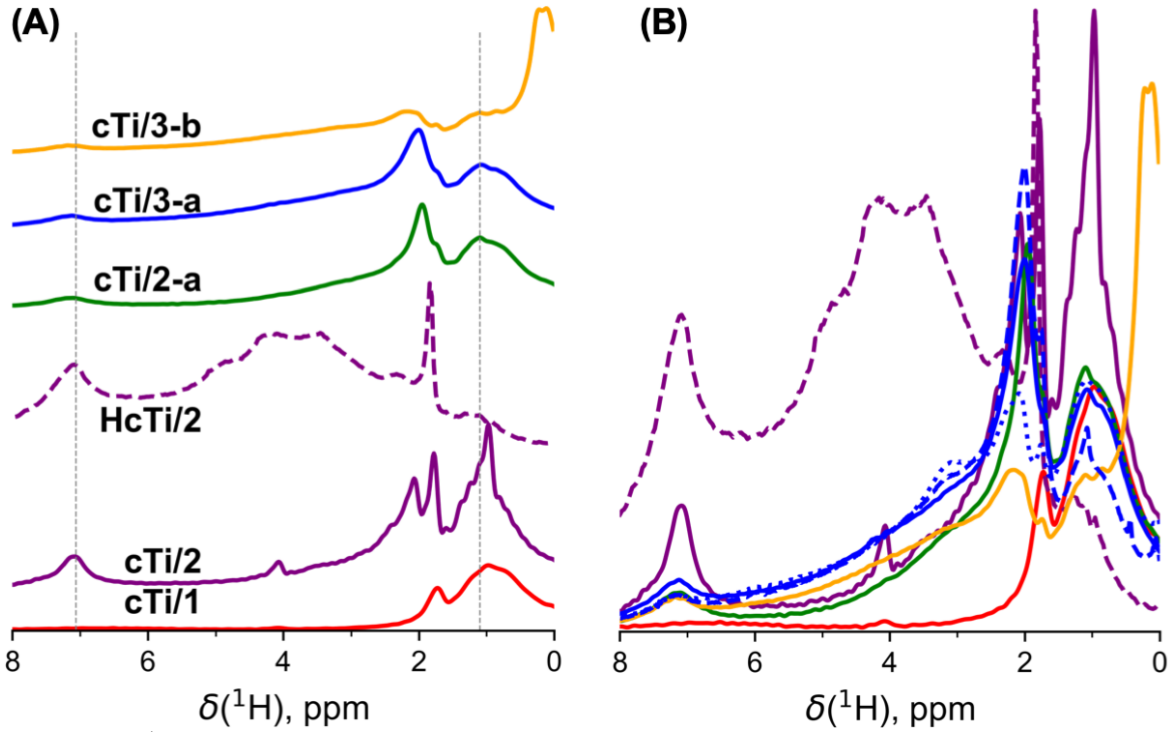

Figure A6.5. ^{1}H MAS NMR spectra normalized by wt% Ti content for samples indicated. **cTi/1**: red; **cTi/2**: purple; **HcTi/2**: dashed purple; **cTi/2-a**: green; **cTi/3-a**: blue; **cTi/3-b**: orange. **(A)** shows staggered spectra, while **(B)** shows an overlay of the same spectra. Blue dotted lines correspond to a different batch (i.e. reproduction) of **cTi/3-a**, while blue dashed line correspond **cTi/3-a-lim** in Table A6.1. Note how resonances of **cTi/2** and **HcTi/2** are more intense than other **cTi/X** materials, despite all spectra being normalized by wt% Ti content, consistent with the spectroscopic uniqueness of calix[4]arene grafted on **2**.

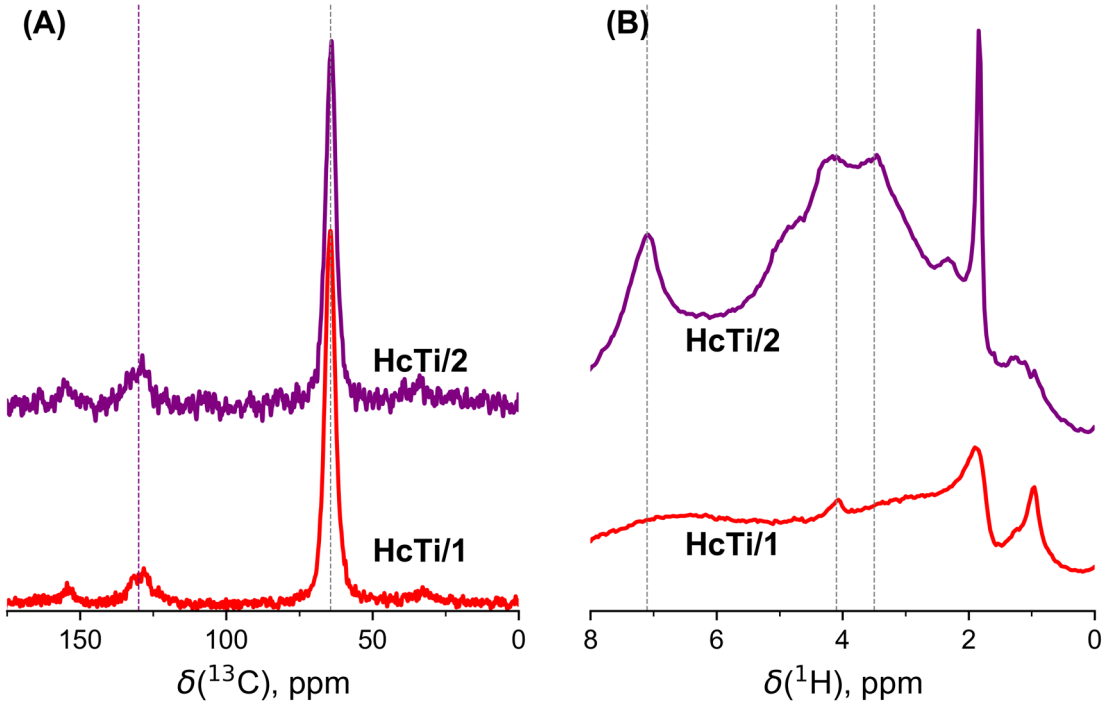

Figure A6.6. (A) ^{13}C-{^{1}H}-CPMAS NMR for **HcTi/1** and **HcTi/2** samples indicated beside each spectrum. In comparison to spectra in Figure 6.3 of the main text, the lack *t*-butyl resonances (~ 30 ppm) are evident; resonances at ~ 130 ppm correspond to aromatic carbons. Vertical lines indicate principal resonances; spectra are normalized to maximum value. **(B)** ^{1}H MAS NMR for the same materials as in **(A)**. Dashed vertical lines highlight principal resonances.

6.5.4. Electronic Structure Calculations

6.5.4.1. Validation of DFT methods

Comparison of DFT-optimized Ti-O and Ti-Cl single-crystal X-ray crystallography (Friedrich and Raidus) in Table A6.3,[37] indicates DFT and crystallography are in agreement within 0.02 Å. **cTi-Cl** contains the same calix[4]arene-Ti functionality as **cTi-cone**, but the H_3SiO^- ligand is replaced by Cl^-; it is used here to test the accuracy of DFT methods, because crystallographic data for **cTi-cone** (or the isopropoxide precursor used for grafting of **cTi** on supports) is not experimentally available. Coordinates of optimized structure included as electronic supplementary information.

Table A6.3. Calculated and measured bond lengths. All bond lengths in Å, and correspond to the pseudotetrahedral coordination sphere (i.e. blue shaded part in Scheme 6.1) and dative Ti-OCH_3 bond (red dashed line in Scheme 6.1).

Bond	DFT (cTi-Cl)	Friedrich and Radius[37]	cTi-cone	cTi-cone/I
Ti-O(calix)	1.825	1.813	1.841	1.828
Ti-O(calix)	1.802	1.796	1.813	1.789
Ti-O(calix)	1.802	1.784	1.813	1.806
Ti-Cl	2.254	2.258	-	-
Ti-OSi	-	-	1.816	1.884
Ti-OCH_3 (dative)	2.58	2.424	2.614	2.673

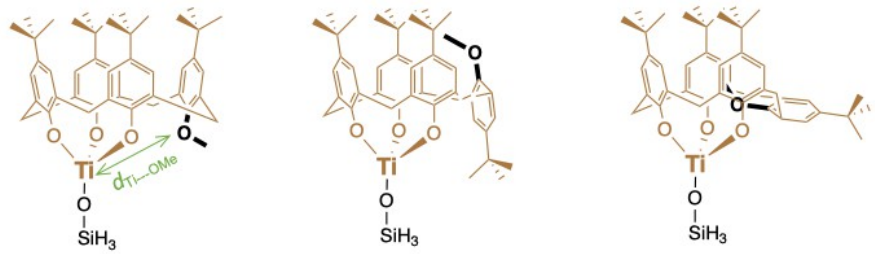

Figure A6.7. Schematic representation of different conformers that can be adopted by **cTi**: cone, partial-cone (pcone), and flattened partial-coned (fpcone). Below each structure, selected parameters from the optimized conformer are shown. $<d_{Ti\text{-}O}>$ is the average distance of the four Ti-O bonds that comprise the inner-coordination sphere of Ti^{IV}; the number in parenthesis indicates the standard deviation for the last significant digit. $d_{Ti\text{---}OMe}$ is the distance of the dative bond between the methoxy lower-rim substituent and the Ti^{IV} center; this distance is indicated in green for **cTi-cone** structure. ΔE is the calculated relative energy of the conformer relative to **cTi-cone**. $\delta(^{13}C)_{DFT}$ is the calculated chemical shift for the methoxy lower-rim substituent (shown bolded) calculated by the Gauge-Independent Atomic Orbital (GIAO) method.[26] Note that the $^{-}OSiH_3$ ligand serves as a proxy for the silicate surface, as done in previous studies.[32] Calculated structures are shown in Figure A6.8.

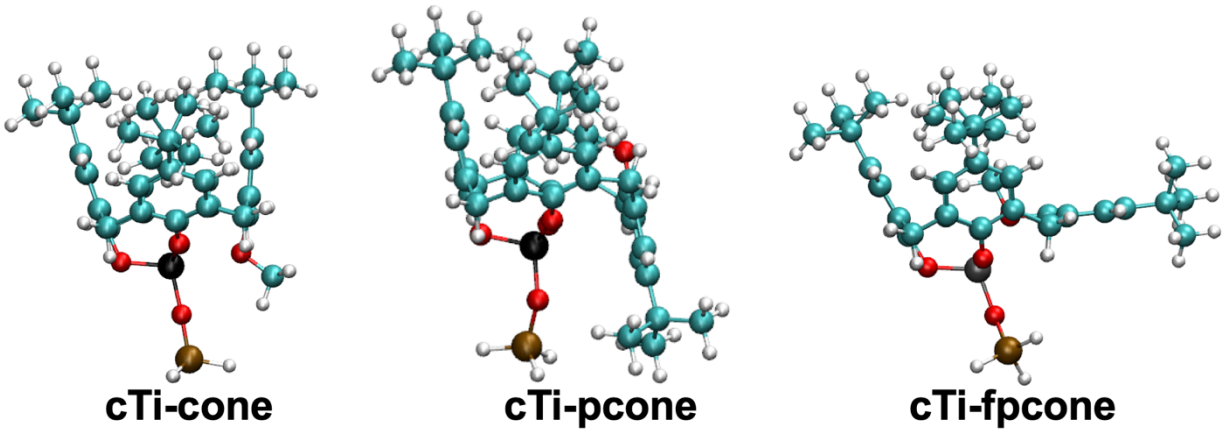

Figure A6.8. DFT-optimized structure of **cTi** conformers represented in Figure A6.7. Red: O; white: H; black: Ti; brown: Si; cyan: C.

6.5.4.2. Comparison of structures in Figure A6.7 and S8:

Figure A6.7 summarizes the different structures and conformations of calix[4]arene-Ti investigated by density functional theory, with results in Figure A6.8. These structures were calculated in order to determine whether these conformations, known for calix[4]arenes in solution,[39] were responsible for the conformation observed in **cTi/2**. Comparison of theoretical results to previous results based on crystallography,[40] shown in Table A6.3, confirm our level of theory is appropriate for predicting $<d_{Ti\text{-}O}>$, the distances of the SiO^- ligands directly bound to Ti^{IV}. The distance of dative interactions, $d_{Ti\text{---}OMe}$, are instead slightly overestimated, consistent with prior conclusions.[43]

The "cone" conformation, **cTi-cone**, is calculated to be the lowest energy conformer, consistent with this being the observed conformation of calix[4]arene-Ti precursors in solution (NMR spectroscopy)[37] and solid-states (X-ray crystallography).[38] The calculated $\delta(^{13}C)_{DFT}$ is 66 ppm, which agrees with experimental observations for calix[4]arene-Ti complexes in solution.[34] The "partial-cone" (**cTi-pcone**), and "flattened partial-coned" (**cTi-fpcone**) are higher in energy, and correspond to different locations the lower-rim methoxy substituent (1 in Scheme 6.1), which is only loosely coordinated to Ti^{IV} through dative interactions. The distance of this dative interaction, $d_{Ti\text{---}OMe}$, is known affect the chemical shift of this lower rim substituent, $\delta(^{13}C)_{DFT}$.[41] **cTi-pcone** results in much longer calculated $d_{Ti\text{---}OMe}$ than **cTi-cone**, and a resulting $\delta(^{13}C)_{DFT}$ is 61 ppm. This is the same chemical shift previously observed when dative interactions between methoxy substituent and a Ti^{IV} center are lacking upon substitution of a Lewis-acidic Ti^{IV} center by a non-Lewis-acidic Si^{IV} center.[16] This 61 ppm chemical shift is more shielded than that observed experimentally for **cTi/2** (63.5 ppm in Table 6.1); we therefore conclude that it is not the conformation adopted in **cTi/2**. **cTi-fpcone** results in calculated $<d_{Ti\text{-}O}>$ that are lengthened relative to **cTi-cone**, as indeed observed in **cTi/2** by EXAFS fits in Table 6.1; however, **cTi-fpcone** also exhibits shorter $d_{Ti\text{---}OMe}$ that result in significant deshielding of the ^{13}C at the lower rim position (1 in Scheme 6.1), resulting in a calculated $\delta(^{13}C)_{DFT}$ of 71 ppm. This deshielding is contrary to what is observed experimentally in **cTi/2**, where an upfield shift in $\delta(^{13}C)$ is observed by ^{13}C-$\{^1H\}$-CPMAS NMR in Figure 6.3A and Table 6.1. We therefore conclude that it is not the conformation adopted in **cTi/2**.

Taken together, these results indicate that **cTi-cone** is the lowest energy conformation of **cTi** in solution, and that neither of the two other possible conformations, **cTi-pcone** and **cTi-fpcone**, are consistent with experimental observations. We therefore conclude that **cTi** remains in its cone conformation in **cTi/2**, but adopts subtle changes in conformation structure, observed in **cTi-cone/I** in Figure 6.2.

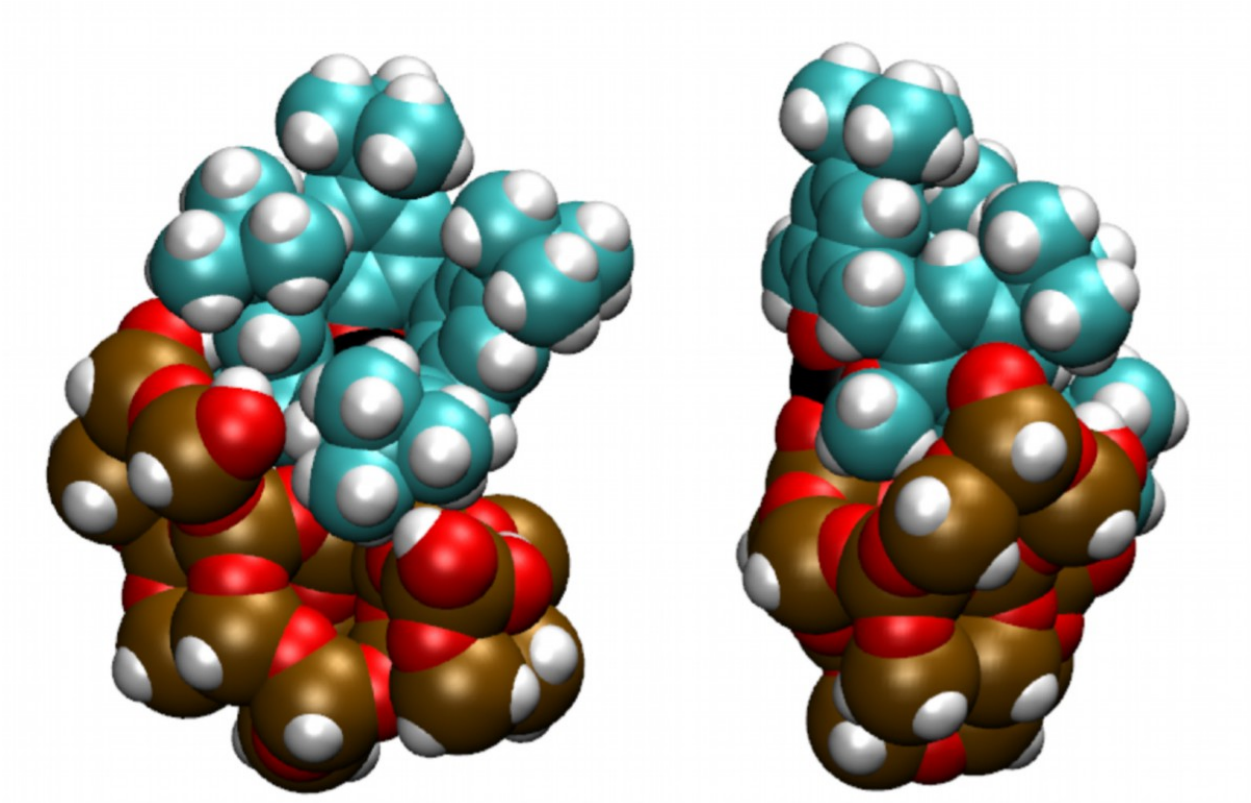

Figure A6.9. Structure **cTi-cone/SiO$_2$**, where additional Si-O-Si bonds and silanols are included to model a more extended silica surface. This model was constructed by removing most of the atoms forming the 12-MR pocket from model **cTi-cone/I**, terminating any coordinatively unsaturated Si^{IV} centers with silanols, and allowing all atomic coordinates to relax during optimization. $\langle d_{Ti\text{-}O} \rangle = 1.82 \pm 0.02$ Å, similar to that in **cTi-cone**, indicating that the inner-sphere TiO_4 coordination shell is appropriately modeled by an -$OSiH_3$ ligand as a proxy for the support, and that additional atoms modelling the silica surface do not affect the conformation of **cTi**. It is also apparent that the calix[4]arene scaffold in this structure makes intimate contact with the SiO_2 structure; however, the bond lengthening in **cTi-cone/I** (increase in length and disordering in $\langle d_{Ti\text{-}O} \rangle = 1.83 \pm 0.04$ Å) does not occur; therefore, confinement by an entire 12-MR pocket is necessary for the coordination sphere of Ti^{IV} to change, as in **cTi-cone/I**.

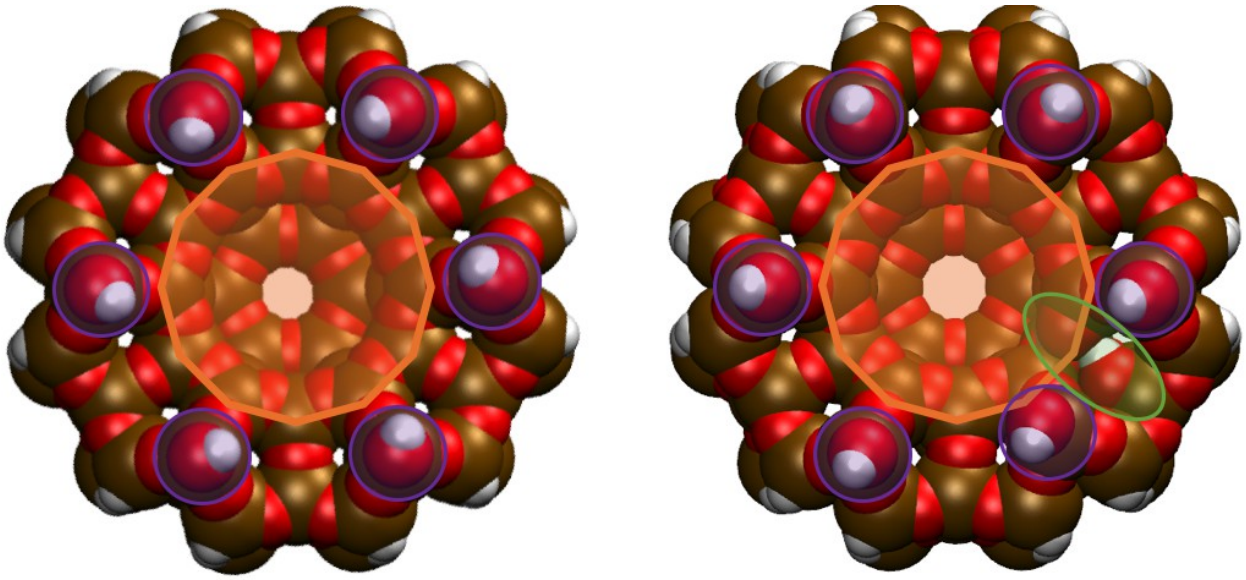

I **II**

Figure A6.10. Model used for 12-MR pocket for structures; corresponds to a view along the a-b plane of the SSZ-70 framework shown in Scheme 6.2. **I** corresponds to a defect-free structure, while **II** corresponds to a structure where a silanol pair defect is located at the top rim of the 12-MR pocket (the silanol pair is highlighted in green). The location of the 12-MR pocket within the SSZ-70 framework is highlighted in orange, and the location of terminal T-site silanols are highlighted in purple, for direct comparison with Scheme 6.2. Red: O; white: H; brown: Si.

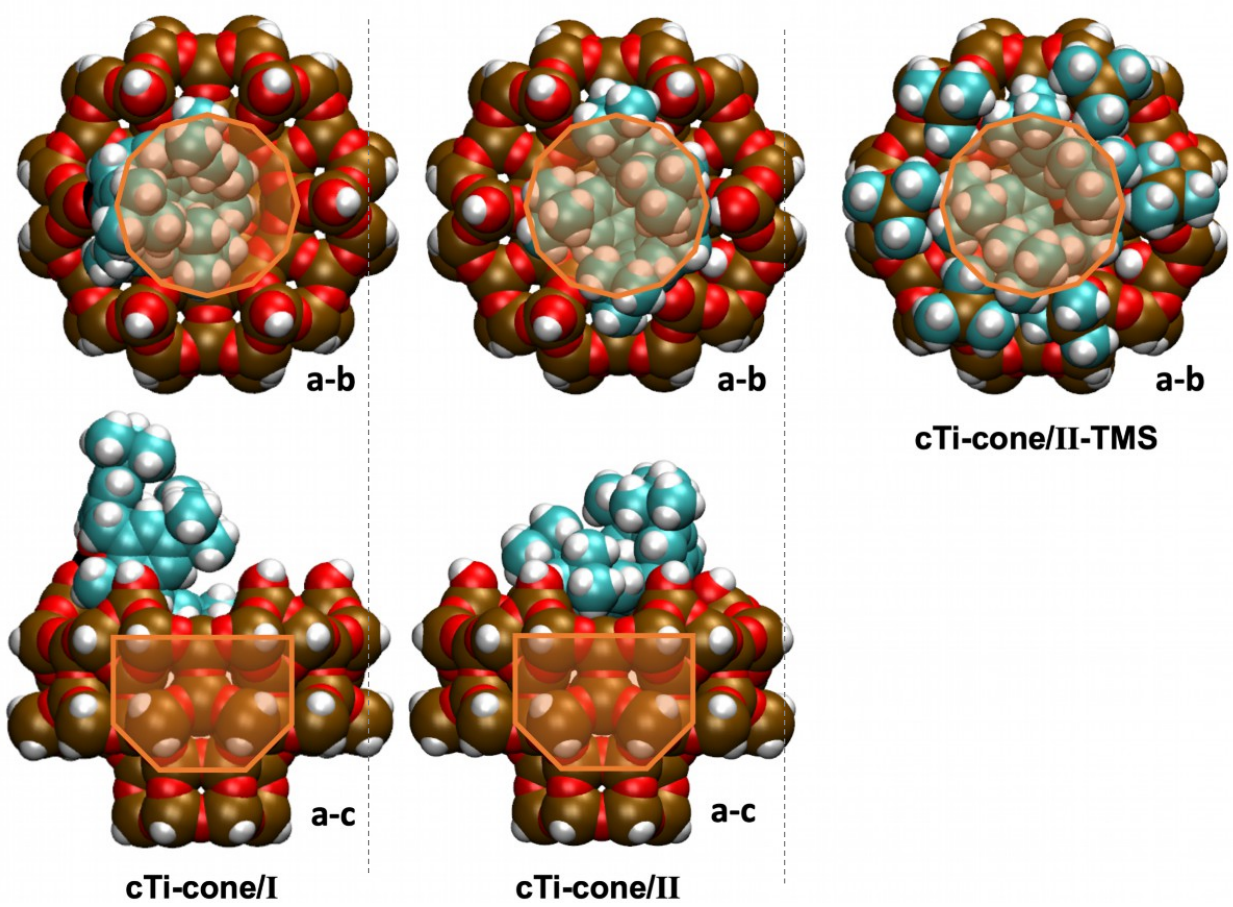

Figure A6.11. Comparison of DFT-optimized structures of **cTi-cone** at different possible framework locations, viewed along the a-b and a-c planes of the SSZ-70 model. **cTi-cone/I** corresponds to the structure show in Figure 6.2 of the main text, with the location of the 12-MR pocket highlighted in orange. Grafting to a silanol in a 12-MR pockets was modeled by a vacancy defect at a T-site (structure **II**, Figure A6.10), and consists of two neighboring silanols within a vacancy defect at the upper-rim of the 12-MR pocket; the **cTi-cone** structure is attached to one of these silanols. **cTi-cone/II** indicates that the **cTi** can be sterically accommodated when attached within this 12-MR pocket; however, the type of specific interactions between a t-butyl group and the 12-MR pocket are not possible: all four *t*-butyl groups are clearly visible outside the 12-MR pocket in **cTi-cone/II**, while one of the *t*-butyl groups points into the 12-MR cavity and is occluded in **cTi-cone/I**. This is because the size of the **cTi** molecule prevents it from freely rotating a *t*-butyl group into the 12-MR pocket. **cTi-cone/II-TMS** shows that the **cTi** can be sterically accommodated even when all external terminal T-site silanols (i.e. **(i)** in Scheme 6.2) are capped by trimethylsilyl groups as occurring in **cTi/3-b**. Red: O; white: H; black: Ti; brown: Si; cyan: C.

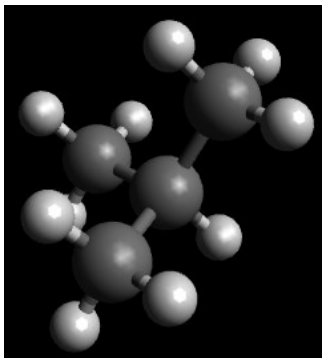

Figure A6.12. Hydride terminated *t*-butyl group, with geometry calculated with RB3LYP/6-311+G(d,p); C: black, H: white. The IEFPCM cavity volume for this structure is 84 Å^3, and surface area is 110 Å^2. This *t*-butyl group can be approximated as an ellipsoid with radii (a, b, c) with volume, V, and surface areas, S, given by $V = \frac{4}{3}\pi abc$ and $S = 4\pi((ab)^{1.6} + (ac)^{1.6} + (bc)^{1.6})^{1/1.6}$. Assuming a circular ellipsoid where $a = b$, the solution of this set of equations gives that $a = b = 3.7$ Å and $c = 1.45$ Å. Figure generated using Avogadro.[47]

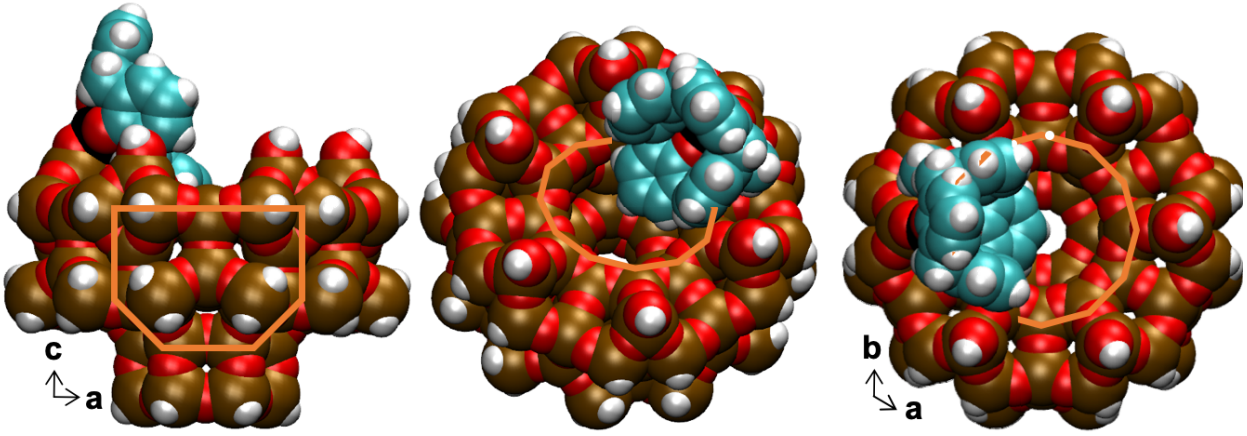

Figure A6.13. Van-der-Waals representations of the DFT-optimized structure **HcTi/I**, where a **HcTi** structure is attached to terminal T-sites (i.e. (**i**) in Scheme 6.2) on a model of the SSZ-70 surface with the 12-MR cavity (Figure A6.10). An overlay of 12-MR cavities is shown in orange for direct comparison with Scheme 6.2. It is apparent that, in the absence of the t-butyl group in **cTi-cone/I** (Figre 2), the calix[4]arene-Ti^{IV} structure lies outside the 12-MR cavity. Red: O; white: H; black: Ti; brown: Si; cyan: C.

6.6 Acknowledgements

Funding from the US Department of Energy (DE-FG02-05ER15696) for catalyst characterization, and the Management and Transfer of Hydrogen via Catalysis Program funded by Chevron Corporation for catalyst synthesis is gratefully acknowledged. We acknowledge the Stanford Synchrotron Radiation Lightsource (SSRL) for access to beam time on beamline 4-3. SSRL, SLAC National Accelerator Laboratory, is supported by DOE, BES, under Contract No. DE-AC02-76SF00515, and the DOE BES funded Consortium for Operando and Advanced Catalyst Characterization via Electronic Spectroscopy and Structure (Co-ACCESS) at SLAC National Accelerator Laboratory. The Molecular Graphics and Computation Facility is funded by the NIH (S10OD023532). We would like to thank Dr. Simon R. Bare, Dr. Adam S. Hoffman, and Dr. Alexey Boubnov for assistance in XAS measurements and insightful discussions. Dr. Andrew Solovyov and Prof. Vitaly Kalchenko is acknowledged for help with calixarene synthesis. Christian Schroeder and Prof. Hubert Koller are acknowledged for MAS NMR characterization and insightful discussions. Dr. David W. Small is acknowledged for assistance performing electronic structure calculations.

6.7. References

(1) Reitmeier, S. J.; Gobin, O. C.; Jentys, A.; Lercher, J. A. Enhancement of Sorption Processes in the Zeolite H-ZSM5 by Postsynthetic Surface Modification. *Angew. Chem. Int. Ed.* **2009**, *48*, 533–538.

(2) Reitmeier, S. J.; Mukti, R. R.; Jentys, A.; Lercher, J. A. Surface Transport Processes and Sticking Probability of Aromatic Molecules in HZSM-5. *J. Phys. Chem. C* **2008**, *112*, 2538–2544.

(3) Qi, X.; Vattipalli, V.; Dauenhauer, P. J.; Fan, W. Silica Nanoparticle Mass Transfer Fins for MFI Composite Materials. *Chem. Mater.* **2018**, *30*, 2353–2361.

(4) Canlas, C. P.; Lu, J.; Ray, N. A.; Grosso-Giordano, N. A.; Lee, S.; Elam, J. W.; Winans, R. E.; Van Duyne, R. P.; Stair, P. C.; Notestein, J. M. Shape-Selective Sieving Layers on an Oxide Catalyst Surface. *Nat. Chem.* **2012**, *4*, 1030–1036.

(5) Radhakrishnan, S.; Goossens, P.-J.; Magusin, P. C. M. M.; Sree, S. P.; Detavernier, C.; Breynaert, E.; Martineau, C.; Taulelle, F.; Martens, J. A. In Situ Solid-State ^{13}C NMR Observation of Pore Mouth Catalysis in Etherification of β-Citronellene with Ethanol on Zeolite Beta. *J. Am. Chem. Soc.* **2016**, *138*, 2802–2808.

(6) Grosso-Giordano, N. A.; Hoffman, A. S.; Boubnov, A.; Small, D. W.; Bare, S. R.; Zones, S. I.; Katz, A. Dynamic Reorganization and Confinement of Ti(IV) Active Sites Controls Olefin Epoxidation Catalysis on Two-Dimensional Zeotypes. *J. Am. Chem. Soc.* **2019**, *141*, 7090–7106.

(7) Martens, J. A.; Souverijns, W.; Verrelst, W.; Parton, R.; Froment, G. F.; Jacobs, P. A. Selective Isomerization of Hydrocarbon Chains on External Surfaces of Zeolite Crystals. *Angew. Chem. Int. Ed.* **1995**, *34*, 2528–2530.

(8) Martens, J. A.; Vanbutsele, G.; Jacobs, P. A.; Denayer, J.; Ocakoglu, R.; Baron, G.; Muñoz Arroyo, J. A.; Thybaut, J.; Marin, G. B. Evidences for Pore Mouth and Key-Lock Catalysis in Hydroisomerization of Long n-Alkanes over 10-Ring Tubular Pore Bifunctional Zeolites. *Catal. Today* **2001**, *65*, 111–116.

(9) Lai, Z.; Bonilla, G.; Diaz, I.; Nery, J. G.; Sujaoti, K.; Amat, M. A.; Kokkoli, E.; Terasaki, O.; Thompson, R. W.; Tsapatsis, M.; Vlachos, D. G. Microstructural Optimization of a Zeolite Membrane for Organic Vapor Separation. *Science* **2003**, *300*, 456–460.

(10) Mintova, S.; Bein, T. Nanosized Zeolite Films for Vapor-Sensing Applications. *Microporous Mesoporous Mater.* **2001**, *50*, 159–166.

(11) Goldsmith, B. R.; Peters, B.; Johnson, J. K.; Gates, B. C.; Scott, S. L. Beyond Ordered Materials: Understanding Catalytic Sites on Amorphous Solids. *ACS Catal.* **2017**, *7*, 7543–7557.

(12) Hoffman, A. S.; Fang, C. Y.; Gates, B. C. Homogeneity of Surface Sites in Supported Single-Site Metal Catalysts: Assessment with Band Widths of Metal Carbonyl Infrared Spectra. *J. Phys. Chem. Lett.* **2016**, *7*, 3854–3860.

(13) Lichtenstein, L.; Büchner, C.; Yang, B.; Shaikhutdinov, S.; Heyde, M.; Sierka, M.; Włoodarczyk, R.; Sauer, J.; Freund, H. J. The Atomic Structure of a Metal-Supported Vitreous Thin Silica Film. *Angew. Chem. Int. Ed.* **2012**, *51*, 404–407.

(14) Harris, J. W.; Liao, W. C.; Di Iorio, J. R.; Henry, A. M.; Ong, T. C.; Comas-Vives, A.; Copéret, C.; Gounder, R. Molecular Structure and Confining Environment of Sn Sites in Single-Site Chabazite Zeolites. *Chem. Mater.* **2017**, *29*, 8824–8837.

(15) Ehresmann, J. O.; Kletnieks, P. W.; Liang, A.; Bhirud, V. A.; Bagatchenko, O. P.; Lee, E. J.; Klaric, M.; Gates, B. C.; Haw, J. F. Evidence from NMR and EXAFS Studies of a Dynamically Uniform Mononuclear Single-Site Zeolite-Supported Rhodium Catalyst. *Angew. Chem. Int. Ed.* **2006**, *45*, 574–576.

(16) Notestein, J. M.; Iglesia, E.; Katz, A. Grafted Metallocalixarenes as Single-Site Surface Organometallic Catalysts. *J. Am. Chem. Soc.* **2004**, *126*, 16478–16486.
(17) Smeets, S.; Berkson, Z. J.; Xie, D.; Zones, S. I.; Wan, W.; Zou, X.; Hsieh, M. F.; Chmelka, B. F.; McCusker, L. B.; Baerlocher, C. Well-Defined Silanols in the Structure of the Calcined High-Silica Zeolite SSZ-70: New Understanding of a Successful Catalytic Material. *J. Am. Chem. Soc.* **2017**, *139*, 16803–16812.
(18) Ogino, I.; Eilertsen, E. A.; Hwang, S.-J.; Rea, T.; Xie, D.; Ouyang, X.; Zones, S. I.; Katz, A. Heteroatom-Tolerant Delamination of Layered Zeolite Precursor Materials. *Chem. Mater.* **2013**, *25*, 1502–1509.
(19) Galletero, M. S.; Corma, A.; Ferrer, B.; Fornés, V.; García, H. Confinement Effects at the External Surface of Delaminated Zeolites (ITQ-2): An Inorganic Mimic of Cyclodextrins. *J. Phys. Chem. B* **2003**, *107*, 1135–1141.
(20) Baerlocher, C.; McCusker, L. B. Database of Zeolite Structures.
(21) Lawton, S. L.; Leonowicz, M. E.; Partridge, R. D.; Chu, P.; Rubin, M. K. Twelve-Ring Pockets on the External Surface of MCM-22 Crystals. *Microporous Mesoporous Mater.* **1998**, *23*, 109–117.
(22) Frisch, M. J. G.; Trucks, W.; Schlegel, H. B.; Scuseria, G. E.; Robb, M. A.; Cheeseman, J. R.; Scalmani, G.; Barone, V.; Mennucci, B.; Petersson, G. A.; Nakatsuji, H.; Caricato, M.; Li, X.; Hratchian, H. P.; Izmaylov, A. F.; Bloino, J.; Zheng, G.; Sonnenberg, J. L. Gaussian 16, Rev. A.03. *Inc.: Wallingford, CT*. 2016.
(23) Becke, A. D. Density-Functional Thermochemistry. III. The Role of Exact Exchange. *J. Chem. Phys.* **1993**, *98*, 5648.
(24) Stephens, P. J.; Devlin, F. J.; Chabalowski, C. F.; Frisch, M. J. Ab Initio Calculation of Vibrational Absorption and Circular Dichroism Spectra Using Density Functional Force Fields. *J. Phys. Chem.* **1994**, *98*, 11623–11627.
(25) Grimme, S.; Antony, J.; Ehrlich, S.; Krieg, H. A Consistent and Accurate Ab Initio Parametrization of Density Functional Dispersion Correction (DFT-D) for the 94 Elements H-Pu. *J. Chem. Phys.* **2010**, *132*, 154104.
(26) London, F. The Quantic Theory of Inter-Atomic Currents in Aromatic Combinations. *J. Phys. Radium* **1937**, *8*, 397–409.
(27) Hsieh, M.-F. Ph.D. Dissertation, University of California, Santa Barbara, CA, 2014.
(28) Koller, H.; Chen, C. Y.; Zones, S. I. Selectivities in Post-Synthetic Modification of Borosilicate Zeolites. *Top. Catal.* **2015**, *58*, 451–479.
(29) Senderov, E.; Halasz, I.; Olson, D. H. On Existence of Hydroxyl Nests in Acid Dealuminated Zeolite Y. *Microporous Mesoporous Mater.* **2014**, *186*, 94–100.
(30) Grosso-Giordano, N. A.; Schroeder, C.; Okrut, A.; Solovyov, A.; Schöttle, C.; Chassé, W.; Marinković, N.; Koller, H.; Zones, S. I.; Katz, A. Outer-Sphere Control of Catalysis on Surfaces: A Comparative Study of Ti(IV) Single-Sites Grafted on Amorphous versus Crystalline Silicates for Alkene Epoxidation. *J. Am. Chem. Soc.* **2018**, *140*, 4956–4960.
(31) Halasz, I.; Senderov, E.; Olson, D. H.; Liang, J. J. Further Search for Hydroxyl Nests in Acid Dealuminated Zeolite Y. *J. Phys. Chem. C* **2015**, *119*, 8619–8625.
(32) Yabushita, M.; Grosso-Giordano, N. A.; Fukuoka, A.; Katz, A. Selective Sequestration of Aromatics from Aqueous Mixtures with Sugars by Hydrophobic Molecular Calixarene Cavities Grafted on Silica. *ACS Appl. Mater. Interfaces* **2018**, *10*, 39670–39678.
(33) Notestein, J. M.; Andrini, L. R.; Kalchenko, V. I.; Requejo, F. G.; Katz, A.; Iglesia, E.

Structural Assessment and Catalytic Consequences of the Oxygen Coordination Environment in Grafted Ti-Calixarenes. *J. Am. Chem. Soc.* **2007**, *129*, 1122–1131.
(34) Notestein, J. M.; Solovyov, A.; Andrini, L. R.; Requejo, F. G.; Katz, A.; Iglesia, E. The Role of Outer-Sphere Surface Acidity in Alkene Epoxidation Catalyzed by Calixarene-Ti(IV) Complexes. *J. Am. Chem. Soc.* **2007**, *129*, 15585–15595.
(35) George, S. D. B.; Brant, P.; Solomon, E. I. Metal and Ligand K-Edge XAS of Organotitanium Complexes: Metal 4p and 3d Contributions to Pre-Edge Intensity and Their Contributions to Bonding. *J. Am. Chem. Soc.* **2005**, *127*, 667–674.
(36) Spanjers, C. S.; Guillo, P.; Tilley, T. D.; Janik, M. J.; Rioux, R. M. Identification of Second Shell Coordination in Transition Metal Species Using Theoretical XANES: Example of Ti-O-(C, Si, Ge) Complexes. *J. Phys. Chem. A* **2017**, *121*, 162–167.
(37) Friedrich, A.; Radius, U. A Calix[4]Arene Monoalkyl Ether as a Model of a Tris(Phenolate) Ligand with a Hemilabile Anisole Moiety: Syntheses, Molecular Structures and Bonding of Calix[4]Arene Ether Supported Titanium Complexes and Their Catalytic Activity in Epoxidation Reactions. *Eur. J. Inorg. Chem.* **2004**, *2004*, 4300–4316.
(38) Zanotti-Gerosa, A.; Solari, E.; Giannini, L.; Floriani, C.; Re, N.; Chiesi-Villa, A.; Rizzoli, C. Titanium-Carbon Functionalities on an Oxo Surface Defined by a Calix [4] Arene Moiety and Its Redox Chemistry. *Inorganica Chim. Acta* **1998**, *270*, 298–311.
(39) Gutsche, C. D.; Dhawan, B.; Levine, J. A.; Hyun No, K.; Bauer, L. J. Calixarenes 9. Conformational Isomers of the Ethers and Esters of Calix[4]Arenes. *Tetrahedron* **1983**, *39*, 409–426.
(40) Radius, U. Shaping the Cavity of the Macrocyclic Ligand in Metallocalix[4]Arenes: The Role of the Ligand Sphere. *Inorg. Chem.* **2001**, *40*, 6637–6642.
(41) Grosso-Giordano, N. A.; Solovyov, A.; Hwang, S.-J.; Katz, A. Effect of Coordination Environment in Grafted Single-Site Ti-SiO_2 Olefin Epoxidation Catalysis. *Top. Catal.* **2016**, *59*, 1110–1122.
(42) Guerrini, L.; Garcia-Ramos, J. V.; Domingo, C.; Sanchez-Cortes, S. Sensing Polycyclic Aromatic Hydrocarbons with Dithiocarbamate- Functionalized Ag Nanoparticles by Surface-Enhanced Raman Scattering. *Anal. Chem.* **2009**, *81*, 953–960.
(43) de Silva, N.; Hwang, S.-J.; Durkin, K. A.; Katz, A. Vanadocalixarenes on Silica: Requirements for Permanent Anchoring and Electronic Communication. *Chem. Mater.* **2009**, *21*, 1852–1860.
(44) De Moor, B. A.; Reyniers, M. F.; Gobin, O. C.; Lercher, J. A.; Marin, G. B. Adsorption of C2-C8 n-Alkanes in Zeolites. *J. Phys. Chem. C* **2011**, *115*, 1204–1219.
(45) Sarazen, M. L.; Iglesia, E. Stability of Bound Species during Alkene Reactions on Solid Acids. *Proc. Natl. Acad. Sci.* **2017**, *114*, E3900–E3908.
(46) Gounder, R.; Iglesia, E. Catalytic Consequences of Spatial Constraints and Acid Site Location for Monomolecular Alkane Activation on Zeolites. *J. Am. Chem. Soc.* **2009**, *131*, 1958–1971.
(47) Hanwell, M. D.; Curtis, D. E.; Lonie, D. C.; Vandermeerschd, T.; Zurek, E.; Hutchison, G. R. Avogadro: An Advanced Semantic Chemical Editor, Visualization, and Analysis Platform. *J. Cheminform.* **2012**, *4*.

Chapter 7

Dynamic Reorganization and Confinement of Ti^{IV} Active Sites Controls Olefin Epoxidation Catalysis on Two-Dimensional Zeotypes

Adapted with permission from Grosso-Giordano, N. A.; Hoffman, A. S.; Boubnov, A.; Small, D. W.; Bare, S. R.; Zones, S. I.; Katz, A. Dynamic Reorganization and Confinement of Ti(IV) Active Sites Controls Olefin Epoxidation Catalysis on Two-Dimensional Zeotypes. *J. Am. Chem. Soc.* **2019**, *141* (17), 7090–7106.

The effect of dynamic reorganization and confinement of isolated Ti^{IV} catalytic centers supported on silicates is investigated for olefin epoxidation. Active sites consist of grafted single-site calix[4]arene–Ti^{IV} centers or their calcined counterparts. Their location is synthetically controlled to be either unconfined at terminal T-atom positions (denoted as type-(**i**)) or within confining 12-MR pockets (denoted as type-(**ii**); diameter ∼7 Å, volume ∼185 $Å^3$) composed of hemispherical cavities on the external surface of zeotypes with *-SVY topology. Electronic structure calculations (density functional theory) indicate that active sites consist of cooperative assemblies of Ti^{IV} centers and silanols. When active sites are located at unconfined type-(**i**) environments, the rate constants for cyclohexene epoxidation (323 K, 0.05 mM Ti^{IV}, 160 mM cyclohexene, 24 mM *tert*-butyl hydroperoxide) are 9 ± 2 M^{-2} s^{-1}; whereas within confining type-(**ii**) 12-MR pockets, there is a ∼5-fold enhancement to 48 ± 8 M^{-2} s^{-1}. When a mixture of both environments is initially present in the catalyst resting state, the rate constants reflect confining environments exclusively (40 ± 11 M^{-2} s^{-1}), indicating that dynamic reorganization processes lead to the preferential location of active sites within 12-MR pockets. While activation enthalpies are $\Delta H^{\ddagger}_{app}$ = 43 ± 1 kJ mol^{-1} irrespective of active site location, confining environments exhibit diminished entropic barriers ($\Delta S^{\ddagger}_{app}$ = −68 J mol^{-1} K^{-1} for unconfined type-(**i**) vs −56 J mol^{-1} K^{-1} for confining type-(**ii**)), indicating that confinement leads to more facile association of reactants at active sites to form transition state structures (volume ∼ 225 $Å^3$). These results open new opportunities for controlling reactivity on surfaces through partial confinement on shallow external-surface pockets, which are accessible to molecules that are too bulky to benefit from traditional confinement within micropores.

7.1. Introduction

Confinement of active sites within micropores in solid catalysts has profound effects on their catalytic properties,[1–13] and enables efficient catalysis for many industrial reactions.[1,6] Such confining environments control reactivity through "outer-sphere" effects, involving non-covalent interactions of pore walls with reacting species, which only indirectly influence bond making and breaking events at the active site "inner-sphere". An emerging area of research involves outer-sphere effects that are manifested by partially confining environments, which are accessible on two-dimensional (2-D) surfaces,[14–22] akin to those commonly invoked in the surface pockets of enzymes and catalytic antibodies.[23,24] These hold the potential to extend outer-sphere confinement effects to classes of molecules that are too large to enter micropores.

In this chapter, we demonstrate outer-sphere effects in catalysis arising from reaction confinement within sub-nanometer hemispherical cavities on the surface of a 2-D silicate zeotype catalyst. Inspired by industrial titanosilicate olefin epoxidation catalysts,[25–27] we use the epoxidation of cyclohexene with *tert*-butyl hydroperoxide as a probe reaction, catalyzed by isolated Ti^{IV} active centers grafted on siliceous supports. We identify dynamic processes that lead to partial confinement of reaction events, and show that this partial confinement results in reduced entropic penalties for forming kinetically relevant transition-state structures.

Our approach strives to achieve molecular-scale precision in the pseudotetrahedral Ti^{IV} coordination environment required for epoxidation catalysis.[25–27] This environment is enforced by a calix[4]arene ligand that chelates Ti^{IV} centers in grafted **cTi** complexes, shown in Figure 7.1, which are known to act as single-site active centers for epoxidation.[28] These **cTi** complexes are grafted onto supports by condensation of precursor **cTi-p** with a surface silanol (SiOH) group,[15,28–30] to result in covalent bonding to the support surface through a single Si-O-Ti connection,[15] as shown in Figure 7.1. The resulting catalytic materials are denoted **cTi/X**, where **X** is the identity of the siliceous support (**X** = **1**, **1-a**, **2**, **3-a**, **3-b**), whose structure is shown in Scheme 7.1 and explained below. Oxidative heat treatment of **cTi/X** combusts the calix[4]arene ligands and results in all-inorganic titanosilicate **Ti/X** catalysts – compositionally resembling those used industrially for olefin epoxidation with organic hydroperoxide as the oxidant.[25–27]

Scheme 7.1 shows the framework structure of the crystalline layers of SSZ-70 zeotypes (*-SVY topology) studied here,[31] which crystallize as thin platelets that preferentially expose their **a**-**b** plane.[32,33] We apply delamination treatments to further expose these layers to the external surface.[34,35] There are two relevant surface environments, as shown in Scheme 7.1: (**i**) unconfined terminal T-atom positions, which are highlighted in purple and (**ii**) partially confining 12-membered-ring (12-MR) pockets.[36] The latter environment (**ii**) consists of shallow hemispherical cavities 7.1 Å wide and 7.0 Å deep.[33] These features are present on the zeotype crystal external surface, fully accessible to the bulk fluid phase, and lack any openings into the intra-crystalline pore system. As such, these are 2-dimensional zeotype surfaces, which exhibit zeotype framework structures but lack any extended porosity, instead containing shallow 12-MR pockets that are partially confining. Active sites are grafted onto the external surface (experimental evidence in section 7.3.2 and 4.2), and are therefore influenced by these zeotype framework structures.

Scheme 7.1. Schematic Representation of Surface Framework Structures and Silanol Environments.

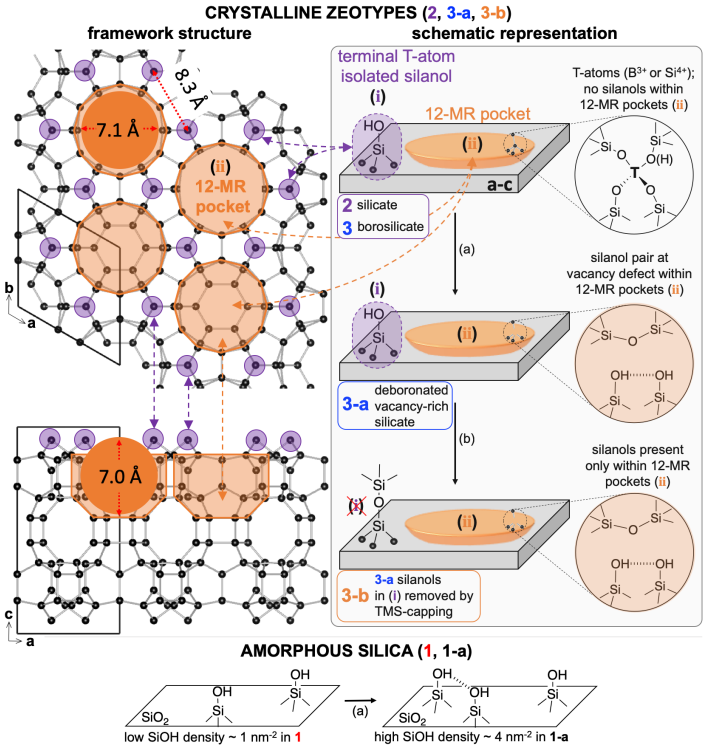

A crystalline framework layer that comprises delaminated SSZ-70 zeotypes (*-SVY topology) is shown along its crystallographic a-b and a-c planes to the left, with its unit cell highlighted between black lines. The majority of crystal surface exposed in platelet-like crystallites corresponds to structures shown along the a-b plane. Vertices correspond to tetrahedrally coordinated T-atoms that make up the zeotype framework; they are connected through oxygen bridges shown as grey lines. T-atoms consist exclusively of Si^{IV} in **2**, but also include B^{III} in **3**. To the right, the zeotype layer is schematically represented along with the two structural environments present, where silanols (and by extension grafted **cTi** as shown in Figure 7.1) can be located. These are: (**i**) highlighted in translucent purple, terminal T-atoms where the framework is interrupted, which share only three oxygens with other framework T-sites; the fourth oxygen forms a silanol (SiOH). These silanols are spaced 8.3 Å apart, leading to a surface density of~ 1.1 nm^{-2}. In defect-free **2**, these are the only framework locations where a silanol can be located. (**ii**) Highlighted in translucent orange are surface pockets defined by a 12 membered-ring (12-MR) of T-atoms; these pockets comprise hemispherical cavities 7.1 Å in diameter and 7.0 Å deep.[33] B^{III} is removed from T-atoms inside the 12-MR pocket during deboronation by acid washing (a) of **3** to generate an ordered silanol pair at a framework vacancy in **3-a**,[15] as shown in circular insets shaded in translucent orange. In **3-a**, silanols are also located terminal T-atom positions (**i**). Capping treatment with trimethylsilyl chloride (b) selectively consumes silanols at terminal T-atom positions (**i**) from **3-a** to synthesize **3-b**, where silanols are therefore only located within 12-MR pockets (**ii**). Amorphous surfaces also contain surface silanols but these lack long-range structural order; their surface density in dehydroxylated **1** is ~1 SiOH nm^{-2}, while that in fully hydroxylated **1-a** is ~4 SiOH nm^{-2}.[37]

We control the location of silanols within specific framework environments by the synthetic strategy shown in Scheme 7.1. Terminal T-atom positions (**i**) are the only crystallographic locations where silanols can occur in defect-free silicate zeotype **2**. They occur immediately outside 12-MR pockets, and are therefore unconfined. Borosilicate **3** is isostructural to silicate **2**, but differs in that it also contains framework B^{III}, which is known to be located within 12-MR pockets.[38] Acid washing of **3** to synthesize silicate **3-a** removes B^{III} and exposes silanol pairs at vacancy defects within these 12-MR pockets (**ii**).[15] Therefore, in **3-a**, silanols occur within partially confining (**ii**) as well as unconfined (**i**) environments. Trimethylsilyl capping selectively consumes silanols in unconfined locations (**i**) from **3-a**, resulting in support **3-b** where silanols are exclusively located within 12-MR pockets (**ii**). We also compare these crystalline environments to the amorphous silicate surface in **1** and **1-a**, which serve as controls of how varying silanol density affects reactivity. We demonstrate how this strategy controls silanol and grafted **cTi** locations, as shown in Figure 7.1, through detailed spectroscopic characterization in sections 7.3.1, 7.3.2, 7.4.1, and 7.4.2.

The well-defined inner-sphere structure for Ti^{IV} in **cTi/X** is enforced by the chelating calix[4]arene ligand and is independent of the surrounding support environment. This enables us to rigorously isolate catalytic effects arising from location of active sites within specific outer-sphere environments. Previously, we used a similar approach to demonstrate olefin epoxidation rate enhancements of up to 5-fold when comparing amorphous support **1** to crystalline **3-A7.15** Here, by selectively locating **cTi** centers within specific (**i**) unconfined vs. (**ii**) confining structural features, we elucidate how dynamic reorganization processes facilitate catalytic enhancements due to confining outer-sphere environments within 12-MR pockets. These dynamic processes are in contrast to more commonly observed dynamics that involve inner-sphere reorganization at the active site of solid catalysts, manifested by changes to the metal-coordination environment.[39–46]

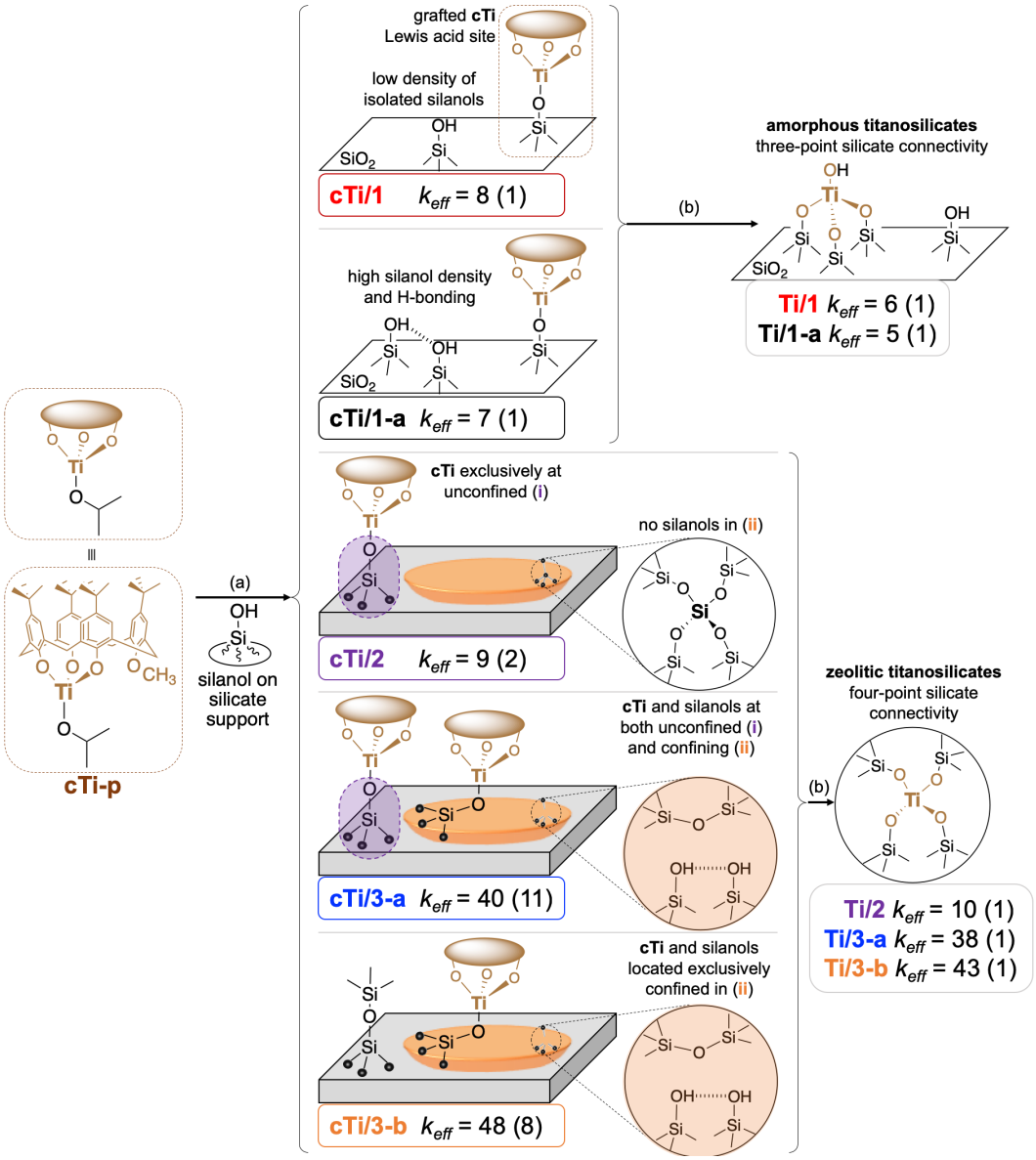

Figure 7.1. Summary of synthetic approach and resulting Ti^{IV} and silanol location in the catalyst resting state, together with associated rates of epoxidation (units $M^{-2}s^{-1}$). Schematic representations of silanol species at unconfined type-(**i**) vs. partially confining 12-MR pocket type-(**ii**) environments are used here; their crystallographic location is shown in Scheme 7.1. In summary, orange structures represent partially confining 12-MR pockets (**ii**), while structures on the grey rectangle (purple SiO^-) are unconfined (**i**). Grafting of calix[4]arene-Ti^{IV} (**cTi**) onto support silanols (a) is accomplished by refluxing of precursor **cTi-p** with the support to result in **cTi/X** materials, where **cTi** is grafted at framework locations where silanols are present; these locations are determined by spectroscopic analysis of supports (section 7. 3.1 and 7.4.1) and the resting state of catalysts (section 7.3.2 and 7.4.2). Calcination (b) yields titanosilicate catalysts **Ti/X**, with isolated Ti^{IV} centers with three-point vs. four-point silicate coordination in amorphous vs. zeotype supports, respectively, as determined from spectroscopic data in section 7.3.3 and 7.4.4.

7.2. Materials and Methods

7.2.1. Support Synthesis

Aerosil® 200 (Evonik) was used as a representative amorphous silica support. It was hydroxylated in refluxing water at 393 K for 16 h, dried, and sieved. Dehydroxylated amorphous SiO_2 **1** was the prepared by dehydroxylation of this pretreated silica under Ar at 823 K for 6 h to achieve a surface dominated by isolated hydroxyl groups (~1 nm^{-2});[37] it was stored under Ar until further handling. Hydroxylated amorphous SiO_2 **1-a** was prepared by treating 500 mg of **1** with 50 mL of 2N HNO_3 at 373 K for 18 h, followed by filtration and washing with copious amounts of H_2O, and drying at 398 K.

Delaminated zeotype UCB-4 materials[31] were synthesized from SSZ-70(P) precursors,[32,47,48] as depicted in Scheme A7.1. Si-UCB-4 (**2**) and B-UCB-4 (**3**) correspond to delaminated purely siliceous Si-SSZ-70(P) (**2-p**) and borosilicate B-SSZ-70(P) (**3-p**) layered zeotype precursors, respectively. Borosilicate precursor **3-p** was crystallized in PTFE autoclaves at 423 K for 8 days, from a synthesis gel with molar composition 1 SiO_2 (Aerosil 200): 30 H_2O: 0.175 1,3-bis(isobutyl)imidazolium hydroxide: 0.1 H_3BO_3. Silicate precursor **2-p** was crystallized in PTFE autoclaves at 433 K for 8 days, from a synthesis gel with molar composition 1 SiO_2 (LUDOX® HS-40): 24 H_2O: 0.34 1,3-bis(cyclohexyl) imidazolium hydroxide. Both zeotypes were washed with copious amount of H_2O and dried at 393 K before further use. The identity of the zeotypes was confirmed by comparison of its powder X-ray diffraction (PXRD) pattern in Figure A7.1 with literature precedent.[48] **2-p** and **3-p** were delaminated to synthesize **2** and **3** by previously reported protocols:[15,31] a mixture of 5.0 g of **2-p** or **3-p** per 5.5 g of cetyltrimethylammonium bromide (CTAB) (Sigma-Aldrich, ≥99.0%), 8.5 g of tetrabutylammonium fluoride trihydrate (TBAF) (Sigma-Aldrich, ≥97%), and 8.5 g of tetrabutylammonium chloride (TBACl) (Sigma-Aldrich, ≥97%) and 20 mL of dimethylformamide (DMF, Fisher Scientific) was placed in a screw-capped 500 mL high pressure glass tube, and stirred at 373 K for 72 h. After cooling, the slurry was sonicated for 1 h in an ice bath, using a Branson digital sonifier 450 operating under pulse mode (1.0 s on and 0.1 s off). The sonicated slurry was centrifuged to separate the solid, and washed with DMF (1x50 mL) and 1,4-dioxane (3x50 mL) under centrifugation, dried at 323 K overnight, and calcined in air at 823 K for 6 h after a 1 K/min ramp. Deboronation removes framework B^{III} from **3** to generate vacancy defects in **3-a**, as depicted in Scheme 7.1, by treatment of 500 mg of delaminated zeolite with 50 mL of 2N HNO_3 at 373 K for 18 h, followed by filtration and washing with copious amounts of H_2O. TMS-capped material **3-b** was synthesized by treatment of 500 mg of **3-a** with 15 mL of neat trimethylsilyl (TMS) chloride under reflux for 18 h, followed by washing with toluene, isopropanol, and methanol. The textural properties of all supports are summarized in Table A7.1.

7.2.2. Ti^{IV} Postsynthetic Incorporation

Ti^{IV} incorporation was achieved by grafting of calix[4]arene-Ti^{IV} (**cTi-p**) precursors by condensation with support silanols, as depicted in Figure 7.1 (a). The choice of this precursor complex leads to deposition of site-isolated Ti^{IV}, and prevents Ti^{IV} incorporation into zeotype micropores, which are too small to accommodate its diffusion.[15] **cTi** was synthesized by previous synthesis protocols,[49,50] and successful synthesis was confirmed by liquid-phase ^1H NMR

spectroscopy. Grafting of **cTi** was achieved by suspending silicate supports (pretreated *in vacuo* at 473 K for 1 h) in anhydrous toluene at room temperature, followed by dropwise addition of a 50 mM toluene solution of **cTi**, to achieve a ratio of 200 μmol of **cTi** per g of support. The suspension was subsequently heated to reflux for 18 h, after which it was filtered, and the filtrate washed with copious amount of hot toluene. This resulted in materials **cTi/X**, where **X** indicates the support **1**, **1-a**, **2**, **3-a**, **3-b**. **Ti/X** materials were synthesized from the corresponding **cTi/X** material by calcination of **cTi/X** in air at 823 K for 6 h after a 1 K/min heating ramp.

7.2.3. General Analytical Methods

Support textural properties were determined from N_2 physisorption measurements performed with a Micromeritics ASAP 2020 instrument at 77 K, after sample evacuation at 623 K for 4 h. External surface areas and micropore volumes were calculated by the t-plot method;[51] surface areas were calculated by the BET method for amorphous supports.

Calix[4]arene contents were determined by thermogravimetric analysis (TGA), performed with a TA Instruments TGA 2950 Thermogravimetric Analyzer. The sample was treated in flowing air from room temperature to 1073 K at a ramp rate of 5 K/min. Calix[4]arene contents were determined by assuming that any additional mass loss during this treatment, when compared to the bare support, was due to combustion of the calix[4]arene. Ti^{IV} contents were measured by ICP-AES at Galbraith Laboratories.

Transmission Fourier-transform infrared (FTIR) spectra of self-supported wafers were recorded with a Nicolet 6700 FTIR spectrometer with a spectral resolution of 2 cm^{-1}. Wafers were loaded into an *in-situ* flow cell (In-situ Research Instruments, Inc., South Bend, IN), and treated under He flow at 473 K during spectral acquisition. Background spectra were collected under identical conditions in the absence of wafer. Integrated intensities of skeleton Si-O-Si overtones in the range 1740 – 2080 cm^{-1} were used to normalize spectra;[52] spectra were baseline corrected assuming intensity of ν(SiO-H) occurs in the 3750 – 3200 cm^{-1} range. Difference spectra shown in Figure 7.2B and A7.5 consist of spectra for support **X** subtracted from corresponding catalyst **cTi/X**. Intense and broad bands from H-bonded silanols (< 3720 cm^{-1}) are evident in Figure A7.6, showing the overlaid spectra before subtraction. These broad features cause spectral subtraction to be subject to significant uncertainty; therefore, analysis of difference spectra is focused on bands > 3720 cm^{-1}**,** which are sharp and could be reproducibly observed.

Diffuse reflectance UV-visible spectra were measured at ambient conditions by using a Varian Cary 4000 Spectrophotometer fitted with a Praying Mantis attachment from Harrick Scientific Instruments. Compacted poly-(tetrafluroethylene) powder was used as a standard perfect reflector for the baseline corrections, and all spectra are reported using Kubelka-Munk pseudoabsorbance, and normalized to the maximum value of absorbance. Ligand-to-metal charge-transfer (LMCT) edge-energies of calix[4]arene-Ti^{IV} containing materials were calculated following established protocols.[15,30] Powder X-ray diffraction patterns were acquired on a D8 Discover GADDS Powder XRD with a Cu-Kα source.

Ti K-edge X-ray absorption spectra of self-supporting wafers were acquired using fluorescence detection and double-crystal Si(111) monochromator at beamline 4-3 at the Stanford Synchrotron Radiation Lightsource. Energies were calibrated in transmission mode against a Ti^0 foil standard

with known absorption edge energy (4966.0 eV), with the edge energy defined as the first inflection point. Spectra were acquired between 4730.0 eV and 5754.0 eV, with a step size in the pre-edge region of 0.1 eV. Multiple spectra were acquired and merged to improve the signal-to-noise ratio. Samples were treated at 473 K (for **cTi/X** materials) or 673 K (for **Ti/X** materials) under 20 mL/min He flow during spectral measurements, in a custom-built *in-situ* reaction cell. These temperatures were chosen because preliminary measurements determined that no changes in spectral features occur above this temperature, indicating full removal of moisture, which is known to affect pre-edge features.[29] Spectra were normalized to a pre-edge straight line fit in the range 4820-4940 eV below the edge, and to 2nd order polynomial fit between 5020 and 5200 eV above the edge. In these normalized spectra, the raising edge was fit to an arctan function, while the pre-edge feature was fit to four Gaussian peaks, labeled A1, A2, A3, and B, in order of ascending energy, with centers constrained to lie within, respectively, 4968–4969 eV, 4969–4971 eV, 4971–4972, and 4973–4974 eV.[29,30,53] Full fits for all materials are shown in Figure A7.10. Pre-edge prominence, A_{rel} in Table 7.1, was calculated as the ratio of areas A2 + A3 to total pre-edge peak area (A1 + A2 + A3 + B); it serves as a descriptor of Ti 3d orbital occupancy, which is directly correlated to epoxidation reactivity.[29] Scripts used for spectrum processing, normalization, and fitting are available at https://github.com/nico2g/preXANES. *In-situ* treatment of **Ti/3-a** with TBHP was performed by cooling the pre-treated wafer to room temperature, followed by redirecting He flow to bubble through a 5.5 M solution of TBHP in nonane. EXAFS spectra were fit using Athena and Artemis XAS analysis software;[54] details of EXAFS model and fits are included in Table A7.2 and Figure A7.11.

7.2.4. Catalysis

Rates of cyclohexene epoxidation with *tert*-butyl-hydroperoxide (TBHP) were measured in Schlenk flask batch reactors with external temperature control. ~25 mg of catalyst and ~300 mg of molecular sieves were evacuated at 393 K (1h) to remove moisture, a known catalyst poison,[55] followed by cooling to the reaction temperature (typically 323 K), and addition of 20 mL of octane (distilled from Na) and 0.3 mL of cylcohexene (distilled from CaH_2). Addition of 0.1 mL of TBHP in *n*-decane (concentration 5.9 M measured by iodometric titration)[56] initiated epoxidation, the progress of which was monitored by comparing gas chromatograph peak areas of aliquots removed from the reactor to external references prepared with known concentration of reactants and products. Reproducible injection volumes were ensured by the *n*-decane internal standard.

Epoxidation rates are known to be proportional to catalyst, alkene, and oxidant concentrations:[28]

$$\text{rate} = \frac{d[\text{TBHP}]}{dt} = k_{eff}[\text{Ti}][\text{alkene}][\text{TBHP}] \qquad (7.1)$$

Square brackets [] denote concentration, while initial concentrations are denoted by $[]_0$. In all reactions, initial [alkene]:[TBHP] ratios were in excess of 5, allowing the determination of a pseudo first-order rate constant, k_{eff}, as the slope of the linear plot of -ln(1-X)/[cyclohexene]/[Ti] vs. time, where conversion X = 1- $[TBHP]/[TBHP]_0$. Linearity of pseudo first-order plots is seen in Figure A7.14. Turnover numbers were measured as TON = [epoxide]/[Ti], and denote the per-active site productivity towards the desired product. All rates are normalized by Ti^{IV} content, as

it has been previously shown that grafted calix[4]arene-Ti^{IV} sites on SiO_2 behave uniformly as single-site heterogeneous olefin epoxidation catalysts that are recyclable and do not leach.[28]

Initial rates were calculated by extrapolating turnover frequencies (TOF), defined as the ratio of TON to reaction time, to initial time using a 2nd order polynomial fit. These TOF values were used to calculate transition state equilibrium constant, $K^{\ddagger}$, from a relation previously developed for alkene epoxidation:[8]

$$\mathrm{TOF} = \frac{k_B T}{h} K^{\ddagger}[\mathrm{alkene}] \tag{7.2}$$

where k_B is Boltzmann's constant, h is Planck's constant, T is temperature. $K^{\ddagger}$ was related to apparent activation enthalpy, $\Delta H^{\ddagger}_{app}$, apparent activation entropy, $\Delta S^{\ddagger}_{app}$, and apparent activation Gibb's free energy, $\Delta G^{\ddagger}_{app}$, by the Eyring equation:[8]

$$K^{\ddagger} = e^{\frac{-G^{\ddagger}_{app}}{RT}} = e^{\frac{-\Delta H^{\ddagger}_{app}}{RT}} e^{\frac{\Delta S^{\ddagger}_{app}}{R}} \tag{7.3}$$

The results of these calculations are shown in Figure 7.5 and Table 7.2.

7.2.5. Electronic Structure Calculations

All geometry optimizations and frequency calculations were performed with the Gaussian 16 revision A03 software,[57] by DFT methods using a spin-symmetry-restricted B3LYP functional[58,59] with a 6-311+G(d,p) basis set. Dispersion interactions were incorporated using DFT-D3(0) methods.[60] Solvent effects were included during optimization and frequency calculations with the polarizable continuum model using the integral equation formalism (IEFPCM) for *n*-octane.[61] Molecular volumes were estimated from solvent cavity volumes from IEFPCM. Free energies were calculated at the reaction temperature of 323 K, scaling frequencies by 0.99.

Active site models were constructed based on the SSZ-70 framework structure,[32] shown schematically in Scheme 7.1. A full 12-MR pocket structure and next-nearest Si^{IV} neighbors were used as the basis to build a cluster model; this 12-MR pocket can be appreciated in structure **XI** in Section 7.7. To model the presence of a silanol in the vicinity of the Ti^{IV} site, a vacancy defect was introduced at a T-site known to be preferentially occupied by B^{III} at the upper-rim of 12-MR pockets;[38] this is an *in-silico* mimic of removal of B^{III} during the synthesis of **3-a** via deboronation of **3** (Scheme 7.1). This vacancy is nominally terminated by four silanols, in a so called "silanol nest";[62,63] however, we have recently shown that only two silanols are observed,[15] because two hydroxyl groups likely spontaneously condense.[64] Based on these experimental observations, hydroxyls with shortest O---O distances in the T-atom vacancies were connected via a single -O- link (i.e. "condensed"), and the next-nearest neighbor Si^{IV} T-atoms and associated oxygen atoms were optimized while freezing all other framework atoms based on crystallographic information. Subsequently, one of the Si^{IV} atoms involved in this two-silanol vacancy was replaced with Ti^{IV}, and the cluster model was optimized allowing relaxation of Ti^{IV} and next-nearest Si^{IV} neighbors (including the silanols) and associated O atoms. The resulting structure is shown in Figure A7.17.

To decrease computational time in reaction pathway modelling, the bulk of the SSZ-70 structure was deleted, and the active site "core" (shown as ball-and-stick in Figure A7.17) was terminated by hydrides that were frozen to simulate framework rigidity; the resulting cluster model [$(H_3SiO)_3TiOH$ $HOSiH_3$] is shown by structure **I** in Figure A.19. We note that this cluster model corresponds to an "open" Ti^{IV} configuration with tripodal coordination to the silicate, and not to a "closed" Ti^{IV} center with four-point silicate connectivity discussed in section 7.4.4. We choose to focus on an "open" configuration because we found that modeling of "closed" [$(H_3SiO)_4Ti$] site while simulating framework connectivity by freezing hydrides resulted in energetically implausible structures for bound peroxo species, in agreement with prior electronic structure calculations.[65] Regardless, if indeed this "closed" site were present in the catalyst resting state, an "open" site could form readily under reaction conditions, as Ti-OSi bonds are known to hydrolyze upon peroxide binding.[66] We also note that this model represents sites in titanosilicate catalysts, **Ti/X**; however, discussion of results in section 7.4.4 indicates that these active sites are analogous to those in **cTi/X**. Therefore, these models serve to rationalize reactivity in **cTi/X** without the additional computational expense of modeling large **cTi** centers.

Prior theoretical studies of Ti^{IV}-catalyzed olefin epoxidation have addressed the requirements for epoxidation when H_2O_2 has been used as the oxidant, including the effect of silanols in the vicinity of active sites.[37,65,67–72] However, to the best of our knowledge, no studies have considered the full epoxidation reaction pathway for organic hydroperoxides, beyond the initial hydroperoxide formation step.[73] We have achieved this here using the [$(H_3SiO)_3TiOH$ $HOSiH_3$] cluster **I** as a model of the active site. To study the influence of silanols on the rate determining step, three variants of this model were constructed, **(A)**, **(B)** and **(C)** shown in Figure 7.6. In models **(A)** and **(B)**, the transition state geometry for oxygen transfer to olefin (i.e. the kinetically relevant step) was optimized while allowing the silanol (and associate hydrides) to relax. All other geometries were found by freezing all hydrides in this transition state structure, and then following the intrinsic reaction coordinate towards reactants and products. In model **(C)**, the silanol group from model **(A)** was removed.

For models of adducts of **cTi** with TBHP shown in Figure 7.7, **VIII** and **IX**, a truncated model for **cTi** was used. The entire calix[4]arene-Ti was modeled based on its structure when grafted on the SiO_2 surface.[28] Connectivity to the support was modeled by attachment of the Ti^{IV} core, through an oxygen bridge, to a -$OSiH_3$ ligand, as performed for related systems.[74] The Ti^{IV} core and associated O bridges and next-nearest C and Si centers were modeled with the 6-311+G(d,p) basis set, while the rest of the calx[4]arene ligand was modelled with a 6-31G(d) basis set.

7.3. Results

7.3.1. Physicochemical and Spectroscopic Characterization of Silicate Supports

Zeotype support materials are synthesized via delamination of layered precursors, as depicted in Scheme A7.1, and their physicochemical properties are summarized in Table A7.1. Delamination increases the external surface area of pure silicate **2** and borosilicate **3** relative to their respective nondelaminated (i.e. 3-D zeotype) counterparts **2-p** and **3-p**, by a factor of ~2. This increase is consistent with previously reported delamination of borosilicate SSZ-70 framework materials,[34,35] though this constitutes the first account of delamination of a purely siliceous SSZ-70 zeotype. Delamination, calcination, acid-washing, or capping treatments did not affect the structural integrity of zeotype frameworks, as characterized by a comparison of intralayer peaks in the PXRD for non-delaminated (**2-p** and **3-p**), delaminated (**2** and **3**), acid washed (**3-a**), and TMS-capped (**3-b**) zeotype variants in Figure A7.1.

Motivated by previous reports of silanols (SiOH) affecting epoxidation catalytic activity of titanosilicates,[30,65,68,75–77] we characterized silanols in all supports by Fourier-transform infrared (FTIR) spectroscopy. These results are shown in Figure 7.2A. Silanols exhibit stretching vibration frequencies ν(O-H) centered at 3747, 3725, 3690, and 3530 cm^{-1}, which are marked by vertical lines in Figure 7.2A. Silanol species exhibiting ν(O-H) at 3747 cm^{-1} correspond to free, isolated silanols, which are not H-bound.[52,78] Such silanols predominate in dehydroxylated silica **1**,[15] as well in the spectrum of purely siliceous zeotype **2**,[32] and are observed as a shoulder in zeotype **3-a**. We observe an increase in intensity of bands at frequencies lower than 3747 cm^{-1} upon acid washing during the synthesis of **1-a** from **1** (Figure 7.2A) and deboronation of **3** to **3-a** (Figure A7.3). These frequencies corresponds to silanols perturbed by hydrogen bonding,[52] which causes a redshift in ν(O-H) relative to the sharp ν(O-H) at 3747 cm^{-1} for free, isolated silanols. These same trends are supported by diffuse-reflectance spectra (DRIFTS) in Figure A7.4.

3-b is synthesized from **3-a** via treatment with chlorotrimethylsilane, which grafts trimethylsilyl (TMS) groups, as confirmed by bands associated with ν(C-H) vibrations from TMS in the region 2810 – 2975 cm^{-1} in Figure A7.6. **3-b** lacks the shoulder at 3747 cm^{-1}, but retains the intensity of H-bonded silanol species < 3720 cm^{-1} in Figure 7.2A.

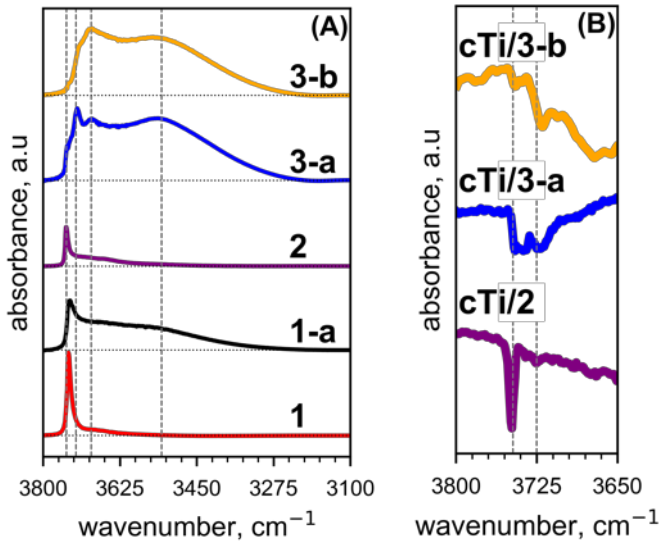

Figure 7.2. (A) Normalized transmission Fourier-transform infrared spectra of the *ν*(SiO-H) region for supports from Table 7.1. Spectra correspond to wafers of the indicated material at 473 K under He flow; pellet of **2** was calcined at 823 K prior to spectrum acquisition (see Figure A7.4). **(B)** Difference spectra between **cTi/X** and bare support **X**, which show spectral changes upon grafting of **cTi** during the synthesis of **cTi/2**, **cTi/3-a** and **cTi/3-b**. Full spectra are shown in Figure A7.5, and raw spectra before subtraction are shown in Figure A7.6. Dotted horizontal lines indicate baseline, while dashed vertical lines indicate stretching bands at 3747, 3725, 3690, 3530 cm^{-1}.

7.3.2. Physicochemical and Spectroscopic Characterization of Grafted cTi Centers in cTi/X

The physicochemical and spectroscopic properties of all **cTi/X** catalysts are summarized in Table 7.1. Measured calix[4]arene-to-Ti ratios (calix:Ti) are ~1.0, consistent with intact grafting of the molecular **cTi** complex in all catalysts. Ti^{IV} grafting densities on an external-surface area basis for all samples are summarized in Table 7.1, and are consistent with prior reports.[15]

Difference FTIR spectra (comprising the spectrum for support **X** subtracted from the spectrum of the corresponding catalyst **cTi/X**) are shown in Figure 7.2B for zeotype materials. Negative bands indicate consumption of species upon grafting of **cTi**. Full difference spectra shown in Figure A7.5 demonstrate the appearance of *ν*(C-H) stretching vibrations in the region of 2800 – 3000 cm^{-1} after grafting, arising from hydrocarbon fragments of calix[4]arene ligands in all **cTi/X** catalysts. For silanol groups, we focus the analysis on bands corresponding to silanol species at 3747 and 3725 cm^{-1}, which are sharp and could be reproducibly analyzed upon spectral subtraction. A sharp negative band at 3747 cm^{-1} is observed for **cTi/2** in Figure 7.2B, indicating that grafting of **cTi** onto **2** consumes silanol species at 3747 cm^{-1}. In contrast, no negative band at 3747 cm^{-1} is observed in the difference spectrum of **cTi/3-b**, consistent with the absence of this band in the spectrum of the bare support **3-b**. For the difference spectrum of **cTi/3-a**, negative bands occur at both 3747 and 3725 cm^{-1}, indicating the consumption of different silanol species upon grafting of **cTi** onto **3-a**. Grafting of **cTi** on amorphous **1** and **1-a** predominantly consumes isolated silanols with stretching frequency at 3747 cm^{-1} (Figure A7.5).

To further understand the Ti^{IV} coordination in **cTi/X**, catalysts were characterized by diffuse-reflectance UV-visible spectroscopy and X-ray absorption spectroscopy. UV-visible spectra of all materials are shown in Figure A7.7, and exhibit bands centered at: (a) 230 nm, indicative of isolated Ti^{IV} sites on silicates,[79] (b) 270-290 nm, representative of π-π* aromatic transitions within the calix[4]arene ligand phenolic subunits, and (c) a broad absorption feature at 290-500 nm, which is known to arise from calixarene(O)-Ti^{IV} ligand to metal charge transfer (LMCT) transitions.[28] The edge-energies associated with these LMCT are measured at 2.28 ± 0.02 eV for all **cTi/X** catalysts, as reported in Table 7.1. The magnitude and imaginary parts of the Fourier-transform of Ti K-edge EXAFS are shown in Figure 7.3, with full data and resulting fits to the data shown in Figure A7.11 (best-fit parameters summarized in Table A7.2). These spectra characterize the coordination sphere of **cTi/3-a** and **cTi/1** to consist of four-fold coordination by oxygen scatterers at a distance of 1.82 ± 0.01 Å. This distance is in agreement with the expected Ti-O distances from calix[4]arene-Ti^{IV} complexes, as determined by single-crystal X-ray diffraction.[50,80]

Table 7.1. Physicochemical and Catalytic Characterization for cTi/X and Ti/X.

Support	Calix:Ti[a]	Ti nm^{-2} [b]	LMCT edge (eV)[c]	$A_{rel,Ti}$[d]	$k_{eff,cTi}$[e]	$k_{eff,Ti}$[e]
1	1.0	0.24	2.29	0.90	8 (1)	6 (1)
1-a	0.9	0.42	2.28	0.90	7 (1)	5 (1)
2	0.9	0.16	2.30	0.89	9 (2)	10 (1)
3-a	0.9	0.31	2.27	0.89	40 (11)[f]	38 (1)
3-b	1.0	0.14	2.28	0.89	48 (8)	43 (1)

[a]Ratio of calix[4]arene, determined by thermogravimetric analysis, to Ti content, determined from elemental analysis in **cTi/X**. [b]Ti content normalized to accessible surface area of the support (Table A7.1). [c]UV-visible calix[4]arene-to-Ti metal-to-ligand charge-transfer edge-energy in **cTi/X**; associated UV-visible spectra are shown in Figure A7.7. [d]Pre-edge prominence as measured by the ratio of Ti K-edge XANES pre-edge area features for **Ti/X**; detail of fitting procedures in section 7.2.3, spectral fits are shown in Figure A7.10. [e]Effective epoxidation rate constant, $M^{-2}s^{-1}$ for **cTi/X** and **Ti/X** catalysts; the number in parenthesis is the uncertainty value based on standard deviations of replicate experiments; the linearity of pseudo-first order fits are shown in Figure A7.14. [f]Uncertainty for replicate experiments of **cTi/3-a** materials from different synthesis batches.

7.3.3. Spectroscopic Characterization of Calcined Ti/X Catalysts

Calcination of **cTi/X** materials at 873 K combusts calix[4]arene ligands and results in purely inorganic titanosilicate **Ti/X** materials. FTIR spectra of **Ti/2** and **Ti/3-a** in Figure A7.12 exhibit bands corresponding to the same silanol species as observed for supports **2** and **3-a** (Figure 7.2A) and grafted **cTi/2** and **cTi/3-a** (Figure A7.6), respectively, indicating that calcination does not alter the type of silanol species present, instead only affecting their relative populations.

Figure A7.8 shows diffuse reflectance UV-visible spectra for **Ti/X**. Virtually no absorbance above 300 nm is observed for any catalyst, consistent with single-site materials that lack extended $(TiO_2)_x$ aggregates, which would otherwise absorb > 300 nm.[53] Absorbance maxima are different

between amorphous **Ti/1** and **Ti/1-a** vs. crystalline zeolitic **Ti/2**, **Ti/3-a**, and **Ti/3-b**, and are respectively centered at ~225 nm (amorphous) vs. ~210 nm (zeolitic).

Ti K-edge XANES spectra of **Ti/X** materials are shown in Figure A7.9 and A7.10. Prominent pre-edge features are observed for all **Ti/X** materials. These pre-edge features arise from electric dipole transitions of core electrons into empty orbitals when non-centrosymmetric coordination of Ti^{IV} enables mixing of 3d and 4p orbitals.[81] As such, pre-edge features are sensitive to the coordination symmetry of Ti^{IV} and its empty $3d^0$ orbital occupancy, the latter being a descriptor of Lewis-acid strength.[29] The pre-edge intensities and positions observed for **Ti/X** here are indicative of Ti^{IV} centers in pseudotetrahedral coordination, as found within zeotype titanium silicalite-1 (i.e. TS-1)[82,83] and previously reported isolated Ti^{IV} centers grafted on amorphous SiO_2.[29,53] Pre-edge peak prominence, $A_{rel,Ti}$ (see section 7.2.3 and Figure A7.10 for details)[29] are ~ 0.9 for all **Ti/X** materials in Table 7.1, indicative of pseudotetrahedral Ti^{IV} centers with similar 3d electron occupancy and Lewis acidity strength.[15,29,53] These pre-edge features are similar in position and prominence ($A_{rel,Ti}$) to pre-edge features in previously published spectra of **cTi** centers grafted on silicates,[15] indicating a similar coordination symmetry and Lewis acidity of **Ti/X** catalysts to Ti^{IV} centers in **cTi**.

The magnitude and imaginary part of the Fourier-transform of Ti K-edge EXAFS are shown in Figure 7.3 for **cTi/X** and **Ti/X** variants supported on amorphous **1** and zeotype **3-a**. The same reduced distance for scattering by the first oxygen coordination shell (vertical dashed line) is observed in **Ti/X** as in the corresponding **cTi/X** catalysts. This is quantitatively confirmed by the best fits of the EXAFS spectra (Figure A7.11, Table A7.2), where the fitted Ti-O scattering distance is 1.80 ± 0.01 Å for **Ti/X** and 1.82 ± 0.01 Å for **cTi/X**. Slightly decreased scattering magnitude (< 20%) in **cTi/X** relative to **Ti/X** is ascribable to variations in average Ti-O distances, as indicated by higher values of the disorder parameter σ^2 for **cTi/X** than for **Ti/X** materials in Table A7.2. This can be accounted for by the mixed calix(O)$^-$ and Si-O$^-$ ligands in **cTi/X** compared with the purely Si-O$^-$ ligands in **Ti/X**.

Therefore, EXAFS results indicate that the oxygen coordination environment of Ti^{IV} remains pseudotetrahedral, whether the Ti^{IV} center is chelated by a calix[4]arene organic ligand in **cTi/X** or by the silicate ligands in the corresponding **Ti/X** catalyst. This is consistent with the similarity of XANES pre-edge features of **Ti/X** to those in prior reports of grafted **cTi**.[15] Thus, the tetrahedral coordination environment of Ti^{IV} does not change significantly upon calcination. In contrast, pre-edge intensity decreases significantly upon treatment of **Ti/3-a** with gas phase *t*-butyl hydroperoxide (Figure A7.13), signifying changes to the Ti^{IV} oxygen coordination sphere upon covalent attachment of hydroperoxide.[84]

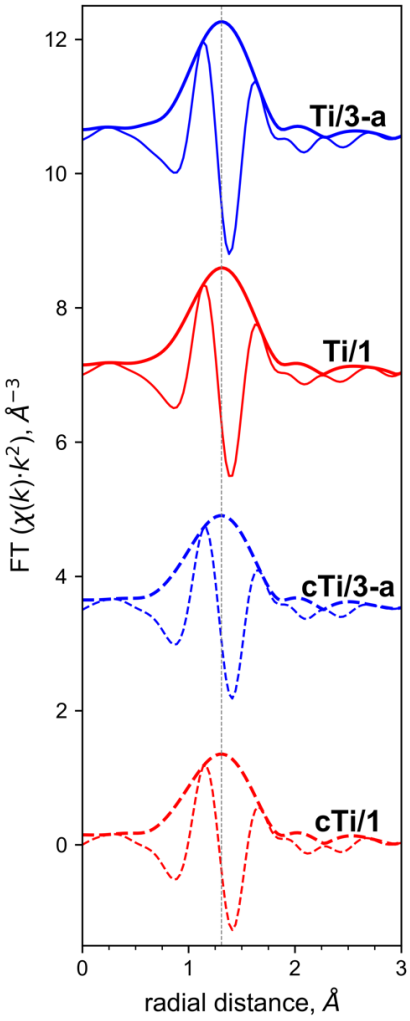

Figure 7.3. Magnitude (thicker line) and imaginary parts (thinner line) of Fourier transforms (FT) of EXAFS spectra for selected **Ti/X** (solid bars) and **cTi/X** (dashed bars) materials, showing the same position for the 1st oxygen coordination shell reduced scattering distance (vertical dashed line). Spectra are staggered for ease of visualization.

7.3.4. Rates of Cyclohexene Epoxidation with *t*-butyl Hydroperoxide

All **cTi/X** catalysts are active in the epoxidation of cyclohexene with *t*-butyl hydroperoxide as oxidant, shown in Scheme 7.2, a reaction commonly used as a probe of olefin epoxidation activity.[8,15,28–30,85,86] Results are shown in Table 7.1 and Figure 7.4, with full kinetic details in Figure A7.14 and A7.15 showing uniformly high selectivity for hydroperoxide conversion to epoxide. Substantial differences in catalytic activity across materials are observed, as evident from rate constants plotted in Figure 7.4. These rate constants can be coarsely classified to fall within two regimes, shown in red in Figure 7.4 for "low activity" catalysts, which exhibit per-Ti rates of 5 – 10 $M^{-2}s^{-1}$, and "high activity" catalysts shown in blue, which exhibit 5-fold greater rates constants of 40 – 50 $M^{-2}s^{-1}$.

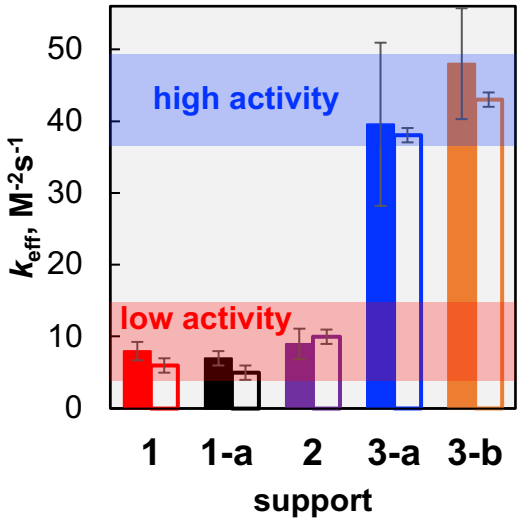

Figure 7.4. Pseudo-first order rate constants (equation (1)) for cyclohexene epoxidation with *t*-butyl hydroperoxide as the oxidant, reported in Table 7.1. Solid bars correspond to **cTi/X** catalysts, while open bars correspond to **Ti/X** catalysts, where **X** is the support indicated on the x-axis. The red band visually encompasses epoxidation with amorphous supports **1**, **1-a**, and zeotype silicate **2**, while the blue band encompasses zeotype supports **3-a** and **3-b**.

An Eyring plot of initial rates is shown in Figure 7.5, from which the apparent enthalpies and entropies of activation shown in Table 7.2 are calculated. Activation enthalpies are measured at $\Delta H^{\ddagger}_{app}$ = 42 ± 1 kJ mol^{-1} for all catalysts, indistinguishable from each other within uncertainty. Apparent entropies of activation $\Delta S^{\ddagger}_{app}$ are measured to be negative for all catalysts, but are less negative (i.e. more favorable) for **cTi/3-a** than for **cTi/2** with $\Delta\Delta S^{\ddagger}_{\mathbf{cTi/3a}\,-\,\mathbf{cTi/2}}$ = 12 J mol^{-1} K^{-1}. This is visually evident in Figure 7.5, where slopes (from which $\Delta H^{\ddagger}_{app}$ is calculated) are similar across blue vs. purple traces, while intercepts (from which $\Delta S^{\ddagger}_{app}$ is calculated) are clearly offset. The overall activation free energies are $\Delta G^{\ddagger}_{app}$ = 61 kJ mol^{-1} for **cTi/3-a** and 66 kJ mol^{-1} for **cTi/2**, indicating lower barriers for epoxidation by catalyst **cTi/3-a**, due to lower entropic barriers.

Trends comparing **cTi/3-a** and **Ti/3-a** in Figure 7.5 are practically indistinguishable, and result in similar activation parameters in Table 7.2, consistent with the lack of significant change to rate constants upon calcination in Figure 7.4 (i.e. less than 30% change is observed when comparing **cTi/X** (solid) and **Ti/X** (open)). This implies that calcination of **cTi/X** to synthesize **Ti/X** does not substantially affect the specific reactivity of Ti^{IV} centers.

Rate data in Figure A7.16 for catalyst **Ti/3-a** show a constant increase in rates of cyclohexene oxide production as a function of cyclohexene concentration, spanning four orders of magnitude. The order of the rate in cyclohexene concentration is measured to be 0.87 ± 0.05, in reasonable agreement with pseudo-1st order dependence in equation (1).

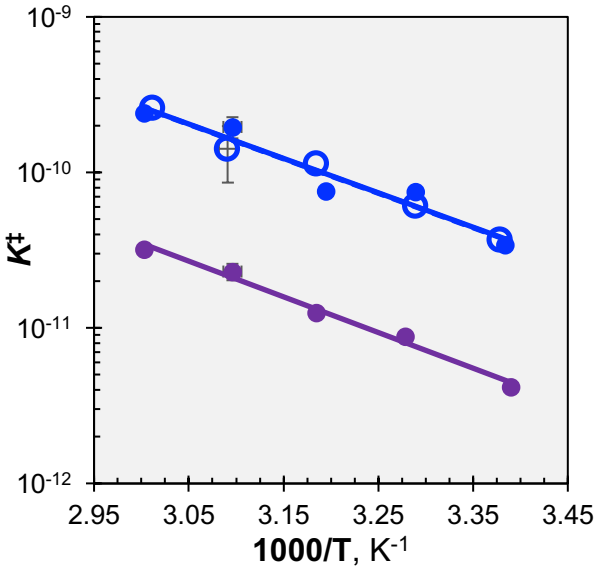

Figure 7.5. Eyring plots of initial epoxidation rates. Linear fit show were used in determination of $\Delta H^{\ddagger}_{app}$ and $\Delta S^{\ddagger}_{app}$ in Table 7.2 according to equation (3). Data is for **cTi/3-a** (solid blue markers and line), **cTi/2** (solid purple markers and line), and **Ti/3** (hollow blue markers, dashed blue line that lies directly under solid blue line). Uncertainty in temperature is 1 K; uncertainties in rates were determined at 323 K from replicate experiments.

Table 7.2. Measured Activation Enthalpies and Entropies for Cyclohexene Epoxidation for Selected Catalysts.

	$\Delta H^{\ddagger}_{app}$ (kJ mol^{-1})	$\Delta S^{\ddagger}_{app}$ (J mol^{-1}K^{-1})	$\Delta G^{\ddagger}_{app}$ (kJ mol^{-1})
cTi/2	44 (3)	-68 (8)	66 (2)
cTi/3-a	42 (6)	-56 (20)	61 (13)
Ti/3-a	42 (3)	-56 (10)	61 (6)

Calculated from slopes and intercepts of Eyring plot shown in Figure 7.5. Numbers in parentheses are uncertainties of linear fits.

7.3.5 Assessment of Transition State Formation and Site Mobility by Electronic Structure Calculations

To understand the site requirements for epoxidation catalysis, reaction pathways were modeled by density functional theory (DFT) methods, based on a cluster model of a "bare" Ti^{IV} active center, without the influence of the confining 12-MR pocket structure. This active site model incorporates a silanol group neighboring a Ti^{IV} center, to understand whether silanols affect epoxidation reactivity, as suggested in prior reports of epoxidation with aqueous H_2O_2.[37,65,67–72] Computational details are provided in section 7.2.5.

Alkene epoxidation involves:e (1) heterolytic coordination of hydroperoxide oxidant to Ti^{IV} centers, (2) attack of this bound peroxo intermediate by the alkene, leading to transfer of oxygen, and (3) co-product alcohol desorption.[30] Full reaction pathways (for model (A), *vide infra*) for

these three steps are shown in Figure A7.18, with calculated structures in Figure A.19. Free energy barriers for (1) hydroperoxide coordination ($\Delta G^{\ddagger}_{int}$ = 15 kJ mol^{-1}) and (3) alcohol product desorption ($\Delta G^{\ddagger}_{int}$ = 43 kJ mol^{-1}) are lower than the apparent ($\Delta G^{\ddagger}_{app}$ = 58 kJ mol^{-1}) or intrinsic barriers ($\Delta G^{\ddagger}_{int}$ = 45 kJ mol^{-1}) calculated for (2) oxygen transfer to olefin. Oxygen transfer is therefore the rate limiting, kinetically relevant reaction event, in agreement with previous findings;[8,30] its calculated free energy barrier is $\Delta G^{\ddagger}_{app}$ = 58 kJ mol^{-1}, in reasonable agreement with that observed experimentally in Table 7.2. The molecular volume of the transition state shown in Figure 7.6(A), estimated from the IEFPCM solvent cavity, is 225 Å^3 for the organic components (i.e. peroxo and olefin, without considering the SiOH and Ti(OSiH$_3$)$_3$ active site).

To understand the role of the silanols on alkene epoxidation, three different active-site models were evaluated, as shown in Figure 7.6: (A) where a silanol interacts via H-bonding with the distal oxygen of a peroxo bound to the Ti^{IV} center; (B) where a silanol interacts via a H-bonding with the oxygen directly coordinated to the Ti^{IV} center; and (C) where the silanol is entirely absent. Model (A) exhibits the lowest free-energy barriers for epoxidation, 6 – 7 kJ mol^{-1} lower than those calculated in (B) and (C).

To understand reactivity in cTi/X catalysts, we calculated energies of various adducts of TBHP with a model of cTi, intended to model heterolytic coordination of hydroperoxide. The results are shown in Section 7.7. Structure VIII corresponds to the lowest energy activated complex if calix(O)-Ti bond cleavage occurs upon TBHP bonding (i.e. Ti-OSi connectivity is preserved); breakage of the other two possible calix(O)-Ti bonds results in structures that are higher in energy, and are not shown here. The formation of structure VIII results in a positive electronic energy change. An energetically favorable process (negative electronic energy change) is instead observed in structure IX, when threefold calix(O)-Ti connectivity is maintained, but Ti-OSi cleavage occurs. Thus, Ti-OSi bond cleavage upon TBHP binding is more favorable than calix(O)-Ti cleavage. In structure XI, the cTi-TBHP species resulting from Ti-OSi bond cleavage is optimized within (but not covalently connected to) a defect-free 12-MR pocket. Dispersion (i.e. Van der Waals) stabilization energies are -352 kJ mol^{-1}, accounting for the majority of the energy change for formation of XI from models of a “free” mobile cTi-TBHP and an “empty” 12-MR pocket.

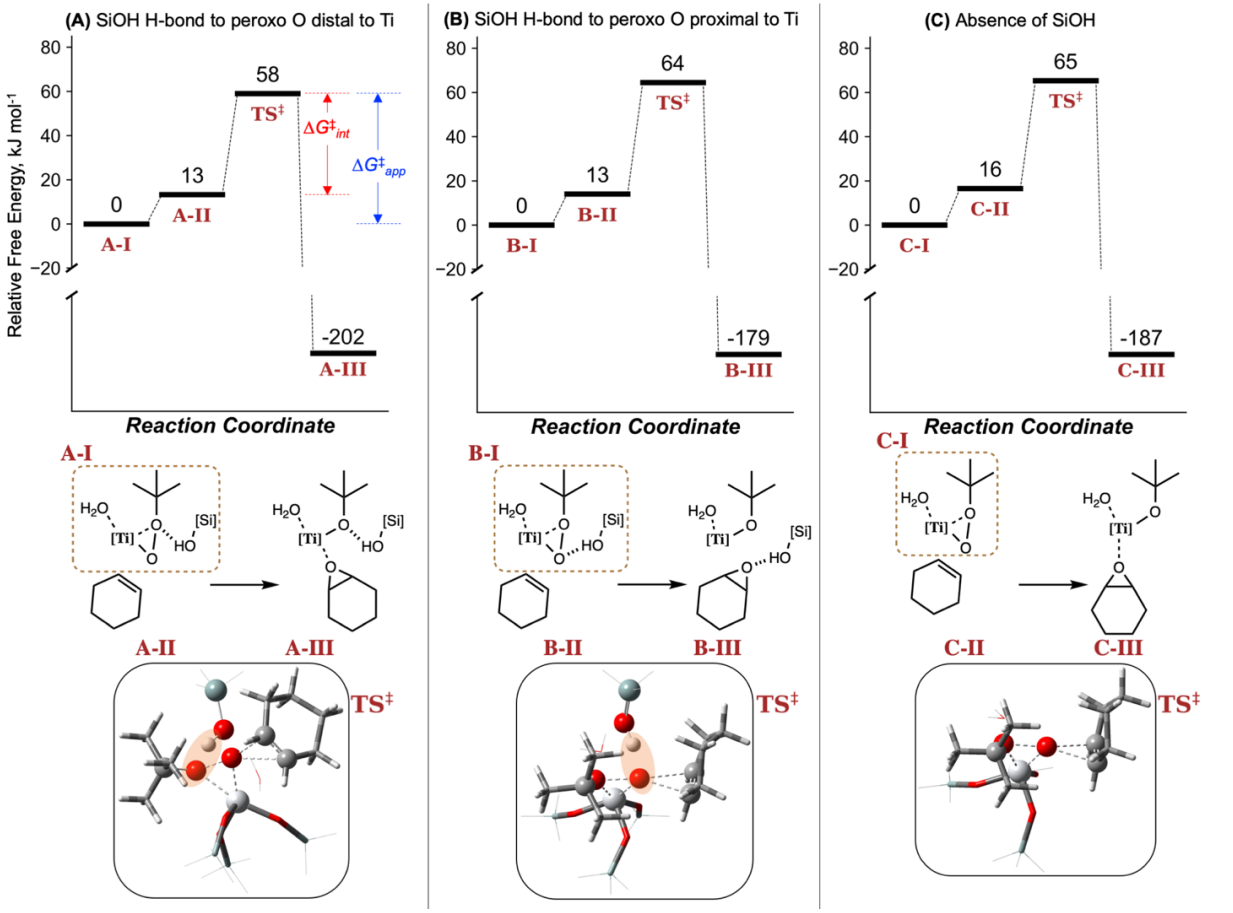

Figure 7.6. Reaction coordinate diagrams (top) showing free energies for oxygen transfer to olefin for three alternative active site models, calculated with RB3LYP-D3/6-311+G(d,p) methods. The species and its associated free energy are noted below and above each calculated intermediate, respectively. Three models were considered: **(A)** A silanol engages in H-bonding interactions at oxygen distal to Ti^{IV} in the bound peroxo, **(B)** a silanol engages in H-bonding interactions at oxygen proximal to Ti^{IV} in the bound peroxo, **(C)** no silanol is present. Below, schematic representations of each intermediate are shown; H-bonding interactions are indicated by hashed bonds, while dative interactions are indicated by dashed bonds; [Ti] refers to Ti^{IV} centers to which silicate ligands (not shown for clarity) are coordinated. Intermediates **A-I**, **B-I**, and **C-I** represent the peroxo bound to a Ti^{IV} center, to which energies are referenced; it is highlighted within the dashed brown rectangle. Coordination of cyclohexene to this structure results in structures **A-II**, **B-II**, and **C-II**, which overcome activation barriers to result in bound epoxide products in structures **A-III**, **B-III**, and **C-III**. Transition state $TS^{‡}$ geometries are shown at the bottom; dashed lines indicated bonds that are formed or broken, and translucent orange indicates H-bonding interactions. White: H, red: O, grey: Si, black: C, off-white: Ti; full ball-and-stick model shown only for atoms directly involved in the reaction events. $\Delta G^{‡}_{int}$ is the intrinsic free energy barrier associated with oxygen transfer; $\Delta G^{‡}_{app}$ is the apparent barrier for epoxidation that includes olefin binding energy. Full reaction coordinate diagrams and calculated structures for model **(A)** are included in Figure A7.18. Files including coordinates for all structures can be found in the Supporting Information.

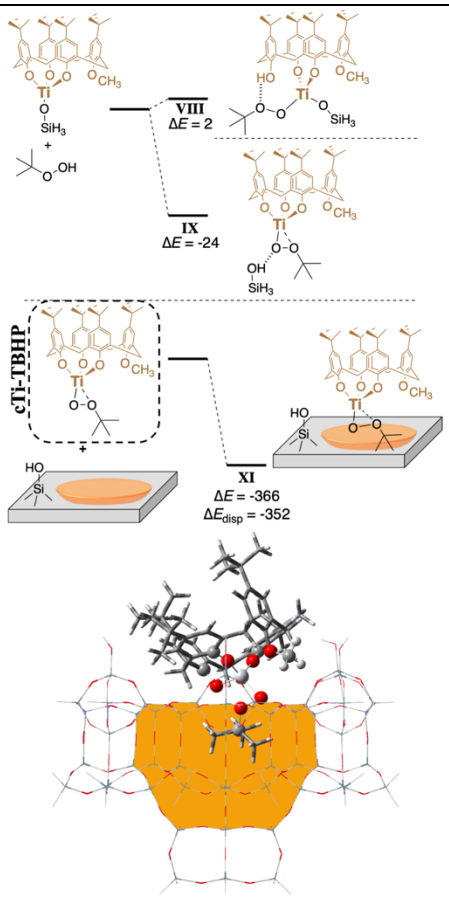

Section 7.7. DFT-calculated structures for binding of TBHP to a model of grafted **cTi** site in several scenarios: (**VIII**) binding involves the breaking of a calix(O)-Ti bond; (**IX**) binding involves the breaking of a Ti-OSi bond; (**XI**) **cTi-TBHP** species derived from **IX** interacts with a defect-free 12-MR pocket. ΔE corresponds to total change in electronic energy, while ΔE_{disp} is the change in energy associated with dispersion (i.e. Van der Waals) interactions as computed with DFT-D3(0).[60] All energies are in kJ mol^{-1}. At the bottom, the optimized structure **XI** is shown, with the orange shading highlighting the 12-MR pocket; the organic part of this structure corresponds to mobile **cTi-TBHP** species. Note that sequence of structure numbering starts at **VIII** for consistency with structures in Figure A7.18, and increases from **IX** to **XI** to avoid confusion with nomenclature used for supports, **X**. Structure files are included in the Supporting Information.

7.4. Discussion

7.4.1. Speciation of Silanols in Silicate Supports

Terminal T-sites (**i**), where the SSZ-70 framework is interrupted, are shown in purple in Scheme 7.1. These sites share only three oxygens with other framework T-sites; the fourth oxygen bond is terminated by a H^+ to form a silanol (SiOH). In the defect-free purely siliceous framework of zeotype **2**, these represent the only crystallographic positions where silanols exist on the **a**-**b** plane. Based on their crystallographic location, which are uniformly separated by 8.3 Å, silanols in these locations are too far apart for H-bonding interactions.[52,87] Consistent with this, we observe only free isolated silanols (3747 cm^{-1} band in Figure 7.2A) in **2** by infrared spectroscopy. Silanols in **2** are therefore located exclusively outside of 12-MR pockets at terminal T-sites (**i**), where they are unconfined (Scheme 7.1). They occur at similar surface densities (calculated at 1.1 SiOH nm^{-2}) to those measured on the surface of amorphous dehydroxylated **1**.[37]

Frequencies corresponding to silanols perturbed by hydrogen bonding (with ν(O-H) lower than 3747 cm^{-1}) are observed in the FTIR spectrum of **3-a** in Figure 7.2A. In particular, the broadness and strong redshift of the band at 3530 cm^{-1} is indicative of silanols strongly perturbed by mutual H-bonding. Such H-bonded silanols are consistent with the synthesis of framework vacancies through B^{III} removal upon acid treatment of **3** to synthesize **3-a**,[62] which is known to result in a pair of adjacent silanols.[15] B^{III} is known to be preferentially located at T-sites within 12-MR pockets in parent B-SSZ-70 used to synthesize **3-a** (section 7.2.1);[38] therefore, we conclude that 12-MR pockets (**ii**) in **3-a** are populated by silanols pairs, as depicted in Scheme 7.1. Other H-bonded silanol species, with bands observed at 3725 and 3690 cm^{-1}, have been previously assigned to confined silanols in zeotype micropores,[88] and may also be present within 12-MR pockets (**ii**). In addition, the small shoulder at 3747 cm^{-1} in the spectrum of **3-a** is characteristic of silanols at terminal T-atom positions (**i**), of the same type as observed in **2**. Therefore, **3-a** exhibits a mixture of silanol environments, within both unconfined (**i**) and confining environments (**ii**).

3-b was synthesized from **3-a** by trimethylsilyl (TMS) capping. Its spectrum in Figure 7.2A shows a lack of the shoulder at 3747 cm^{-1}, indicating that isolated silanol species in unconfined environments (**i**) are completely consumed by capping, as depicted in Scheme 7.1. Because the same intensity of H-bound species (with ν(O-H) lower than 3720 cm^{-1}) is maintained after capping, we conclude that silanols at framework vacancies within 12-MR pockets are unaffected by TMS capping. This is consistent with prior reports of trimethylsilyl chloride reacting selectively with free silanols.[89,90] Thus, **3-b** serves as a crucial comparator to **3-a**, as its silanols are exclusively located within confining 12-MR pockets (**ii**).

7.4.2. Location of Grafted cTi Centers within Specific Support Environments in Catalyst Resting States

Grafting densities normalized on an external surface basis, reported in Table 7.1, are lower on all zeotypes than 0.42 Ti nm^{-2} measured for a fully hydroxylated silicate surface in **cTi/1-a**. If any grafting occurred within internal micropores in zeotypes (with a measured BET surface area of ~500 m^2/g, much larger than S_{ext} ~ 130 m^2/g measured by the t-plot method; see Table A7.1), grafting densities normalized on an external surface basis would be expected to be much higher

than on the flat non-porous surface of **cTi/1-a** (0.42 Ti nm^{-2}). Therefore, we conclude that no grafting occurs within micropores, and occurs instead exclusively on the external surface of zeotypes. This is expected, based on the large size of **cTi-p** precursor ~1.4 nm in diameter,[16] too large to enter micropores smaller than the 7.1 Å diameter of 12-MR pockets. This location of **cTi** ensures that active centers are equally accessible on the external 2-D surface of the zeotype supports, unhindered by steric limitations imposed by micropores, thereby enabling a direct comparison of intrinsic Ti^{IV} reactivity across all catalysts. This contrasts with prior reports of epoxidation catalysis using organic hydroperoxides as oxidants, where the intrinsic reactivity of Ti^{IV} sites in zeotype TS-1 was limited due to steric limitations of its micropores, when compared to amorphous grafted Ti-on-SiO_2 catalysts.[91,92]

In general, grafted **cTi** on the external surface of SSZ-70 zeotypes can be located either at unconfined terminal T-atom positions (**i**), or within confining 12-MR pockets (**ii**), as determined by the location of silanols onto which **cTi** grafts. Difference infrared spectra for **cTi/2** in Figure 7.2B indicate a single sharp negative band at 3747 cm^{-1} for silanols consumed upon grafting **cTi** complexes to synthesize **cTi/2**, leading us to conclude that only silanols at terminal T-atom positions (**i**) serve to graft **cTi** sites in this material. This is expected, based on silanols in **2** being exclusively located at terminal T-atom positions (**i**), which are unconfined. In contrast, when synthesizing **cTi/3-b**, no negative band at 3747 cm^{-1} is observed in the difference spectrum following grafting (Figure 7.2B), indicating absence of grafting at terminal T-atom positions (**i**). This is also expected, because silanols at unconfined positions (**i**) were removed by TMS capping treatment in **3-b** prior to grafting. We therefore conclude that grafted **cTi** centers in **cTi/3-b** must be located solely within confining 12-MR pockets (**ii**). In **cTi/3-a**, the difference spectrum exhibits consumption of bands at 3747 and 3725 cm^{-1}, indicating a mixture of grafting environments for **cTi** both at unconfined terminal T-atom positions (**i**) and within confining 12-MR pockets (**ii**). This mixture is expected, because silanols in **3-a** are located in both of these environments.

The sum of the grafting densities (Table 7.1) of **cTi/2** (0.16 nm^{-2}, grafting at terminal T-atom positions (**i**)) and **cTi/3-b** (0.14 nm^{-2}, grafting within 12-MR pockets (**ii**)) add to 0.3 nm^{-2}, which corresponds to the observed site density in **cTi/3-a** (0.31 nm^{-2}, grafting at both (**i**) and (**ii**)). This observation of additive grafting densities suggests that silanols within each of these locations act independently as grafting centers; i.e. grafting of **cTi** at unconfined T-atom positions (**i**) does not influence **cTi** grafting within 12-MR pockets (**ii**). This type of site independence is enabled by the isolation of silanols within specific structural features of the crystalline zeotype surface. Such structural isolation is not generally observed in other support surfaces, as exemplified by considering a comparison of amorphous **1** and zeotype **2** as supports. On both of these supports, silanols occur at similar densities ~ 1 nm^{-2}, yet grafting densities are 50% higher in **cTi/1** than in **cTi/2**. We surmise this to be a consequence of the geometric constraints of silanols in **2**, which are uniformly separated by 8.3 Å; too close for any grafting to occur on adjacent silanols given the ~14 Å diameter footprint of **cTi**.[16] In contrast, the non-uniform distribution of silanols in amorphous **1** relaxes these geometric constraints, leading the surface to accommodate a higher grafting density. As such, crystalline zeotype supports present new opportunities to control catalytic environments by enforcing the location of active centers within particular structural features that are not accessible with amorphous supports.

The locations of grafted **cTi** centers as determined from these spectroscopic considerations are

represented in Figure 7.1. In summary, **cTi** is located exclusively at unconfined terminal T-atom positions (**i**) in **cTi/2**, vs. exclusively within confining 12-MR pockets (**ii**) in **cTi/3-b**. A comparison of these two catalysts therefore serves to independently probe the structural and catalytic consequences of confining (**ii**) vs. unconfined (**i**) environments, which are both found as a mixture in **cTi/3-a**.

7.4.3. Support Effects on Dynamic Ti^{IV} Active Centers During Epoxidation by cTi/X Catalysts

Catalytic activities of grafted **cTi** centers on different supports span nearly an order of magnitude in Figure 7.4. To understand the molecular-structural effects controlling these differences in reactivity, we first consider whether changes to inner-sphere ligands of Ti^{IV} active centers exist across **cTi/X** catalysts. UV-visible calix(O)-Ti LMCT edge-energies, known to be sensitive to the number of covalent connections between calix[4]arene oxygens and grafted Ti^{IV} cations,[93] are shown in Table 7.1. Their uniform value of 2.28 ± 0.02 eV for all **cTi/X** catalysts is indicative of identical connectivity across all Ti^{IV} surface complexes, consisting of a tridentate connection to phenolic structural units of the calix[4]arene, and single-point connectivity to the support,[15] as depicted in Figure 7.1. These values of UV-visible LMCT edge-energies for **cTi** centers grafted on silicates were previously shown to correspond to Ti^{IV} centers with identical electronic structure and inner-sphere coordination by Ti K-edge XANES.[15] We thus conclude that Ti^{IV} centers in all **cTi/X** catalysts exhibit the same electronic and inner-sphere coordination environments, which are indistinguishable from each other, independent of their location within individual support structural features. This result is an intended consequence of our materials design strategy, where the pseudotetrahedral $Ti^{IV}O_4$ coordination that is known to be required in the catalyst resting state for epoxidation[25–27] is uniformly enforced by chelating calix[4]arene macrocycles, which define the inner-sphere of Ti^{IV} in a manner that is irrespective of the support.

Given the identical inner-sphere coordination of Ti^{IV} observed across all **cTi/X** catalysts, **cTi** centers would be expected to exhibit similar catalytic properties, if pseudotetrahedral Ti^{IV} coordination were the only feature controlling epoxidation catalysis. Instead, we observe rates of **cTi/X** materials that fall into "low activity" vs. "high activity" regimes in Figure 7.4. It follows that these catalytic differences must be controlled by the outer-sphere environment surrounding grafted **cTi** centers on the support surface.[15,30] These outer-sphere effects cannot be explained by (a) the elemental composition of the support, which comprises purely siliceous SiO_2 networks in all catalysts, or (b) the degree of support crystallinity, because zeotype **cTi/2** lies within the same "low activity" region as amorphous **cTi/1** and **cTi/1-a**. To account for these outer-sphere effects, we note that **cTi** and silanols located at unconfined terminal T-atom positions (**i**) result in "low activity" rate constants for **cTi/2**. These rate constants are similar to non-porous amorphous **cTi/1** and **cTi/1-a**, where no confining structural features are present whatsoever. In contrast, silanols and **cTi** are located exclusively within confining 12-MR ring pockets (**ii**) in **cTi/3-b**, resulting in "high-activity" catalysts. We conclude that confinement of both silanols and **cTi** within 12-MR pockets is responsible for catalytic enhancements by outer-sphere effects.

An epoxidation rate constant of 48 ± 8 $M^{-2}s^{-1}$ (Table 7.1) for **cTi/3-b** reflects the intrinsic reactivity of "high activity" sites found exclusively within 12-MR pockets (**ii**). In contrast, an epoxidation rate constant of 9 ± 2 $M^{-2}s^{-1}$ for **cTi/2** reflects the intrinsic reactivity of "low activity"

sites that are unconfined at terminal T-atom positions (**i**). Yet, as discussed in section 7.4.2, **cTi** sites in the resting state of **cTi/3-a** are located in a mixture of grafting environments, at both terminal T-atom positions (**i**) as well as within 12-MR pockets (**ii**). If this same mixture of sites in the resting state of **cTi/3-a** were also present in its working state (i.e. during catalysis), the magnitude of the resulting rate constant would have to be intermediate between those observed for **cTi/2** and **cTi/3-b**. Instead, the observed epoxidation rate constant of 40 ± 11 $M^{-2}s^{-1}$ for **cTi/3-a** is virtually indistinguishable within experimental uncertainty from **cTi/3-b**, and corresponds to "high activity". We therefore surmise that active species initially located in a mixture of environments in the resting state of catalyst **cTi/3-a** must be located preferentially within confining 12-MR pockets (**ii**) under reaction conditions, where they manifest themselves as "high activity" sites.

This result necessitates that **cTi** sites in **cTi/3-a** become mobile under catalytic conditions, undergoing dynamic changes that transfer **cTi** sites originally grafted at terminal T-atom positions (**i**) in the catalyst resting state, to confined environments within 12-MR pockets (**ii**) during catalysis. On the molecular level, this dynamic mobility requires Ti-OSi bond cleavage upon TBHP bonding to **cTi** sites, because the Ti-OSi bond represents the only covalent attachment of **cTi** to the support in the catalyst resting state (Figure 7.1). DFT calculations (Section 7.7, section 3.5) indicate that cleavage of this Ti-OSi bond indeed occurs upon TBHP bonding to Ti^{IV}, rather than cleavage of the calix(O)-Ti, consistent with previous hypotheses.[30] The formation of the resulting mobile species is likely additionally favored by entropic gains. Therefore, the synthesis of mobile sites (inferred from kinetic measurements) is consistent with DFT calculations, which indicate that their formation is energetically favorable. We conclude that catalytic activity in **cTi/X** catalysts is mediated by activated mobile species, which we denote **cTi-TBHP**, as shown in Section 7.7 and Scheme 7.2.

DFT calculations indicate a high-degree of noncovalent stabilization of **cTi-TBHP** by dispersion (i.e. Van der Waals) interactions with the walls of the 12-MR pockets (structure **XI** in Section 7.7). This suggests that **cTi-TBHP** species are selectively located within 12-MR pockets (**ii**) under dynamic catalysis conditions, consistent with rate constants reflecting sites exclusively within these pockets under reaction conditions in **cTi/3-a** (where a fraction of sites are originally grafted outside of these 12-MR pockets). This non-covalent stabilization is reminiscent of the interactions between adsorbates and pore walls within fully-confining micropores of traditional zeolites,[4,94,95] but occurs here within partially-confining sub-nanometer cavities, which are accessible to the bulk external fluid phase. These accessible sub-nanometer cavities therefore serve to partially confine bulky reacting species such as **cTi-TBHP** (>1 nm in diameter, as measured in structure **XI**), which are too large to enter zeolite micropores.

7.4.4. Analogous Active-site Environments in cTi/X and Ti/X Catalysts

Absorption maxima in UV-visible spectra for **Ti/X** (Figure A7.8) correspond to Ti^{IV} centers with three-point connectivity to silicate ligands ($[Ti(OSi)_3OH]$, ~225 nm) in amorphous Ti^{IV} sites, comparted to four-point connectivity to silicate ligands ($[Ti(OSi)_4]$, < 210 nm) in crystalline-framework Ti^{IV} sites.[96] These structural assignments are represented in Figure 7.1.

The intensity of Ti K-edge pre-edge features observed in Figure A7.10 is lower for **Ti/2** than

Ti/3-b or **Ti/3-a**, indicating a higher distortion from ideal tetrahedral coordination symmetry[81] of Ti^{IV} in **Ti/2**. This difference can be rationalized by the observation that in **2**, silanols at terminal T-atom positions (**i**) are too far apart (8.3 Å, Scheme 7.1) for multi-point grafting of Ti^{IV} (multi-point grafting requires more closely spaced silicate ligands; for example, Si-Si distances in calculated structure **A-I** are 3.5 – 4.6 Å). We therefore surmise that framework Ti^{IV} sites in **2** consist of an interstitial Ti^{IV} center, located at the rim of 12-MR pockets, formed by Si-O-Si ring opening and disruption of the zeotype framework during calcination. This is in contrast to **3-a** and **3-b**, where T-sites vacancy defects can be re-occupied by cations such as Ti^{IV},[97] consistent with the higher tetrahedral symmetry of Ti^{IV} reflected in higher pre-edge features of **Ti/3-a** and **Ti/3-b**. Notably, no framework Ti^{IV} is observed in amorphous **Ti/1**, where UV-visible spectroscopy indicates that Ti^{IV} is instead grafted on the external surface (i.e. three-point connectivity) rather than embedded within a silica network (i.e. four-point connectivity), despite its silanols also being free and isolated as in **2** (FTIR in Figure 7.2A). A similar difference favoring framework-embedded cations in zeotype versus surface-grafting in amorphous silicates has been previously observed for Fe^{III} cations.[98]

XANES and EXAFS results in section 7.3.3 indicate that the tetrahedral coordination geometry of Ti^{IV} centers, required for epoxidation catalysis,[25,27,30] does not change upon calcination. This is consistent with rate constants for epoxidation (Figure 7.4) and activation free energies (Table 7.2) that are largely insensitive to calcination. Grafted **cTi** single-sites in **cTi/X** are therefore direct structural analogues of isolated Ti^{IV} centers on silicates in **Ti/X**. Uniform chelation of Ti^{IV} centers by calix[4]arene ligands ensures uniform inner-sphere coordination in **cTi/X**, thereby serving as a model system to rigorously understand reactivity in **Ti/X**, where Ti^{IV} centers resemble those invoked to be active in industrial formulations of epoxidation catalysts,[25–27,96,99] but where uniform inner-sphere coordination is not maintained (i.e. differences in UV-visible spectra in Figure A7.8). Given this structural and catalytic analogy between active sites with and without calix[4]arene ligands, we posit that the same outer-sphere catalytic effects that govern reactivity differences for **cTi/X** catalysts are also responsible for similar catalytic differences across **Ti/X** catalysts. In particular, for **Ti/2**, this implies that the grafted Ti^{IV} are located on the outside of 12-MR pockets, rather than inside of these. Additionally, this analogy implies that results of DFT calculations in section 7.3.5, based on titanosilicate (i.e. **Ti/X**) active sites models, without calix[4]arene ligands, are equally relevant to understanding the reactivity across all catalysts, including **cTi/X**.

The similarity of outer-sphere effects for **cTi/X**, where sites are dynamic under catalysis conditions (section 7.4.3), to **Ti/X**, where sites are immobilized via anchoring by three or more connections to the support (Figure 7.1), suggests that the outer-sphere of **Ti/X** is the same as **cTi/X**, in the active (dynamic) state. This is expected for **Ti/3-b**, where **cTi** is already grafted within 12-MR pockets (**ii**) before calcination, and for **Ti/2**, where **cTi** sites are grafted at terminal T-atom positions (**i**) outside 12-MR pockets before calcination (section 7.4.2). What is more profound, however, is the high activity of **Ti/3-a**, suggesting that active sites that were initially found in a mixture of environments before calcination (in **cTi/3-a**) reside within the 12-MR pockets (**ii**) of **Ti/3-a** after calcination. This observation is also consistent with the analysis of pre-edge features of Ti K-edge spectra for **Ti/3-a** and **Ti/3-b** in Figure A7.10, which both exhibit a position at 4970.1 eV and height of 0.84 ± 0.01. This combination of pre-edge position and height is not observed in any other **Ti/X** materials, suggesting that Ti^{IV} centers in **Ti/3-a** and **Ti/3-**

b are within identical grafting environments, unique among the various **Ti/X** catalysts. This unique environment consists of T-site vacancies within 12-MR pockets, the only grafting environment present in **3-b**, which is not present in **1**, **1-a**, or **2**. The grafting of all Ti^{IV} centers within 12-MR pockets (**ii**) in **Ti/3-a** requires that Ti^{IV} centers that were grafted at terminal T-atom positions (**i**) become mobile during calcination and combustion of calix[4]arene ligands from **cTi/3-a**, to be instead grafted within 12-MR pockets (**ii**) in **Ti/3-a**. Indeed, mobility of Ti^{IV} centers grafted on silicates has been previously observed,[100] and has been invoked as a contributing factor to long-term deactivation of industrial catalysts.[101]

7.4.5. Mechanistic Implications: Confinement within 12-MR Pockets Lowers Entropic Barriers for Reactant Activation

A lower free energy barrier is calculated for the formation of the epoxidation transition state in active site model **(A)** in Figure 7.6, where H-bonding occurs between a silanol and the peroxo oxygen distal to the olefin, compared with model **(C)**, where H-bonding interactions are absent. This indicates that silanols engage in cooperative interactions with peroxo species bound to Ti^{IV} active centers, which lowers the barrier for the kinetically relevant oxygen transfer to the olefin, consistent with prior theoretical and experimental results implicating catalytic effects of silanols in titanosilicate epoxidation catalysts.[30,65,68,75–77] When H-bonding interactions occur at the oxygen being transferred to the olefin – as in model **(B)** – a higher free-energy barrier for transition state formation is observed compared to model **(A)** in Figure 7.6. This indicates that H-bonding interactions must occur at the oxygen distal to the olefin for the reaction to proceed through the lowest energy pathway. As such, the cooperative effects involving a Lewis acidic Ti^{IV} center and a weakly Brønsted acidic SiOH functionality on the silicate surface appear to be mediated by the precise orientation of these moieties and the attacking olefin. Such a specific organization would result in significant entropy loss for the formation of transition states from initially mobile reacting species, including an olefin in solution and **cTi-TBHP** species in **cTi/X** catalysts. This is indeed observed experimentally in the negative entropies of activation in Table 7.2. We therefore conclude that epoxidation events occur by formation of a precisely organized transition-state structure involving peroxo species bound to Ti^{IV} centers, cooperating silanol, and attacking olefin, as shown in Scheme 7.2. The observation that cooperativity of Ti^{IV} centers with silanols is required at the active site is consistent with our prior observation that **cTi** analogues in solution (i.e. in the absence of silanols on a silica surface) are inactive as homogeneous catalysts.[30]

Transitions states cannot form within confining 12-MR pockets in **cTi/2**, despite the presence of 12-MR pocket framework structures, because these pockets are defect-free and would therefore lack the required silanol at the active site. Therefore, transition states can only form at silanols that are unconfined at external terminal T-sites (**i**) in **cTi/2**. Instead, in **cTi/3-a** and **cTi/3-b**, the mobility of **cTi-TBHP** enables assembly of reacting species into the required geometric orientation at the transition state, at silanols located within confining 12-MR pockets (**ii**). In calcined **Ti/X** catalysts, Ti^{IV} sites may cooperate with a silanol that is already present in the surrounding silicate surface, or a silanol that may form via cleavage of a Ti-OSi bond upon hydroperoxide binding. Such a formation of silanol functionality *via* Ti-OSi bond cleavage has been observed upon H_2O_2 binding to Ti^{IV} centers in TS-1,[66] and can be inferred from similarity of rates between native titanosilicates and those in which silanols have been removed by extensive

TMS capping.[55,102]

Catalytic data discussed in section 7.4.3 indicate that the location of silanols and Ti^{IV} centers within confining 12-MR pockets (**ii**) results in materials with a "high activity" for epoxidation in Figure 7.4. This suggests that the formation of kinetically relevant transition states is facilitated by the surrounding confining outer-sphere environment. Such stabilization by confinement is known to require an intimate "fit" of kinetically relevant transition states within molecular voids that confine reaction events.[103] The molecular volume of peroxo and olefin within the calculated transition state structure of **A-II → A-III** in Figure 7.6 is 225 $Å^3$, which is similar in size to the volume of the 12-MR cavities (~ 7.1 Å in diameter and 7 Å in depth for a volume of 185 $Å^3$).[33] As such, the transition state fits "tightly" within 12-MR pockets, and can be expected to be sterically influenced by the confining cavity surface. Below, we consider how this transition state confinement affects its formation, to give rise to increased rates.

Epoxidation rate constants in Figure 7.4 for **cTi** sites grafted onto amorphous silica are insensitive to whether surface silanols occur as predominantly isolated species with densities ~1 SiOH nm^{-2} in **cTi/1**, or predominantly H-bonded species with densities ~4 SiOH nm^{-2} in **cTi/1-a**.[37] Thus, the epoxidation reactivity of cooperative Ti^{IV}–silanol assemblies does not appear to be affected by local speciation or surface density of silanols. We attribute this to two effects: (a) silanols being formed during catalysis via cleavage of the Ti−OSi bond after organic hydroperoxide binding, and (b) the mobility of **cTi-TBHP** activated complexes, which arises as a result of (a). This mobility enables an optimal assembly of **cTi-TBHP** active species with a surface silanol to form active sites, irrespective of the local density of silanols on the surface. This is in contrast with catalysis involving tethered amine sites, where the local density of cooperating silanol moieties in the outer-sphere directly influences catalysis.[104,105] It is also in contrast with recent reports on epoxidation with aqueous H_2O_2, where cooperativity was observed to be mediated by intraporous H_2O networks.[75]

Rates are uninhibited by increasing olefin concentrations (results in section 7.3.4, Figure A7.16), consistent with previous observations.[28] The lack of rate inhibition with increasing olefin concentration indicates a lack of significant binding of epoxide to Ti^{IV} centers after reaction, which would otherwise result in product inhibition.[8,85] By extension, we would not anticipate that olefins – which coordinate less strongly than epoxides – would be pre-adsorbed at Ti^{IV} centers prior to reaction. This agrees with calculated structures in Figure 7.6, showing a positive change in free energy upon olefin binding (i.e. comparing structure **A-I** and **A-II**), driven by losses of translational entropy. Therefore, the lack of pre-adsorption of the olefin implies that sorption processes cannot account for the observed rate acceleration by confinement. Instead, transition states assemble by a direct attack of an olefin to cooperative Ti^{IV} – silanol assemblies at the active site.

Similar activation enthalpies are observed for **cTi/3-a**, **Ti/3-a**, and **cTi/2** catalysts in Table 7.2. We surmise that, mechanistically, the kinetically relevant transition state (and associated reaction pathway) is energetically equivalent irrespective of whether epoxidation events are confined within 12-MR pockets (**ii**), as in **cTi/3-a**, or unconfined in (**i**), as in **cTi/2**. It is also energetically equivalent regardless of whether the Ti^{IV} species originates from a mobile **cTi-TBHP**, as in **cTi/3-a**, or a Ti^{IV} center permanently bound to the silicate surface, as in **Ti/3-a**. Measured apparent entropies of activation in Table 7.2 are less negative for **cTi/3-a** relative to **cTi/2**, indicating that

confined environments result in lower entropic barriers for formation of kinetically relevant transition states. We therefore rationalize the partially confining 12-MR pockets (**ii**) as spatially constrained environments that facilitate association of reacting species for forming the transition state structures for catalysis, as illustrated in Scheme 7.2.

Prior studies have also observed the lowering of entropic barriers accompanied by otherwise similar enthalpic barriers, when reactions occur within fully confining environments, relative to reactions that are unconfined. In a recent study, Lercher and coworkers observed such trends for reactions that occurred within confining micropores of BEA zeolites and were catalyzed by hydronium ions. These reactions exhibited a lower entropy of activation for reactants confined within the micropores relative to those unconfined in the bulk aqueous phase, which was attributed to the lower entropy of reactants within three-dimensional micropores.[3] Diminished entropic barriers have also been observed in supramolecular systems, which fully encapsulate molecular substrates within their interior. These are thought to occur because substrates are encapsulated in a preorganized conformation that is conducive to reaction.[106] In both of these studies, however, the diminished entropic barriers occurred within fully confined environments, inside of which the reactant molecules are entirely encapsulated. In contrast, the entropic acceleration observed in our study occurs within partially confining shallow hemispherical cavities, which are exposed to the bulk fluid phase. To the best of our knowledge, such an observation of catalytic confinement effects within an accessible inorganic pocket (on the external surface) lowering the activation entropy for catalysis is unprecedented.

Scheme 7.2. Confinement of epoxidation transitions states lowers entropic penalties to activation.

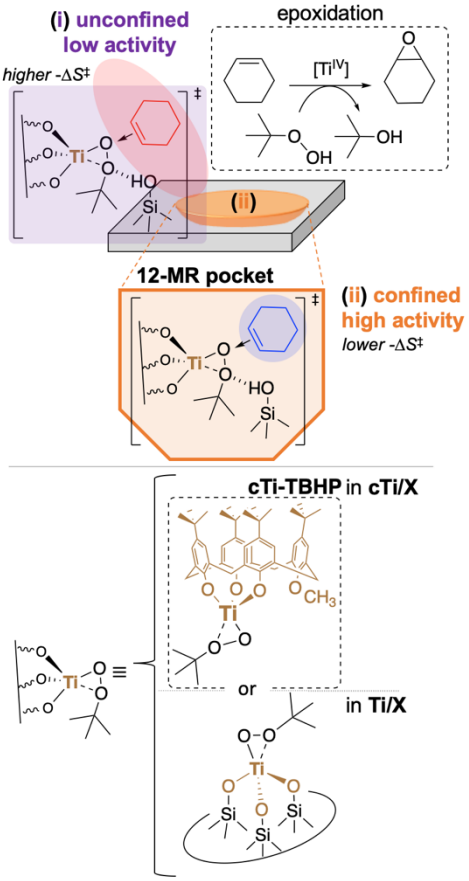

7.5. Conclusions

Grafted Ti^{IV} sites on siliceous supports serve as active centers for olefin epoxidation, whether or not they are confined within 12-MR pockets on the surface of 2-D SSZ-70 zeotypes. Confining outer-sphere environments result in rate constants for cyclohexene epoxidation with *t*-butyl hydroperoxide that are up to 5-fold higher, i.e. when using support **3-b**, as compared to support **2** where reaction events are unconfined. In support **3-a**, where Ti^{IV} centers are initially grafted both outside and inside 12-MR pockets, rate constants reflect confined transition states under reaction conditions, instead of a mixture of environments. Therefore, Ti^{IV} centers become mobile during catalytic conditions, undergoing dynamic changes that enable their confinement within 12-MR pockets, either via formation of **cTi-TBHP** species during olefin epoxidation in **cTi/3-a**, or via calcination treatment during synthesis of **Ti/3-a**. Molecular modeling identifies kinetically relevant transition states consisting of a peroxo bound to a Ti^{IV} center, a cooperating silanol, and an attacking olefin. Kinetic measurements indicate that spatially constrained confining environments in 12-MR pockets lower the entropic penalty for the association of these species into the transition state.

These confinement effects occur at external-surface 12-MR pockets, fully accessible to the fluid phase, and involve bulky reacting species such as **cTi-TBHP** (> 1 nm in diameter), too large diffuse into the micropores traditionally required for confinement effects in solid acid catalysts. This phenomenon is therefore distinct from traditional confinement effects in three-dimensional zeolite micropores,[1] which are limited to reactants smaller than micropore openings. As such, our observations hold the potential to extend beneficial confinement effects to a much wider range of reactions, involving intermediates too bulky to access micropores, but which can nonetheless access the shallower and partially confining pockets on a 2-D surface. We envision extension of these effects to other 2-D zeotype frameworks,[107–109] and to other reactions where the spatial constraints imposed by zeolite micropores limits catalytic productivity.

7.6. Appendices

7.6.1. Synthesis and Characterization of Supports

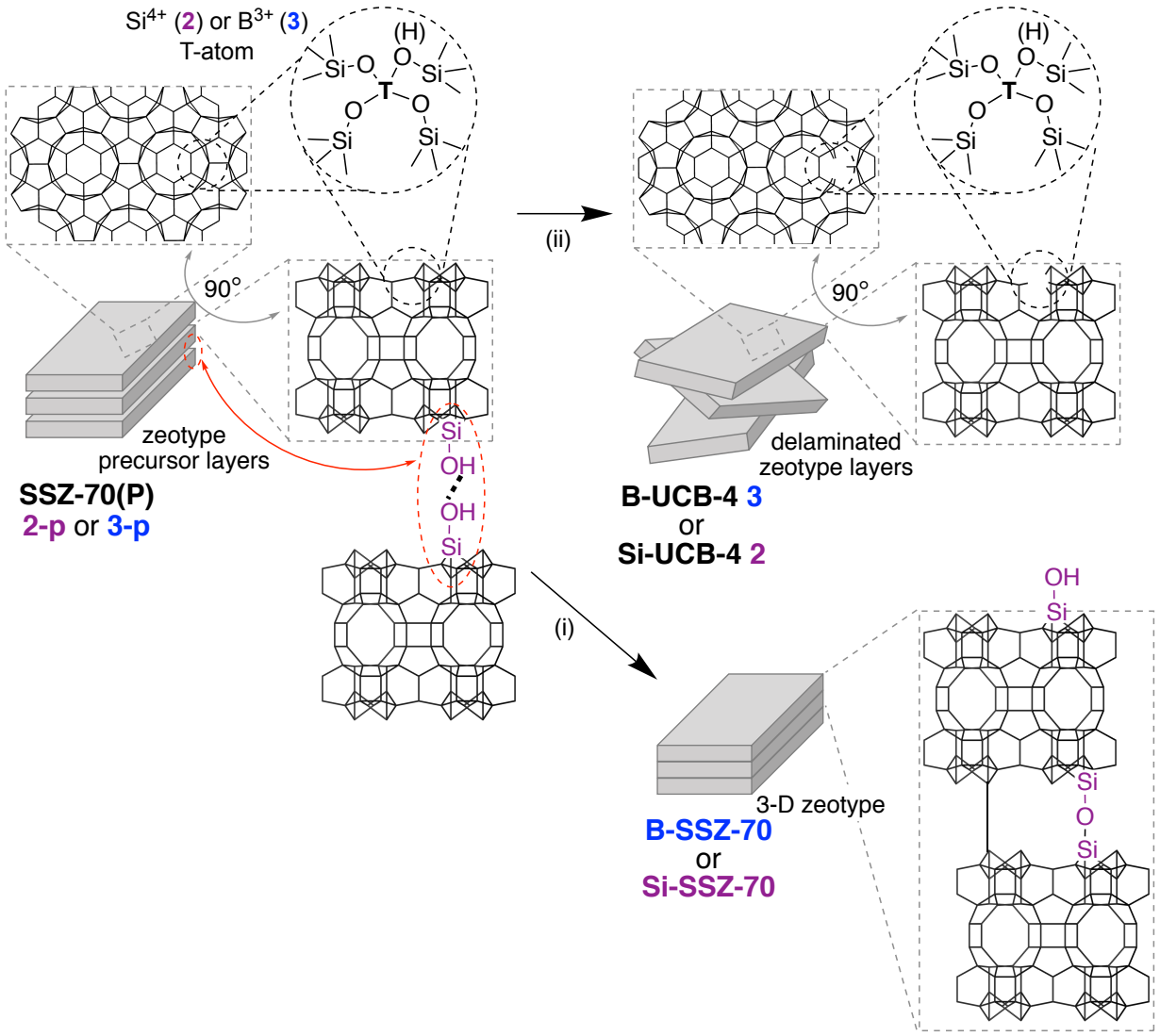

Scheme A7.1. Schematic representation of zeotype delamination. (i) Calcination of layered zeotype precursor SSZ-70(P) results in condensation of zeotype layers (rectangles) that were previously H-bonded, resulting in a 3-D zeotype SSZ-70. (ii) Delamination occurs by exfoliation of these non-covalently bound zeotype layers into a disordered arrangement through swelling in the presence of surfactant and ammonium halide salts, followed by sonication, washing, calcination. Details of the crystalline zeotype framework of SSZ-70 and UCB-4 are shown along the a-c plane and rotated 90° along the a-b plane (top left), with vertices representing $SiO_{4/2}$ tetrahedra centers and lines Si-O-Si bonds. The process can be applied to borosilicate **3-p** or pure silicate **2-p**.

Table A7.1. Physicochemical Characterization of Support Materials and their Precursors

Material	Description	S_{acc} (m^2/g)[a]	V_{tot} (cm^3/g)[c]	V_{micro} (cm^3/g)[d]
1	Amorphous SiO_2	190	1.19	-
2-p[b]	Si-SSZ-70	39	0.31	0.18
2	Si-UCB-4	89	0.40	0.10
3-p[b]	B-SSZ-70	66	0.32	0.20
3	B-UCB-4	135	0.41	0.16
3-a	deboronated UCB-4	135	0.46	0.15
3-b	deboronated UCB-4, TMS capped	122	0.30	0.07

[a]Accessible surface area, determined by the BET method for SiO_2, and from the t-plot external surface area for microporous zeotypes. [b]Corresponds to calcined version layered precursors. [c]Total pore volume. [d]Micropore volume, determined from t-plot method; SiO_2 is non-porous fumed silica with no microporosity. Raw isotherms are shown in in Figure A7.2.

The textural properties of delaminated silicate **2** and borosilicate **3** zeotypes and their precursors (**2-p** and **3-p** respectively) are summarized in Table A7.1. Precursors **2-p** and **3-p** comprise non-covalently-bound zeolitic layers that upon calcination form zeotype SSZ-70[32] in its purely siliceous (**2-p**) and borosilicate (**3-p**) forms, respectively.[48] Upon delamination, increases in external surface area and decreases in micropore volume are apparent when comparing **2** and **3** to **2-p** and **3-p**, respectively. This is reflected in an increase in the slope of the isotherms in Figure A7.2 between P/P_0 of 0.1 to 0.5, reflecting adsorption on the increased external surface. Total pore volume (V_{tot}) also increases as a consequence of additional mesoporosity between zeotype layers upon delamination, relative to nondelaminated counterparts; this is reflected in a higher quantity adsorbed at $P/P_0 = 1$ in Figure A7.2. These changes are consistent with delamination exfoliating precursor layers into a disordered arrangement, thereby exposing on the external (accessible surface) crystalline domains that would otherwise lie in microporous voids between layers (Scheme A7.1).[31] We refer to the reader to other work detailing the characterization of successful delamination, including by microscopy,[110] as well as the challenges associated with achieving this delamination.[31,34,35] These challenges result in only partial exfoliation of the precursor layers, and not full delamination to single lamellar sheets (which would otherwise result in theoretical maximum external surface areas closer to 500 m^2/g)[22].

Deboronation by acid-washing of **3** to **3-a** has negligible effects on textural properties (Table 7.1) or isotherms (Figure A7.2). TMS capping in **3-b** results in a decrease in pore volumes, presumably because of blockage of some pores by TMS groups; nevertheless, the external surface area remains similar. This is reflected in an isotherm in Figure A7.2 that is vertically shifted down but retains a similar slope between P/P_0 of 0.1 to 0.5. Thus, the external surface remains accessible for grafting of **cTi** centers after TMS capping.

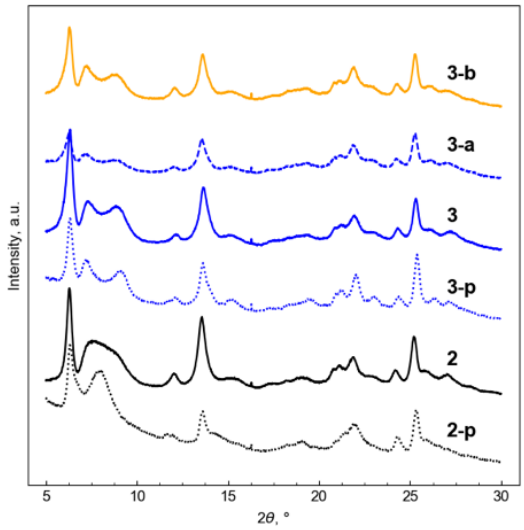

Figure A7.1. Powder X-ray diffraction patterns of materials in Table A7.1. The similarity in the patterns of all materials confirms long-range structural preservation upon delamination, acid-washing, and trimethylsilyl capping of zeotype materials. In particular, the intra-layer reflection (~ 26 º of 2θ)[31,111] retains its position and sharpness in all materials, irrespective of delamination, acid-washing, or TMS capping treatments.

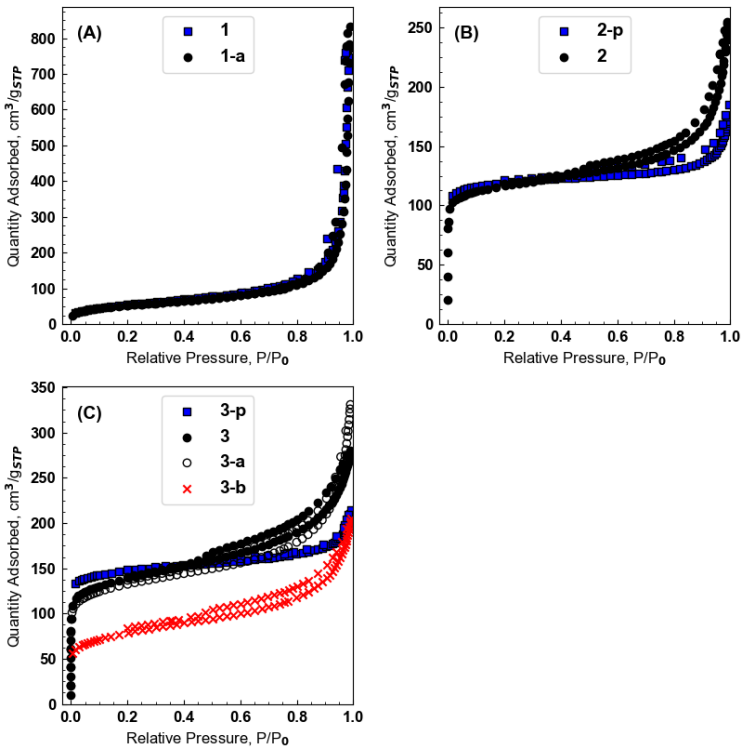

Figure A7.2. N_2 adsorption-desorption physisorption isotherms at 77 K used to calculate textural properties for materials in Table A7.1. All silicates, except **3-b**, were calcined at 823 K prior to measurements.

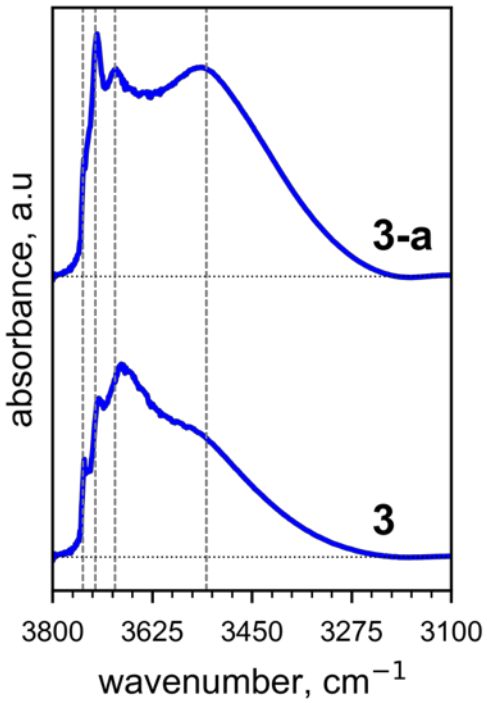

Figure A7.3. Normalized transmission Fourier-transform infrared spectra of the *ν*(SiO-H) region comparing **3** to **3-a** (the latter spectrum shown in Figure 7.2**(A)**). Dotted horizontal lines indicate baseline, while dashed vertical lines indicate bands at 3747, 3725, 3690, 3530 cm^{-1}.

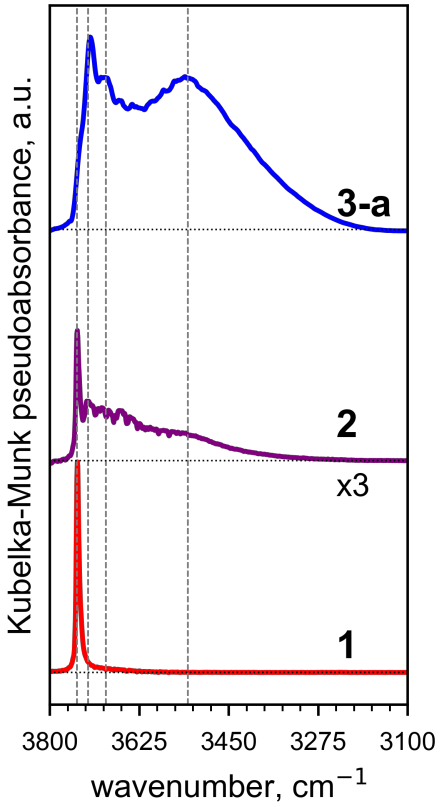

Figure A7.4. Normalized diffuse reflectance Fourier-transform infrared spectra (DRIFTS) of the *v*(SiO-H) region comparing **1, 2** (magnified 3 times), and **3-a**, acquired at 473 K under He flow. Dotted horizontal lines indicate baseline, while dashed vertical lines indicate bands at 3747, 3725, 3690, 3530 cm^{-1}. While transmission spectra were used for subtraction analyses in Figure 7.2B, A7.5 and A7.6, we compared spectra of supports in transmission and diffuse-reflectance modes, because the latter is more reflective of the actual state of the support as it does not involve pressing of sample wafers. Deboronated zeotype **3-a** exhibits similar bands in Figures 7.2A (transmission of pressed wafer) and A7.4 (DRIFTS). Amorphous silica **1** also exhibits similar bands in Figures 7.2A (transmission of pressed wafer) and A7.4 (DRIFTS); however, transmission results exhibit very slight intensity lower than 3747 cm^{-1} in frequency, compared to the DRIFTS spectrum. Comparison of **2** as a powder in DRIFTS mode (Figure A7.4) and a wafer of **2** in transmission mode (solid lines in Figure A7.6) reveals slightly more H-bound silanols for the transmission-mode spectrum. For this reason, we chose to calcine the wafer of **2** prior to acquiring the spectrum shown in Figure 7.2A of the main text, which results in a spectrum that more closely resembles the actual state of the bare silicate observed by DRIFTS.

7.6.2. Spectroscopic Characterization of cTi/X

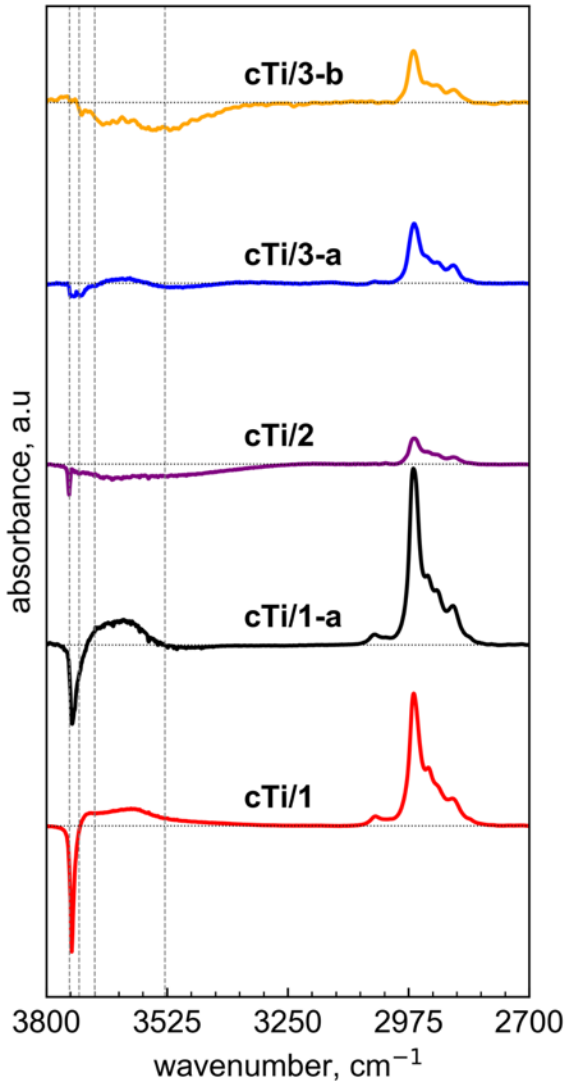

Figure A7.5. Difference FTIR spectra comparing **cTi/X** and to bare support **X**, which show spectral changes upon grafting of **cTi** for all supports. Raw spectra before subtraction are shown in Figure A7.6. Dotted horizontal lines indicate baseline, while dashed vertical lines indicate bands at 3747, 3725, 3690, 3530 cm^{-1}.

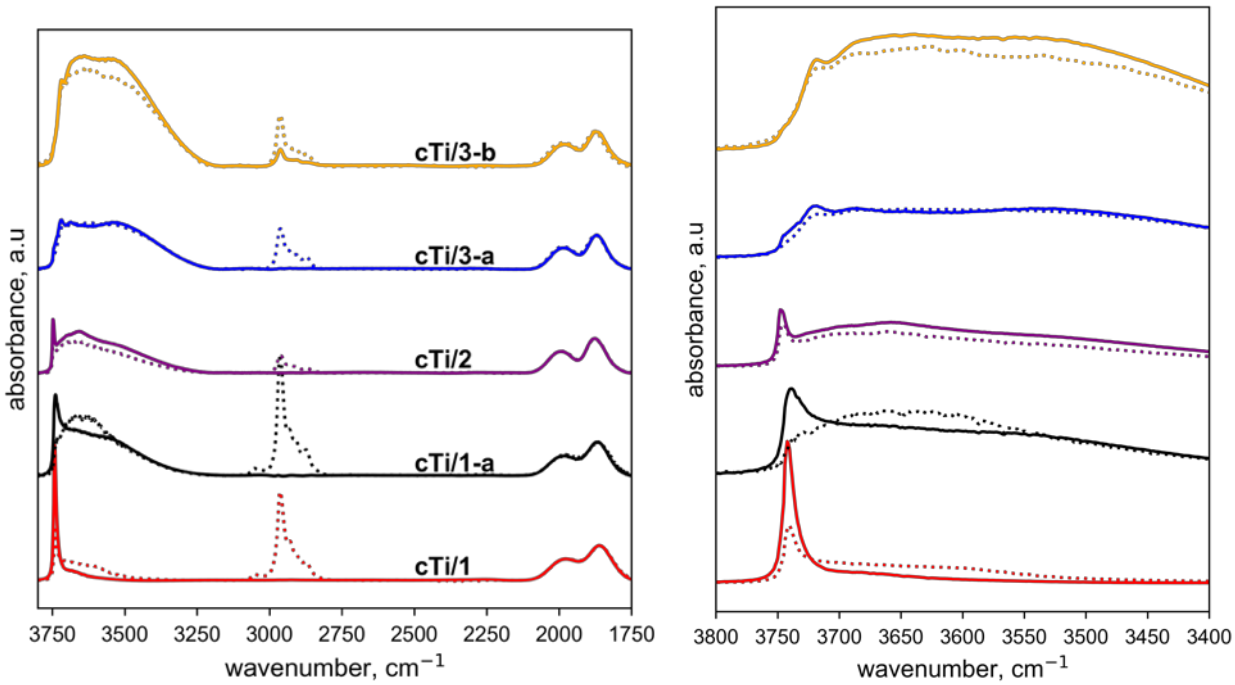

Figure A7.6. Raw FTIR spectra used to compute difference spectra in Figure 7.2(B) and Figure A7.5, for the material indicated. The spectrum of the support **X** is shown as a solid line and the spectrum of the grafted **cTi/X** as a dotted line. To the right, the region between 3400 and 3800 cm^{-1} is shown in greater detail, where the changes associated with bands of silanol species at 3747 cm^{-1} and 3725 cm^{-1} are clearly visible. All spectra were acquired on self-supported wafers that were pressed and treated under He flow at 473 K in the IR cell during spectral acquisition.

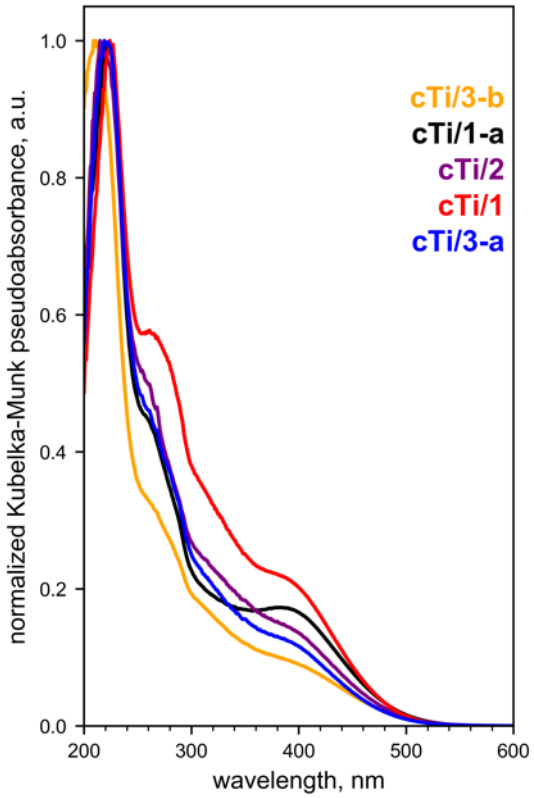

Figure A7.7. Diffuse-reflectance UV-visible spectra of **cTi/X**; specific material is indicated by the color on the right of each spectrum.

7.6.3. Spectroscopic Characterization of Ti/X

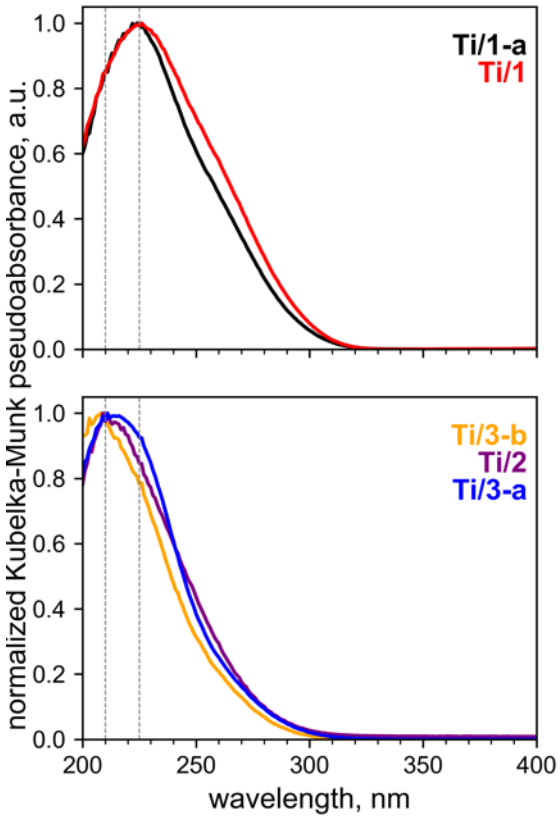

Figure A7.8. Diffuse-reflectance UV-visible spectra of amorphous (top) vs. zeolitic (bottom) **Ti/X** catalysts; vertical lines indicate maxima at 225 nm for amorphous vs. 210 nm for zeolitic catalysts.

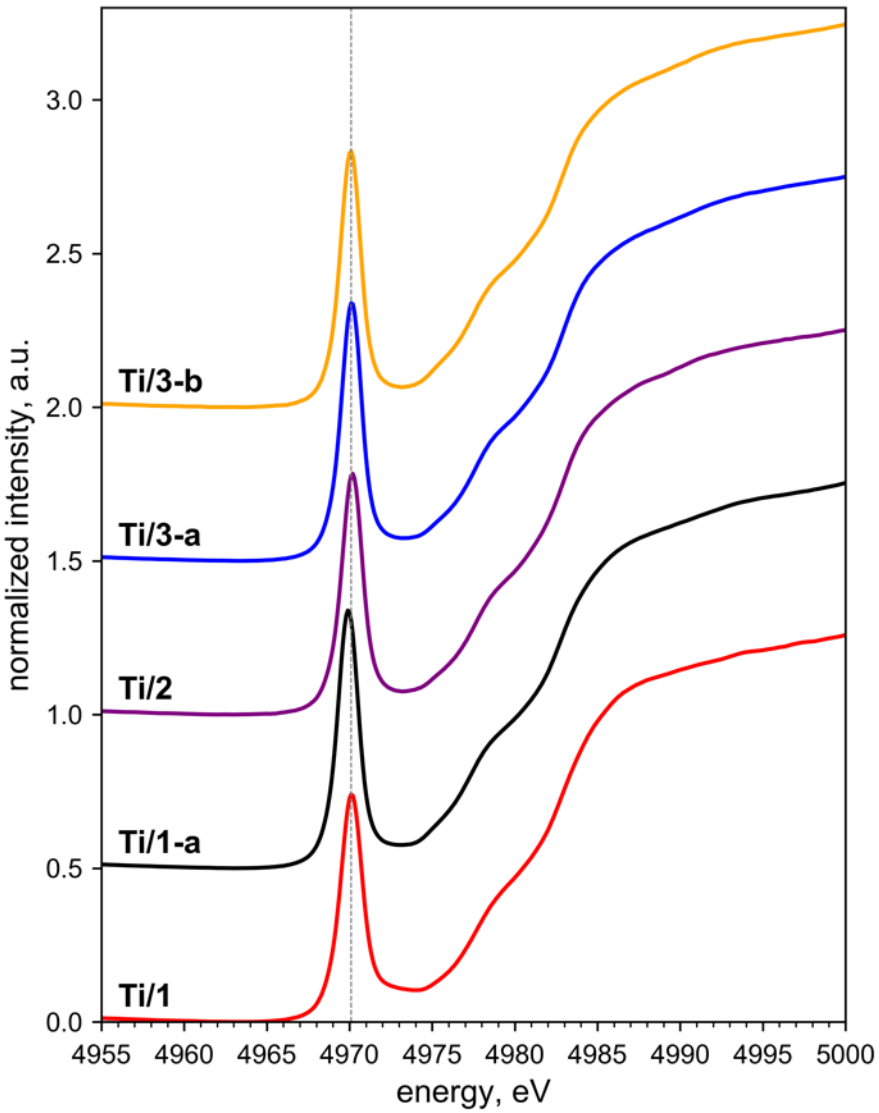

Figure A7.9. Normalized Ti K-edge XANES spectra, highlighting pre-edge features for all materials, which occur at ~ 4970.0 eV (dashed line). Spectra are staggered for clarity.

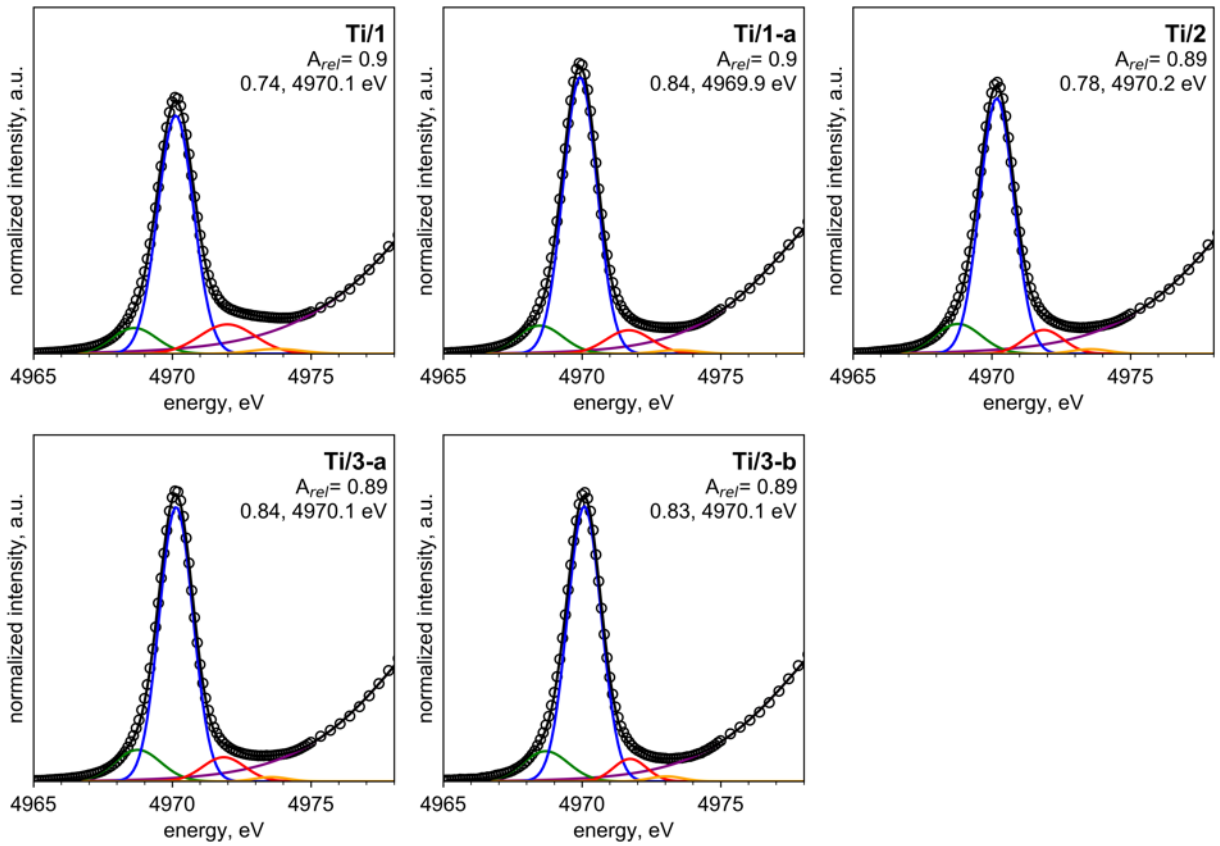

Figure A7.10. Detail of Ti K-edge XANES pre-edge features and deconvolution into Gaussian area components: arctangent of raising edge (purple), A1 (green), A2 (red), A3 (blue), B (orange). For each material, the value of relative areas A_{rel} = (A2 + A3)/(A1+ A2 + A3 + B) is given, followed by the normalized peak height and pre-edge peak position, defined as the energy of maximum intensity.

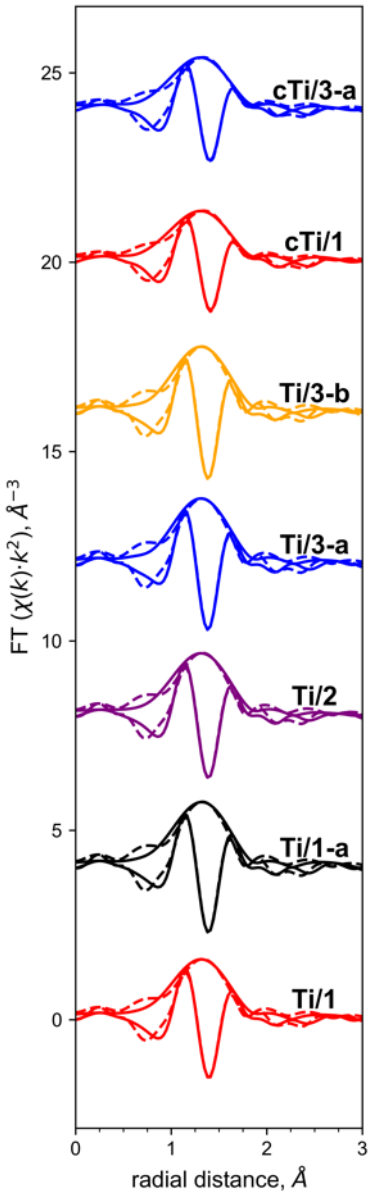

Figure A7.11. Summary of EXAFS and fits characterizing **Ti/X** and select **cTi/X** samples, with sample indicated beside each spectrum. Data are shown as solid lines, while fits are shown as dashed lines. Both magnitude and Imaginary part of the of the Fourier Transform are shown.

Table A7.2. Summary of EXAFS Fit Parameters Characterizing Ti/X and Select cTi/X Samples; Spectra and Fits Shown in Figure A7.11.

Sample	*R* (Å)	σ^2 (Å^2)
Ti/1	1.81 ± 0.02	0.002 ± 0.002
Ti/1-a	1.80 ± 0.01	0.001 ± 0.001
Ti/2	1.80 ± 0.01	0.001 ± 0.002
Ti/3-a	1.80 ± 0.01	0.001 ± 0.001
Ti/3-b	1.80 ± 0.01	0.001 ± 0.002
cTi/1	1.83 ± 0.01	0.003 ± 0.001
cTi/1-a	1.82 ± 0.01	0.003 ± 0.001

Data collected under He flow at 473 K and or 673 K for **cTi/X** and **Ti/X**, respectively. S_0^2 denotes amplitude reduction factor; σ^2, disorder term; *R*, distance between absorber and backscatter. A single Ti-O absorber-backscattering path is considered. Values of coordination number *N* were fixed to 4, because all materials were exhibit Ti in a pseudotetrahedral coordination environment (see UV-visible results in section 7.3.3 and 7.4.4). S_0^2 (amplitude correction factor) and ΔE_0 (energy correction term) were determined by fitting to the same value across all samples; their values were $S_0^2 = 0.77 \pm 0.05$ and $\Delta E_0 = -2.7 \pm 0.8$ eV. Samples were fitted in the *k*-range 3.1 to 10.2 Å^{-1}, and an *R*-range of 1 to 2.2 Å.

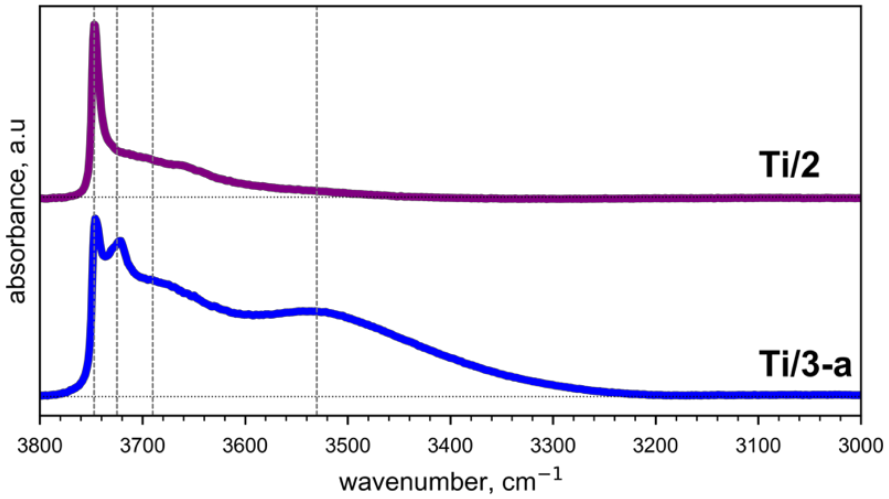

Figure A7.12. FTIR spectra of **Ti/2** and **Ti/3-a**. Spectra acquired for self-supported pellets that were calcined at 823 K prior to measurements of under He flow at 473 K. Dotted lines indicate baseline, while dashed lines indicate bands at 3747, 3725, 3690, and 3530 cm^{-1}. The spectrum of **Ti/2** is dominated by intensity of band at 3747 cm^{-1}, while that of **Ti/3-a** exhibits intensity for all four silanol bands, like its parent support in Figure 7.2(A). This confirms that calcination of **cTi/X** does not affect the presence of different silanol species.

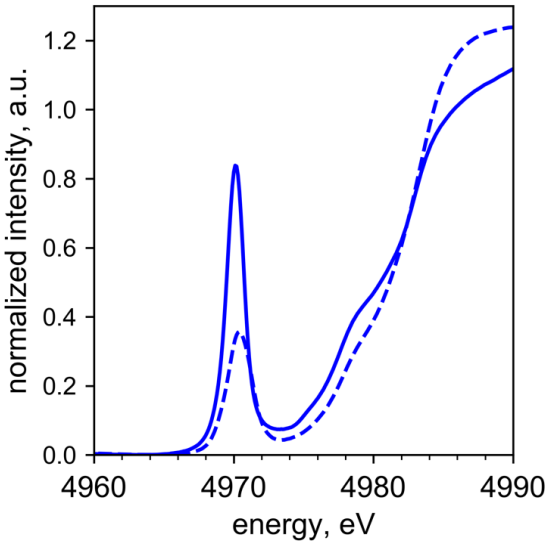

Figure A7.13. Normalized Ti K-edge spectra showing changes to pre-edge features for **Ti/3-a** (solid blue) following *in-situ* TBHP treatment (dashed blue). The position of the pre-edge maximum shifts from 4970.1 eV to 4970.4 eV.

7.6.4. Details of Kinetic Measurements of Cyclohexene Epoxidation with *t*-butyl Hydroperoxide

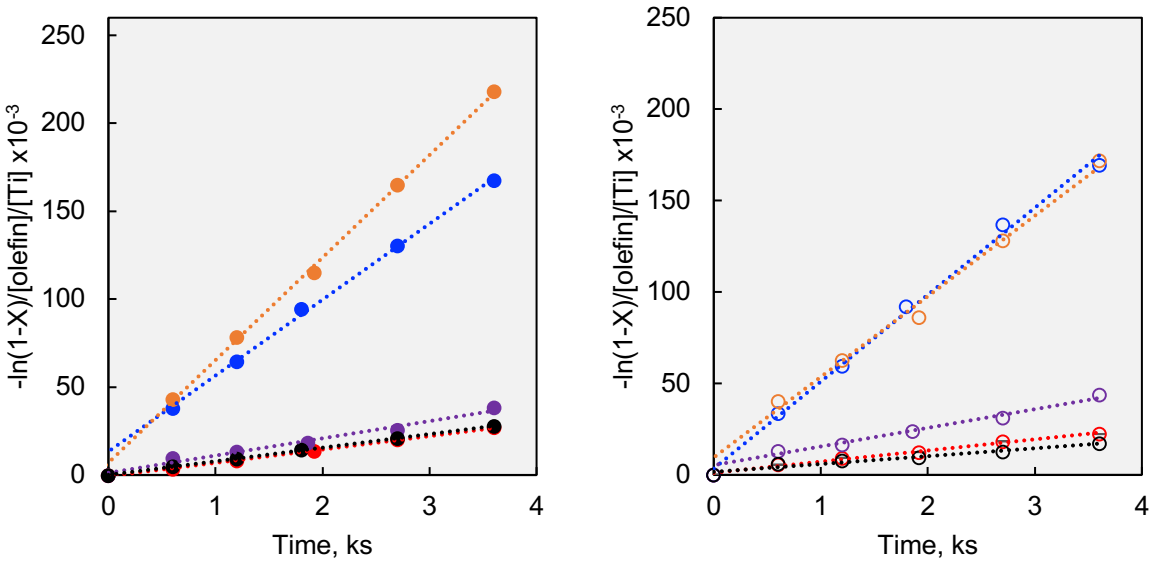

Figure A7.14. First-order rate constant plot for epoxidation of cyclohexene with *t*-butyl hydroperoxide, based on conversion (X) of the oxidant, used to calculate k_{eff} values reported in Table 7.1 and Figure 7.4. Filled markers (left) indicate **cTi/X** catalysts, while hollow markers (right) indicate **Ti/X** catalysts. Color coding consistent with Scheme 7.1 and Figure 7.1: **1** (red), **1-a** (black), **2** (purple), **3-a** (blue), **3-b** (orange).

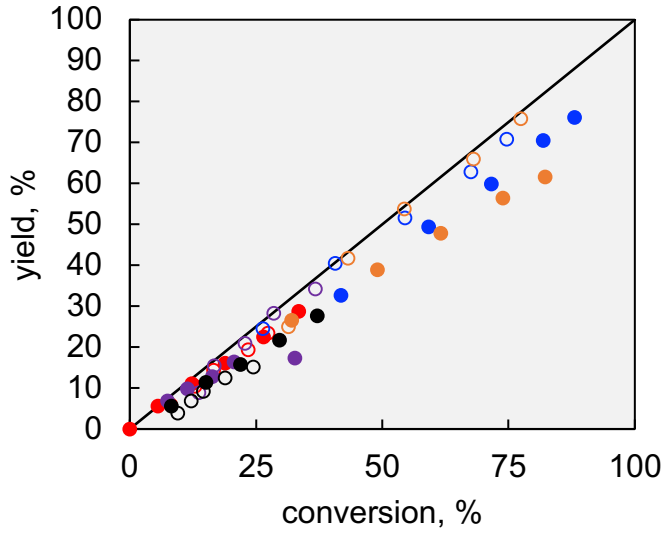

Figure A7.15. Yield of cyclohexene oxide as a function of cyclohexene conversion for all experiments shown in Figure 7.4. Data near parity lines indicates that conversion of oxidant results in stoichiometric production of epoxide (i.e. circa full selectivity). Color coding as in Figure A7.14.

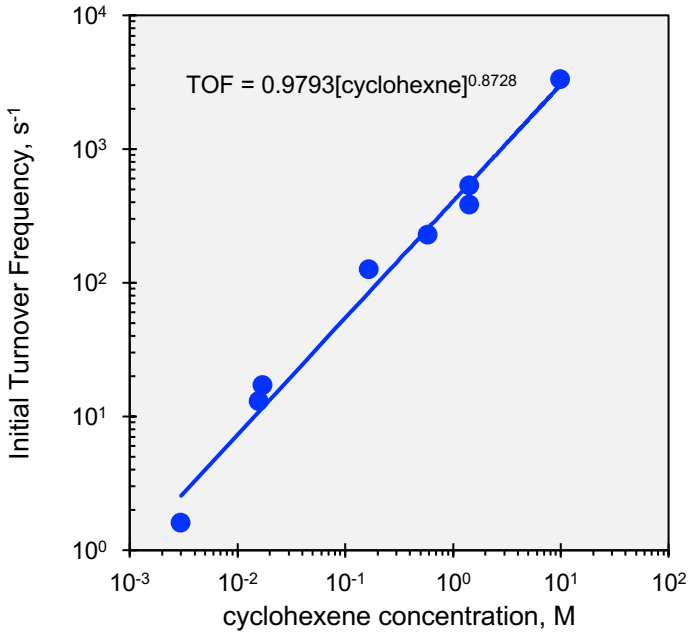

Figure A7.16. Initial turnover frequency for production of cyclohexene oxide catalyzed by **Ti/3-a**, as a function of cyclohexene concentration in octane (up to pure cyclohexene), while keeping initial TBHP concentration constant (see conditions in section 7.2.4). All experiments were performed at 323 K. Exponential fit is 0.87 ± 0.05, indicating that rates are pseudo-1st order in olefin at all concentrations

7.6.5. Details of Electronic Structure Calculations

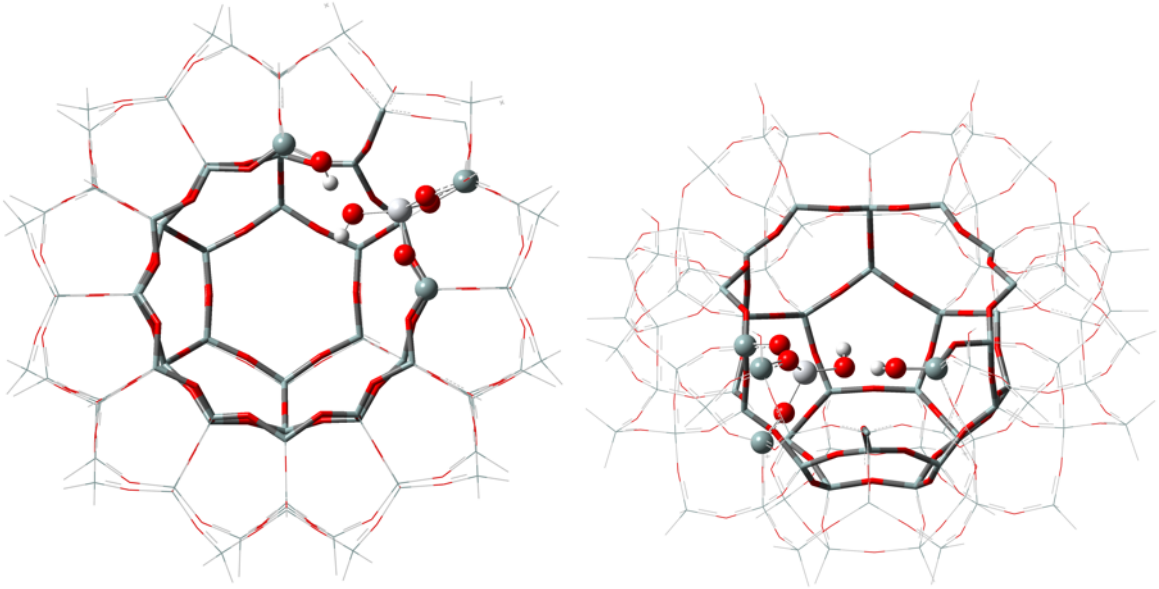

Figure A7.17. Views of the full 12-MR cup model used in building a model active-site. Oxygen in red, silicon in grey, and titanium (large) and hydrogen (small) in white. All atoms except those shown as full spheres were frozen in space based on SSZ-70 crystallographic information. Atoms shown as full spheres were allowed to fully relax and optimize at RB3LYLP-D3/6-311+G(d,p) level of theory. The rest of the atoms of the surrounding framework, treated at the RB3LYP-D3/6-31G level of theory, were deleted following optimization, and framework connectivity was modeled by frozen terminal hydrides, as shown in model active sites in Figure A.19. The atoms delimiting 12-MR external surface cup are shown as thick wire-and-frame model, while those of other atoms included are shown as thin wire-and-frame.

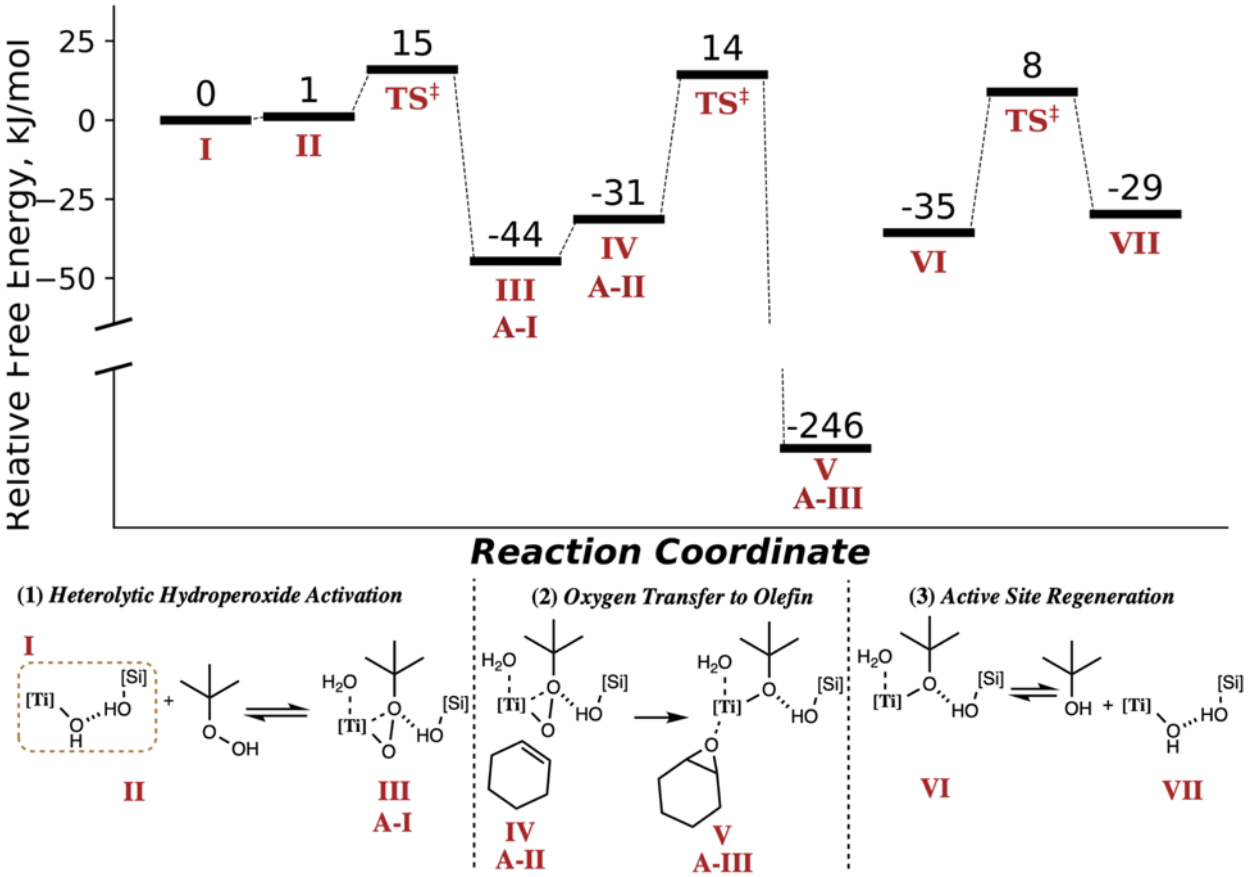

Figure A7.18. Reaction coordinate diagram showing calculated relative free energies of reaction intermediates **I** – **VII**, for elementary steps (1) – (3) involved in olefin epoxidation described in section 7.3.5. H-boding interactions are indicated by hashed bonds, while dative interactions are indicated by dashed bonds. The cluster model used in calculations corresponds to model **(A)** in Figure 7.6. The equivalence of certain species to those shown for model **(A)** in Figure 7.6 of the main text is indicated below each structure. Calculated structures **I** – **VII** and associated transition states are shown in Figure A.19.

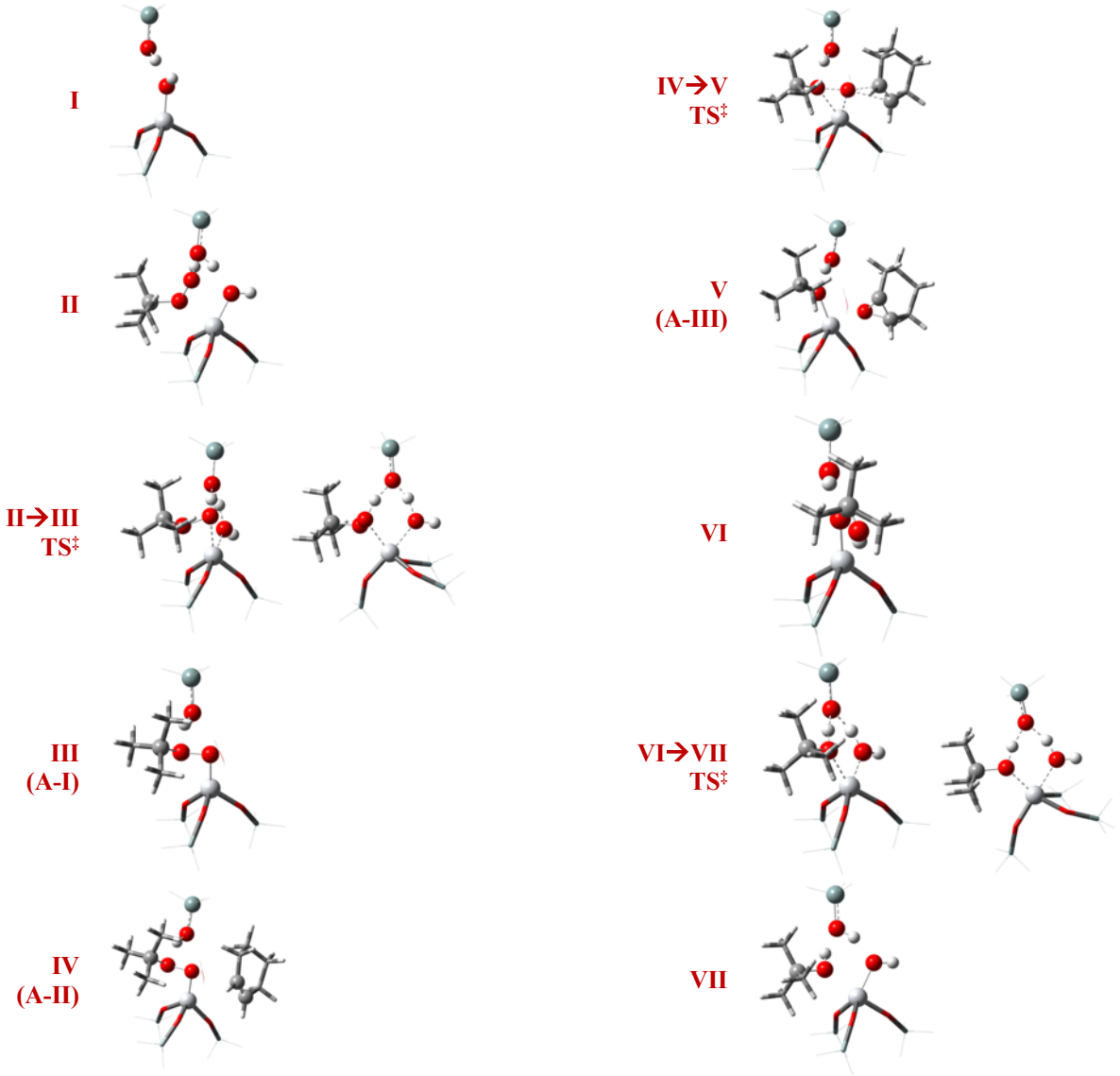

Figure A.19. Calculated structures whose energy is shown in Figure A7.18. H atoms are shown in white, O atoms in red, Si atoms in grey, C atoms in black, and the Ti center in off white; full ball-and-stick model shown only for atoms directly involved in the reaction events; frozen hydrides used as in the cluster models are shown as thinnest wires. Select transition state structures are shown from two different viewpoints.

7.7 References

(1) Degnan, T. F. The Implications of the Fundamentals of Shape Selectivity for the Development of Catalysts for the Petroleum and Petrochemical Industries. *J. Catal.* **2003**, *216*, 32–46.

(2) Corma, A. State of the Art and Future Challenges of Zeolites as Catalysts. *J. Catal.* **2003**, *216*, 298–312.

(3) Liu, Y.; Vjunov, A.; Shi, H.; Eckstein, S.; Camaioni, D. M.; Mei, D.; Baráth, E.; Lercher, J. A. Enhancing the Catalytic Activity of Hydronium Ions through Constrained Environments. *Nat. Commun.* **2017**, *8*, 14113.

(4) De Moor, B. A.; Reyniers, M. F.; Gobin, O. C.; Lercher, J. A.; Marin, G. B. Adsorption of C2-C8 n-Alkanes in Zeolites. *J. Phys. Chem. C* **2011**, *115*, 1204–1219.

(5) Ogino, I.; Chen, C. Y.; Gates, B. C. Zeolite-Supported Metal Complexes of Rhodium and of Ruthenium: A General Synthesis Method Influenced by Molecular Sieving Effects. *Dalt. Trans.* **2010**, *39*, 8423.

(6) Vermeiren, W.; Gilson, J. P. Impact of Zeolites on the Petroleum and Petrochemical Industry. *Top. Catal.* **2009**, *52*, 1131–1161.

(7) Csicsery, S. M. Shape-Selective Catalysis in Zeolites. *Zeolites* **1984**, *4*, 202–213.

(8) Bregante, D. T.; Thornburg, N. E.; Notestein, J. M.; Flaherty, D. W. Consequences of Confinement for Alkene Epoxidation with Hydrogen Peroxide on Highly Dispersed Group 4 and 5 Metal Oxide Catalysts. *ACS Catal.* **2018**, *8*, 2995–3010.

(9) Gounder, R.; Iglesia, E. The Roles of Entropy and Enthalpy in Stabilizing Ion-Pairs at Transition States in Zeolite Acid Catalysis. *Acc. Chem. Res.* **2012**, *42*, 229–238.

(10) Cordon, M. J.; Harris, J. W.; Vega-Vila, J. C.; Bates, J. S.; Kaur, S.; Gupta, M.; Witzke, M. E.; Wegener, E. C.; Miller, J. T.; Flaherty, D. W.; Hibbitts, D. D.; Gounder, R. The Dominant Role of Entropy in Stabilizing Sugar Isomerization Transition States within Hydrophobic Zeolite Pores. *J. Am. Chem. Soc.* **2018**, *140*, 14244–14266.

(11) Jones, A. J.; Zones, S. I.; Iglesia, E. Implications of Transition State Confinement within Small Voids for Acid Catalysis. *J. Phys. Chem. C* **2014**, *118*, 17787–17800.

(12) Khouw, C. B.; Davis, M. E. Shape-Selective Catalysis with Zeolites and Molecular Sieves. In *Selectivity in Catalysis*; ACS Symposium Series; American Chemical Society, 1993; Vol. 517, pp 14–206.

(13) Zou, X.; Wong, K. L.; Thomas, S.; Metzger, T. H.; Valtchev, V.; Mintova, S. Platinum Clusters Confined in FAU-LTA Hierarchical Porous Composite with a Core-Shell Structure. *Catal. Today* **2011**, *168*, 140–146.

(14) Tsapatsis, M. 2-Dimensional Zeolites. *AIChE J.* **2014**, *60*, 2374–2381.

(15) Grosso-Giordano, N. A.; Schroeder, C.; Okrut, A.; Solovyov, A.; Schöttle, C.; Chassé, W.; Marinković, N.; Koller, H.; Zones, S. I.; Katz, A. Outer-Sphere Control of Catalysis on Surfaces: A Comparative Study of Ti(IV) Single-Sites Grafted on Amorphous versus Crystalline Silicates for Alkene Epoxidation. *J. Am. Chem. Soc.* **2018**, *140*, 4956–4960.

(16) Canlas, C. P.; Lu, J.; Ray, N. A.; Grosso-Giordano, N. A.; Lee, S.; Elam, J. W.; Winans, R. E.; Van Duyne, R. P.; Stair, P. C.; Notestein, J. M. Shape-Selective Sieving Layers on an Oxide Catalyst Surface. *Nat. Chem.* **2012**, *4*, 1030–1036.

(17) Lin, F.; Zhang, J.; Liu, D.; Chin, Y.-H. (Cathy). Cascade Reactions in Tunable Lamellar Micro- and Mesopores for C=C Bond Coupling and Hydrocarbon Synthesis. *Angew. Chem. Int. Ed.* **2018**, *57*, 12886–12890.

(18) Radhakrishnan, S.; Goossens, P.-J.; Magusin, P. C. M. M.; Sree, S. P.; Detavernier, C.; Breynaert, E.; Martineau, C.; Taulelle, F.; Martens, J. A. In Situ Solid-State ^{13}C NMR Observation of Pore Mouth Catalysis in Etherification of β-Citronellene with Ethanol on Zeolite Beta. *J. Am. Chem. Soc.* **2016**, *138*, 2802–2808.
(19) Qin, Z.; Cychosz, K. A.; Melinte, G.; El Siblani, H.; Gilson, J.-P.; Thommes, M.; Fernandez, C.; Mintova, S.; Ersen, O.; Valtchev, V. Opening the Cages of Faujasite-Type Zeolite. *J. Am. Chem. Soc.* **2017**, *139*, 17273–17276.
(20) Rigoreau, J.; Laforge, S.; Gnep, N. S. S.; Guisnet, M. Alkylation of Toluene with Propene over H-MCM-22 Zeolite. Location of the Main and Secondary Reactions. *J. Catal.* **2005**, *236*, 45–54.
(21) Haw, K. G.; Gilson, J. P.; Nesterenko, N.; Akouche, M.; El Siblani, H.; Goupil, J. M.; Rigaud, B.; Minoux, D.; Dath, J. P.; Valtchev, V. Supported Embryonic Zeolites and Their Use to Process Bulky Molecules. *ACS Catal.* **2018**, *8*, 8199–8212.
(22) Luo, H. Y.; Michaelis, V. K.; Hodges, S.; Griffin, R. G.; Román-Leshkov, Y.; Roman-Leshkov, Y. One-Pot Synthesis of MWW Zeolite Nanosheets Using a Rationally Designed Organic Structure-Directing Agent. *Chem. Sci.* **2015**, *6*, 6320–6324.
(23) Wolfenden, R.; Snider, M. J. The Depth of Chemical Time and the Power of Enzymes as Catalysts. *Acc. Chem. Res.* **2001**, *34*, 938–945.
(24) Romesberg, F. E.; Spiller, B.; Schultz, P. G.; Stevens, R. C. Immunological Origins of Binding and Catalysis in a Diels-Alderase Antibody. *Science* **1998**, *279*, 1929–1933.
(25) Oyama, S. T. *Mechanisms in Homogeneous and Heterogeneous Epoxidation Catalysis*; Elsevier: Amsterdam, 2011.
(26) Sheldon, R. A.; Van Doorn, J. A. Metal-Catalyzed Epoxidation of Olefins with Organic Hydroperoxides. I. A Comparison of Various Metal Catalysts. *J. Catal.* **1973**, *31*, 427–437.
(27) Sheldon, R. A. Synthetic and Mechanistic Aspects of Metal-Catalysed Epoxidations with Hydroperoxides. *J. Mol. Catal.* **1980**, *7*, 107–126.
(28) Notestein, J. M.; Iglesia, E.; Katz, A. Grafted Metallocalixarenes as Single-Site Surface Organometallic Catalysts. *J. Am. Chem. Soc.* **2004**, *126*, 16478–16486.
(29) Notestein, J. M.; Andrini, L. R.; Kalchenko, V. I.; Requejo, F. G.; Katz, A.; Iglesia, E. Structural Assessment and Catalytic Consequences of the Oxygen Coordination Environment in Grafted Ti-Calixarenes. *J. Am. Chem. Soc.* **2007**, *129*, 1122–1131.
(30) Notestein, J. M.; Solovyov, A.; Andrini, L. R.; Requejo, F. G.; Katz, A.; Iglesia, E. The Role of Outer-Sphere Surface Acidity in Alkene Epoxidation Catalyzed by Calixarene-Ti(IV) Complexes. *J. Am. Chem. Soc.* **2007**, *129*, 15585–15595.
(31) Ogino, I.; Eilertsen, E. A.; Hwang, S.-J.; Rea, T.; Xie, D.; Ouyang, X.; Zones, S. I.; Katz, A. Heteroatom-Tolerant Delamination of Layered Zeolite Precursor Materials. *Chem. Mater.* **2013**, *25*, 1502–1509.
(32) Smeets, S.; Berkson, Z. J.; Xie, D.; Zones, S. I.; Wan, W.; Zou, X.; Hsieh, M. F.; Chmelka, B. F.; McCusker, L. B.; Baerlocher, C. Well-Defined Silanols in the Structure of the Calcined High-Silica Zeolite SSZ-70: New Understanding of a Successful Catalytic Material. *J. Am. Chem. Soc.* **2017**, *139*, 16803–16812.
(33) Lawton, S. L.; Leonowicz, M. E.; Partridge, R. D.; Chu, P.; Rubin, M. K. Twelve-Ring Pockets on the External Surface of MCM-22 Crystals. *Microporous Mesoporous Mater.* **1998**, *23*, 109–117.
(34) Eilertsen, E. A.; Ogino, I.; Hwang, S.-J.; Rea, T.; Yeh, S.; Zones, S. I.; Katz, A.

Nonaqueous Fluoride/Chloride Anion-Promoted Delamination of Layered Zeolite Precursors: Synthesis and Characterization of UCB-2. *Chem. Mater.* **2011**, *23*, 5404–5408.
(35) Okrut, A.; Aigner, M.; Schöttle, C.; Grosso-Giordano, N. A.; Hwang, S.-J.; Ouyang, X.; Zones, S.; Katz, A. SSZ-70 Borosilicate Delamination without Sonication: Effect of Framework Topology on Olefin Epoxidation Catalysis. *Dalt. Trans.* **2018**, *47*, 15082–15090.
(36) Galletero, M. S.; Corma, A.; Ferrer, B.; Fornés, V.; García, H. Confinement Effects at the External Surface of Delaminated Zeolites (ITQ-2): An Inorganic Mimic of Cyclodextrins. *J. Phys. Chem. B* **2003**, *107*, 1135–1141.
(37) Ek, S.; Root, A.; Peussa, M.; Niinistö, L. Determination of the Hydroxyl Group Content in Silica by Thermogravimetry and a Comparison with ^{1}H MAS NMR Results. *Thermochim. Acta* **2001**, *379*, 201–212.
(38) Hsieh, M.-F. Ph.D. Dissertation, University of California, Santa Barbara, CA, 2014.
(39) Bayram, E.; Lu, J.; Aydin, C.; Browning, N. D.; Özkar, S.; Finney, E.; Gates, B. C.; Finke, R. G. Agglomerative Sintering of an Atomically Dispersed Ir_1Zeolite Y Catalyst: Compelling Evidence Against Ostwald Ripening but for Bimolecular and Autocatalytic Agglomeration Catalyst Sintering Steps. *ACS Catal.* **2015**, *5*, 3514−3527.
(40) Uzon, A.; Gates, B. C. Real-Time Characterization of Formation and Breakup of Iridium Clusters in Highly Dealuminated Zeolite Y. *Angew. Chem. Int. Ed.* **2008**, *47*, 9245–9248.
(41) Bouh, A. O.; Rice, G. L.; Scott, S. L. Mono- and Dinuclear Silica-Supported Titanium(IV) Complexes and the Effect of TiOTi Connectivity on Reactivity. *J. Am. Chem. Soc.* **1999**, *121*, 7201–7210.
(42) Tao, F.; Dag, S.; Wang, L. W.; Liu, Z.; Butcher, D. R.; Bluhm, H.; Salmeron, M.; Somorjai, G. A. Break-up of Stepped Platinum Catalyst Surfaces by High Co Coverage. *Science* **2010**, *327*, 850–853.
(43) Moliner, M.; Gabay, J. E.; Kliewer, C. E.; Carr, R. T.; Guzman, J.; Casty, G. L.; Serna, P.; Corma, A. Reversible Transformation of Pt Nanoparticles into Single Atoms inside High-Silica Chabazite Zeolite. *J. Am. Chem. Soc.* **2016**, *138*, 15743–15750.
(44) Zugic, B.; Wang, L.; Heine, C.; Zakharov, D. N.; Lechner, B. A. J.; Stach, E. A.; Biener, J.; Salmeron, M.; Madix, R. J.; Friend, C. M. Dynamic Restructuring Drives Catalytic Activity on Nanoporous Gold-Silver Alloy Catalysts. *Nat. Mater.* **2017**, No. 16, 558–564.
(45) Paolucci, C.; Khurana, I.; Parekh, A. A.; Li, S.; Shih, A. J.; Li, H.; Di Iorio, J. R.; Albarracin-Caballero, J. D.; Yezerets, A.; Miller, J. T.; Delgass, W. N.; Ribeiro, F. H.; Schneider, W. F.; Gounder, R. Dynamic Multinuclear Sites Formed by Mobilized Copper Ions in NOx Selective Catalytic Reduction. *Science* **2017**, *357*, 898–903.
(46) Howell, J. G.; Li, Y.-P.; Bell, A. T. Propene Metathesis over Supported Tungsten Oxide Catalysts: A Study of Active Site Formation. *ACS Catal.* **2016**, *6*, 7728–7738.
(47) Archer, R. H.; Carpenter, J. R.; Hwang, S.-J.; Burton, A. W.; Chen, C.-Y.; Zones, S. I.; Davis, M. E. Physicochemical Properties and Catalytic Behavior of the Molecular Sieve SSZ-70. *Chem. Mater.* **2010**, *22*, 2563–2572.
(48) Archer, R. H.; Zones, S. I.; Davis, M. E. Imidazolium Structure Directing Agents in Zeolite Synthesis: Exploring Guest/Host Relationships in the Synthesis of SSZ-70. *Microporous Mesoporous Mater.* **2010**, *130*, 255–265.
(49) Groenen, L. C.; Ruël, B. H. M.; Casnati, A.; Verboom, W.; Pochini, A.; Ungaro, R.; Reinhoudt, D. N. Synthesis of Monoalkylated Calix[4]Arenes via Direct Alkylation. *Tetrahedron* **1991**, *47*, 8379–8384.

(50) Friedrich, A.; Radius, U. A Calix[4]Arene Monoalkyl Ether as a Model of a Tris(Phenolate) Ligand with a Hemilabile Anisole Moiety: Syntheses, Molecular Structures and Bonding of Calix[4]Arene Ether Supported Titanium Complexes and Their Catalytic Activity in Epoxidation Reactions. *Eur. J. Inorg. Chem.* **2004**, *2004*, 4300–4316.
(51) Ertl, G.; Knözinger, H.; Weitkamp, J. *Handbook of Heterogeneous Catalysis*; Wiley: Weinheim, Germany, 1997.
(52) Vansant, E. F.; Voort, P. Van Der; Vrancken, K. C. *Characterization and Chemical Modification of the Silica Surface*, 1st ed.; Elsevier, 1995; Vol. 93.
(53) Eaton, T. R.; Campos, M. P.; Gray, K. A.; Notestein, J. M. Quantifying Accessible Sites and Reactivity on Titania-Silica (Photo)Catalysts: Refining TOF Calculations. *J. Catal.* **2014**, *309*, 156–165.
(54) Ravel, B.; Newville, M. ATHENA, ARTEMIS, HEPHAESTUS: Data Analysis for X-Ray Absorption Spectroscopy Using IFEFFIT. *J. Synchrotron Radiat.* **2005**, *12*, 537–541.
(55) Corma, A.; Domine, M.; Gaona, J. A.; Jordá, J. L.; Navarro, M. T.; Rey, F.; Pérez-Pariente, J.; Tsuji, J.; McCulloch, B.; Nemeth, L. T. Strategies to Improve the Epoxidation Activity and Selectivity of Ti-MCM-41. *Chem. Commun.* **1998**, No. 20, 2211–2212.
(56) Zawadiak, J.; Gilner, D.; Kulicki, Z.; Baj, S. Concurrent Iodimetric Determination of Cumene Hydroperoxide and Dicumenyl Peroxide Used for Reaction Control in Dicumenyl Peroxide Synthesis. *Analyst* **1993**, *118*, 1081.
(57) Frisch, M. J. G.; Trucks, W.; Schlegel, H. B.; Scuseria, G. E.; Robb, M. A.; Cheeseman, J. R.; Scalmani, G.; Barone, V.; Mennucci, B.; Petersson, G. A.; Nakatsuji, H.; Caricato, M.; Li, X.; Hratchian, H. P.; Izmaylov, A. F.; Bloino, J.; Zheng, G.; Sonnenberg, J. L. *Gaussian 16, Rev. A.03*; 2016.
(58) Becke, A. D. Density-Functional Thermochemistry. III. The Role of Exact Exchange. *J. Chem. Phys.* **1993**, *98*, 5648.
(59) Stephens, P. J.; Devlin, F. J.; Chabalowski, C. F.; Frisch, M. J. Ab Initio Calculation of Vibrational Absorption and Circular Dichroism Spectra Using Density Functional Force Fields. *J. Phys. Chem.* **1994**, *98*, 11623–11627.
(60) Grimme, S.; Antony, J.; Ehrlich, S.; Krieg, H. A Consistent and Accurate Ab Initio Parametrization of Density Functional Dispersion Correction (DFT-D) for the 94 Elements H-Pu. *J. Chem. Phys.* **2010**, *132*, 154104.
(61) Tomasi, J.; Mennucci, B.; Cammi, R. Quantum Mechanical Continuum Solvation Models. *Chem. Rev.* **2005**, *105*, 2999–3094.
(62) Koller, H.; Chen, C. Y.; Zones, S. I. Selectivities in Post-Synthetic Modification of Borosilicate Zeolites. *Top. Catal.* **2015**, *58*, 451–479.
(63) Senderov, E.; Halasz, I.; Olson, D. H. On Existence of Hydroxyl Nests in Acid Dealuminated Zeolite Y. *Microporous Mesoporous Mater.* **2014**, *186*, 94–100.
(64) Halasz, I.; Senderov, E.; Olson, D. H.; Liang, J. J. Further Search for Hydroxyl Nests in Acid Dealuminated Zeolite Y. *J. Phys. Chem. C* **2015**, *119*, 8619–8625.
(65) Wells, D. H.; Delgass, W. N.; Thomson, K. T. Evidence of Defect-Promoted Reactivity for Epoxidation of Propylene in Titanosilicate (TS-1) Catalysts: A DFT Study. *J. Am. Chem. Soc.* **2004**, *126*, 2956–2962.
(66) Lin, W.; Frei, H. Photochemical and FT-IR Probing of the Active Site of Hydrogen Peroxide in Ti Silicalite Sieve. *J. Am. Chem. Soc.* **2002**, *124*, 9292–9298.
(67) Neurock, M.; Manzer, L. E. Theoretical Insights on the Mechanism of Alkene Epoxidation

by H_2O_2 with Titanium Silicalite. *Chem. Commun.* **1996**, No. 10, 1133.
(68) Wells, D. H.; Joshi, A. M.; Delgass, W. N.; Thomson, K. T. A Quantum Chemical Study of Comparison of Various Propylene Epoxidation Mechanisms Using H_2O_2 and TS-1 Catalyst. *J. Phys. Chem. B* **2006**, *110*, 14627–14639.
(69) Lundin, A.; Panas, I.; Ahlberg, E. Quantum Chemical Modeling of Propene and Butene Epoxidation with Hydrogen Peroxide. *J. Phys. Chem. A* **2009**, *113*, 282–290.
(70) Sever, R. R.; Root, T. W. DFT Study of Solvent Coordination Effects on Titanium-Based Epoxidation Catalysts. Part One: Formation of the Titanium Hydroperoxo Intermediate. *J. Phys. Chem. B* **2003**, *107*, 4080–4089.
(71) Sever, R. R.; Root, T. W. DFT Study of Solvent Coordination Effects on Titanium-Based Epoxidation Catalysts. Part Two: Reactivity of Titanium Hydroperoxo Complexes in Ethylene Epoxidation. *J. Phys. Chem. B* **2003**, *107*, 4090–4099.
(72) V., Y. I.; Philip, G.; Cristiana, D. V.; Notker, R. Activity of Peroxo and Hydroperoxo Complexes of Ti^{IV} in Olefin Epoxidation: A Density Functional Model Study of Energetics and Mechanism. *Eur. J. Inorg. Chem.* **1999**, *1999*, 2135–2145.
(73) Barker, C. M.; Gleeson, D.; Kaltsoyannis, N.; Catlow, C. R. A.; Sankar, G.; Thomas, J. M. On the Structure and Coordination of the Oxygen-Donating Species in Ti↑MCM-41/TBHP Oxidation Catalysts: A Density Functional Theory and EXAFS Study. *Phys. Chem. Chem. Phys.* **2002**, *4*, 1228–1240.
(74) Yabushita, M.; Grosso-Giordano, N. A.; Fukuoka, A.; Katz, A. Selective Sequestration of Aromatics from Aqueous Mixtures with Sugars by Hydrophobic Molecular Calixarene Cavities Grafted on Silica. *ACS Appl. Mater. Interfaces* **2018**, *10*, 39670–39678.
(75) Bregante, D. T.; Johnson, A. M.; Patel, A. Y.; Ayla, E. Z.; Cordon, M. J.; Bukowski, B. C.; Greeley, J.; Gounder, R.; Flaherty, D. W. Cooperative Effects between Hydrophilic Pores and Solvents: Catalytic Consequences of Hydrogen Bonding on Alkene Epoxidation in Zeolites. *J. Am. Chem. Soc.* **2019**.
(76) Khouw, C. B.; Davis, M. E. Catalytic Activity of Titanium Silicates Synthesized in the Presence of Alkali-Metal and Alkaline-Earth Ions. *J. Catal.* **1995**, *151*, 77–86.
(77) Vayssilov, G. N.; Van Santen, R. A. Catalytic Activity of Titanium Silicalites - A DFT Study. *J. Catal.* **1998**, *175*, 170–174.
(78) Bordiga, S.; Roggero, I.; Ugliengo, P.; Zecchina, A.; Bolis, V.; Artioli, G.; Buzzoni, R.; Marra, G.; Rivetti, F.; Spanò, G.; Lamberti, C. Characterisation of Defective Silicalites. *J. Chem. Soc. Dalt. Trans.* **2000**, No. 21, 3921–3929.
(79) Marchese, L.; Maschmeyer, T.; Gianotti, E.; Coluccia, S.; Thomas, J. M. Probing the Titanium Sites in Ti−MCM41 by Diffuse Reflectance and Photoluminescence UV−Vis Spectroscopies. *J. Phys. Chem. B* **1997**, *101*, 8836–8838.
(80) Zanotti-Gerosa, A.; Solari, E.; Giannini, L.; Floriani, C.; Re, N.; Chiesi-Villa, A.; Rizzoli, C. Titanium-Carbon Functionalities on an Oxo Surface Defined by a Calix [4] Arene Moiety and Its Redox Chemistry. *Inorganica Chim. Acta* **1998**, *270*, 298–311.
(81) George, S. D. B.; Brant, P.; Solomon, E. I. Metal and Ligand K-Edge XAS of Organotitanium Complexes: Metal 4p and 3d Contributions to Pre-Edge Intensity and Their Contributions to Bonding. *J. Am. Chem. Soc.* **2005**, *127*, 667–674.
(82) Bordiga, S.; Coluccia, S.; Lamberti, C.; Marchese, L.; Zecchina, A.; Boscherini, F.; Buffa, F.; Genoni, F.; Leofanti, G.; Petrini, G.; Vlaic, G. XAFS Study of Ti-Silicalite: Structure of Framework Ti(IV) in the Presence and Absence of Reactive Molecules (H_2O, NH_3) and

Comparison with Ultraviolet-Visible and IR Results. *J. Phys. Chem.* **1994**, *98*, 4125–4132.
(83) Ricchiardi, G.; Damin, A.; Bordiga, S.; Lamberti, C.; Spanò, G.; Rivetti, F.; Zecchina, A. Vibrational Structure of Titanium Silicate Catalysts. A Spectroscopic and Theoretical Study. *J. Am. Chem. Soc.* **2001**, *123*, 11409–11419.
(84) Bravo-Suárez, J. J.; Bando, K. K.; Lu, J.; Haruta, M.; Fujitani, T.; Oyama, S. T. Transient Technique for Identification of True Reaction Intermediates: Hydroperoxide Species in Propylene Epoxidation on Gold/Titanosilicate Catalysts by X-Ray Absorption Fine Structure Spectroscopy. *J. Phys. Chem. C* **2008**, *112*, 1115–1123.
(85) Bregante, D. T.; Flaherty, D. W. Periodic Trends in Olefin Epoxidation over Group IV and v Framework-Substituted Zeolite Catalysts: A Kinetic and Spectroscopic Study. *J. Am. Chem. Soc.* **2017**, *139*, 6888–6898.
(86) Thornburg, N. E.; Thompson, A. B.; Notestein, J. M. Periodic Trends in Highly Dispersed Groups IV and V Supported Metal Oxide Catalysts for Alkene Epoxidation with H_2O_2. *ACS Catal.* **2015**, *5*, 5077–5088.
(87) Hoffmann, P.; Knözinger, E. Novel Aspects of Mid and Far IR Fourier Spectroscopy Applied to Surface and Adsorption Studies on SiO2. *Surf. Sci.* **1987**, *188*, 181–198.
(88) Zecchina, A.; Bordiga, S.; Spoto, G.; Marchese, L.; Petrini, G.; Leofanti, G.; Padovan, M. Silicalite Characterization. 2. IR Spectroscopy of the Interaction of Carbon Monoxide with Internal and External Hydroxyl Groups. *J. Phys. Chem.* **1992**, *96*, 4991–4997.
(89) Sato, H. Acidity Control and Catalysis of Pentasil Zeolites. *Catal. Rev. - Sci. Eng.* **1997**, *39*, 395–424.
(90) Kawai, T.; Tsutsumi, K. Reactivity of Silanol Groups on Zeolite Surfaces. *Colloid Polym. Sci.* **1998**, *276*, 992–998.
(91) Blasco, T.; Corma, A.; Navarro, M. T.; Pérez Pariente, J. Synthesis, Characterization, and Catalytic Activity of Ti-MCM-41 Structures. *J. Catal.* **1995**, *156*, 65–74.
(92) Khouw, C.; Dartt, C. B.; Labinger, J. A.; Davis, M. E. Studies on the Catalytic-Oxidation of Alkanes and Alkenes by Titanium Silicates. *J. Catal.* **1994**, *149*, 195–205.
(93) Grosso-Giordano, N. A.; Solovyov, A.; Hwang, S.-J.; Katz, A. Effect of Coordination Environment in Grafted Single-Site Ti-SiO_2 Olefin Epoxidation Catalysis. *Top. Catal.* **2016**, *59*, 1110–1122.
(94) Gounder, R.; Iglesia, E. The Catalytic Diversity of Zeolites: Confinement and Solvation Effects within Voids of Molecular Dimensions. *Chem. Commun.* **2013**, *49*, 3491.
(95) Gounder, R.; Iglesia, E. Catalytic Consequences of Spatial Constraints and Acid Site Location for Monomolecular Alkane Activation on Zeolites. *J. Am. Chem. Soc.* **2009**, *131*, 1958–1971.
(96) Ratnasamy, P.; Srinivas, D.; Knözinger, H. Active Sites and Reactive Intermediates in Titanium Silicate Molecular Sieves. *Adv. Catal.* **2004**, *48*, 1–169.
(97) Ouyang, X.; Hwang, S.-J.; Xie, D.; Rea, T.; Zones, S. I.; Katz, A. Heteroatom-Substituted Delaminated Zeolites as Solid Lewis Acid Catalysts. *ACS Catal.* **2015**, *5*, 3108–3119.
(98) Grosso-Giordano, N. A.; Yeh, A. J.; Okrut, A.; Xiao, D. J.; Grandjean, F.; Long, G. J.; Zones, S. I.; Katz, A. Effect of Defect Site Preorganization on Fe(III) Grafting and Stability: A Comparative Study of Delaminated Zeolite vs Amorphous Silica Supports. *Chem. Mater.* **2017**, *29*, 6480–6492.
(99) Sankar, G.; Thomas, J. M.; Catlow, C. R. A.; Barker, C. M.; Gleeson, D.; Kaltsoyannis, N. The Three-Dimensional Structure of the Titanium-Centered Active Site during Steady-State

Catalytic Epoxidation of Alkenes. *J. Phys. Chem. B* **2001**, *105*, 9028–9030.
(100) Mania, P.; Verel, R.; Jenny, F.; Hammond, C.; Hermans, I. Thermal Restructuring of Silica-Grafted $TiCl_x$ Species and Consequences for Epoxidation Catalysis. *Chem. - A Eur. J.* **2013**, *19*, 9849 – 9858.
(101) Buijink, J. K. F.; Lange, J. P.; Bos, A. N. R.; Horton, A. D.; Niele, F. G. M. Propylene Epoxidation Via Shell's Smpo Process: 30 Years of Research and Operation. In *Mechanisms in Homogeneous and Heterogeneous Epoxidation Catalysis*; 2008; pp 355–371.
(102) Sever, R. R.; Alcala, R.; Dumesic, J. A.; Root, T. W. Vapor-Phase Silylation of MCM-41 and Ti-MCM-41. *Microporous Mesoporous Mater.* **2003**, *66*, 53–67.
(103) Herrmann, S.; Iglesia, E. Elementary Steps in Acetone Condensation Reactions Catalyzed by Aluminosilicates with Diverse Void Structures. *J. Catal.* **2017**, *346*, 134–153.
(104) Nigra, M. M.; Katz, A. Cooperative Catalysis on Solid Surfaces versus Soluble Molecules. In *Cooperative Catalysis: Designing Efficient Catalysts for Synthesis*; 2015; pp 351–371.
(105) Bass, J. D.; Solovyov, A.; Pascall, A. J.; Katz, A. Acid-Base Bifunctional and Dielectric Outer-Sphere Effects in Heterogeneous Catalysis: A Comparative Investigation of Model Primary Amine Catalysts. *J. Am. Chem. Soc.* **2006**, *128*, 3737–3747.
(106) Hastings, C. J.; Fiedler, D.; Bergman, R. G.; Raymond, K. N. Aza Cope Rearrangement of Propargyl Enammonium Cations Catalyzed By a Self-Assembled "Nanozyme." *J. Am. Chem. Soc.* **2008**, *130*, 10977–10983.
(107) Roth, W. J.; Čejka, J. Two-Dimensional Zeolites: Dream or Reality? *Catal. Sci. Technol.* **2011**, *1*, 43.
(108) Opanasenko, M. V; Roth, W. J.; Cejka, J. Two-Dimensional Zeolites in Catalysis: Current Status and Perspectives. *Catal. Sci. Technol.* **2016**, 2467–2484.
(109) Witman, M.; Ling, S.; Boyd, P.; Barthel, S.; Haranczyk, M.; Slater, B.; Smit, B. Cutting Materials in Half: A Graph Theory Approach for Generating Crystal Surfaces and Its Prediction of 2D Zeolites. *ACS Cent. Sci.* **2018**, *4*, 235–245.
(110) Arslan, I.; Roehling, J. D.; Ogino, I.; Batenburg, K. J.; Zones, S. I.; Gates, B. C.; Katz, A. Genesis of Delaminated-Zeolite Morphology: 3-D Characterization of Changes by STEM Tomography. *J. Phys. Chem. Lett.* **2015**, *6*, 2598–2602.
(111) Millini, R.; Perego, G.; Parker, W. O.; Bellussi, G.; Carluccio, L. Layered Structure of ERB-1 Microporous Borosilicate Precursor and Its Intercalation Properties towards Polar Molecules. *Microporous Mater.* **1995**, *4*, 221–230.

Conclusions and Outlook

This thesis developed synthetic approaches and experimental methods (Chapter 2, 4, 5) to understand how the molecular environment surrounding a grafted cation impacts the stability of active sites (Chapter 3), conformation of adsorbates (Chapter 6) and rates of catalysis (Chapter 7). This data demonstrates the crucial role of designing surface structures, and not just surface compositions, in order to control the outer-sphere environment surrounding an active site. For catalysis, this leads to new approaches for achieving optimal reactivity and stability of oxide catalysts. The synthetic control over active-site structure required to reach these conclusions was developed through a multi-faceted approach, involving an organic ligand that protects the cation from the 'top' during grafting, and a silicate surface which controls the grafted environment from the 'bottom'.

The location of the cation on the surface is dictated by surface silanols which act as sites for grafting. This motivated the detailed investigation of the location of these silanol groups, which led to resolving outstanding questions on their speciation in Chapter 2. In particular, this chapter leads to an important conclusion: that despite being compositionally identical SiO_2 networks, crystalline zeotypes exhibit distinct advantages over amorphous silica supports: (1) they provide structural uniformity for understanding the location of silanols and active sites grafted onto them, and (2) they act as mechanically stable networks as compared to amorphous silica. These two fundamental differences have repercussion for the rest of the work in this thesis.

The consequences of mechanical stability are demonstrated in Chapter 3, where uniform and stable vacancy defects in zeotype frameworks act as chelating grafting environment for Fe^{3+} centers. During harsh thermal and hydrothermal treatments, these Fe^{3+} centers remain stable when part of a crystalline zeotype, but leach and aggregate when incorporated into an amorphous silica network under similar conditions. These observations suggest that mechanically rigid zeotype frameworks can be used to construct metallosilicate catalysts with superior stability relative to conventional amorphous-silica catalysts. Many such amorphous catalysts are used industrially (Ti/SiO_2 for epoxidation, W/SiO_2 for olefin metathesis, Cr/SiO_2 for polymerization, for example). As such, the use of crystalline zeotypes supports may open the door for designing potentially more robust and tunable next generation catalysts for these reactions.

Chapter 4 demonstrates the use of calix[4]arene organic ligands to control the coordination environment of a Ti^{IV} center, an active site for olefin epoxidation, from the 'top'. By using this approach, the inner-sphere coordination environment (i.e. the ligands directly bound to the Ti^{IV} center) can be tuned, independent of the support. The UV-visible spectroscopic methods established in this chapter are important in understanding Ti^{IV} coordination in grafted calix[4]arene-Ti^{IV} centers that are the focus of Chapters 5-7.

In Chapter 5, I used this grafted calix[4]arene-Ti^{IV} synthesis approach to fix the pseudo-tetrahedral coordination environment of Ti^{IV} across different silicate supports. Given this fixed inner-sphere environment of Ti^{IV}, independent of silicate support, the increased epoxidation reactivity of zeolitic supports can be rigorously ascribed solely to the outer-sphere surface structures surrounding Ti^{IV} centers. In addition, the location of Ti^{IV} centers on the external surface of the zeotype only (as opposed to conventional zeolite micropores), enforced by the bulkiness of the calix[4]arene-Ti^{IV} complex, enabled the comparison of rates in the absence of steric constraints. Such constraints had hitherto prevented a rigorous comparison of amorphous

titanosilicates (used industrially for propylene epoxidation with organic hydroperoxides) and zeolitic titanosilicates (used industrially for propylene epoxidation with hydrogen peroxide, but historically poor catalysts with organic hydroperoxides) as epoxidation catalysts, despite decades of research. The calix[4]arene-Ti^{IV} approach resolved these issues, demonstrating that superior reactivity can be achieved using structurally uniform silicates surfaces as catalysts supports.

Chapters 6 and 7 introduce a synthetic method that enables rigorous control over the location of an calix[4]arene-Ti^{IV} complex in an MWW-type zeotype surface. By synthetically controlling the location of silanols, the grafting of this complex can be directed to occur within a partially confining 12-MR surface pocket (7 Å in diameter), versus nonconfining terminal T-atom immediately outside of this pocket. Such precise synthetic control over the location of a grafted structure is largely unprecedented, and enables the observation of how unique structures (external-surface pockets) impact adsorption and catalysis in these two chapters.

In Chapter 6, I demonstrate how this synthetic method can be used to construct crystallographically equivalent grafted structures at the precise interface between a surface and the partially confining 12-MR pocket. This leads to a unique molecular conformation of a macrocycle that is partially confined by a microporous cavity, altering its conformation. Such a partially confined structure provides a "molecular snapshot" of a molecule as it penetrates the pore. This "snapshot" helps explain previously postulated effects of partial confinement on adsorption and catalysis, and demonstrates that 12-MR pockets on the surface of zeotypes act as partially confining structures.

The catalytic repercussions of partial confinement within these 12-MR pockets is examined in Chapter 7. In this chapter, the location of active sites for olefin epoxidation is directed to be within partially confining 12-MR pockets, or directly outside of them. When active sites (and reactions) are located within these pockets, 5-fold rate enhancements are observed, relative to nonconfined active sites located immediately outside – but not within – 12-MR pockets. Kinetic measurements reveal that these rate enchantments are due to diminished entropic barriers that accompany reactions within the sterically constrained 12-MR pockets. These observations demonstrate how reactivity can be controlled through partial confinement of reactions within shallow external-surface pockets.

Significantly, 12-MR pockets are accessible to molecules that are too bulky to benefit from traditional confinement within micropores. As such, partially confining structures hold the potential to extend beneficial confinement effects to a much wider range of reactions, involving intermediates too bulky to access micropores, but which can nonetheless access partially confining structures on a 2-D surface. This motivates the importance of research into so called "2-dimensional zeolites", which exhibit a high degree of external surface area: this external surface, as demonstrated in Chapter 7, provides unique opportunities for controlling reactivity by partial confinement. This partial confinement can be maximized by developing methods to increase the specific external surface area of 2-D zeotypes (thereby exposing more partially confining structures), and could be tuned by choice of a different 2-D zeotype topology.

Taken together, the results in this thesis point towards using zeotype supports for controlling catalysis by tuning in the microenvironment that surrounds an active site on an external surface. This can lead to fundamentally new knowledge on the structure and function of active sites, as demonstrated for Ti^{IV}-catalyzed epoxidation in this thesis, as well as new approaches for

controlling catalysis on solid surfaces that have no parallel when using amorphous supports. Such new understandings of active site requirements for catalysis build an important bridge between mechanical features of environment on the molecular level and catalytically active sites. We anticipate they will guide the development of the next generation of industrial heterogenous catalysts, whose rational design on the molecular level still remains as an elusive goal.